Geodetic observations and modeling of gravity field, sea level, and ocean dynamics in the Norwegian coastal zone

Geodetiske observasjoner og modellering av tyngdefelt, havnivå og havdynamikk i den norske kystsonen

Philosophiae Doctor (PhD) Thesis

Vegard Ophaug

Faculty of Science and Technology
Norwegian University of Life Sciences

Ås 2017

Thesis number 2017:24
ISSN 1894-6402
ISBN 978-82-575-1428-0

A doctoral thesis at the Norwegian University of Life Sciences consists of either a monograph or a compendium of papers in published or manuscript form. In the latter case, the introductory part, from an overall perspective, summarizes and collates the research objectives, theoretical fundamentals, results, and conclusions presented in the separate papers, and documents the coherence of the thesis.

Evaluation committee

First opponent
Prof. Nicolaas J. Sneeuw
Institute of Geodesy, University of Stuttgart
Stuttgart, Germany

Second opponent
Prof. Philip L. Woodworth
National Oceanography Centre
Liverpool, United Kingdom

Committee coordinator
Assoc. Prof. Ola Øvstedal
Faculty of Science and Technology,
Norwegian University of Life Sciences (NMBU)
Ås, Norway

Supervisors

Prof. Bjørn R. Pettersen (Main supervisor)
Faculty of Science and Technology,
Norwegian University of Life Sciences (NMBU)
Ås, Norway

Dr. Christian Gerlach (Co-supervisor)[1]
Commission of Geodesy and Glaciology,
Bavarian Academy of Sciences and Humanities
Munich, Germany

Dr. Kristian Breili (Co-supervisor)[1]
Geodetic Institute, Norwegian Mapping Authority
Hønefoss, Norway

[1] Assoc. Prof. at the Faculty of Science and Technology, Norwegian University of Life Sciences (NMBU), Ås, Norway

“Gravity is a habit that is hard to shake off.”

Sir Terry Pratchett (1948-2015), *Small Gods*

Summary

Geodesy can contribute to a quantitative understanding of ocean circulation variability at northern high latitudes, which is crucial to environmental and climate-related studies. Coastal ocean dynamics has gained recent interest due to its importance for shipping, fishery, coastal ecosystem processes, other on- and offshore activities, and sea-level change. If the oceans were at rest, the ocean surface would be in hydrostatic equilibrium and coincide with the geoid. Dynamical processes in the ocean cause deviations of the sea surface from the geoid, and the steady-state component of the dynamical processes is known as the mean dynamic topography (MDT). It may be determined by the ocean approach, using numerical ocean circulation models, or by the geodetic approach, where MDT is the height of the mean sea surface (MSS) observed by satellite altimetry, or mean sea level (MSL) observed by tide gauges, above the geoid. This thesis is an investigation of geodetic topics related to geoid and MDT determination in the Norwegian coastal zone: Optimal combination of recent satellite and regional gravity data, dedicated coastal altimetry products, modern regional geoid computation techniques, and temporal gravity field variations due to vertical land motion.

A suite of regional geoid models were validated in terms of standard deviations of differences to GNSS/leveling. In addition to existing regional geoid models, new GOCE-based geoid models were computed by a filtering approach, whereby an already existing regional geoid model was taken as terrestrial information, and combined with GOCE-based global gravity models by filtering in the spatial domain. GRACE and GOCE have substantially improved the geoid over the last decade, with a drop from 8.5 cm (pre-GRACE) through 4.6 cm (GRACE) to $\sim$3 cm (GOCE). There is a tendency that filter-combinations that put more weight on GOCE than on the terrestrial gravity data are the best. The formal geoid errors are lower and show larger variations depending on the relative weighting of satellite and terrestrial data than the empirical errors from the GNSS/leveling validation, which suggests that the empirical error is dominated by the quality of the GNSS/leveling data.

In a benchmark study, the level of agreement between new geodetic and recent ocean MDTs along the Norwegian coast was investigated. New GOCE-based geoids, conventional altimetry as well as dedicated coastal altimetry products Envisat/CTOH and Jason-2/PISTACH were used. Geodetic and ocean MDTs agree on the $\sim$3-7 cm level at the tide gauges, and on the $\sim$5-11 cm on the altimetry sites. The contributions to the error budget are estimated as follows; ocean MDT: $\leq$5 cm, altimetric MSS: $\leq$7 cm, tide-gauge MSL: $\leq$3 cm, and geoid: $\leq$4 cm. The coastal altimetry products generally do not offer an improvement over the conventional products they are based on.

The SAR altimetry satellite CryoSat-2 observes the sea surface in areas previously uncovered by conventional altimetry. Compared with 10-minute sea level observations at 22 tide gauges, the standard deviations of differences are between 7-20 cm, with the largest values at tide gauges well inside fjords with relatively few altimetry observations. When replacing the standard ocean tide and atmospheric corrections with local corrections derived from ocean tide predictions and pressure observations, a 2-5 cm improvement in standard deviations of differences is observed at 19 out of 22 tide gauges.

Using CryoSat-2 and new GOCE-based regional geoid models, three geodetic MDT surfaces were determined. In addition, geostrophic surface currents were derived from the MDT surfaces, and compared with the coastal numerical ocean model NorKyst800. At the tide gauges, the CryoSat-2 MDTs agree on the ~3-5 cm level with both tide-gauge and ocean MDTs. The CryoSat-2 MDT surfaces show standard deviations of differences of 6-8 cm to NorKyst800. The general pattern of the Norwegian Sea circulation is evident in the CryoSat-2 MDTs, but variations are seen depending on the geoid used. The CryoSat-2 MDT surfaces use regional geoid models which are all based on the latest release of GOCE global gravity models. Thus, the observed variation emphasizes the importance of terrestrial gravity information for the geodetic MDT. The quality of regional geoid models is higher on land than over the ocean, which may be due to the fact that geoid models are often tuned to fit validation data on land, where the bulk of terrestrial gravity observations are.

Furthermore, three methods for regional geoid computation were compared theoretically and numerically in a unified framework. Stokes's formula, least-squares collocation (LSC) and radial base functions using the spline kernel (SK) are theoretically equivalent methods in the global case. LSC and SKs need a modification to provide the same results as Stokes's formula in regional applications, where the Stokes integration is restricted to a spherical cap around the computation point. The methods are also equal in practice, as shown in numerical examples. At the 5 arcmin resolution, all methods agree within 2×10^{-2} mm to 5.9 mm in the target areas, where the largest RMS differences are due to the discretization of Stokes's formula. At the 2.5 arcmin resolution, all methods agree within 6×10^{-2} mm to 2.4 mm. The SKs are shown to depend on the signal resolution rather than the number of observations, while the opposite holds true for LSC, as the size of the auto-covariance matrix to be inverted corresponds to the number of observations, independent of the signal resolution. It is important to note that the modification of LSC and SKs is not a general necessity when applying these methods, but it is critical in direct comparison with Stokes's formula.

The main source of temporal variations of the gravity field in Fennoscandia is glacial isostatic adjustment (GIA). The extent to which secular gravity trends derived from absolute gravity observations are applicable for GIA studies was investigated. All Norwegian FG5-type absolute gravity observations (1993-2014) were compiled and analyzed, raw observations consistently reprocessed, and adopted observations carefully incorporated into the data set with updated uncertainties. In comparison with a GIA model, empirical gravity rates based on a refined modeling of ocean tide loading, non-tidal ocean loading, atmospheric, and global hydrological gravitational effects mainly impact sites where GIA is not the dominant signal. This suggests that a refined modeling is meaningful at sites that are affected by various unmodeled or insufficiently modeled effects. From a subset of 10 rates mainly reflecting GIA, estimated gravity-to-height rate of change ratios are within -0.133 (±0.030) to -0.167 (±0.045) $\mu\mathrm{Gal\ mm^{-1}}$, in agreement with previous estimates (-0.154 to -0.217 $\mu\mathrm{Gal\ mm^{-1}}$).

Keywords: absolute gravity · geoid · GIA · gravity change · mean dynamic topography · ocean currents · ocean model · physical heights · SAR altimetry · satellite altimetry · tide gauges

Sammenfatning

Geodesi kan bidra til en kvantitativ forståelse av variabiliteten i havsirkulasjon på nordlige breddegrader, som er avgjørende for miljø- og klimarelaterte studier. I de senere år har vi sett en økt interesse for havdynamikk i kystsonen på grunn av dennes betydning for sjøfart, fiskeri, kystnære økosystemprosesser, andre on- og offshoreaktiviteter samt havnivåendringer. Dersom havet var i ro, ville havoverflaten vært i hydrostatisk likevekt og dermed parallell med geoiden. Dynamiske prosesser i havet forårsaker derimot avvik i havoverflaten fra geoiden, og den stasjonære komponenten til de dynamiske prosessene er kjent som midlere dynamisk topografi (MDT). Den kan bestemmes ved numeriske havmodeller i en såkalt oseanografisk tilnærming, eller ved en geodetisk tilnærming, der MDT enten er midlere havoverflates (MSS) høyde bestemt ved satellittaltimetri, eller middelvanns (MSL) høyde bestemt i vannstandsmålere, over geoiden. Denne avhandlingen undersøker geodetiske emner relatert til bestemmelse av geoide og MDT den norske kystsonen: Optimal kombinasjon av nye satellitt- og regionale tyngdedata, dedikerte kystaltimetriprodukter, moderne regionale geoideberegningsteknikker, og tids-variasjoner i tyngdefeltet grunnet landhevning.

Et knippe regionale geoidemodeller ble validert i form av standardavvik til differanser mot GNSS/nivellement. I tillegg til eksisterende regionale geoidemodeller, ble nye GOCE-baserte geoidemodeller beregnet ved en filtreringsteknikk, der en eksisterende regional geoidemodell ble benyttet som terrestrisk informasjon og kombinert med GOCE-baserte globale geoidemodeller ved filtrering i det romlige domenet. I løpet av det siste tiåret har GRACE og GOCE forbedret geoiden betraktelig, fra 8.5 cm før GRACE, til 4.6 cm med GRACE, og til $\sim$3 cm med GOCE. Det er en tendens til at filtrerte løsninger som legger mer vekt på GOCE enn på terrestriske tyngdedata er de beste. De formelle geoidefeilene er små og varierer langt mer avhengig av den relative vektingen av satellitt- og terrestriske data enn de empiriske feilene fra valideringen mot GNSS/nivellement. Dette tyder på at den empiriske feilen domineres av kvaliteten til sistnevnte.

I en benchmark-studie ble samsvaret mellom nye geodetiske og oseanografiske MDTer undersøkt. Nye GOCE-baserte geoidemodeller, konvensjonell altimetri samt dedikerte kystaltimetriprodukter Envisat/CTOH og Jason-2/PISTACH ble benyttet. Geodetiske og oseanografiske MDTer stemmer overens på $\sim$3-7 cm nivå i vannstandsmålerne og på $\sim$5-11 cm nivå i altimetripunktene. Bidragene til det totale feilbudsjettet estimeres til; oseanografisk MDT: $\leq$5 cm, MSS fra altimetri: $\leq$7 cm, MSL fra vannstandsmåler: $\leq$3 cm, samt geoide: $\leq$4 cm. De dedikerte kystaltimetriproduktene gir ingen forbedring sammenlignet med de konvensjonelle produktene de er basert på.

SAR-altimetrisatelliten CryoSat-2 observerer havoverflaten i områder som tidligere ikke var tilgjengelige for konvensjonell altimetri. Sammenlignet med 10-minutters vannstandsobservasjoner i 22 vannstandsmålere, er standardavvik til differanser mellom 7-20 cm, med de største verdiene i vannstandsmålere langt inne i fjorder, med relativt få altimetriobservasjoner. Når standardkorreksjoner for tidevann og atmosfære byttes ut med lokale korreksjoner bestemt fra predikert tidevann og lufttrykksobservasjoner, forbedrer dette standardavviket til differansene med 2-5 cm i 19 av 22 vannstandsmålere.

Ved bruk av CryoSat-2 og nye GOCE-baserte regionale geoidemodeller ble tre geodetiske MDT-flater bestemt. I tillegg ble geostrofiske overflatestrømmer avledet fra MDT-flatene og sammenlignet med den kystnære numeriske havmodellen NorKyst800. I vannstandsmålerpunktene stemmer CryoSat-2 MDTer overens med vannstandsmåler-MDT og oseanografisk MDT på ∼3-5 cm nivå. CryoSat-2 MDT-flatene viser standardavvik til differanser mot NorKyst800 på 6-8 cm. Det overordnete sirkulasjonsmønsteret i Norskehavet fremkommer i CryoSat-2 MDTene. Likevel er det variasjoner i mønsteret avhengig av hvilken geoide som ligger til grunn. CryoSat-2 MDTene benytter regionale geoidemodeller som alle er basert på den siste utgivelsen av GOCE globale tyngdemodeller. Derfor understreker den observerte variasjonen betydningen av terrestrisk tyngdeinformasjon for den geodetiske MDT. Kvaliteten til de regionale geoidene er bedre på land enn til sjøs, hvilket kan skyldes at geoidene ofte tilpasses valideringsdata på land, hvor også brorparten av terrestriske tyngdedata befinner seg.

Videre ble tre metoder for regional geoideberegning sammenlignet teoretisk og numerisk i et enhetlig rammeverk. Stokes' formel, minste kvadraters kollokasjon (LSC) og radielle basisfunksjoner med splinekjerne (SK) er teoretisk ekvivalente metoder i det globale tilfellet. LSC og SKer trenger en modifikasjon for å gi resultater tilsvarende Stokes' formel i regionale anvendelser, der integrasjonen er avgrenset til en sfærisk kappe rundt beregningspunktet. Metodene er like også i praksis, som vist i numeriske eksempler. Med 5 minutters oppløsning, samsvarer alle metoder innenfor $2{\times}10^{-2}$ mm til 5.9 mm i målområdene, hvor de største RMS-differansene skyldes diskretiseringen av Stokes' formel. Med 2.5 minutters oppløsning, samsvarer alle metoder innenfor $6{\times}10^{-2}$ mm til 2.4 mm. SKene avhenger av signalets oppløsning heller enn antallet observasjoner, mens det motsatte gjelder for LSC, der størrelsen til autokovariansmatrisen som skal inverteres korresponderer til antallet observasjoner, uavhengig av signalets oppløsning. Det er viktig å merke seg at modifiseringen av LSC og SKene ikke er en generell nødvendighet i den praktiske anvendelsen av metodene, men er avgjørende i direkte sammenligning med Stokes' formel.

Hovedårsaken til tids-variasjoner i tyngdefeltet i Fennoskandia er postglasial landhevning (GIA). I hvilken grad tyngdekraftens endringsrate, bestemt fra absolutte tyngdemålinger, kan anvendes i GIA-studier, ble undersøkt. Alle norske absolutte tyngdemålinger utført med instrumenter av FG5-typen (1993-2014) ble samlet og analysert, råobservasjoner ble enhetlig reprosessert og observasjoner fra andre kilder inkludert i datasettet med oppdaterte usikkerhetsmål. I sammenligning med en GIA-modell påvirker empiriske tyngderater basert på en foredlet modellering av ocean tide loading, non-tidal ocean loading, atmosfærisk samt global hydrologisk gravitasjonseffekt i hovedsak tyngdestasjoner der GIA ikke er det dominerende signal. Dette tyder på at en foredlet modellering er meningsfylt i stasjoner som er påvirket av forskjellige umodellerte eller utilstrekkelig modellerte effekter. Forhold mellom tyngderate og høyderate ble bestemt fra en delmengde på 10 tyngderater som i hovedsak reflekterer GIA, og er mellom -0.133 (± 0.030) og -0.167 (± 0.045) $\mu\mathrm{Gal\ mm^{-1}}$, i samsvar med tidligere estimater (-0.154 til -0.217 $\mu\mathrm{Gal\ mm^{-1}}$).

Nøkkelord: absolutt tyngde · fysiske høyder · geoide · GIA · havmodell · havstrømmer · midlere dynamisk topografi · SAR-altimetri · satellittaltimetri · tyngdekraftens endringsrate · vannstandsmålere

Acknowledgments

The thesis at hand summarizes my three years as a PhD candidate at the Norwegian University of Life Sciences. They have been fast and intensive years, where I've learned a lot. The thesis would not have come into existence without the contributions from great supervisors, colleagues, and supporters, all to whom these words are devoted.

I'm grateful for the support from my supervisor, Prof. Bjørn Ragnvald Pettersen, without whom I wouldn't have thought of doing a PhD. He is a great source of inspiration, and has an impressive knack for problem solving on the scientific ladder and loophole identification in bureaucratic limbo.

I'm indebted to my co-supervisors Dr. Kristian Breili and Dr. Christian Gerlach, who both have been very engaged in my work. They've always welcomed me to the Norwegian Mapping Authority and the Bavarian Academy of Sciences and Humanities. Thanks for the positive spirit, guidance, encouragement, and patience.

Operation of the FG5-226 absolute gravimeter would not have been possible without Prof. Jon Glenn Gjevestad. Whether in a tunnel below the Svartisen glacier or on Vega island, it was always possible to reach his hotline, for which I'm very grateful.

Many others have helped me along the way, including fellow graduate students and colleagues at the Geomatics section. Thanks to Dr. Kennedy Were and Dr. Michal Šprlák for your support and fellowship.

Life in the office took a dramatic turn for the better with the addition of my colleague and friend Martina Idžanović. She has an omnipresent positive attitude which, at times, is almost puzzling. Thanks for the great teamwork and for being a good discussion partner, whether the topic has been geodesy or everyday agonies of life.

A special thanks goes to Dr. Ole Baltazar Andersen, who has shown great interest in this work, and gave Martina and me the opportunity to visit DTU Space for four months. Ole, as well as his colleagues and graduate students at DTU Space, are greatly acknowledged for always having time for a question or two.

I would also like to thank the members of the evaluation committee: Prof. Nico Sneeuw, Prof. Phil Woodworth, and Assoc. Prof. Ola Øvstedal.

As ever, I am deeply grateful for the support and encouragement from my family.

Ås, January 26, 2017 *Vegard Ophaug*

Contents

Chapter 1

Introduction

1.1 Background and motivation

Earth science is highly interdisciplinary, comprising studies of the solid Earth, atmosphere, hydrosphere, and biosphere (Tarbuck and Lutgens, 2015). All branches of Earth science change with time, interact, and depend on each other. Therefore, a common way to view Earth is by the systems approach, see Figure 1.1. This approach offers a deeper understanding of the interactions that determine past, present and future states of the dynamical Earth. As such, Earth science is environmental science. Monitoring changes in the Earth system is highly motivated by the ambition to unveil the anthropogenic dimension of global environmental change.

The ocean is an important part of the Earth system due to its large heat storage and heat transport capacity. The study of its physical properties and dynamics is known as physical oceanography (Stewart, 2008). Moreover, physical oceanography comprises the interaction between ocean and atmosphere, the oceanic heat budget, water mass formation, currents and coastal dynamics. Precise knowledge of ocean currents and sea-level change is crucial to environmental and climate-related studies (Vallis, 2012). The deep ocean comprises 90% of the total ocean mass. It is dominated by the meridional overturning circulation (MOC), which is due to the formation of deep water in the North Atlantic Ocean between Greenland and Norway, and in the Weddell Sea in Antarctica.

Between the Arctic Ocean to the north and the North Atlantic Ocean to the south are the Nordic Seas, a common designation for the Iceland, Greenland, Norwegian, and Barents seas. The major currents in the Nordic Seas are characterized by a southward flow of relatively fresh and cold Arctic Water in the west (East Greenland Current), and a northward flow of relatively salty and warm Atlantic Water in the east (Norwegian Atlantic Current), see Figure 1.2. The poleward heat transport results in a convective overturning of the water column known as North Atlantic Deep Water formation, sustaining the MOC (Rhines et al., 2008).

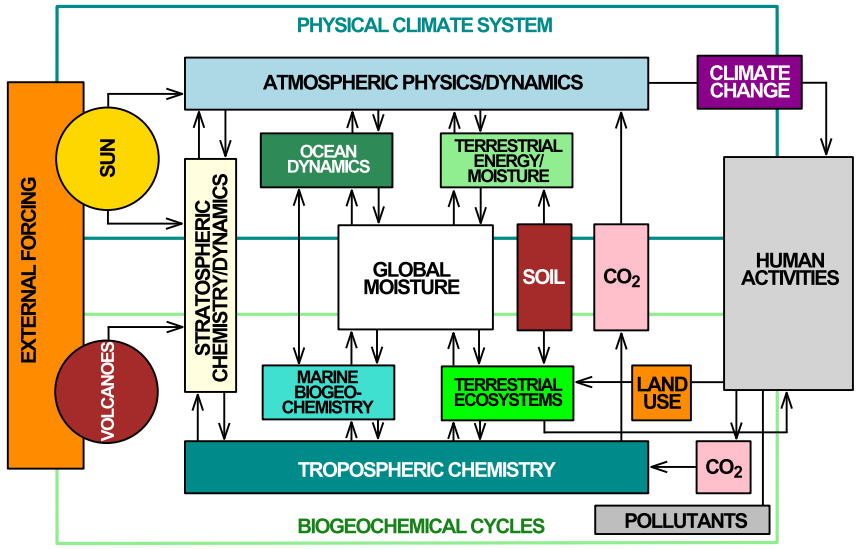

Figure 1.1: The simplified Bretherton diagram. It illustrates the Earth system and subsystems, all of them of equal value as they act and react on each other. Adapted from NASA Earth System Sciences Committee (1988).

The Norwegian Atlantic Current splits into several branches (Orvik et al., 2001; Skagseth et al., 2008), partly recirculating in the Nordic Seas, partly flowing west of Spitsbergen as the West Spitsbergen Current into the Arctic Ocean through the Fram Strait, and partly flowing into the Barents Sea. The Norwegian Coastal Current (NCC) transports warm and relatively fresh water along the Norwegian coast and into the Barents Sea, with its origin in Baltic Water entering Skagerrak (Skagseth et al., 2011). Along its way northward, it is fed by additional freshwater discharge. The NCC is important for the regional marine ecosystem and contributes to the poleward transport of warm Atlantic Water. It is of particular interest to studies of sea-level variations in the Norwegian coastal zone.

Ocean circulation in the Nordic Seas is influenced, among other factors, by winds, variations in the upper ocean and sea-ice interaction, ice sheet mass changes and their effect on regional sea level, changes in freshwater fluxes, and variability in both large-scale and regional atmospheric pressure (Chafik et al., 2015). Changes in the Arctic-Subarctic ocean flux, i.e., the exchange of water between the Arctic and the surrounding seas have far-reaching influences on regional and global environment and climate variability. Therefore, a quantitative understanding of high-latitude ocean currents and their variations is of high importance (Johannessen et al., 2014; Hattermann et al., 2016).

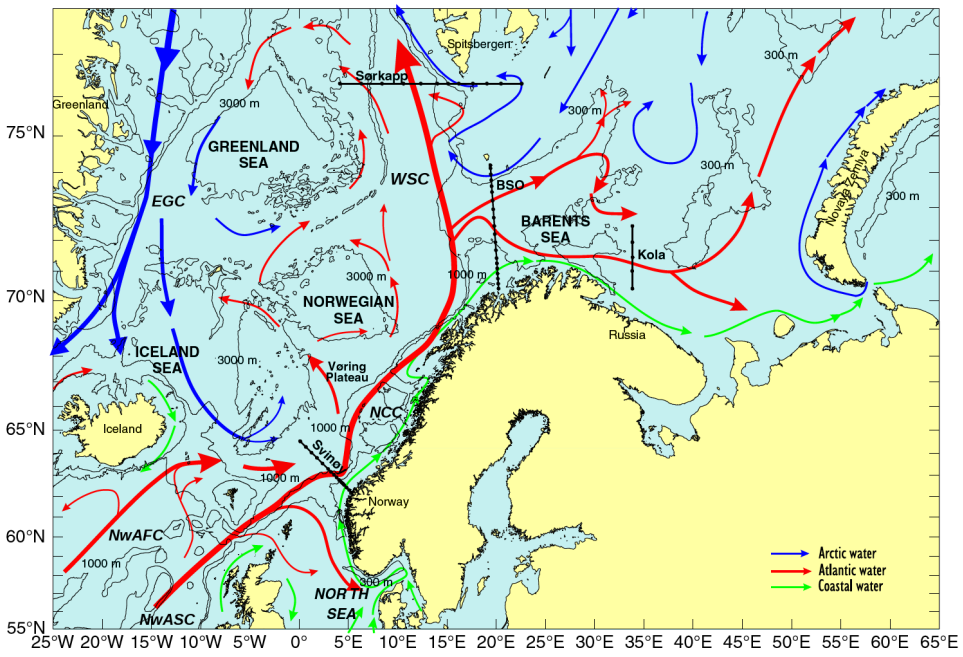

Figure 1.2: Schematic of the Nordic Seas with major ocean currents. Inflowing Atlantic Water is shown in red, where the Norwegian Atlantic Front Current (NwAFC), the Norwegian Atlantic Slope Current (NwASC), and the West Spitsbergen Current (WSC) are prominent. Outflowing Arctic Water is shown in blue, such as the prominent East Greenland Current (EGC). Fresh coastal water is shown in green, where the Norwegian Coastal Current (NCC) is of particular interest for this thesis. In addition, the repeated hydrographic sections Svinøy, Barents Sea Opening (BSO), Kola, and Sørkapp are shown. Adapted from Skagseth et al. (2008).

A quantitative understanding of ocean parameters, or, indeed, any Earth system parameter, is closely linked to the science of geodesy. Geodesy has traditionally been concerned with the determination of static Earth's size, shape, rotation and gravity field, also known as the "pillars of geodesy" (Rummel et al., 2005). However, the interaction of the Earth system components, i.e., their dynamics, influence the pillars of geodesy. Today, advances in geodetic observational techniques allow global monitoring of the whole Earth system in time. This, for example, has led to the establishment of the Global Geodetic Observing System, which aims to integrate the pillars of geodesy through monitoring geodetic parameters and their temporal variations, and thus monitoring the Earth system (Plag and Pearlman, 2009).

Global navigation satellite systems (GNSS) are important geodetic techniques for navigation and surveying, providing point coordinates in east, north and vertical directions on Earth's surface to centimeter accuracy (Rothacher, 2002; Tegedor et al., 2014). The vertical component is the height above a conventional reference ellipsoid, referred to a global geodetic reference frame. All geodetic data must be related to a common geodetic reference frame (e.g., ITRF2008) prior to comparison or combination.

While positioning and reference frames form the basis of what may be termed geometrical geodesy, physical geodesy aims at determining Earth's external gravity field (Hofmann-Wellenhof and Moritz, 2006). Gravity is a fundamental force describing the physics of the Earth. The gravity vector defines the direction of "up" and "down", making it indispensable for the definition of physical heights, and a key observable within physical geodesy.

If the oceans were at rest, the ocean surface would be in hydrostatic equilibrium. It would coincide with the one equipotential surface of Earth's gravity field which geodesists call the geoid. The geoid is close to mean sea level, and horizontal in the physical sense, which is important in many science and engineering applications, since it is gravity and not height which governs fluid flow (Torge and Müller, 2012). It acts as a reference surface for orthometric heights (i.e., physical heights above sea level) and the definition of vertical reference systems (height systems). We cannot observe the geoid directly, but rather derive it from gravity observations by solving the geodetic boundary value problem.

The gravimetric satellite mission GOCE (Gravity and steady-state Ocean Circulation Explorer) (Drinkwater et al., 2003) aims at the derivation of a global mean geoid with homogeneous accuracy of about $1\,\mathrm{cm}$, but limited to spatial resolutions of about $100\,\mathrm{km}$. Higher spatial resolutions may be obtained with additional air- or shipborne as well as terrestrial gravity information (Denker, 2013). Today, a regional geoid on land can be determined to the centimeter level, provided that the quality and density of the gravity data are sufficiently high.

Satellite altimeters have been measuring sea surface heights (SSHs) above a reference ellipsoid for several decades, leading to the knowledge of the global mean sea surface (MSS) with approximately 2 cm accuracy, averaged over a time period (Pugh and Woodworth, 2014). Satellite altimetry has extensively improved our knowledge of ocean dynamics, ocean mass redistribution, and the marine gravity field. It plays a key role in determining sea-level rise, a major indicator of climate change. Conventional altimeters send pulse-limited radar signals to the surface and derive the satellite height above the surface from the round-trip travel time of the returned radar echoes. Depending on the surface properties (open ocean, land, sea ice, etc.) the echoes generate different waveforms, from which the travel time must be estimated. Numerous retracking algorithms exist to take care of the different waveform characteristics (Gommenginger et al., 2011). Conventional altimeters have an almost circular footprint of several kilometers in diameter. Sea surface heights can be derived from range observations if the satellite orbit is known and after application of instrumental and geophysical corrections.

For a long time, satellite altimetry was restricted to the open ocean, several tens of kilometers off the coast, due to the contamination of the radar footprint by land masses, degradation of the tropospheric corrections due to increased atmospheric variability and imperfections of global ocean tide models in the coastal zone (Vignudelli et al., 2011). In recent years, coastal altimetry has gained interest due to its high relevance for monitoring the coastal environment and assessing the impact of sea-level rise and variability along the coast. Consequently, there have been attempts by the European Space Agency (ESA) and the French Space Agency (CNES) to provide operational coastal altimetry products for the users (COASTALT respectively PISTACH), based on conventional altimetry.

CryoSat-2 is the first of a new generation of satellite altimeter missions which carry a Synthetic Aperture Radar (SAR) altimeter instead of the conventional pulse-limited system (Wingham et al., 2006). The SAR altimeter provides higher range precision and a higher along-track resolution of ~300 m as opposed to several kilometers, allowing to track finer structures of the sea surface and obtain observations closer to the coast. In favorable conditions, CryoSat-2 may deliver dense observations even in deep, narrow fjords, where conventional altimeters fail to provide data. SAR altimeters of CryoSat-2 heritage are also found on the Sentinel-3 series of the European Copernicus program (Sentinel-3A was launched on February 16, 2016, and Sentinel-3B is expected to be launched in 2017) and on the Jason-CS/Sentinel-6 series (the first of which is planned to launch in 2020).

In light of the above it is clear that geoid and MSS form important physical quantities within both physical oceanography and geodesy. For an undisturbed ocean at rest, the sea surface would be closely parallel to the geoid (Pugh and Woodworth,

2014). Dynamical processes in the ocean cause deviations from hydrostatic equilibrium, leading to deviations of the sea surface from the geoid, known as dynamic ocean topography (DOT). The DOT can be separated into a time-variable and a time-averaged, steady-state component. The latter is known as the mean dynamic topography (MDT), see Figure 1.3. It describes the average transport rate in the ocean, while the time-variable component is driven, e.g., by winds, increased flux of freshwater, or warming of the oceans, and is an indicator of climate change. The slope of the MDT reveals the magnitude and direction of ocean surface geostrophic currents (Wunsch and Stammer, 1998). Thus, if the MDT is known accurately, we know the mean surface circulation of the ocean. Furthermore, with additional hydrographic information and models, ocean circulation at all depths may be determined. This important Earth system constituent may in turn be included in numerical climate models.

Historically, the global ocean circulation was determined by means of hydrographic measurements of temperature and salinity (in situ data) from ships only (Pugh and Woodworth, 2014). Today, the ocean flow is determined from numerical ocean circulation models, which employ a set of dynamical equations and driving forces provided by in situ data sets and meteorological wind and air pressure information. One outcome of a model run is the SSH that arises from the ocean's circulation, i.e., sea level relative to an implicit geopotential surface. Thus, an average of such heights over a given time period will be equivalent to oceanographic MDT.

A precise geoid in combination with observations of the MSS by means of satellite altimetry allows a geodetic approach to determine the MDT (Woodworth et al., 2012), see Figure 1.4. Altimetric observations yield ellipsoidal heights of the MSS, and together with ellipsoidal heights of the geoid, the MDT may be derived through a purely geometrical approach based on geodetic observations. Yet another alternative to the altimetric determination of the sea surface are ellipsoidal heights of MSL observed by tide gauges connected to GNSS receivers. As a result, we have two computational approaches to the geodetic MDT supplementing the oceanographic MDT.

The geodetic MDT is given by

$$\mathrm{MDT} = h - N, \tag{1.1}$$

where the MSS/MSL is expressed as height h above a conventional reference ellipsoid, N is the geoid height above a conventional reference ellipsoid and their difference yields the MDT, at height H above the geoid. Although the computation of a geodetic MDT is conceptually simple, there are important issues to consider. The MSS and geoid must be consistent in terms of reference system and permanent tide system. In addition, the geoid heights are often the result of a globally

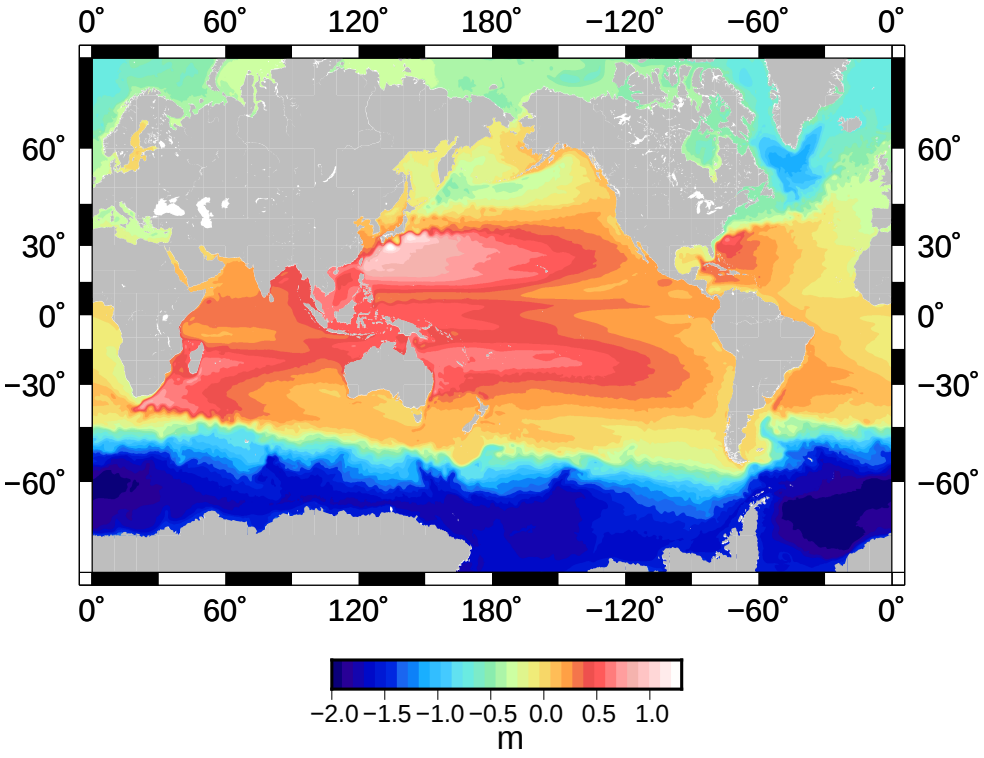

Figure 1.3: MDT for the 1996-2000 period from the 0.1° Oceanic general circulation model For the Earth Simulator (OFES) numerical model (Sasaki et al., 2008). We observe that the MDT varies up to a few meters globally. The large-scale ocean circulation follows the contours of the dynamical topography. We observe features such as the world's largest current, the Antarctic Circumpolar Current, as well as the Gulf Stream (off the east coast of North America), Kuroshio Current (off the east coast of Japan), and the Agulhas Current (off the east coast of South Africa). These features have amplitudes on the level of a meter or more. Upon closer inspection, we can also observe smaller decimeter-level current systems, such as the NwASC.

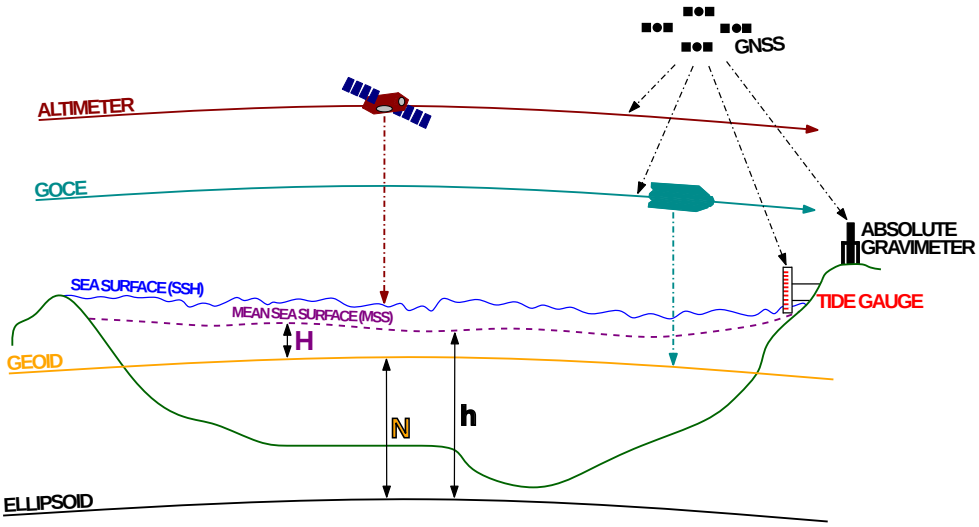

Figure 1.4: Schematic showing techniques and geometrical quantities h and N involved in the geodetic approach to determine $H = \mathrm{MDT}$. Inspired from Tapley and Kim (2001).

defined band-limited spherical harmonic expansion, while the heights of MSS/MSL are given point-wise along satellite ground tracks or at tide gauges and are essentially non band-limited. That is, the MSS/MSL contains short-scale features that a satellite-only based geoid lacks. Consequently, the MSS and geoid surfaces must be made spectrally consistent, usually by applying a suitable filter to the MSS, before they can be subtracted (Albertella and Rummel, 2014). Using a pure satellite-based geoid from GOCE and state-of-the-art altimetry-based MSS models, the MDT can be resolved with centimetric accuracy for spatial scales down to ~130 km (Bingham et al., 2014). At this spatial scale and beyond, the geoid accounts for most of the MDT error. In order to resolve the smallest spatial scales of the gravity field and thus reduce the geoid error, a regional geoid model must be used, which will make the geoid and MSS spectrally consistent and lessen the need to filter the MSS.

In addition to the purely oceanographic and geodetic MDTs, there exist assimilated numerical models incorporating a range of oceanographic and geodetic observations constraining ocean flow. Disregarding the assimilated ocean models, we have multiple independent MDT computation schemes which should provide the same quantity. These MDT models may then act as each other's buddy check, increasing confidence in the ocean and geoid models in use. However, both geodetic and oceanographic approaches contain different error sources and have their limitations in resolving the geophysical signal they want to describe. These error contributions

and limitations can be quantified by setting up the following MDT budget equation,

$$\varepsilon = \mathrm{MDT} - (h - N), \tag{1.2}$$

where MDT is derived from an ocean model, and the parenthesis represents the geodetic approach (**Paper A**). ε is the misfit between the two and contains errors of tide-gauge or altimetry observations, geoid errors, imperfections of the numerical ocean models, and generally also effects due to different spatial or temporal resolutions. The misfit is an empirical error estimate that should reflect the formal error budget of MDT, h, and N. If we assume that these errors are uncorrelated, the following MDT error budget equation can be set up,

$$\sigma_{\mathrm{tot}} = \sqrt{\sigma^2_{\mathrm{MDT}} + \sigma^2_h + \sigma^2_N}, \tag{1.3}$$

where σ indicates formal error standard deviations. If the error estimates of the different components are realistic, then formal error propagation should allow σ_{tot} to reflect the empirical misfit ε. Discrepancies between ε and σ_{tot} may arise from unmodeled correlations between the different quantities and from systematic error contributions not covered by formal error propagation.

Traditionally, national vertical reference systems have referred to an official MSL value at a specific tide gauge (e.g., Lysaker et al., 2007). The datum (reference level) MSL value would be transferred to other locations by means of geometric leveling, yielding networks of "heights above sea level". The problem with this approach is that different leveling networks not referring to the same tide gauge will be related to different equipotential surfaces due to the spatial variation of the MDT. This leads to height offsets between national vertical reference systems, which need to be quantified, e.g., when a bridge spanning the systems is to be built. The problem could be avoided if the different vertical reference systems would refer to the same geoid (e.g., Rummel, 2012; Gerlach and Rummel, 2013).

Determination of a geodetic MDT by Eq. (1.1) is the ocean analogue to combining GNSS and leveling on land, where heights H above sea level are determined from GNSS measurements h if geoid heights N are available. The improved quality of regional geoid models based on GOCE data allows this method to detect systematic distortions in national leveling networks (Rülke et al., 2012; Amjadiparvar et al., 2016). Consequently, the current leveling-based vertical reference frame can be controlled and the possibility of a future geoid-based vertical reference frame investigated. In, e.g., North America, the leveling-based vertical reference frame is being abandoned in favor of a geoid-based vertical reference frame (Li et al., 2016).

Earth's gravity field changes with time. For example, Fennoscandia is strongly affected by land uplift due to glacial isostatic adjustment (GIA) (Milne et al., 2001; Steffen and Wu, 2011). GIA is the response of solid Earth to past changes in surface loading by ice and water (glaciation and deglaciation). Thereby, GIA distorts the vertical reference frame. Furthermore, GIA is important for relative sea-level change studies, as relative sea-level rates must be adjusted for both land uplift and geoid changes (Simpson et al., 2015). In Fennoscandia, most of the time-variable change in the geoid is due to GIA. A future geoid-based frame for Norway would strongly depend on the monitoring of the dynamic component of the vertical reference frame, i.e., its temporal evolution due to GIA.

Long-term monitoring by GNSS of positions on Earth's surface reveals both horizontal and vertical land motion, due to plate tectonics and land uplift, respectively. Absolute gravimetry is an alternative technique for deriving vertical land motion, and is independent of the geodetic reference frame. Thus, time series of GNSS and absolute gravity observations together form a powerful tool for studying land uplift processes (Steffen and Wu, 2011) and monitoring the reference frame (Collilieux et al., 2014). Ideally, the observation of long-term gravity changes requires a decade of annual measurements (Van Camp et al., 2016). As many absolute gravity time series are shorter than this, their further extension is important to exploit the full potential of this technique.

The coastal zone implies a multitude of challenges when it comes to geoid and MDT determination. Both satellite altimetry (for geodetic MDT) and oceanographic MDT models show irregularities close to the coast (Woodworth et al., 2012; Featherstone and Filmer, 2012; Filmer, 2014). As mentioned, land contaminates coastal altimetry observations (Gommenginger et al., 2011) and tide-gauge observations are affected by vertical land motion (Wöppelmann and Marcos, 2016). Tides become more complex along the coast (Ray et al., 2011), and global tide models loose validity there. Furthermore, it is generally challenging to make observations from land, open sea and coast consistent with each other (Woodworth et al., 2012). Only a few coastal ocean models and selected coastal altimetry products have been developed for pilot studies or for specific areas. A thorough validation of the quality of coastal products, specifically for the Norwegian coast, does not exist. The Norwegian coast adds further complications, not only due to land uplift as described in the above, but also due to the extreme topography manifested by many islands, mountains and deep, narrow fjords. Also, the semi-diurnal tidal range is considerable. Some of the data products do not cover the entire Norwegian coast.

1.2 Research objectives and rationale

With Section 1.1 as backdrop, this thesis investigates the deemed remedial effect of recent developments within geodesy on Norwegian geoid and MDT determination: Optimal combination of GOCE and regional gravity data, retracked and novel coastal altimetry data, improved geophysical corrections, modern regional geoid computation techniques, and temporal gravity field variations due to vertical land motion. Consequently, the following overarching research question was formed:

- Can recent developments within geodesy improve our understanding of sea level, ocean dynamics, and gravity field in the Norwegian coastal zone?

With an aim of contributing to answering this question, the thesis considers the following four objectives:

1. Compute and quality-assess a regional geoid model in optimal combination with the GOCE geoid
2. Determine the geodetic MDT and associated currents using tide-gauge data, coastal altimetry data, and a regional GOCE-based geoid, and assess its quality by comparison with independent oceanographic data
3. Review and compare methods for regional geoid computation
4. Map temporal variations of the gravity field

The objectives resulted in six papers listed below.

Paper A A comparative assessment of coastal mean dynamic topography in Norway by geodetic and ocean approaches

Paper B Absolute gravity observations in Norway (1993-2014) for glacial isostatic adjustment studies: The influence of gravitational loading effects

Paper C On the equivalence of spherical splines with least-squares collocation and Stokes's formula for regional geoid computation

Paper D Coastal sea level from CryoSat-2 SAR altimetry in Norway

Paper E The Norwegian Coastal Current observed by CryoSat-2 and GOCE

Paper F Accuracy of Regional Geoid Modelling with GOCE

Objectives 1 and 2 are treated in **Paper A**, which is a benchmark study for the Norwegian coast. In this paper we exploit GOCE and conventional radar altimeter data (Envisat and Jason-2) and provide a comprehensive quality assessment of state-of-the-art oceanographic and geodetic MDTs. Standard altimetric geophysical data records as well as dedicated coastal altimetry products Envisat/CTOH and Jason-2/PISTACH are used. **Paper A** explores the level of agreement between new geodetic and recent ocean MDTs along the Norwegian coast, investigates whether new GOCE-based geoids offer an improvement over existing models, whether dedicated coastal altimetry products offer an improvement over the conventional altimetry products they are based on, and also reveals subtle differences between using data from different Norwegian height systems. The paper gives a first estimate of the MDT budget for the Norwegian coastal zone.

In **Paper A**, the new GOCE-based geoid models are computed by a filtering approach, whereby an already existing regional geoid model is taken as terrestrial information (rather than performing the conventional field transformation from gravity observations to geoid heights), and combined with recent GOCE-based global gravity models by filtering in the spatial domain using a basic Gaussian kernel. Concerning objective 1 in particular, an extended study of the filter-combined approach using a stochastically optimal filter (taking the errors of both regional and global geoid into account) is found in **Paper F**.

Paper A considers conventional radar altimeter data, and the MDT is determined pointwise at 19 tide gauges and at Envisat and Jason-2 observation sites. The advent of new-generation SAR altimetry data in the Norwegian coastal zone as observed by CryoSat-2 motivated a new study of the geodetic MDT. **Paper D** and **Paper E** also focus on objectives 1 and 2, and explore CryoSat-2 SAR altimetry in the Norwegian coastal zone. Specifically, **Paper D** evaluates the performance of SAR altimetry by comparing CryoSat-2 SSHs with sea-level observations at 22 tide gauges. In particular, we explore whether the substitution of the two major standard geophysical corrections of ocean tide and dynamic atmosphere with locally determined corrections improve the SSHs. With increased confidence in CryoSat-2 observations in the Norwegian coastal zone, we use a suite of state-of-the-art regional geoid models and determine geodetic MDT surfaces for Norway in **Paper E**. In this paper we also determine geostrophic surface currents, and compare current patterns with one derived from an independent operational high-resolution coastal numerical ocean model. For the first time, the NCC is revealed by geodetic techniques.

The regional geoid models determined within the frame of this thesis are of the filter-combined type (Section 2.3.5). A consequence of the filter-combined approach is that there is little room for optimization and error assessment of the regional geoid model used (as it is already determined). As mentioned in Section 1.1, and indeed

also in **Paper A**, ideally, a regional marine geoid model should be determined from scratch using the latest GOCE geoid in combination with existing and recently acquired airborne, marine, and terrestrial gravity data. Regional geoid computation is time-consuming, and unfortunately outside the scope of this work. However, if a regional geoid model is to be computed in the future, there are different methods available. The two classic methods of Stokes integration and least-squares collocation (LSC), as well as the increasingly used radial base functions (RBFs) should all be equivalent methods, which is the concern of objective 3. This objective is explored in **Paper C**, which reviews the three methods for regional geoid computation.

Objective 4 is a decisive element for long-term monitoring of a geoid-based vertical reference frame. Furthermore, it is important to note that, while altimeter observations are absolute, tide gauges observe sea level relative to the land on which they are located. They must therefore be corrected for vertical land uplift or subsidence. We have seen that in Fennoscandia, the main component of vertical land movement is GIA, which is addressed by **Paper B**. In this paper we explore to what extent secular gravity trends derived from absolute gravity observations are applicable for GIA studies. All Norwegian FG5-type absolute gravity observations from the 1993-2014 period are compiled and analyzed. Raw observations have been reprocessed using a common scheme, and adopted observations by other agencies have been carefully incorporated in the data set, with updated uncertainties. A particular focus of **Paper B** is on whether it is possible to improve the separation of the different gravity rate signal contributors by computing refined corrections for geophysical processes other than GIA. Specifically, refined gravitational corrections due to ocean tide loading (OTL), non-tidal ocean loading (NTL), as well as atmospheric and global hydrological mass variations are computed. Secular gravity trends are computed using both standard and refined corrections and subsequently compared with modeled gravity rates based on a GIA model.

1.3 Thesis outline

The thesis is organized as follows. Chapter 2 describes the theory and methods used in the appended papers. The findings of this research are discussed, as well as some limitations identified, in Chapter 3, while Chapter 4 concludes the thesis with recommendations for future work.

1.4 Posters and talks of this research

2017 Idžanović, M., Ophaug, V., Andersen, O. B. 'Coastal Sea Level from CryoSat-2 SAR altimetry in Norway', Poster presented at the 10th Coastal Altimetry Workshop, February 21-24, Florence, Italy.

2017 Idžanović, M., Ophaug, V., Andersen, O. B. 'The Norwegian Coastal Current observed by CryoSat-2 and GOCE', Poster presented at the 10th Coastal Altimetry Workshop, February 21-24, Florence, Italy.

2016 Idžanović, M., Ophaug, V., Andersen, O. B. 'The Norwegian Coastal Current observed by CryoSat-2 SARIn altimetry', Poster presented at the International Symposium on Gravity, Geoid and Height Systems, September 18-23, Thessaloniki, Greece.

2016 Gerlach, C., Ophaug, V. 'Accuracy of Regional Geoid Modeling with GOCE', Poster presented at the International Symposium on Gravity, Geoid and Height Systems, September 18-23, Thessaloniki, Greece.

2016 Idžanović, M., Ophaug, V., Andersen, O. B. 'Coastal sea level in Norway from CryoSat-2 interferometric SAR altimetry', Poster presented at the ESA Living Planet Symposium, May 9-13, Prague, Czech Republic.

2016 Ophaug, V., Breili, K., Gerlach, C. 'A comparative assessment of coastal mean dynamic topography in Norway by geodetic and ocean approaches', Talk given at the ESA Living Planet Symposium, May 9-13, Prague, Czech Republic.

2016 Ophaug, V. 'On MDT accuracy in Norway', Talk given at the ESA GOCE++ First Project Meeting, February 16, Copenhagen, Denmark.

2015 Ophaug, V., 'Geodetic determination of the ocean topography along the Norwegian coast' (in Norwegian), Talk given at Geodesi- og hydrografidagene, November 18-19, Sundvollen, Norway.

2015 Ophaug, V. and Gerlach, C., 'A comparison of Stokes's formula, collocation, and radial base functions for regional gravity field modeling', Poster presented at the 26th International Union of Geodesy and Geophysics General Assembly, June 22 - July 2, Prague, Czech Republic.

2014 Ophaug, V., Breili, K., Gerlach, C., Hughes, C. W., and Pettersen, B. R., 'Mean dynamic topography at Norwegian tide gauges using new GOCE-based regional geoid models', Poster presented at the 5th International GOCE User Workshop, November 25-28, Paris, France.

2014 Breili, K., and Ophaug, V., 'Assessment of coastal altimetry observations along the Norwegian coast — preliminary results', Poster presented at the 8th Coastal Altimetry Workshop, October 23-24, Lake Constance, Germany

2014 Ophaug, V., 'A comparison of methods for regional gravity field modeling: Closed-loop simulations and regularization', Talk given at the Nordic Commission of Geodesy General Assembly, September 1-4, Gothenburg, Sweden.

2014 Ophaug, V., 'Gravity field modeling with spherical radial basis functions: A closed-loop simulation applying regularization', Poster presented at the European Geosciences Union General Assembly, April 27 - May 2, Vienna, Austria.

In addition, there is a popular article on the results from **Paper D** published at the ESA web pages, at `http://www.esa.int/Our_Activities/Observing_the_Earth/CryoSat/CryoSat_sets_new_standard_for_measuring_sea_levels`.

Chapter 2

Theory and methods

The investigations in this thesis span a range of topics and methods within both geodesy and oceanography. Figure 2.1 summarizes the theoretical background, concepts and techniques, including their relations to the objectives of this thesis. The gray elements in the figure serve as a reference for the topics of this chapter.

The theory behind objectives 1 and 3 comprises

- Earth's gravity field (Section 2.1), as well as
- gravimetry (Section 2.2), and
- regional geoid computation (Section 2.3).

Objective 2 is linked to the theory behind objective 1, as well as

- satellite altimetry (Section 2.5) and
- ocean dynamics (Section 2.6).

Objective 4 relies on

- terrestrial gravimetry (Section 2.2.1).

Different aspects of heights (Section 2.4) are relevant to all objectives.

2.1 Earth's gravity field

Gravitation is described by Newton's law of universal gravitation, which can be written as follows:

$$F = G\frac{mm_0}{r^2}, \tag{2.1}$$

where F is a mutual force between a particle of mass m and a particle of mass m_0, separated by a distance r (Blakely, 1996). G is Newton's gravitational constant, G =6.6742$\cdot 10^{-11}\,\mathrm{m^3 kg^{-1} s^{-2}}$.

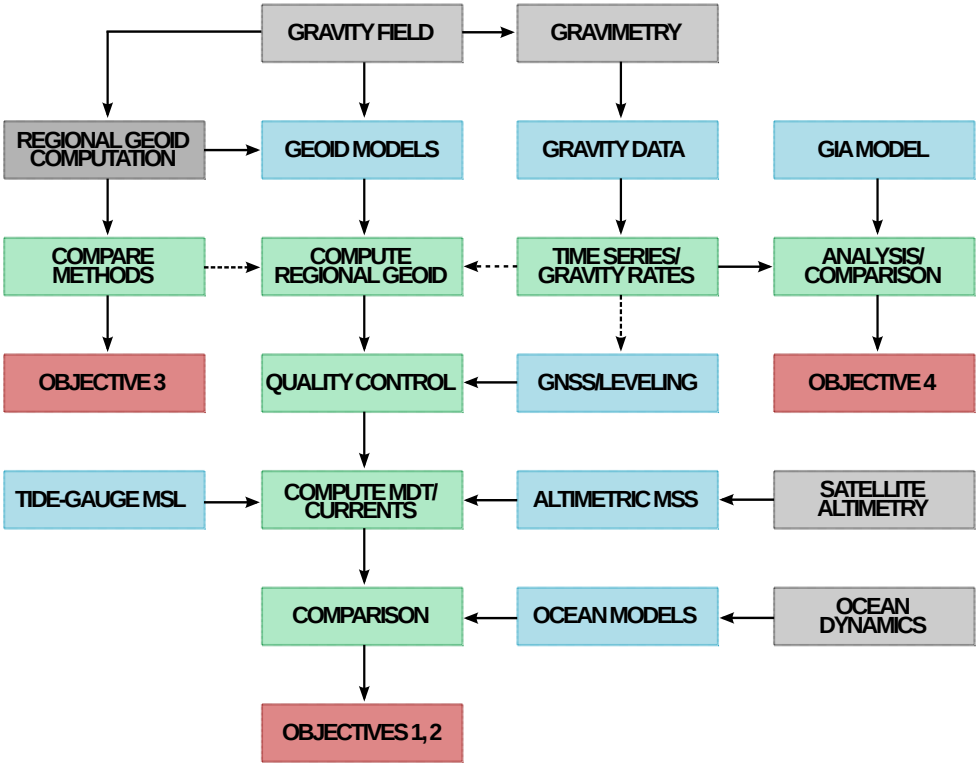

Figure 2.1: Schematic showing the relationship between different research elements: Fundamentals (gray), data (blue), methods (green), and objectives (red). The dashed arrows denote steps that were not within the scope of this thesis, but are considered natural next steps in future work. Considered, in particular, are the computation of a regional marine geoid model for Norway, with special attention to the coastal zone, and investigations of the quality of the current leveling-based and feasability of future geoid-based height systems in Norway.

In this context we are interested in the gravitational field generated by the single mass m. We let m_0 be an arbitrary mass at point P by dividing Eq. (2.1) by m_0 and obtain

$$a = G\frac{m}{r^2}, \tag{2.2}$$

where a is the gravitational attraction of m at P, at a distance r from m.

The gravitational field is a conservative vector force field which can be represented as the gradient of the scalar gravitational potential V,

$$a = \nabla V, \tag{2.3}$$

where

$$V = G\frac{m}{r}. \tag{2.4}$$

The gravitational potential of a system of n point masses is given by the sum of the gravitational potential due to the individual masses,

$$V = \sum_{i=1}^{n} \frac{Gm_i}{r_i}. \tag{2.5}$$

If we let the point masses be continuously distributed over a volume v with density $\rho = \mathrm{d}m/\mathrm{d}v$, where $\mathrm{d}m$ is a mass element, and $\mathrm{d}v$ is a volume element, the gravitational potential is given by Newton's integral,

$$V = G \iiint_v \frac{1}{r}\,\mathrm{d}m = G \iiint_v \frac{1}{r}\rho\,\mathrm{d}v, \tag{2.6}$$

where r is the distance between the mass element $\mathrm{d}m = \rho\,\mathrm{d}v$ and the attracted point P.

Inside the masses, the gravitational potential satisfies Poisson's differential equation,

$$\Delta V = -4\pi G\rho, \tag{2.7}$$

where $\Delta = \nabla^2$ is the Laplacian operator.

Outside the masses, $\rho = 0$, and the gravitational potential satisfies the simpler Laplace differential equation,

$$\Delta V = 0. \tag{2.8}$$

Solutions to Laplace's equation are called harmonic, i.e., the gravitational potential is harmonic outside the masses.

Expressed in geocentric spherical coordinates (r,θ,λ), where $\theta = 90^\circ - \varphi$ is the colatitude, and solved by separation of variables, it can be shown that the solution of Eq. (2.8) is a convergent spherical harmonic series (Hofmann-Wellenhof and Moritz, 2006), given by

$$V(r,\theta,\lambda) = \frac{GM}{R}\sum_{n=0}^{\infty}\left(\frac{R}{r}\right)^{n+1}\sum_{m=0}^{n}\bar{P}_{nm}(\cos\theta)\left[\bar{C}_{nm}\cos m\lambda + \bar{S}_{nm}\sin m\lambda\right], \quad (2.9)$$

where $\bar{P}_{nm}(\cos\theta)$ are the fully normalized associated Legendre functions of degree n and order m, and $\bar{C}_{nm}$ and $\bar{S}_{nm}$ are the fully normalized and dimensionless potential coefficients, containing the spectral amplitudes of the signal. GM is the product of Newton's gravitational constant and Earth's mass, R a mean Earth radius and r the distance from Earth's center of mass to the computation point P.

Eq. (2.9) corresponds to a Fourier expansion of V with spherical harmonic base functions $Y^C_{nm}(\theta,\lambda) = \bar{P}_{nm}(\cos\theta)\cos m\lambda$ and $Y^S_{nm}(\theta,\lambda) = \bar{P}_{nm}(\cos\theta)\sin m\lambda$ (Schmidt, 2001). Moreover, Eq. (2.9) is a continuous function in theory, but the number of potential coefficients will be finite in practice, requiring a truncation at a maximum degree $N_{\max}$ (Section 2.2.2).

Earth's gravity field is due to the sum of gravitation, or the attraction of Earth's mass, and the centrifugal force due to Earth's rotation. If we assume that Earth is rotating with constant angular velocity ω about its spin axis, the centrifugal potential Π can be written as

$$\Pi = \frac{1}{2}\omega^2 r^2 (\sin\theta)^2 . \quad (2.10)$$

Consequently, the gravity potential is given by

$$W = V + \Pi = G\iiint_v \frac{\rho}{r}\,\mathrm{d}v + \frac{1}{2}\omega^2 r^2 (\sin\theta)^2 , \quad (2.11)$$

or, in terms of Eq. (2.9),

$$W = \frac{GM}{R}\sum_{n=0}^{\infty}\left(\frac{R}{r}\right)^{n+1}\sum_{m=0}^{n}\bar{P}_{nm}(\cos\theta)\left[\bar{C}_{nm}\cos m\lambda + \bar{S}_{nm}\sin m\lambda\right] + \frac{1}{2}\omega^2 r^2 (\sin\theta)^2 . \quad (2.12)$$

The gravity acceleration is given by the gradient of the gravity potential, expressed in cartesian coordinates (x,y,z) as

$$\mathbf{g} = \nabla W = \left[\frac{\partial W}{\partial x}, \frac{\partial W}{\partial y}, \frac{\partial W}{\partial z}\right], \quad (2.13)$$

where the magnitude of $\mathbf{g}$ is generally known as gravity, and measured in Gal, where $1\,\mathrm{Gal} = 0.01\,\mathrm{ms}^{-2}$.

The coordinates of a point P may be represented in natural coordinates (Φ, Λ, H), which depend on the gravity field. The astronomical latitude and longitude, Φ, Λ, describe the direction of the plumb line in P. Thus, for the gravity vector, we may write

$$\mathbf{g} = \nabla W = -g \begin{pmatrix} \cos\Phi\cos\Lambda \\ \cos\Phi\sin\Lambda \\ \sin\Phi \end{pmatrix}. \tag{2.14}$$

A surface on which $W = \mathrm{const.}$ is termed an equipotential or level surface, to which the gravity vector is always perpendicular. Thus, we have no acceleration along an equipotential surface, and fluids will not flow along it. The particular equipotential surface corresponding to the mean ocean surface level has become known as the geoid, defined by $W = W_0 = \mathrm{const.}$ (Hofmann-Wellenhof and Moritz, 2006). The properties of the geoid make it a suitable reference surface for heights. The plumb lines that intersect every equipotential surface at right angles, are slightly curved, and the gravity vector is tangent to the plumb line at the same point. The orthometric height, or height above sea level, H, is measured along the plumb line, starting on the geoid. Figure 2.2 summarizes the constituents of Earth's gravity field.

All gravity field observations l are functions of the gravity potential W and their location P, which conceptually can be formulated as (Rummel and Pail, 2011)

$$l = l(P, W). \tag{2.15}$$

The determination of P and W from observations l, i.e., the inversion of Eq. (2.15), is a nonlinear task, and in general, linearization requires approximate values for both P and W. These approximate values are found from an Earth model.

A better approximation of Earth's shape than a sphere would be a slightly flattened ellipsoid, where its mass is set equal to Earth's actual mass, and its semi-minor axis coincides with Earth's mean rotational axis. This ellipsoid will generate a gravitational potential V^N. Moreover, if we let this ellipsoid rotate with the same angular velocity as the Earth, it will generate a gravity potential U similar to Earth's actual potential,

$$U = V^N + \Pi, \tag{2.16}$$

which is known as the normal potential. It is defined by two geometrical parameters a, f, together with two physical parameters GM,ω, and forms a geodetic reference system. See Table 2.1 for three commonly used geodetic reference systems.

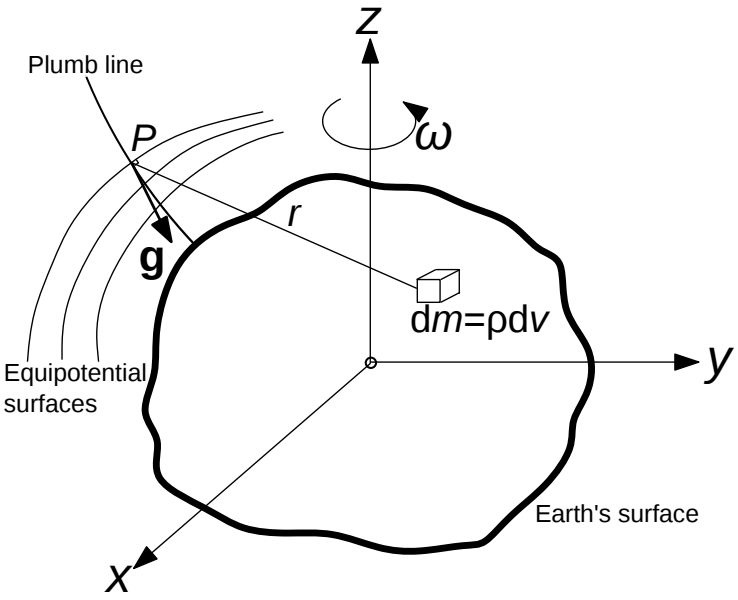

Figure 2.2: Earth's gravity field is generated by the gravitational potential V due to all mass elements $\mathrm{d}m$ of Earth's body as well as the centrifugal potential Π due to Earth's rotation. The gravity vector $\mathbf{g}$ is the gradient of the gravity potential $W = V + \Pi$. Surfaces on which the gravity potential remains constant are termed equipotential or level surfaces.

Table 2.1: Three common geodetic reference systems

	GM ($10^9\,\mathrm{m^3\,s^{-2}}$)	a (m)	f	ω ($10^{-5}\,\mathrm{rad^3\,s^{-1}}$)
GRS80	398600.5	6378137	1/298.257222101	7.292115
WGS84	398600.4418	6378137	1/298.257223563	7.292115167
TOPEX	398600.4415	6378136.3	1/298.25765	7.292115

The appropriate coordinate system in such a geodetic Earth model is ellipsoidal, using geodetic coordinates of ellipsoidal height h along the ellipsoidal normal and ellipsoidal latitude, longitude φ, λ. The connection between the purely geometrical geodetic coordinates, and the gravity-dependent physical natural coordinates, is the difference between the direction of the plumb line and the direction of the ellipsoidal normal, termed the deflection of the vertical.

The normal potential has the following spherical harmonic expansion (Hofmann-Wellenhof and Moritz, 2006),

$$U(r,\theta) = \frac{GM}{R}\sum_{n=0}^{\infty}\left(\frac{R}{r}\right)^{n+1}\bar{C}^N_{n0}\bar{P}_{n0}(\cos\theta) + \frac{1}{2}\omega^2 r^2(\sin\theta)^2. \tag{2.17}$$

From Eq. (2.17) we note that the normal gravity field is rotationally symmetric, and therefore independent of λ, such that only zonal terms ($m = 0$) remain. Furthermore, the normal gravity field is symmetric about the equator, which results in even zonal terms only. The main contribution to the ellipsoidal shape of the Earth is governed by the zonal $\bar{C}_{20}$ coefficient, also known as the dynamical form factor, with smaller contributions from the higher degree coefficients. Thus, for the normal gravity field we can safely truncate the summation in Eq. (2.17) at a low degree, e.g., $N_{\max} = 10$.

In accordance with the definition of gravity $\mathbf{g}$, normal gravity γ is the gradient of the normal potential,

$$\gamma = \nabla U = \left[\frac{\partial U}{\partial x}, \frac{\partial U}{\partial y}, \frac{\partial U}{\partial z}\right]. \tag{2.18}$$

We are now in the position to consider the remaining deviation between the actual gravity field and the normal gravity field, which is small enough to be considered linear (Sansò and Sideris, 2013). We return to Eq. (2.15), and introduce approximate values for the geometric position and the physical gravity potential, i.e., $P = P_0 + \Delta P$

and $W = U + T$. In classical physical geodesy, both position and gravity potential are linearized, giving the *anomaly* of l,

$$\Delta l = l(P,W) - l(P_0,U). \tag{2.19}$$

With the advent of GNSS, the position of the observation can be determined, and we only need to linearize the physical quantity, giving the *disturbance* of l,

$$\delta l = l(P,W) - l(P,U). \tag{2.20}$$

Subtracting Eq. (2.17) from Eq. (2.12), the centrifugal term vanishes and we get the disturbing (or anomalous) potential T, which also fulfills Laplace's equation, i.e., $\Delta T = 0$. We get the following spherical harmonic expansion of T:

$$T(r,\theta,\lambda) = \frac{GM}{R}\sum_{n=2}^{\infty}\left(\frac{R}{r}\right)^{n+1}\sum_{m=0}^{n}\bar{P}_{nm}(\cos\theta)\left[\Delta\bar{C}_{nm}\cos m\lambda + \Delta\bar{S}_{nm}\sin m\lambda\right], \tag{2.21}$$

where

$$\Delta\bar{C}_{nm} = \begin{cases}\bar{C}_{nm} - \bar{C}^{N}_{nm} & m = 0 \ \wedge \ n \in \{2,4,6,8,\ldots,N_{\max}\} \\ \bar{C}_{nm} & \text{else.}\end{cases} \tag{2.22}$$

$$\Delta\bar{S}_{nm} = \bar{S}_{nm}. \tag{2.23}$$

The summation in Eq. (2.21) begins at $n = 2$. The zero-degree coefficient represents GM/R, and cancels if the mass and radius of both Earth and ellipsoid is equal. The first-degree coefficients are proportional to the coordinates of Earth's center of mass, and vanish if Earth's center of mass coincides with the origin of the ellipsoid.

A number of functionals of the disturbing potential may be formed. In accordance with Eq. (2.20), the gravity disturbance is given by

$$\delta g_P = g_P - \gamma_P, \tag{2.24}$$

where g is observed gravity in point P, and γ in the same point can be computed by a closed formula. The difference in direction of the gravity vector $\mathbf{g}$ and the normal gravity vector γ is given by the deflection of the vertical, which has a north-south component ξ and an east-west component η, i.e.:

$$\xi = \Phi - \varphi, \tag{2.25}$$

$$\eta = (\Lambda - \lambda)\cos\varphi. \tag{2.26}$$

The disturbing potential describes the unknown remaining part of Earth's gravity field, and it is the determination of T which remains the main task of physical geodesy (Sansò and Sideris, 2013). In order to compute it, a boundary value problem (BVP) is solved, whereby a function's exterior value is determined from its value on a bounding surface as well as its behavior in space (Torge and Müller, 2012). Its behavior in space is governed by Laplace's equation, while different boundary conditions exist depending on the functional. The geodetic boundary value problem (GBVP) uses the fundamental equation of physical geodesy, in spherical approximation, as boundary condition,

$$\Delta g = -\frac{\partial T}{\partial r} - \frac{2}{R}T, \tag{2.27}$$

which is a linear combination of T and the partial derivative of T with respect to a surface normal. It relates observable gravity to the non-observable potential.

The classical Stokes approach uses the geoid as boundary surface, where the gravity anomalies must refer to the geoid (Hofmann-Wellenhof and Moritz, 2006). If the point $P = P_0$ is on the geoid, and thus has the potential $W = W_0$, the geoid height N is determined by Bruns's formula, see Figure 2.14

$$N_{P_0} = \frac{T_{P_0}}{\gamma_{Q_0}}. \tag{2.28}$$

Similar to Eq. (2.24), and in accordance with Eq. (2.19), the gravity anomaly is given by

$$\Delta g_{P_0} = g_{P_0} - \gamma_{Q_0}. \tag{2.29}$$

It is important to note that Eq. (2.28) and Eq. (2.29) suppose that the geoid is the boundary surface, and that gravity is measured on it (Torge and Müller, 2012). This, however, is not the case in practice due to the topographic and atmospheric masses outside the geoid and the fact that we observe gravity on Earth's surface. By this approach, the masses outside the geoid must be shifted inside Earth's interior, and the gravity observations must be reduced to the geoid surface. Both the shifting of masses and reduction requires knowledge of the density of the masses, which normally is not known to sufficient accuracy. Consequently, hypotheses are always used in this approach.

In order to reduce gravity to the geoid, we theoretically need to know the gravity gradient. It is generally unknown, and the free-air anomaly is approximated by the free-air gradient of normal gravity (Hofmann-Wellenhof and Moritz, 2006),

$$\Delta g_{P_0} = \left(g_P - \frac{\partial g}{\partial h}H\right) - \gamma_{Q_0} \approx \overbrace{\left(g_P - \frac{\partial \gamma}{\partial h}H\right)}^{g_{P_0}} - \gamma_{Q_0}. \tag{2.30}$$

In addition, we must correct gravity for the effect of the topography, which can be approximated by an infinite horizontal layer of density ρ and thickness H called a Bouguer plate, giving the simple Bouguer correction (Torge and Müller, 2012),

$$A_B = 2\pi G\rho H. \tag{2.31}$$

We may further take the deviation of the Bouguer plate from the actual topography into account, by forming a refined Bouguer correction,

$$A_T = A_B - c_P, \tag{2.32}$$

with the terrain correction c_P given by (Torge and Müller, 2012)

$$c_P = G\rho \iint_{\sigma} \left[\int_{H_P}^{h} \frac{h - H_P}{r^3} \, \mathrm{d}H \right] \mathrm{d}\sigma. \tag{2.33}$$

In 1945, the Russian geodesist M. S. Molodensky suggested an alternative approach using Earth's surface as boundary surface, and thereby avoiding topographic reductions (Hofmann-Wellenhof and Moritz, 2006). Then, a different reference point Q can be chosen for the normal gravity. The point Q is situated on the ellipsoidal normal through P and satisfies $U_Q = W_P$, see Figure 2.15. The pointwise projection of points P to points Q gives a surface called the telluroid, which is not an equipotential surface. The distance along the ellipsoidal normal from the telluroid to Earth's surface is called the height anomaly, ζ, and is given by Eq. (2.28),

$$\zeta_P = \frac{T_P}{\gamma_Q}. \tag{2.34}$$

Moreover, on Earth's surface, the gravity anomaly is given by

$$\Delta g_P = g_P - \gamma_Q, \tag{2.35}$$

where g is observed gravity in point P, and γ in Q can be computed by a closed formula.

If the height anomaly is taken from the surface of the ellipsoid, the quasigeoid is obtained, and their relation is shown in Figure 2.15. Although the quasigeoid takes the role of the geoid, the quasigeoid is rougher and not an equipotential surface. An approximation to the quasigeoid to geoid separation is given by

$$N - \zeta \approx \frac{\Delta g_B}{\gamma_0} H, \tag{2.36}$$

where Δg_B is the simple Bouguer anomaly, cf. Eq. (2.31). Eq. (2.36) shows that quasigeoid and geoid can be assumed to coincide over the oceans, where $H = 0$.

The focus of this thesis is mainly on the coastal zone where the quasigeoid to geoid separation is assumed to be negligible, and often throughout the thesis the term geoid is used in a loose fashion. However, the geoid and quasigeoid are strictly different vertical reference surfaces, and differences in their determination are pointed out when necessary. The theory in Section 2.3 can be equally applied to geoid and quasigeoid determination. Regarding the data sets, all the geoid models used in this thesis and appended papers are strictly quasigeoids, with the exception of the numerical examples in **Paper C**, where synthetic geoids determined from the same GGM are compared in a closed-loop environment.

2.2 Gravimetry

2.2.1 Terrestrial gravimetry

Terrestrial gravimetry concerns the measurement of gravity and the gravity gradient on or close to Earth's surface (Timmen, 2010). Absolute gravity measurements refer directly to length and time standards, while relative measurements rely on a counterweight principle to determine gravity differences. The increased precision of terrestrial gravimeters during the last decades has enabled the detection of a range of geophysical phenomena which affect gravity (Crossley et al., 2013), see Figure 2.3. Consequently, terrestrial gravimetry is an important tool for monitoring global change. Many time-variable gravity signals show amplitudes in the 0.1-10 $\mu\mathrm{Gal}$ range, and some, such as GIA, require monitoring over several decades to be described sufficiently.

The forerunner of today's gravimeters is the pendulum gravimeter, which ruled gravimetry for ~300 years, before being abandoned in favor of ballistic absolute gravimeters (Crossley et al., 2013). The latter applies the free-fall principle, where a test mass is dropped in vacuum (Timmen, 2010). A laser interferometer as length standard, and an atomic clock as time standard are used to obtain time-distance pairs, and Newton's equations of motion are solved to obtain the acceleration, i.e.,

$$m\ddot{z} = mg(z), \tag{2.37}$$

where m is the mass, z is taken along the local vertical, and $\ddot{z} = d^2z/dt^2 = g$. If we assume a homogeneous gravity field along the fall distance, double integration of Eq. (2.37) will give

$$z = z_0 + \dot{z}_0 t + \frac{g}{2}t^2, \tag{2.38}$$

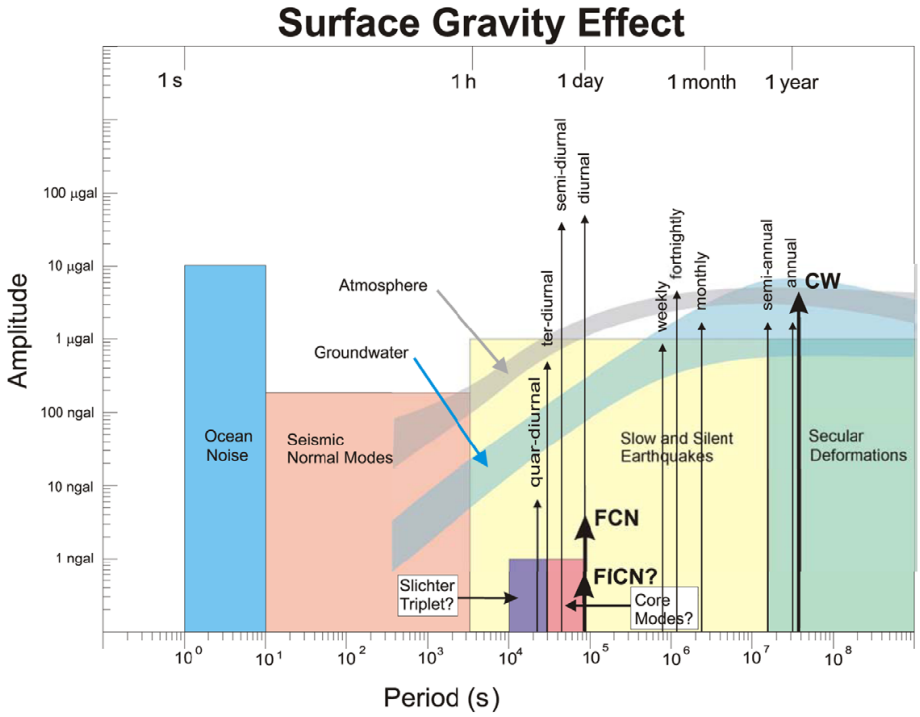

Figure 2.3: Schematic showing the spectrum of terrestrial gravity signal contributors. **FCN** and **FICN** denote the Free Core Nutation and Free Inner Core Nutation, respectively. **CW** denotes the Chandler Wobble. Taken from Crossley et al. (2013).

which relates the position z of the free-falling test mass at time t to the gravity acceleration. The integration constants z_0 and $\dot{z}_0$ represent z and $\dot{z} = dz/dt$ at the beginning of the experiment ($t = 0$). If the time-distance pairs are plotted, we get an almost parabolic curve. In practice, through the precise length and time measurements, hundreds of time-distance pairs are recorded and adjusted to the fitting curve in a least-squares sense, giving an estimate of z_0, $\dot{z}_0$, and g (Timmen, 2010). A more realistic approach is to assume that the gravity field is not homogeneous over the length of the drop, but changes slightly (according to Newton's law, Eq. (2.1)). Because the length of the drop is small ($\sim$20 cm) we can assume that the gravity change over this distance is linear. If we can determine this vertical gradient $\partial g/\partial z$ (e.g., by relative gravity measurements (see below) at different heights above the ground), and refer the measurement of g to a reference height at the observation site, we get an unambigous description. Eq. (2.37) is extended by the linear approximation of gravity change,

$$\ddot{z} = g_0 + \frac{\partial g}{\partial z}(z - z_0), \tag{2.39}$$

which has the following solution (Micro-g LaCoste, 2012),

$$z(t) = z_0 + \dot{z}_0 \left(t + \frac{1}{6} \frac{\partial g}{\partial z} t^3 \right) + \frac{1}{2} g_0 \left(t^2 + \frac{\partial g}{\partial z} \frac{t^4}{12} \right). \tag{2.40}$$

The most common absolute gravimeter today is the FG5 (Niebauer et al., 1995; Micro-g LaCoste, 2012), see Figure 2.4. It has an accuracy of ~2 $\mu\mathrm{Gal}$. The FG5 system comprises a vacuum chamber, interferometer, superspring, laser, computer, and controlling electronics. The test mass is dropped in the vacuum chamber, the interferometer monitors the position of the test mass, and the superspring compensates for external vibrations due to, e.g., microseismics. The computer runs a software which allows for monitoring the system, collecting data, analyzing and storing the results.

The FG5 uses a helium neon (HeNe) laser (λ =633 nm) as length standard, and a rubidium atomic frequency as time standard (Niebauer et al., 1995). The test mass is dropped in vacuum (10^{-4} Pa), and inteference patterns are detected in a Mach-Zehnder interferometer. The time is recorded at every minimum (destructive interference), giving time-distance pairs at every $\lambda/2$, see Figure 2.5. From the ~700,000 interference fringes which are obtained, around 700 time-distance pairs are inserted into Eq (2.40) for the determination of g. A typical observation campaign lasts 1-2 days, including several hourly data sets where a set consists of 50-100 drops of the test mass.

Relative gravimeters are smaller and easier to transport than absolute gravimeters (Timmen, 2010). They can only observe gravity differences, and are therefore typically used to densify gravity networks with known absolute gravity values, monitor temporal gravity changes, and support absolute gravity campaigns by observing the gravity gradient. The expected accuracy of relative gravity measurements is ~10-15 $\mu\mathrm{Gal}$. The most widely used relative gravimeters are the spring gravimeters, which are based on the principle of counterbalancing a change in gravity by a change in the length of a spring system, keeping a test mass in equilibrium (Crossley et al., 2013). If the test mass hangs vertically by the spring, a gravity change will give only small changes in the length of the spring. Consequently, the typical design is a general lever spring balance, see Figure 2.6, where the spring is inclined. This design makes the spring length more sensitive to changing gravity. The lever spring design principle is applied in the widely-used LaCoste and Romberg inclined zero-length spring gravimeters, where the spring is specifically designed such that it has zero length in the unstretched condition. The balance of torques is given by (Torge and Müller, 2012)

$$mga \sin(\alpha + \delta) - kbd \frac{l - l_0}{l} \sin\alpha = 0, \tag{2.41}$$

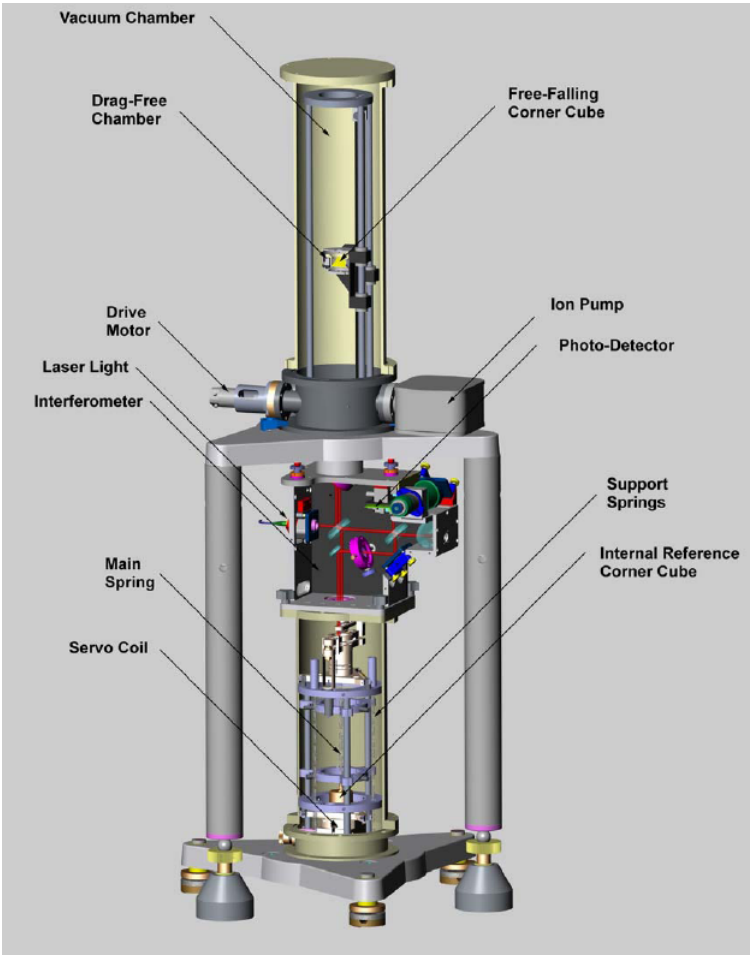

Figure 2.4: Schematic showing the FG5 system. Taken from Micro-g LaCoste (2012).

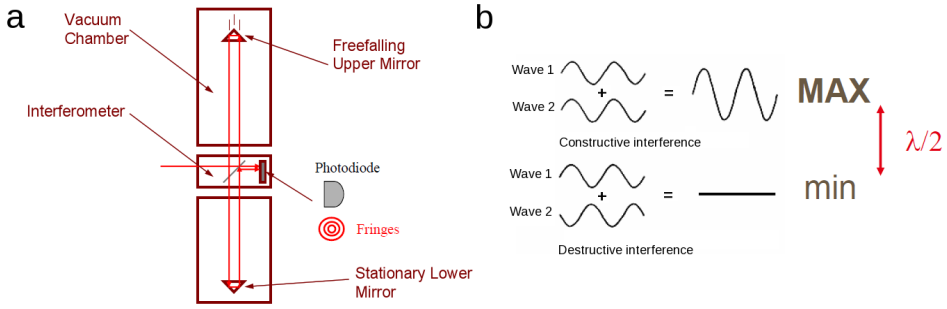

Figure 2.5: FG5 principle of operation, modified from Micro-g LaCoste (2012); (a) a freely falling reflective test mass is dropped in vacuum, (b) causing optical interference fringes to be detected by an interferometer. Time is recorded at each minimum giving time-distance pairs at every $\lambda/2$, giving ~700,000 fringes, from which typically 700 time-distance pairs are inserted into Eq (2.40) for the determination of g.

with the quantities shown in Figure 2.6.

The test mass will deviate from its equilibrium position due to a change in gravity, and the equilibrium position is found by adjusting a dial on the gravimeter (Timmen, 2010). This adjustment can be transformed to a gravity change by a calibration function. The biggest challenge with spring gravimeters is that the equilibrium position may change with time due to environmental disturbances (e.g., temperature and air pressure changes). The spring will drift due to aging and short-term changes in the field due to small vibrations and shocks, typically by a few tens of $\mu\mathrm{Gal}$ per hour. The drift is usually determined by repeated site occupations during one day and subsequent modeling.

As mentioned in the beginning of this section, observed gravity includes a range of time-variable gravity effects which it is typically corrected for using different models (Timmen, 2010). Which effects we need to correct for will depend on the duration of the measurement campaign and the sensitivity of the gravimeter. Table 2.2 shows the magnitude of some constituents of gravity.

Relative gravity observations are typically corrected for the solid Earth tide, which has an amplitude larger than the measurement uncertainty (Timmen, 2010). In addition, the gravity observations are corrected for the measurement height. During a typical relative gravity campaign, although possibly larger than the measurement uncertainty, gravitational effects due to ocean tide loading, atmospheric loading, polar motion, and hydrology will be close to constant and need not be corrected for. Absolute gravity measurements are much more precise and measure over a longer time, and are corrected for these effects, which is typically done in the absolute

Table 2.2: Order of magnitude of some gravity signal contributors. $1\,\mathrm{Gal} = 0.01\,\mathrm{ms}^{-2}$. Taken from Breili (2009) and **Paper B**.

Amplitude	Signal
$10\ \mathrm{ms}^{-2}$	Gravitation of the Earth
$10^{-2}\ \mathrm{ms}^{-2}$	Earth's flattening and rotation
$10^{-3}\ \mathrm{ms}^{-2}$	Mountains and ocean trenches
$10^{-4}\ \mathrm{ms}^{-2}$	Internal mass distribution of the Earth
$10^{-5}\ \mathrm{ms}^{-2}$	Large reservoirs
	Gravity anomalies due to, e.g., a salt dome
$10^{-6}\ \mathrm{ms}^{-2}$	Tidal acceleration due to the Sun and the Moon
	Distant earthquakes
$10^{-7}\ \mathrm{ms}^{-2}$	Cryospheric changes
	Local hydrological changes
	Ocean tide loading at coastal sites
$10^{-8}\ \mathrm{ms}^{-2}$	Ocean tide loading at inland sites
	Non-tidal ocean loading
	Global hydrological changes
	Nearby large buildings
	GIA
	Pole tide
	Atmospheric loading
$10^{-11} - 10^{-20}\ \mathrm{ms}^{-2}$	Tidal acceleration due to other planets

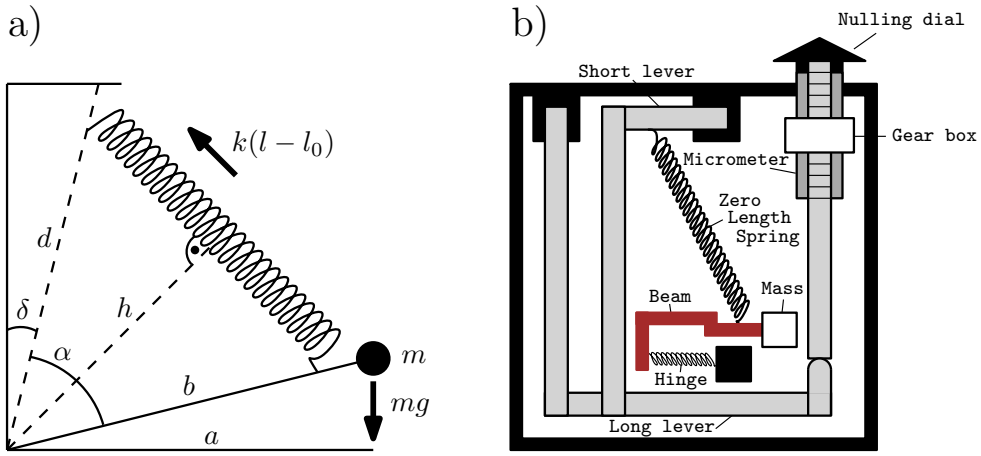

Figure 2.6: Principle of the general lever spring balance (a), and its implementation in the LaCoste and Romberg relative gravimeter (b). Adapted from Torge and Müller (2012) and Crossley et al. (2013).

gravity processing software. More elaborate methods to determine the gravitational effects due to atmospheric and ocean loading, as well as effects often unaccounted for such as the hydrological effect on gravity, form an important part of **Paper B**.

Gravimetry is also performed from moving platforms such as ships and airplanes, which are particularly efficient methods in regions that are difficult to reach by foot, e.g., oceans, extreme topography, thick forests, and polar regions (Torge and Müller, 2012). These instruments are also relative, i.e., what is measured are gravity differences to a fixed value in the harbor or at the airport. The main additional challenges when observing gravity from such platforms are gravity sensor orientation and corrections due to the fact that the observations are performed on a moving platform in a rotating Earth system (see Section 2.6.2). The typical accuracy that can be obtained with airborne gravimetry is ±1 mGal to ±3 mGal at a 5-7 km resolution. With shipborne gravimetry the accuracy is typically between ±0.5 mGal to ±2 mGal at $\sim$1 km resolution.

2.2.2 Satellite gravimetry

Because of the rapid attenuation of Earth's gravity signal with increasing height, high-resolution gravity observation from space requires satellites in low orbits and with highly sensitive sensors (Torge and Müller, 2012). This has been achieved

by the practical realization of the satellite-to-satellite tracking (SST) and satellite gravity gradiometry (SGG) principles.

Up till now, SST has used microwave systems to measure range and range rates between satellites (Torge and Müller, 2012). It is realized either in high-low mode (Figure 2.7a), with several high and one low-flying satellite, or in low-low mode (Figure 2.7b), with two low-flying satellites at the same altitude. A combination of both is also possible. The CHAllenging Minisatellite Payload (CHAMP, 2000-2010) mission used the high-low mode, with the satellite itself being the sensor (Reigber et al., 2002). Precise orbit determination of the low-flying (~450 km) CHAMP satellite was done by high-flying GNSS satellites. The satellite orbit is perturbed by the gravity field, and with an onboard accelerometer measuring non-gravitational forces acting on the satellite (e.g., atmospheric drag), the gravity field can be inferred from orbit analysis. The CHAMP global gravity field could be determined to roughly degree and order 70 (~280 km). The Gravity Recovery And Climate Experiment (GRACE, 2002-) mission uses SST in low-low mode, where, in addition to GNSS satellites, the distance and its rate of change between two low-flying (~500 km) CHAMP-type satellites are measured very accurately (Tapley et al., 2004). The ranges are strongly influenced by variations in the gravity field, allowing for the determination of the global gravity field to roughly degree and order 150 (~130 km).

SST allows for the precise determination of the long-wavelength part of the gravity field, because the satellite orbit gives almost global coverage. However, the short-wavelength part of the gravity field cannot be observed because of the attenuation of the gravity signal with increased orbit height. By SGG, differences in gravity acceleration, i.e., the second derivatives of the gravitational potential, are measured

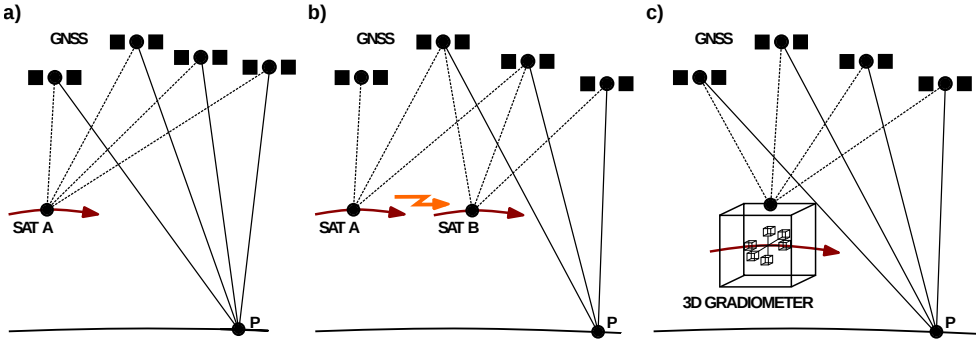

Figure 2.7: Schematic showing the satellite-to-satellite tracking principle in (a) high-low mode, and (b) low-low mode, as well as (c) the satellite gravity gradiometry principle. Adapted from Torge and Müller (2012).

in three dimensions, see Figure 2.7c. Thereby the attenuation of the gravity field is counteracted by measuring its finer structures. The GOCE (Drinkwater et al., 2003) mission (2009-2013) was the first to employ SGG. The GOCE gradiometer consists of six accelerometers, placed pairwise on three orthogonal axes. They observe different gravitational gradient components, which are combined in the Marussi tensor

$$\mathbf{V}'' = \begin{bmatrix} V_{xx} & V_{xy} & V_{xz} \\ V_{yx} & V_{yy} & V_{yz} \\ V_{zx} & V_{zy} & V_{zz}, \end{bmatrix}, \tag{2.42}$$

where the x-axis is in flight direction, the y-axis in cross-track direction, and the z-axis in the outward radial direction (Torge and Müller, 2012). Due to the symmetry $V_{xy} = V_{yx}$, $V_{xz} = V_{zx}$, $V_{zy} = V_{yz}$ as well as the Laplace equation, $\Delta V = V_{xx} + V_{yy} + V_{zz} = 0$, only five of the nine elements in Eq. (2.42) are mutually independent. The accelerometers register the forces necessary to keep each test mass in their center position. The measurement accuracy of the second derivatives as well as the accuracy of the orbit determination must be high, and the latter is usually based on GNSS tracking. In addition, a drag-free system accounts for the considerable air drag due to the low altitude ($\sim$280 km). GOCE has observed the global gravity field up to roughly degree and order 250 ($\sim$80 km).

Classic gravity field recovery from satellite data was based on analysis of accumulated orbit perturbations of different satellites, starting from an initial orbit determined from models and independent observation of the satellite's motion (Torge and Müller, 2012). Prior to onboard tracking systems such as GNSS, the independent tracking of the satellite was performed on Earth's surface, e.g., by precise satellite laser ranging (SLR). The advent of dedicated satellite gravimetry missions, which all give almost continuous, precise observation of their orbits, opened up a range of different approaches to gravity field analysis, see, e.g., Liu (2008) or Yi (2012) for an overview.

Eq. (2.9) is a convenient means to compute a disturbing gravity quantity in arbitrary points on or outside the Earth surface. Only a set of spherical harmonic potential coefficients $\{\bar{C}_{nm}, \bar{S}_{nm}\}$ is needed. The coefficients refer to a sphere with radius R, and are scaled by GM. These three quantities define a global gravity model (GGM). In practice, the number of coefficients is finite, where the maximum degree n of the GGM is termed $N_{\max}$.

Satellite gravimetry gives the global gravity field, and is the predominant data source for GGMs. In addition to being created from independent satellite tracking techniques (e.g., GNSS and SLR), satellite orbit perturbations, inter-satellite links, or gravity gradiometry, a GGM can be enhanced (i.e., its resolution increased) by including terrestrial gravity and altimetry-derived gravity over the oceans, giving com-

Table 2.3: GGMs used in this thesis.

Model	$N_{\max}$	Data sources	Reference
GOCO05s	280	GOCE, GRACE, GPS-tracked orbits, SLR	(Mayer-Gürr et al., 2015)
GOCE TIM5	280	GOCE	(Brockmann et al., 2014)
GOCE DIR5	300	GOCE, GRACE, SLR	(Bruinsma et al., 2013)
EGM2008	2190	GRACE, terrestrial gravity, altimetry	(Pavlis et al., 2012)

bined GGMs as opposed to the satellite-only GGMs. See Table 2.3 for the GGMs considered in this thesis. The spherical harmonic degree of a GGM is related to the spatial resolution Δ on the sphere according to (Rummel and Pail, 2011)

$$\Delta = \frac{\pi R}{n} \approx \frac{20000\,\mathrm{km}}{n}. \tag{2.43}$$

The relations between T and other gravity field functionals allow spherical harmonic expansions of, e.g., the geoid height, the height anomaly, the gravity disturbance, and the gravity anomaly . We can generalize Eq. (2.21) as follows,

$$f(r,\theta,\lambda) = \sum_n f^{\mathrm{upw}} \lambda_n \sum_m \bar{P}_{nm}(\cos\theta)\left[\Delta\bar{C}_{nm}\cos m\lambda + \Delta\bar{S}_{nm}\sin m\lambda\right], \tag{2.44}$$

where f is a quantity of the disturbing gravity field, related to T by λ_n, which here includes the spectral eigenvalue as well as dimensioning. The spectral eigenvalues allow easy transfer between the different functionals in the spectral domain (e.g., Meissl, 1971; Rummel and Pail, 2011). f^{upw} is the upward continuation operator. Table 2.4 lists some relations for different disturbing gravity field quantities.

A GGM can only provide the potential on Earth's surface; hence, the geoid is not directly computable from a GGM (Section 2.1), but can be computed by first determining ζ from a GGM, and then consider the geoid to quasigeoid separation (Eq. (2.36)).

The signal degree variance represents the contribution of each spherical harmonic degree to the total signal variance, and thus gives information on the signal content of a gravity field functional (Torge and Müller, 2012). The dimensionless signal degree variances may be calculated from a set of spherical harmonic coefficients $\{\Delta\bar{C}_{nm}, \Delta\bar{S}_{nm}\}$,

$$c_n = \sum_{m=0}^{n}\left(\Delta\bar{C}_{nm}^2 + \Delta\bar{S}_{nm}^2\right), \tag{2.45}$$

Table 2.4: Relations for different gravity field quantities.

f	f^{upw}	λ_n
T	$\left(\frac{R}{r}\right)^{n+1}$	$\frac{GM}{R}$
ζ	$\left(\frac{R}{r}\right)^{n+1}$	R
Δg	$\left(\frac{R}{r}\right)^{n+2}$	$\frac{GM}{R^2}(n-1)$
δg	$\left(\frac{R}{r}\right)^{n+2}$	$\frac{GM}{R^2}(n+1)$
T_{rr}	$\left(\frac{R}{r}\right)^{n+3}$	$\frac{GM}{R^3}(n+1)(n+2)$

as obtained from a global gravity model (GGM), or by different empirical degree-variance models. The signal covariance function for arbitrary gravity field functionals can be computed using signal degree variances, see Eq. (2.56).

The coefficients of a GGM also have uncertainties, and the degree variances computed from the errors of the coefficients are termed error degree variances (Rummel and Pail, 2011). They are part of the GGM, and constitute the commission error. The signal content above $N_{\max}$, on the other hand, is known as the omission error, and must be computed from an empirical degree variance model. If the signal degree variances of a GGM is plotted together with the error degree variances, the point where the curves cross defines the resolution of the GGM.

Finally, it should be noted that there are different ways of dealing with the tides (Torge and Müller, 2012). The tidal gravitational attraction is included in every gravity observation, making Laplace's equation problematic, as the Sun and the Moon are outside the Earth. The tidal effect is split into a direct effect due to the actual change in the potential due to the attraction from the Sun and the Moon, and an indirect effect due to the tidal forces causing Earth deformation, which also changes the potential.

Furthermore, the tidal forces affecting every gravity observation can be split into time-dependent and time-independent parts, where the time-dependent periodic part is caused by Earth's rotation and the orbits of Sun and Moon, and evens out over time (Torge and Müller, 2012). The time-indepedent part, however, must be considered in gravity field determination, and is known as the permanent tide. In the mean-tide (MT) system, the time-dependent part of the tidal forces is removed from the observed gravity field quantity. In the zero-tide (ZT) system, the direct effect of the permanent part is also removed. For geometry-related quantities such as site positions on Earth's surface, ZT is synonymous with MT. If the indirect effect is removed as well, we are in the tide-free (TF) system, supposing no Sun and Moon

exists and consequently no tidal forces. This theoretical condition can only be determined through a conventional model, giving a conventional TF system. As different geodetic data sets are often given in different tidal systems, we must make sure they are brought into a unified tidal system before their combination.

2.3 Regional geoid computation

The global gravity field is typically modeled using well-suited spherical harmonics (Section 2.2.2). When using a satellite-only GGM for gravity field determination, small-scale structures of the gravity field are lost, which typically amount to ~30 cm in terms of geoid heights. In order to increase the resolution of the geoid, the GGMs are combined with terrestrial data, usually restricted to an area of interest. Modeling the high-resolution structure of the geoid on local to regional scales is the topic of regional geoid computation (Denker, 2013).

The solution of the GBVP typically consists of two steps, namely the spherical harmonic synthesis of a GGM using Eq. (2.21), and the field transformation of residual gravity anomalies (subsequent to the subtraction of the part of the signal covered by the GGM), see Section 2.3.4. There exist several methods for computing the residual gravity field, where integral formula solutions to the GBVP and least-squares techniques can be seen as classical methods. Radial base functions form a more modern approach.

2.3.1 Integral formulae

The geoid height N at point P can be obtained from gravity anomalies at point q by the integral formula of Stokes (1849). It globally integrates the gravity anomalies over the whole sphere σ, using Stokes function S as integration kernel (or weight),

$$N(P) = \frac{R}{4\pi\gamma} \iint_{\sigma} S(\psi_{Pq}) \Delta g_q \, \mathrm{d}\sigma, \tag{2.46}$$

where R is the spherical Earth radius, γ is normal gravity evaluated on the surface of the reference ellipsoid, and ψ_{Pq} is the spherical distance between computation point P and data point q.

The integral formulae are spherical convolutions of a signal function with a kernel, and can be solved exactly by either numerical integration or by a one-dimensional

Fast Fourier Transform (1D-FFT), as described by Haagmans et al. (1993). Thereby, the FFT is performed along parallels only, according to

$$N(\varphi_P) = \frac{R\Delta\varphi\Delta\lambda}{4\pi\gamma}\mathcal{F}_1^{-1}\left\{\sum_{\varphi}\mathcal{F}_1\left\{S(\Delta\lambda)\right\}\cdot\mathcal{F}_1\left\{\Delta g_q\cos\varphi\right\}\right\}, \tag{2.47}$$

where $\mathcal{F}_1$ denotes the 1D-FFT operator and $\mathcal{F}_1^{-1}$ its inverse, and $\Delta\varphi$ and $\Delta\lambda$ are the latitudinal and longitudinal spacing of the computation grid, respectively.

The Stokes function has the following closed-form expression (Torge and Müller, 2012),

$$S(\psi_{Pq}) = \frac{1}{\sin\frac{\psi_{Pq}}{2}} + 1 - 5\cos\psi_{Pq} - 6\sin\frac{\psi_{Pq}}{2} - 3\cos\psi_{Pq}\ln\left[\sin\frac{\psi_{Pq}}{2} + \left(\sin\frac{\psi_{Pq}}{2}\right)^2\right], \tag{2.48}$$

and ψ_{Pq} is given by

$$\cos\psi_{Pq} = \sin\varphi_P\sin\varphi_q + \cos\varphi_P\cos\varphi_q\cos(\lambda_q - \lambda_P). \tag{2.49}$$

The Stokes function can also be expressed as a Legendre series,

$$S(\psi_{Pq}) = \sum_{n=2}^{\infty}\frac{2n+1}{n-1}P_n\left(\cos\psi_{Pq}\right). \tag{2.50}$$

Molodensky's formula is given by

$$\zeta(P) = \frac{R}{4\pi\gamma}\iint_{\sigma}S(\psi_{Pq})\left(\Delta g_q + g_1 + g_2 + \cdots\right)\mathrm{d}\sigma, \tag{2.51}$$

where the higher-order Molodensky terms $(g_1, g_2, \ldots)$ all depend on the terrain inclination, which means they can be neglected in flat areas (Hofmann-Wellenhof and Moritz, 2006). The g_1 term can be approximated by the terrain correction (Eq. (2.33)).

2.3.2 Least-squares collocation

Least-squares collocation (LSC) is an optimal estimation method which allows the estimation of arbitrary gravity field quantities from inhomogeneously distributed point observations (Moritz, 1980). LSC combines parameter estimation, prediction, and filtering. It takes advantage of the known signal characteristics, described by the signal covariance function.

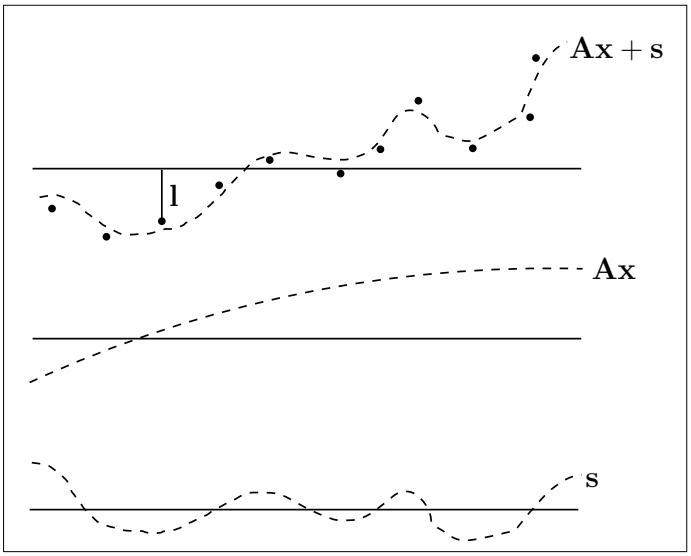

Figure 2.8: Schematic of the LSC model. The top solid curve is to be determined from observations (dots), which, in turn, are affected by errors $\mathbf{n}$. The curve which we seek to interpolate consists of a systematic part $\mathbf{Ax}$ and a random part $\mathbf{s}$. Adapted from Moritz (1980).

The standard linear model of standard least-squares adjustment is extended according to

$$\mathbf{l} = \mathbf{Ax} + \mathbf{s} + \mathbf{n}, \tag{2.52}$$

where $\mathbf{l}$ is the observation vector, $\mathbf{n}$ the noise or residual vector, $\mathbf{x}$ is the vector of unknown parameters, and $\mathbf{A}$ is the design matrix, characterizing the effect of the parameters $\mathbf{x}$ on the observations $\mathbf{l}$. The linear model has been extended by the signal vector $\mathbf{s}$. Thereby, the observation l is made up of a systematic part $\mathbf{Ax}$, and two random parts s and n. Typically, the systematic part is non-linear and is linearized by Taylor's theorem. The signal may exist at points other than the observation points, and may in fact vary continuously although l is observed at discrete points only. Thereby, this linear model is applicable for interpolation, see Figure 2.8.

The signal $\mathbf{s}$ is unknown, and, unlike for the parameters, the connection between known and unknown quantities is not given through a functional relation, but rather in terms of covariance matrices. It may be shown that the linear minimum unbiased parameter and signal estimates are given by (Moritz, 1980)

$$\hat{\mathbf{x}} = \left(\mathbf{A}^T \bar{\mathbf{C}}_{ll}^{-1} \mathbf{A}\right)^{-1} \mathbf{A}^T \bar{\mathbf{C}}_{ll}^{-1} \mathbf{l}, \tag{2.53a}$$

$$\hat{\mathbf{s}} = \mathbf{C}_{sl} \bar{\mathbf{C}}_{ll}^{-1} \left(\mathbf{l} - \mathbf{A}\hat{\mathbf{x}}\right), \tag{2.53b}$$

respectively, where we have set $\bar{\mathbf{C}} = \mathbf{C}_{tt} + \mathbf{C}_{nn}$, such that the covariance matrix of $\mathbf{l}$ is obtained by adding the covariance matrices of its signal and noise parts. $\mathbf{C}_{sl}$ is a matrix containing the signal cross-covariances between the functionals between computation point and observations, and $\mathbf{C}_{ll}$ is the auto-covariance matrix between all combinations of observations.

The error covariance matrix of the estimated signals is given by (Moritz, 1980)

$$\mathbf{E}_{ss} = \mathbf{C}_{ss} - \mathbf{C}_{sl}\bar{\mathbf{C}}_{ll}^{-1}\mathbf{C}_{ls}, \tag{2.54}$$

where its diagonal terms are the error variances of the estimated signals.

All covariances $\mathbf{C}_{sl}$, $\mathbf{C}_{ll}$ are obtained from the same covariance function $C(\psi)$, assumed to depend only on the horizontal distance ψ between the considered points (Moritz, 1980). In physical geodesy, we typically take the covariance function of the disturbing potential T to be the basic covariance function, from which all covariances are computed by covariance propagation. The covariance function can be written as

$$C(\psi_{Pq}) = \frac{1}{8\pi^2}\int_{\lambda=0}^{2\pi}\int_{\theta=0}^{\pi}\int_{\alpha=0}^{2\pi} T(\theta_P,\lambda_P)T(\theta_q,\lambda_q)\,\sin\theta \mathrm{d}\theta\mathrm{d}\lambda\mathrm{d}\alpha, \tag{2.55}$$

where (θ,λ) are spherical coordinates, and the points $P(\theta,\lambda)$, $q(\theta,\lambda)$ are on the surface of the unit sphere.

The global integral in Eq. (2.55) can also be expressed as a Legendre series,

$$C(\psi_{Pq}) = \sum_{n=2}^{\infty}(\lambda_n^T)^2 c_n P_n(\cos\psi_{Pq}), \tag{2.56}$$

where $P_n(\cos\psi_{Pq})$ are the Legendre polynomials, and c_n are the dimensionless signal degree variances (Eq. (2.45)), with $\lambda_n^T = GM/R$.

Several gravity field functionals are related to T by isotropic spectral eigenvalues, such as gravity anomalies, gravity disturbances, geoid heights, or height anomalies (Rummel and Pail, 2011). The upward continuation operator can be expressed as a spectral eigenvalue as well, see Section 2.2.2. However, some functionals, such as the deflections of the vertical, do not have the isotropic link, and more complex differential operations must be performed to determine the covariance (Hofmann-Wellenhof and Moritz, 2006).

If we restrict LSC to the case of geoid computation from gravity anomalies, making it directly comparable with Stokes's formula (Eq. (2.46)), it can be written as

$$N(P) = \mathbf{C}_{Pq}^{Ng}\left(\mathbf{C}_{qq}^{gg}\right)^{-1}\Delta g_q. \tag{2.57}$$

2.3.3 Radial base functions

Spherical harmonics are global base functions, which means they are different from zero everywhere on the globe. The associated spherical harmonic coefficients have optimal frequency localization (they are directly related to the frequency values degree n and order m) (Schmidt, 2001). Localization refers to the area in the frequency or spatial domain in which a function does not vanish, and the function localizes better as this area shrinks. Dirac functions represent the direct opposite of spherical harmonics as they are different from zero at a single point only, i.e., they have optimal space localization. Due to the uncertainty principle it is not possible for a function to have both perfect frequency and space localization (Freeden et al., 1998). A good compromise between ideal frequency localization and ideal space localization is given by the kernel functions known as radial base functions (RBFs).

RBFs are limited to a certain spatial region, making them suitable for regional gravity field modeling due to their space-localizing properties. There is a vast amount of RBFs to choose from, as long as they represent harmonic kernel functions. They are versatile in that their approximation characteristics and spatial distribution can be adjusted, making it possible to use them for all kinds of data sets and for combining different types of observations (Lieb et al., 2016). In addition to considering a suitable size for the target area (which should correspond to the signal bandwith), as well as a suitable margin to avoid boundary effects, an appropriate point grid for the placement of the RBFs (network design), the actual RBF itself with its bandwidth, and a suitable regularization method must be chosen. This versatility makes the establishment of a standard RBF modeling method challenging, and, in practice, different RBF modeling groups have adopted different frameworks (Eicker, 2008; Wittwer, 2009; Bentel, 2013; Naeimi, 2013).

Regional gravity field modeling with RBFs can be done using numerical integration or least-squares estimation approaches, and this thesis focuses on the latter, which is the common geodetic approach facilitating error analysis and propagation.

As spherical isotropic functions, the RBF can be written as a Legendre series (Bentel, 2013),

$$B(\psi_{Pk}) = \sum_{n=2}^{\infty} \frac{2n+1}{4\pi R^2} \lambda_n B_n P_n(\cos\psi_{Pk}), \tag{2.58}$$

where ψ_{Pk} is the spherical distance between computation point P and the origin of the RBF at grid point k, and λ_n are the spectral eigenvalues including dimensioning. As mentioned, there are many choices of the RBF itself, and its bandwidth must be chosen properly such that the RBF approximates the signal in an optimal way

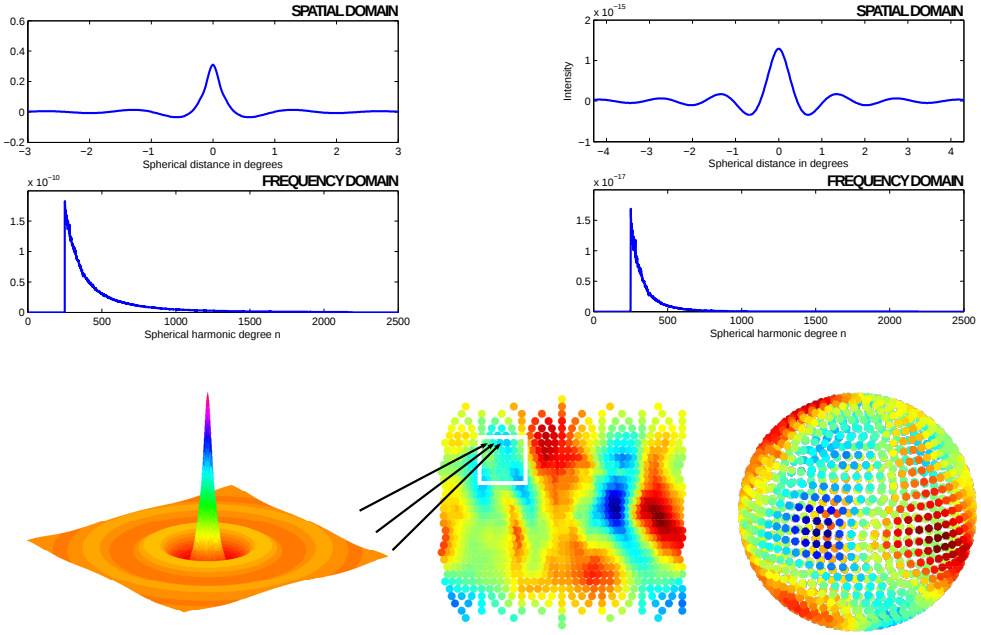

Figure 2.9: Schematic showing the RBF using the SK (upper left) as well as the covariance function of LSC (upper right) in the spatial and frequency domains. The lower panel shows the RBF using the SK in 3D, as well as its placement on the equidistributed Reuter grid in the global case.

(Wittwer, 2009). The spectral characteristics of the RBF depends on the choice of Legendre coefficients B_n. In this thesis, we let B_n take the frequency response of the signal into account, characterized by the signal degree variances. These RBFs are known as spherical splines (Freeden et al., 1998; Jekeli, 2005; Eicker, 2008), with the spline kernel (SK) defined by

$$B_n^{SK} = \frac{\sigma_n}{\sqrt{2n+1}}, \tag{2.59}$$

where $\sigma_n = \sqrt{c_n}$ are the degree standard deviations.

An example of a band-limited SK is shown in Figure 2.9, together with the covariance function of LSC, to show their similar behavior. One of the objectives of this thesis is to demonstrate the equivalence of SKs and LSC, addressed in **Paper C**. The synthesis of a gravity signal from known point-specific spline coefficients $\hat{d}_k$ is given by

$$s(P) = \sum_{k=1}^{K} \hat{d}_k B(\psi_{Pk}). \tag{2.60}$$

In matrix notation, Eq. (2.60), can be written as

$$s(P) = \mathbf{A}\mathbf{d}, \tag{2.61}$$

where $\mathbf{d}$ contains the spline coefficients $\hat{d}_k$ according to Eq. (2.60), and $\mathbf{A}$ represents the design matrix according to Eq. (2.58). The spline coefficients are derived from observations in an analysis step, by inversion of the linear model

$$\mathbf{l} + \mathbf{v} = \mathbf{A}\mathbf{d}. \tag{2.62}$$

Thereby, $\mathbf{l}$ is the observation vector and $\mathbf{v}$ is the error vector. By inversion of Eq. (2.62), one coefficient for each SK needs to be determined. This is typically an ill-conditioned linear inverse problem, for which a regularization of the normal matrix is necessary. Numerous regularization methods exist (Bentel, 2013; Naeimi, 2013). In this thesis we have used Tikhonov regularization (Tikhonov, 1963), where the regularized solution is given by

$$\hat{d}_k = \left[(\mathbf{A})^T\mathbf{A} + \alpha\mathbf{R}\right]^{-1}(\mathbf{A})^T\mathbf{l}, \tag{2.63}$$

where α is the regularization parameter, balancing the contribution of observations and prior information to the solution. We determine the regularization parameter α by the L-curve method of Hansen and O'Leary (1993). Regardless of the regularization method, an initial guess of the regularization parameter, α_0, must be made. Here, we make an initial guess based on the condition number of the normal matrix and the maximum SH degree $N_{\max}$, i.e., $\alpha_0 = 8\|\mathbf{N}\|/N_{\max}^3$ (Naeimi, 2013). Furthermore, Eicker (2008) has shown that the approximation $\mathbf{R} = \mathbf{I}$ holds, for which a small discussion is found in **Paper C**.

If we restrict ourselves to the case of geoid computation from gravity anomalies, the analysis step is given by

$$\Delta\mathbf{g} + \mathbf{v} = \mathbf{A}^g\mathbf{d}, \tag{2.64}$$

where the elements of $\mathbf{A}^g$ are given by

$$A^g_{kq} = \sum_{n=2}^{\infty}\sqrt{2n+1}/(4\pi R^2)\lambda_n^g B_n^{SK} P_n\left(\cos\psi_{kq}\right), \tag{2.65}$$

and with $\lambda_n^g = GM/R^2(n-1)$. The synthesis step is given by

$$N(P) = \mathbf{A}^N\mathbf{d}, \tag{2.66}$$

with design matrix elements

$$A^N_{Pk} = \sum_{n=2}^{\infty}\sqrt{2n+1}/(4\pi R^2)\lambda_n^N B_n^{SK} P_n\left(\cos\psi_{Pk}\right), \tag{2.67}$$

and with $\lambda_n^N = GM/(R\gamma)$.

In **Paper C** we consider an extended grid area for the RBF positions, with outer margin widths $w \approx 4 \cdot 180°/(N_{\max} + 1)$ (Bentel, 2013). As a result, the number of RBFs will typically be slightly larger than the number of observations, but practically equal. Several point grids are available for the RBF positions, and we have chosen to use the equidistributed Reuter grid, shown in Figure 2.9. A Reuter grid is defined by points expressed in spherical coordinates (θ, λ) for a chosen level γ (to define the number of points), and may be constructed as follows (Reuter, 1982):

$$
\begin{aligned}
&\theta_0 = 0, \lambda_{0,1} = 0, && \text{North Pole} \\
&\Delta\theta = \pi/\gamma, \\
&\theta_i = i\Delta\theta, && 1 \le i \le \gamma - 1 \\
&\gamma_i = 2\pi/\cos\left((\cos\Delta\theta - (\cos\theta_i)^2)/(\sin\theta_i)^2\right)^{-1}, \\
&\lambda_{i,j} = \left(j - \frac{1}{2}\right)(2\pi/\gamma_i), && 1 \le j \le \gamma_i \\
&\theta_0 = \pi, \lambda_{\gamma,1} = 0. && \text{South Pole}
\end{aligned}
\tag{2.68}
$$

2.3.4 Remove-compute-restore technique

We have seen that GGMs have global coverage, but lack the short wavelengths of the gravity field. Terrestrial data have higher resolution, but are not available globally. As a result, both data sources are combined in practical geoid computation (Denker, 2013). The long-wavelength part of the gravity signal is determined from a GGM, and removed from the terrestrial data. In addition, the short wavelengths of the gravity signal, represented by the topography, are also removed by aid of a digital elevation model (DEM). The residual gravity data then become relatively smooth and get small signal amplitudes, which make them easy to grid. In turn, a regional geoid computation method is applied to the residual gravity data in a limited area where terrestrial data are available only. The modeling results are residual geoid heights. Finally, the long-wavelength part of the GGM and the effect of topography are restored to obtain the final geoid. This procedure is known as the remove-compute-restore technique, and is schematically shown in Figure 2.10.

There are many advantages to the remove-compute-restore technique. The computationally intensive integral formulae can be restricted to consider available terrestrial gravity data in a spherical cap σ_0 with radius ψ_0 around the computation point only. The omitted gravity signal outside the cap is taken care of by the GGM, and the error due to the spherical approximation of the regional methods is reduced as the residual gravity signal is only a small part of the total signal.

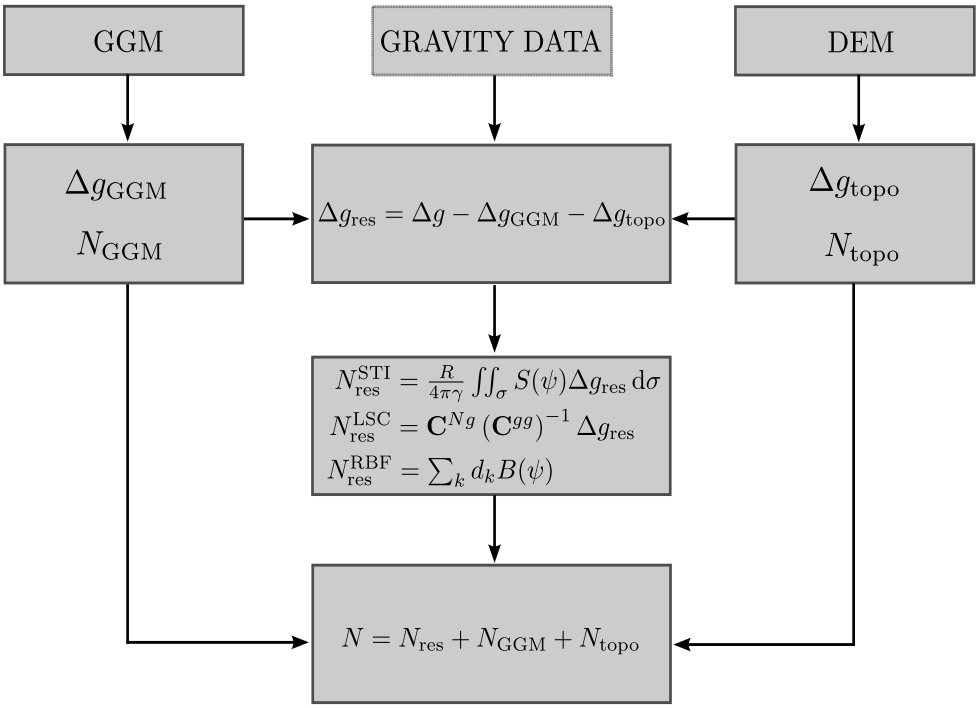

Figure 2.10: The remove-compute-restore regional geoid computation scheme. $N_{\mathrm{res}}^{\mathrm{STI}}$, $N_{\mathrm{res}}^{\mathrm{LSC}}$, and $N_{\mathrm{res}}^{\mathrm{RBF}}$, denote geoid heights computed from Stokes integration, Least-squares collocation, and radial base functions, respectively. Adapted from Rummel et al. (2015).

Typically ψ_0 is chosen such that the resulting omission error is negligible, which depends on $N_{\max}$ of the GGM. The cap is typically called the inner zone, and denoted by σ_0. Stokes's formula applied to the near zone only gives

$$N(P) = \frac{R}{4\pi\gamma} \iint_{\sigma} \bar{S}(\psi_{Pq}) \Delta\bar{g}_q \, \mathrm{d}\sigma, \tag{2.69}$$

with

$$\bar{S}(\psi_{Pq}) = \begin{cases} S(\psi_{Pq}), & 0^\circ \leq \psi < \psi_0 \\ 0, & \psi_0 \leq \psi \leq \pi \end{cases} . \tag{2.70}$$

The spectral form of $\bar{S}(\psi_{Pq})$ can be written as (de Min, 1995)

$$\bar{S}(\psi_{Pq}) = \sum_{n=2}^{\infty} \left[\frac{2}{n-1} - Q_n(\psi_0) \right] \frac{2n+1}{2} P_n(\cos\psi_{Pq}), \tag{2.71}$$

where $Q_n(\psi_0)$ are the Molodensky coefficients, which can be computed by the recurrence relation of Paul (1973).

Two basic methods for the combination of gravity data exist; combination in the frequency (or spectral) domain, which is the classical remove-compute-restore approach, and combination in the spatial domain (Šprlák, 2010). Both approaches can be modified to include different kernel modifications (or weighting schemes for the GGM and terrestrial data). We will restrict ourselves to the combination in the frequency domain in the following, in the case of regional geoid computation using Stokes's formula.

We introduce a spectral weight function w_n in the Stokes kernel (Eq. (2.50)), giving (Rummel et al., 2015)

$$S_1(\psi_{Pq}) = \sum_{n=2}^{\infty} \frac{2n+1}{n-1} w_n P_n \left(\cos\psi_{Pq}\right), \tag{2.72}$$

and

$$S_2(\psi_{Pq}) = \sum_{n=2}^{\infty} \frac{2n+1}{n-1} \left(1 - w_n\right) P_n \left(\cos\psi_{Pq}\right). \tag{2.73}$$

The geoid height can be computed by either a GGM or by Stokes's formula, according to

$$\begin{aligned} N(P) &= \frac{R}{2\gamma} \sum_{n=2}^{\infty} \frac{2}{n-1} w_n \Delta g_n^{\mathrm{GGM}} + \frac{R}{2\gamma} \sum_{n=2}^{\infty} \frac{2}{n-1} \left(1 - w_n\right) \Delta g_n^{\mathrm{GGM}} \\ &= \frac{R}{4\pi\gamma} \iint_{\sigma} S_1(\psi_{Pq}) \Delta g_q \, \mathrm{d}\sigma + \frac{R}{4\pi\gamma} \iint_{\sigma} S_2(\psi_{Pq}) \Delta g_q \, \mathrm{d}\sigma \\ &= N_1 + N_2. \end{aligned} \tag{2.74}$$

If we use a GGM for N_1 and Stokes's formula for N_2, we can write

$$N(P) = \frac{R}{2\gamma} \sum_{n=2}^{\infty} \frac{2}{n-1} w_n \Delta g_n^{\mathrm{GGM}} + \frac{R}{4\pi\gamma} \iint_{\sigma} S_2(\psi_{Pq}) \Delta g_q \, \mathrm{d}\sigma. \tag{2.75}$$

In practice, the summation in the first term of Eq. (2.75) is performed to the maximum degree of the GGM, and Stokes's formula is limited to the spherical cap σ_0. If we separate the two terms, we get

$$\begin{aligned} N(P) &= \frac{R}{2\gamma}\sum_{n=2}^{N_{\max}}\frac{2}{n-1}w_n\Delta g_n^{\mathrm{GGM}} + \frac{R}{2\gamma}\sum_{n=N_{\max}+1}^{\infty}\frac{2}{n-1}w_n\Delta g_n^{\mathrm{GGM}} \\ &\quad + \frac{R}{4\pi\gamma}\iint_{\sigma_0} S_2(\psi_{Pq})\Delta g_q\,\mathrm{d}\sigma + \frac{R}{4\pi\gamma}\iint_{\sigma-\sigma_0} S_2(\psi_{Pq})\Delta g_q\,\mathrm{d}\sigma \\ &= N_{11} + N_{12} + N_{21} + N_{22}. \end{aligned} \tag{2.76}$$

Here, N_{12} is the contribution above the maximum degree of the GGM, and N_{22} is the contribution from terrestrial gravity data outside the spherical cap. Both represent truncation (or omission) errors and are neglected in practical geoid computation. The goal of kernel modifications is then to reduce the truncation error, either by deterministic modifications which aim to minimize the truncation error and provide faster convergence, or by stochastic modifications which aim to reduce the truncation error, the GGM error, as well as the terrestrial error in a least-squares sense.

The Wenzel kernel modification (Wenzel, 1981, 1982; Wichiencharoen, 1984) is a stochastic approach for optimal data weighting, whereby the error degree variances of the GGM (σ_n^{GGM}) and the terrestrial data ($\sigma_n^{\Delta g}$) are combined in a Wiener-type filtering, according to

$$w_n = \frac{\left(\sigma_n^{\mathrm{GGM}}\right)^2}{\left(\sigma_n^{\mathrm{GGM}}\right)^2 + \left(\sigma_n^{\Delta g}\right)^2}, \tag{2.77}$$

where w_n are the spectral filter weights for the satellite data and $(1 - w_n)$ are the complementary weights for the terrestrial data.

The isotropic spatial filter functions are computed by

$$W(\psi) = \sum_{n=2}^{\infty} w_n P_n\left(\cos\psi\right), \tag{2.78}$$

where, in practice, the summation is carried out to a high spherical harmonic degree (e.g., $n = 10{,}000$), and the integration is limited to a spherical cap around the computation point.

A simple deterministic weighting scheme is given by the Gaussian mean kernel (Jekeli, 1981),

$$G(\psi, b) = \exp\left[-b(1-\cos\psi)\right], \tag{2.79}$$

with the spatial filter function

$$W(\psi, b) = \frac{2b\, G(\psi, b)}{1 - \exp(-2b)}, \tag{2.80}$$

where b is given by

$$b = \frac{\ln 2}{1 - \cos \psi_{HM}} \tag{2.81}$$

and ψ_{HM} is the spherical distance at half-maximum.

For the computation of the regional geoid model in Norway, NMA2014, the deterministic kernel modification of Wong and Gore (1969) is used. It removes the low-degree Legendre polynomials $n < K$ from the Stokes kernel. The idea is that when only high frequencies are present in the kernel, the lower frequencies will never be multiplied by the terrestrial Δg_q data. The lower frequencies are readily available in the harmonic coefficients of $\Delta g_n^{\mathrm{GGM}}$. Wong and Gore's kernel modification thus acts as a high-pass filter. The modified Stokes kernel is given by

$$\begin{aligned} S(\psi_{Pq})^{\mathrm{WG}} &= \sum_{n=2}^{\infty} \frac{2n+1}{n-1} P_n\left(\cos \psi_{Pq}\right) - \sum_{n=2}^{K-1} \frac{2n+1}{n-1} P_n\left(\cos \psi_{Pq}\right) \\ &= \sum_{n=K}^{\infty} \frac{2n+1}{n-1} P_n\left(\cos \psi_{Pq}\right). \end{aligned} \tag{2.82}$$

2.3.5 Filter-combined regional geoid model

To minimize the computational burden, the classic field transformation from gravity anomalies to geoid heights can be avoided altogether by using an already existing recent regional geoid model to represent the terrestrial gravity information (Rülke et al., 2012). Thereby geoid heights are computed on the spatial grid of the existing regional geoid model using a GGM, and low-pass filtered using a suitable weighting scheme (Šprlák et al., 2012), as described in Section 2.3.4. The regional geoid model is high-pass filtered with the complementary filter, and the two filtered geoids are added to form a filter-combined geoid model, see Figure 2.11 and Rülke et al. (2012).

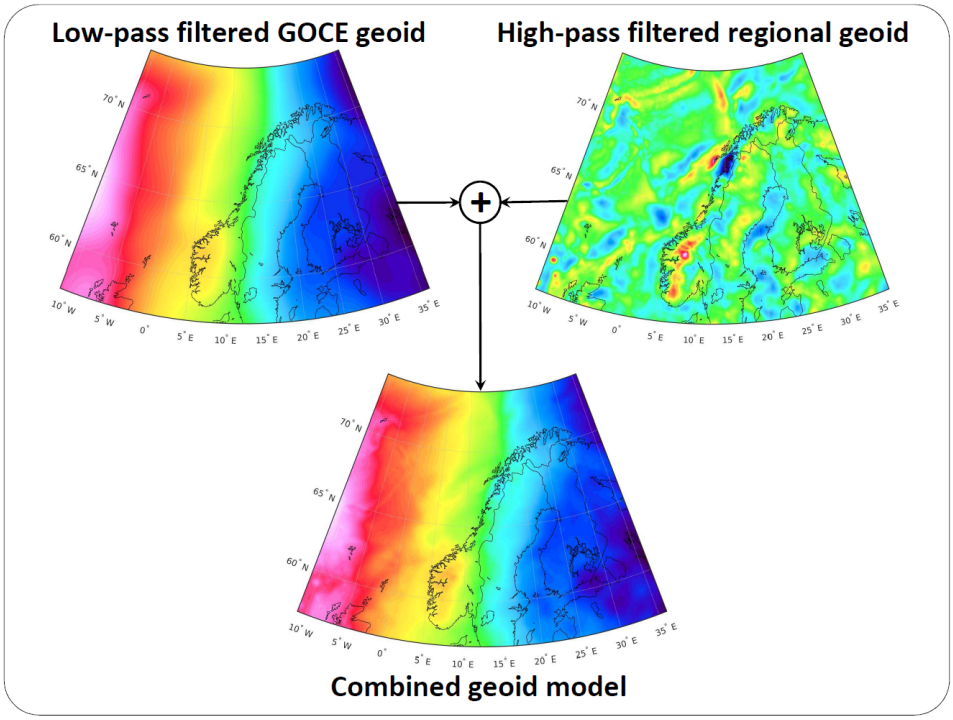

Figure 2.11: Schematic showing the concept of combining geoid heights computed from a GGM with an already existing regional geoid model, thus effectively replacing the GGM which was used for determining the regional model.

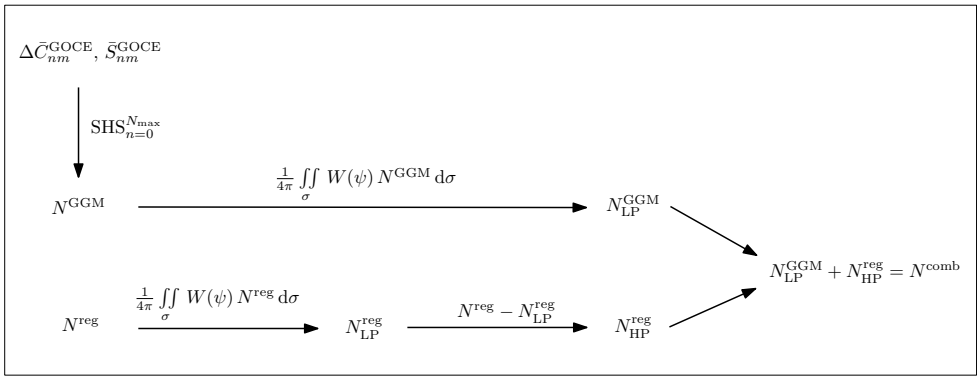

Figure 2.12: Principle of combining a GGM-based geoid N^{GGM} and an existing regional geoid model N^{reg} by a suitable filter $W(\psi)$ in the spatial domain.

In this thesis the Wong and Gore kernel, the simple Gaussian mean kernel as well as the Wenzel kernel have been tested. The filter-combined solutions are computed according to

$$\begin{aligned} N^{\mathrm{comb}} &= \frac{1}{4\pi}\iint_{\sigma} W(\psi) N^{\mathrm{GGM}}\,\mathrm{d}\sigma + \left(N^{\mathrm{reg}} - \frac{1}{4\pi}\iint_{\sigma} W(\psi) N^{\mathrm{reg}}\,\mathrm{d}\sigma \right) \\ &= N_{\mathrm{LP}}^{\mathrm{GGM}} + N_{\mathrm{HP}}^{\mathrm{reg}} = N^{\mathrm{comb}}, \end{aligned} \tag{2.83}$$

see Figure 2.12.

2.4 Heights

Three fundamental vertical reference surfaces (vertical datums) are considered in geodesy: the reference ellipsoid, the geoid, and the quasigeoid. The height of a point forms a one-dimensional coordinate system, and is the metric distance to the point from a reference surface along a well-defined path (Featherstone and Kuhn, 2006). Although a simple definition at first glance, height systems can be defined in different ways, giving different height values for the same point. The reference surface has the largest influence on the height value, but also the path along which we measure the height contributes significantly. The ellipsoidal height is a vertical reference for geometric (nonphysical) heights, while the geoid and quasigeoid are vertical references for physical heights (orthometric and normal heights, respectively).

2.4.1 Ellipsoidal height

The ellipsoidal height is the straight-line distance measured along the ellipsoidal normal from the geometrical surface of the reference ellipsoid to a point P on Earth's surface, see Figure 2.13. Together with geodetic latitude and longitude it forms the geodetic coordinates (Hofmann-Wellenhof and Moritz, 2006). Ellipsoidal heights will necessarily depend on how the ellipsoid is defined, i.e., one must always specify the geodetic reference system associated with the geodetic coordinates.

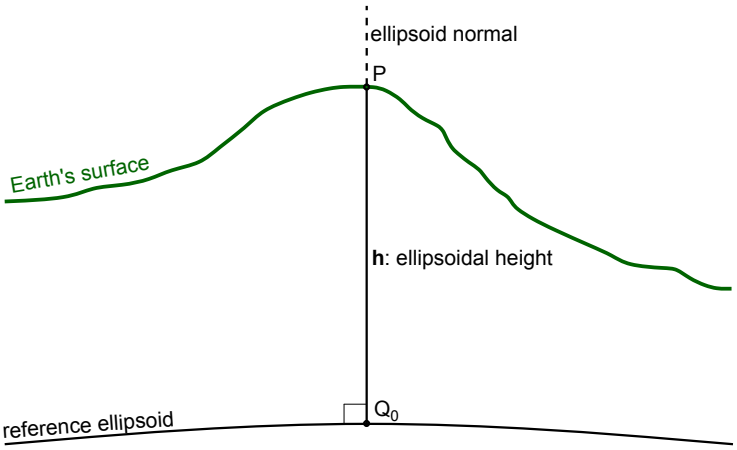

Figure 2.13: The ellipsoidal height h is the straight-line distance measured along the ellipsoidal normal from the point Q_0 on the surface of the reference ellipsoid to a point P on Earth's surface. Adapted from Featherstone and Kuhn (2006).

2.4.2 Orthometric height

The orthometric height was already introduced in Section 2.1 as a physical height related to Earth's gravity potential, see Figure 2.14. As any physical height system it is based on the geopotential number C, which is the difference between the potential at a reference level and at the point of interest (Hofmann-Wellenhof and Moritz, 2006). We cannot observe the potential directly, but rather derive it from the combination of leveling and gravity measurements. In the case of orthometric heights, the reference surface is the geoid. The orthometric height is given by

$$C_P = W_0 - W = \int_0^{H_P} g \, \mathrm{d}H, \tag{2.84}$$

or, alternatively,

$$H = -\int_{W_0}^{W_P} \frac{\mathrm{d}W}{g} = \int_{0}^{C_P} \frac{\mathrm{d}C}{g}. \tag{2.85}$$

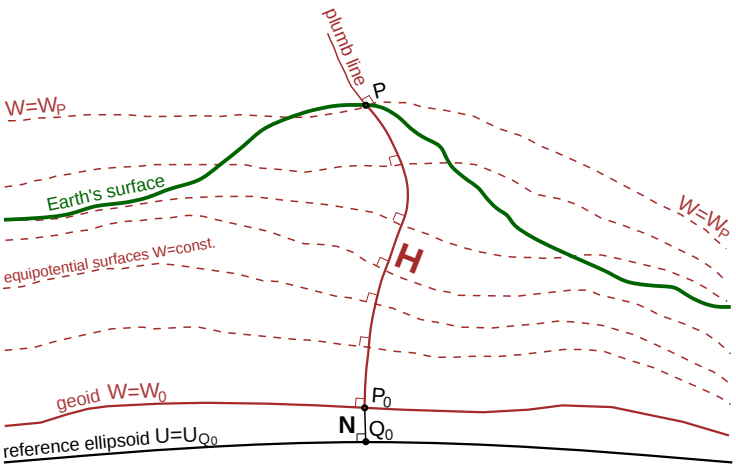

Figure 2.14: The orthometric height H is the curved-line distance measured along the plumb line from the point P_0 on the geoid to a point P on Earth's surface. The geoid height N is the straight-line distance along the ellipsoidal normal from the point Q_0 on the surface of the reference ellipsoid to a point P_0 on the geoid. The curvatures of the equipotential surfaces and the plumb line are exaggerated in the figure. Adapted from Featherstone and Kuhn (2006).

A pure orthometric height system is difficult to realize, because we must know the course of the pumb line inside the topographic masses between the geoid and P. In addition, we need to know gravity along the plumb line, for which the internal density distribution within the topography needs to be known to an accuracy not available today. In practice, an orthometric height system is almost exclusively based on Helmert heights, which are an approximation to the pure orthometric heights (Hofmann-Wellenhof and Moritz, 2006):

$$H = \frac{C_P}{\bar{g}}, \tag{2.86}$$

where $\bar{g}$ is mean gravity along the plumb line, which relies on density information.

2.4.3 Normal height

Molodensky proposed to use "orthometric heights" in the normal gravity field, termed normal heights, see Figure 2.15 (Hofmann-Wellenhof and Moritz, 2006). Normal heights are based on assuming that the actual gravity potential is equal to the normal potential of the reference ellipsoid, $W = U$. Thereby, the physical Earth surface can be determined solely by geodetic measurements, without density hypothesis.

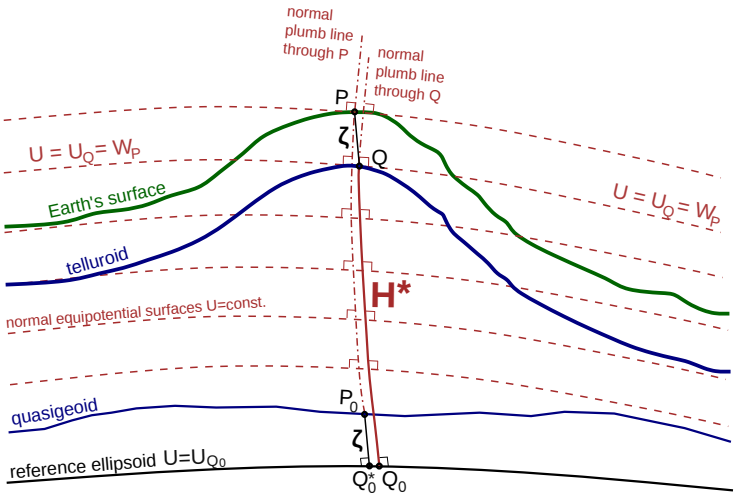

Figure 2.15: The normal height H^* is the curved-line distance measured along the normal plumb line from the point Q_0 on the surface of the reference ellipsoid to a point Q on the telluroid. The quasigeoid height ζ is the straight-line distance along the ellipsoidal normal from the point Q_0^* on the surface of the reference ellipsoid to a point P_0 on the quasigeoid. The quasigeoid height equals the height anomaly ζ, which is the straight-line distance along the ellipsoidal normal from a point P on Earth's surface to a point Q on the telluroid. Adapted from Featherstone and Kuhn (2006).

Geometrically, the normal heights are the distance from the reference ellipsoid to a surface which is called the telluroid. The telluroid is found by pointwise projection of points P on Earth's surface along the straight ellipsoidal normal to points Q with equal potential in the normal gravity field U_Q as the original points in Earth's gravity field W_P. As a result, the telluroid is not an equipotential surface, but rather an approximation of the actual Earth surface, or the topography of a "normal Earth".

Normal heights are defined in the same way as the orthometric heights, but are scaled according to the normal gravity field of the reference ellipsoid,

$$C_P = \int_0^{H_P^*} \gamma \, \mathrm{d}H^*, \tag{2.87}$$

$$H^* = \frac{C_P}{\bar{\gamma}}. \tag{2.88}$$

In eqs. (2.87) and (2.88), C_P is the geopotential number (difference in gravity potential on the reference ellipsoid and the telluroid), H^* is the normal height, γ is normal gravity, and $\bar{\gamma}$ is the mean normal gravity along the ellipsoidal normal, which may be computed by closed formulas without having to know the density distribution within the topography.

2.4.4 Dynamic height

The dynamic height is closely related to the geopotential number (Hofmann-Wellenhof and Moritz, 2006). If we divide the geopotential number with a constant gravity value, we obtain a dynamical height. Typically, the normal gravity at ± 45° latitude is used, and we get

$$H^{\mathrm{dyn}} = \frac{C_P}{\gamma_{45°}}. \tag{2.89}$$

Note that the dynamic height has no geometrical interpretation as it is simply a scaled geopotential number such that a length unit is obtained. Although not used much in geodesy, dynamic heights have an interesting connection to the mean dynamic topography (Section 2.6.5).

2.4.5 Physical heights with GNSS

The combination of GNSS-derived ellipsoidal height and a precise regional geoid makes it possible to derive orthometric heights without the need for leveling. Comparing figures 2.13 and 2.14 we see that, if the plumb lines were straight and perpendicular to the reference ellipsoid, we would get the following exact relationship (Hofmann-Wellenhof and Moritz, 2006):

$$H = h - N. \tag{2.90}$$

Although Eq. (2.90) is an approximation, it is applicable in practice, and one of the main motivations of the national mapping authorities for computing a regional geoid model. Comparing figures 2.13 and 2.15 we easily see that the same relationship holds in Molodensky's theory:

$$H^* = h - \zeta, \tag{2.91}$$

which then gives us normal heights if a precise quasigeoid is available.

2.4.6 Ellipsoidal height of MSL

While altimeters give the ellipsoidal (absolute) height of the sea surface directly (Section 2.5), tide gauges (TGs) give sea-level measurements relative to the land they reside on (and are thus subject to vertical land motion). Typically, TG measurements are referred to a TG benchmark (TGBM). Ideally, the absolute height of MSL should be determined directly by GNSS, either continuously or by precise campaign measurements at the TG itself or a nearby benchmark with a leveled connection to a TGBM (Woodworth et al., 2017).

Unfortunately, a TGBM often has not been observed by GNSS with sufficient accuracy, or, while some TGs have GNSS receivers mounted on them, they lack the necessary connection between the antenna reference point and the TG zero, because they were installed with the aim of monitoring vertical site displacements only (Santamaría-Gómez et al., 2012). An alternative approach is to derive the ellipsoidal height of MSL by using a height reference conversion surface (HRCS). This surface is typically a geoid fitted to benchmarks with known heights in both the national height system by means of leveling, and ellipsoidal heights h observed by GNSS, enabling the conversion of heights H in the national height system into ellipsoidal ones by the simple relation shown in Eq. (2.90),

$$h = H + \mathrm{HRCS}. \tag{2.92}$$

Using Eq. (2.92) to determine the absolute height of MSL is not the ideal solution as it is a derived and not an observed quantity. The total error budget is complicated by additional errors in the geoid on which the conversion surface is based, errors from GNSS/leveling benchmark interpolation, as well as errors in the national leveling network (Featherstone, 2008).

2.5 Satellite altimetry

The principle of satellite altimetry is that the altimeter onboard the satellite measures its own height above Earth's surface by observing the two-way travel time of a radar

pulse that is transmitted from the altimeter, and partly reflected back from Earth's surface (Chelton et al., 2001). The distance, or range, R, between the satellite and the surface is derived when the two-way travel time Δt is multiplied with the speed of light c, and divided by two (to get the one-way range),

$$R = c \cdot \frac{\Delta t}{2}. \tag{2.93}$$

If the satellite's height h in a particular reference frame is known (i.e., its precise orbit), the sea surface height (SSH) may be found in the same reference frame by subtracting the measured distance R from the height of the satellite,

$$\mathrm{SSH} = h - R. \tag{2.94}$$

Today, satellite altimetry is our foremost technique for observing sea-level change and ocean topography (Pugh and Woodworth, 2014). Satellite altimetry was first given a try from the American space station Skylab early in the 1970s, while the first dedicated altimeter satellite, GEOS-3, was launched in 1975, see Table 2.5. The first missions gave data of rather poor quality compared with today's observations. The altimeter onboard GEOS-3 had an accuracy of about 25 cm, and the satellite orbit was determined within roughly 10 m. In addition, the satellite had no ability to measure the atmospheric effects on the observations. Still, the observations from these early systems mapped previously unknown details in the geoid and the ocean surface. In the 1990s satellite altimetry became an established technique; especially with the launch of TOPEX/Poseidon and ERS-1.

Altimetry satellites of today can measure the distance to Earth's surface with an accuracy of around 2 cm (Pugh and Woodworth, 2014). This accuracy is achieved by using a two-frequency radar, such that the effect of the ionosphere on the range observation can be eliminated. In addition, the latest altimetry satellites have a radiometer on board, measuring the effect of the troposphere. Today we also have global observational networks monitoring the atmosphere such that both the effects of ionosphere and troposphere can be computed from models. Most important is the fact that altimetry satellites of today are equipped with satellite tracking systems for precise orbit determination (POD); primarily GNSS, DORIS and SLR. These systems allow orbit determination with an accuracy of 2 cm. All these improvements together make altimetry satellites precise and effective tools for observing the Earth system. Future altimetry missions will give higher spatial and temporal resolution, but should also overlap previous missions, in order to get as long a time series as possible, with few observational gaps, see Table 2.5. For example, Jason-CS/Sentinel-6 will be the fifth TOPEX/Poseidon-type satellite altimeter, aiming for the continuation of the time series started in 1992 (Scharroo et al., 2016).

Table 2.5: Past, present, and future satellite altimetry missions. Adapted from Pugh and Woodworth (2014)

Satellite	Agency	Operation	Orbit height (km)	Repeat period (d)	Inclination (°)	Comment
Skylab	NASA	1973-1974	435	–	50	Proof of concept
GEOS-3	NASA	1975-1978	845	–	115	
Seasat	NASA	1978	800	~17	108	
GEOSAT	US NAVY	1985-1986	800	–	108	Geodetic mission
		1986-1990		17.05		Exact repeat mission
GEOSAT FO	US NAVY	1998-2008	800	17.05	108	GEOSAT Follow-On
ERS-1	ESA	1991-1996	785	35	98.52	
ERS-2	ESA	1995-2011	785	35	98.52	
Envisat	ESA	2002-2012	785	35	98.52	
TOPEX/Poseidon	NASA/CNES	1992-2005	1336	9.9156	66	
Jason-1	NASA/CNES	2001-2012	1336	9.9156	66	
		2012-2013	1336	406	66	Geodetic mission
OSTM/Jason-2	NASA/CNES	2008-	1336	9.9156	66	
CryoSat-2	ESA	2010-	717	369	92	With 30-day subcycles. First SAR(In) altimeter.
HY-2A	NSOAS	2011-	971	14 and 168	99.35	China Geodetic mission
SARAL/AltiKa	ISRO/CNES	2013-	785	35	98.52	India/France
Jason-3	NASA/CNES/ EUMETSAT/NOAA	2016-	1336	9.9156	66	
Sentinel-3	ESA	2016-	814	27	98.65	SAR. A pair of satellites 3A (2016) and 3B (2017)
Jason-CS/ Sentinel-6	EUMETSAT/ ESA/NOAA	2020	1336	9.9156	66	SAR. A pair of satellites CS-A, CS-B
SWOT	CNES/NASA/ CSA/UKSA	2020	890	21	77.6	SARIn measuring along ±60 km swath

2.5.1 Orbit considerations

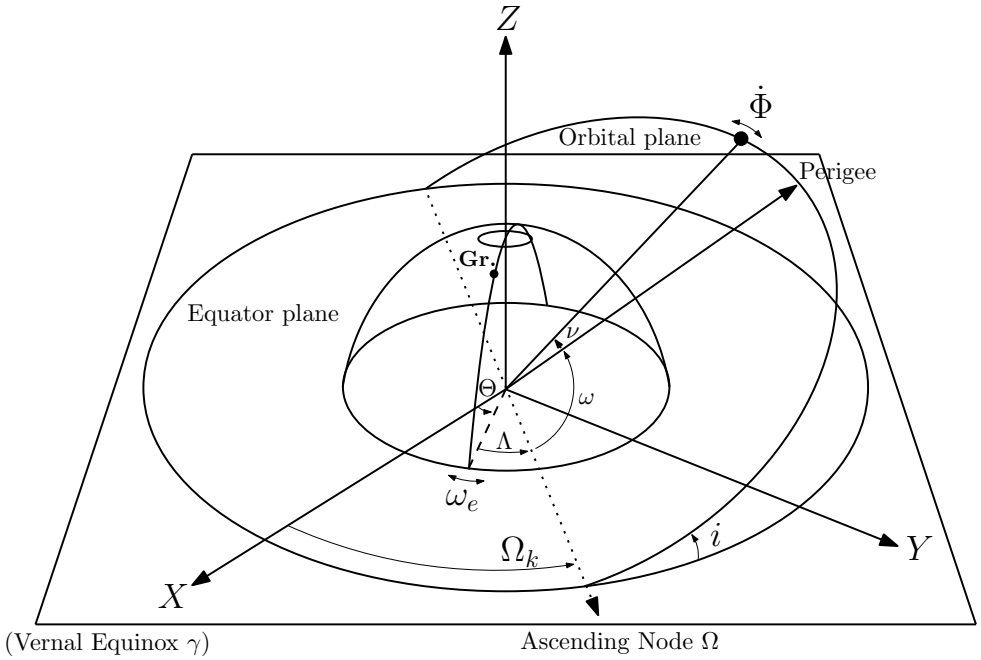

Figure 2.16: The Kepler elements of an elliptic satellite orbit: semi-major axis a, inclination i, longitude of the ascending node Ω_k, argument of perigee ω, and true anomaly ν. Adapted from Sneeuw (2000).

Kepler's first law states that all planets move in elliptical orbits, with the Sun at one focus. The law also applies for satellites orbiting the Earth. Six orbital elements are used to describe the Kepler orbit around a body (Seeber, 2003), see Figure 2.16.

The actual satellite orbit deviates from the perfect elliptical Kepler orbit due to

- the non-uniform gravity field of the Earth,
- the gravitational attraction from the Sun and the Moon,
- atmospheric drag,
- direct and reflected radiation pressure from the Sun, as well as
- Earth and oceanic tidal forces (indirect gravitational attraction from the Sun and the Moon).

These forces, gravitational and non-gravitational, perturb the satellite orbit, and must be taken into account.

The orbit height is one of several important factors when choosing the satellite orbit (Chelton et al., 2001). The main source of error in the dynamical models mentioned in the previous paragraph are gravitational perturbations of the satellite orbit, which decrease substantially with increased orbit height, as does the perturbation from air drag. On the other hand, the power of the radar echo decreases with increased height, and the radiation environment becomes less favorable. The orbit height determines the orbit period T. An altimeter satellite is in a near-circular orbit (an orbit with small eccentricity), and the time between every subsequent ascending crossing of the equatorial plane is given by

$$T = 2\pi\sqrt{\frac{a^3}{GM}}\left[1 - \frac{3J_2}{2}\left(\frac{R_e}{a}\right)^2 (4(\cos i)^2 - 1)\right], \tag{2.95}$$

where a is the semi-major axis of the elliptical satellite orbit, GM is the product of the universal gravitational constant and Earth's mass, R_e =6378 km is Earth's equatorial radius, i the inclination of the satellite orbit, and $J_2 = -C_{20}$ is the dynamical form factor.

The projection of the satellite's position along the ellipsoidal normal on Earth's surface is called the sub-satellite point. The path of successive sub-satellite points is the projection of the satellite orbit on the surface, and is known as the groundtrack. Because the Earth is rotating at $0.25^\circ \mathrm{min}^{-1}$ relative to the orbital plane, the groundtrack with successive orbits is translated westwards, see Figure 2.17 (Chelton et al., 2001). The track separation depends on the period T.

It is also important to consider the ability of the altimeter electronics to track the radar echo from mean sea level (Chelton et al., 2001). The tracking unit has limited ability to lock on a point when the distance between the altimeter and the sea surface varies from one radar pulse to the next. The Earth flattening can give rise to changes in the vertical velocity component, up to $30\,\mathrm{ms}^{-1}$ (or more, if the orbit is elliptical), which causes the distance to change. Thus, for altimetry, the orbit eccentricity must not exceed 0.001 (near-circular orbits). Furthermore, the ground speed should be practically constant, such that the range observations are as evenly spaced along the groundtrack as possible, and variations in the ground speed increases when eccentricity increases.

If the satellite moves eastward in the same manner as the Sun, it is termed sun-synchronous (Chelton et al., 2001). In addition to deciding the approximate orbit height, and whether the satellite should be sun-synchronous, the orbit inclination must be chosen. Satellites orbiting in the direction of Earth's rotation, with i <90°,

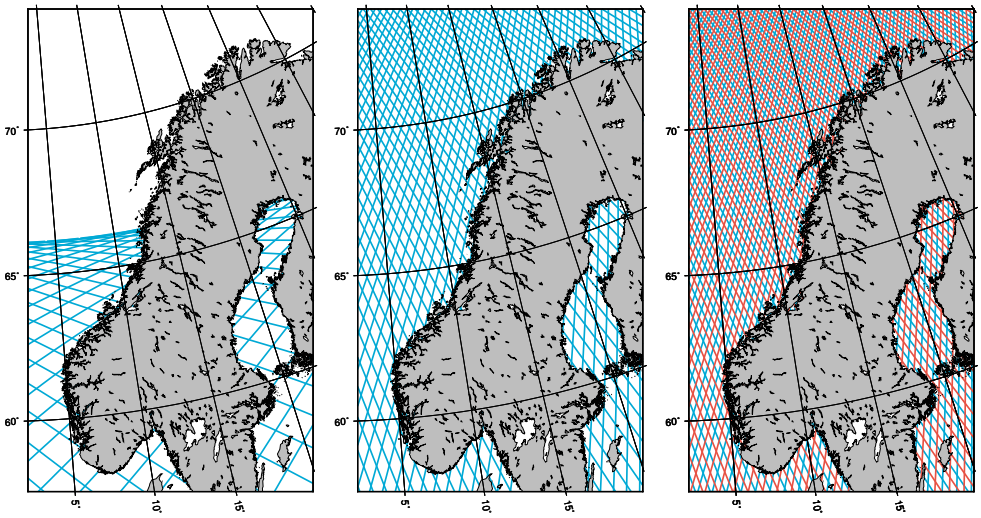

Figure 2.17: Theoretical altimeter groundtracks in the Norwegian coastal zone for TOPEX/Poseidon-type orbits (left), Envisat-type orbits (middle), and the interleaved twin-satellite Sentinel-type orbit (right). See also Figure 2.25.

are called prograde, while orbits with $i > 90°$ are called retrograde. The resulting maximum latitude becomes

$$|\varphi_{\max}| = i, \tag{2.96}$$

$$|\varphi_{\max}| = 180° - i \tag{2.97}$$

for prograde and retrograde orbits, respectively. The TOPEX/Poseidon-type orbit is prograde, with $i = 66°$, while the ERS-type orbit is retrograde and sun-synchronous, with $i = 98°$, thus covering $\varphi = \pm 82°$.

If the groundtrack is periodic, i.e., repeats after a given number of days, α, and revolutions, β, the orbit is called a repeat orbit (Chelton et al., 2001). The repeat configuration has proven itself very useful, because it allows a satellite to pass the same area on Earth's surface after a given time interval. The periodicity allows a comparison of observations at specific observation sites, for calibration and validation purposes, as well as monitoring time-variable geophysical and climate-related phenomena. Satellite altimeters in repeat orbits monitor variations in sea surface height. In the following we will see that there is always a trade-off between high temporal and spatial resolutions. A satellite may also be set in a so-called geodetic orbit with a long repeat period, which increases the spatial resolution considerably (e.g., CryoSat-2, see Section 2.5.3).

The duration of one cycle is called the repeat period (Chelton et al., 2001). The repeat period of a satellite is expressed using the nodal day, α, defined to be the time needed for Earth to rotate one complete revolution, relative to the orbital plane of the satellite. Exact repeat orbits consist of a groundtrack which is repeated an integer number of revolutions, β, during an integer number of nodal days, α. For a repeat period of α nodal days, the exact repeat period, in solar days, is given by

$$T_{\text{rep}} = \frac{2\pi\alpha}{\omega - \dot{\Omega}}, \tag{2.98}$$

where

$$\dot{\Omega} = -\frac{3}{2}\frac{GM}{a^3} J_2 \left[\frac{R_e}{a(1-e^2)}\right]^2 \cos i \tag{2.99}$$

is the motion of the longitude of the ascending node in the equatorial plane, and ω_e is Earth's rotation velocity.

Thus, a 10-day TOPEX/Poseidon-type orbit will give a repeat period of 9.9156 solar days. The ERS-type orbit is sun-synchronous with $\dot{\Omega}$ =$2\pi/365.2422$, such that the orbital plane rotates eastwards with the exact same motion as Earth orbits the Sun. For sun-synchronous orbits the repeat period is the same in solar days as in nodal days, since $\omega - \dot{\Omega} = 2\pi$.

The satellite groundtrack pattern depends on i, α, and β. The longitudinal distance between two groundtracks, in radians, is given by $2\pi/\beta$ (Sneeuw, 2000). In kilometers, the distance may be expressed as

$$\Delta x = \frac{222.4\pi}{\beta} \cos\varphi. \tag{2.100}$$

We get a repeat orbit if

$$\frac{\beta}{\alpha} = \frac{\dot{\Phi}}{|\dot{\Lambda}|} \tag{2.101}$$

is the ratio of two integers.

When choosing a satellite orbit, we choose i, α, and an approximate orbit height h (Chelton et al., 2001). The number of orbit revolutions per repeat period, β, is chosen to get an orbit height close to h. In the case of the TOPEX/Poseidon-type orbit, an inclination of i =66°, and α =10 days, have been chosen. Odd integers between β =143 and β =129 gives orbits between h =700-1400 km. NASA/CNES wanted an orbit height of around 1300 km, where β = 127 gives h =1336 km, and β = 129 gives h =1254 km.

$\beta = \dot{\Phi}T/2\pi$ depends more on the repeat period than the orbit height. From Eq. (2.100) it is clear that the groundtrack spacing decreases with increased period.

Around a particular orbit height h, β increases with increased repeat period; therefore, a satellite orbit configuration will always be a compromise between spatial and temporal resolution.

2.5.2 Conventional altimetry

Due to the physical properties of the sea surface and the atmosphere, the frequency band of 2-18 GHz suits the altimeter best (Chelton et al., 2001). This includes the S (1.55-4.20 GHz), C (4.20-5.75 GHz), X (5.75-10.9 GHz) and Ku (10.9-22.0 GHz) bands. In the Ku band, emitted radiation from the sea surface is low, and the water reflectivity large. This makes it easier to distinguish between the actual radar return and natural radiation. When frequencies become higher than 18 GHz, atmospheric attenuation increases, and the power of the transmitted and received signal decreases. For lower frequencies, refraction of electromagnetic (EM) radiation in the ionosphere increases; interference from ground-based civil or military sources of EM radiation also increases. The recent SARAL/AltiKa mission (Verron et al., 2015) is the first to test a single frequency in the Ka (26.5-40 GHz) band, which is less affected by the ionosphere, and eliminates the need of a dual-frequency altimeter (Section 2.5.5).

The radar altimeter will radiate an area on the Earth surface which is known as the footprint. The footprint size must be large enough such that the effect of small waves and other irregularities are averaged out. However, the footprint must be small enough to give a precise observation of the wave height. In other words, the footprint size is a compromise between

- spatial resolution (must be high enough to uncover mesoscale variations, eddies etc.),
- averaging (large enough to average out irregularities and small waves), as well as
- homogenization (wave and wind fields as homogeneous as possible over the footprint).

With a footprint size of 1-10 km, the above criteria are fulfilled (Chelton et al., 2001).

There are two methods for controlling the footprint size. In a beam-width limited system, the opening angle of the radar pulse γ controls the footprint size (Chelton et al., 2001),

$$\gamma = k\frac{\lambda}{d}, \tag{2.102}$$

where λ is the radar wavelength, k is an antenna constant, and d is the radar antenna diameter.

The size of the antenna footprint on the sea surface is proportional to the wavelength of the EM radiation, and inversely proportional to the antenna size. Thus, a 5 km footprint will demand an unpractically big antenna diameter of 7.7 m for the Ku frequency of 13.6 GHz in a TOPEX/Poseidon-type orbit. Therefore, we rather use systems where the footprint size is controlled by the duration of the radar pulse, termed pulse-length limited systems. The pulse duration τ of TOPEX/Poseidon was 3.125 ns, with a relatively large opening angle of 1-2 degrees. This pulse is transmitted vertically towards the sea surface. Note that we do not always measure directly towards nadir. Out on the open sea, the shortest distance R_0 will be practically equal to the nadir distance; however, in the coastal zone, if a part of the footprint contains a mountain, the shortest distnace will be to the mountain, and not the sea surface in nadir.

The backscattered signal as measured by the altimeter, consists of the total return from all facets perpendicular to the incoming radiation within the footprint. These facets are reflecting scatterers, usually called specular scatterers, see Figure 2.18.

In the satellite, the power of the backscattered signal is registered as a function of time (Chelton et al., 2001). Different parts of the radar pulse will be backscattered to the satellite at different times, and from different parts of the footprint. Therefore, the task of measuring the travel time of the radar pulse is neither unambiguous nor trivial. Furthermore, it is not obvious which distance the measured travel time actually represents, because the distance between the satellite and different parts of the footprint varies. To overcome these issues, we will have to introduce three different travel times. We assume the crest-to-trough wave height H_w to be uniform within the footprint, defining a plane intersecting the wave crests, and a plane intersecting the wave troughs. It is from these planes we imagine the radar pulse is reflected, see Figure 2.19.

In Figure 2.19a, the first radar echo comes from the part of the leading edge of the radar pulse that is backscattered to the satellite from the wave crests in nadir (Chelton et al., 2001). The time t_0, when it arrives, is given by

$$t_0 = \frac{2R_0}{c}, \tag{2.103}$$

where R_0 is the distance between satellite and wave crests in nadir.

In Figure 2.19b, the last part of the satellite's radar pulse will have to move a distance equal to R_0 plus the wave height H_w, before hitting the wave troughs in nadir (Chel-

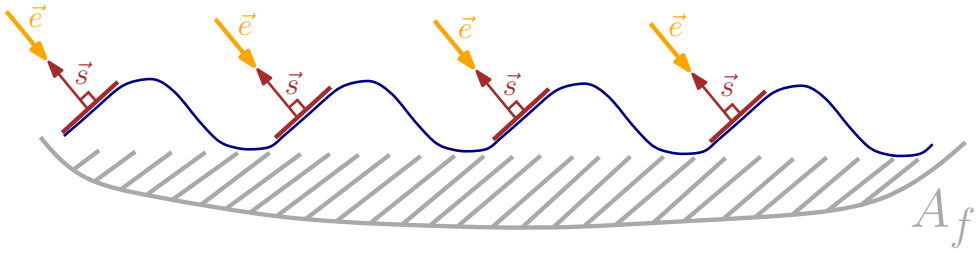

Figure 2.18: Backscattered signal, as measured by the satellite, consists of the total return from all facets that are perpendicular to the incoming radiation within the footprint.

ton et al., 2001). This travel time of the trailing edge of the radar pulse, reflected from wave troughs in nadir, is given by:

$$t_1 = \frac{2(R_0 + H_w)}{c} + \tau. \tag{2.104}$$

Because the time is measured with respect to the point in time when the radar pulse left the satellite, we must add the pulse duration τ.

The radius, r_f, of the footprint on the sea surface is controlled through τ, but is dependent on H_w and R_0 (Chelton et al., 2001). At two-way travel time t_1, when the footprint takes the shape of an annulus, r_f is given by

$$r_f = \left[\frac{(c\tau + 2H_w)\, R_0}{1 + R_0/R_e}\right]^{\frac{1}{2}}. \tag{2.105}$$

From Eq. (2.105) we observe that the footprint size increases as time increases. The corresponding area of the footprint is given by:

$$A_f = \pi r_f^2 = \frac{\pi\,(c\tau + 2H_w)\, R_0}{1 + R_0/R_e}. \tag{2.106}$$

Due to waves, the ocean surface is not flat, and the signal is backscattered first from the wave crests, then from the wave troughs (Chelton et al., 2001), see Figure 2.19. As time passes, the footprint evolves into a growing circle, and the received power increases linearly. As soon as the trailing edge of the radar pulse has reached the wave troughs, the circle turns into an annulus, which circumference increases with time, but the area of the footprint remains constant. Thus, the received power in the satellite is also constant, although it is not practically constant due to bearing deviations from nadir. Rather, the backscattered power will decrease after reaching its maximum, forming a slightly inclined plateau. We want to determine the mean sea

level ; thus, the actual signal travel time is determined from the time of transmission, and the time when the signal has reached half of its maximum effect, $t_{1/2}$, which corresponds to backscattering from mean sea level in nadir. Illustrated in Figure 2.19d is the travel time for the middle of the radar pulse, $t_{1/2}$, given by:

$$t_{1/2} = \frac{2\left(R_0 + \frac{H_w}{2}\right)}{c} + \frac{\tau}{2}. \tag{2.107}$$

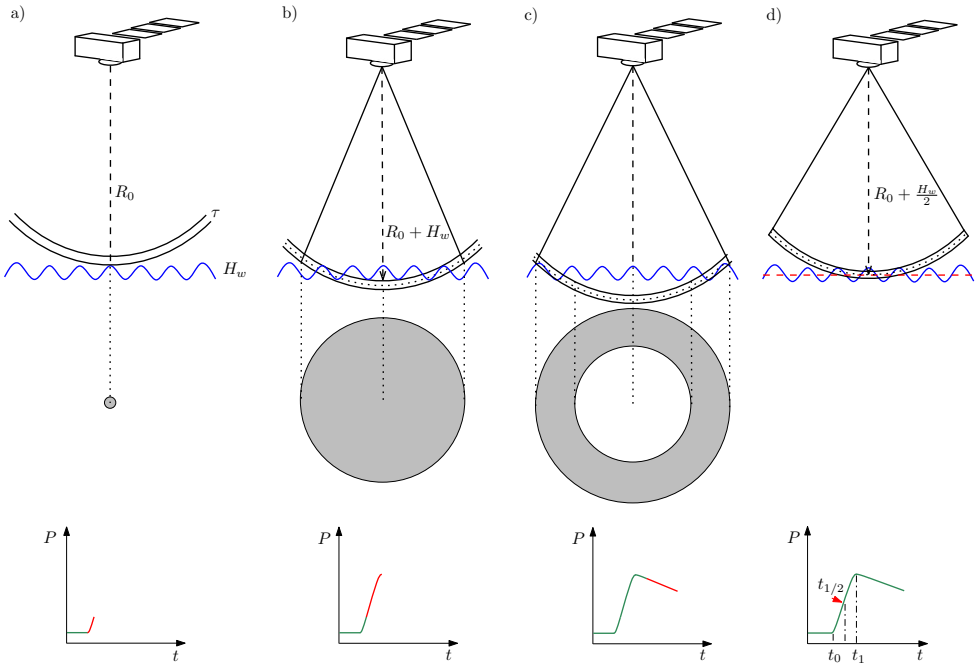

Figure 2.19: Different parts of the radar pulse will be backscattered to the satellite at different times, and from different parts of the footprint. (a) Initially, the signal is reflected from wave crests in nadir at t_0, (b) the footprint is an ever growing circle until the trailing edge of the radar pulse has reached the wave troughs in nadir at t_1. (c) Beyond t_1, the footprint will take the shape of an annulus with growing circumference (but constant area). The middle part of the radar pulse reflected from mean sea level in nadir at $t_{1/2}$ is shown in (d). The lower part of the figure shows the time-variable signal strength of the radar echo. The echo takes a characteristic ramp shape, where the signal strength increases linearly up to a plateau, where it slowly decreases. The travel time $t_{1/2}$ corresponds to the time when the signal reaches half of its strength (the middle of the linear slope of the ramp function). This is a schematic of the returned waveform, and in practice, for the real ocean surface, it will be very noisy. Adapted from Chelton et al. (2001) and `http://aviso.altimetry.fr`

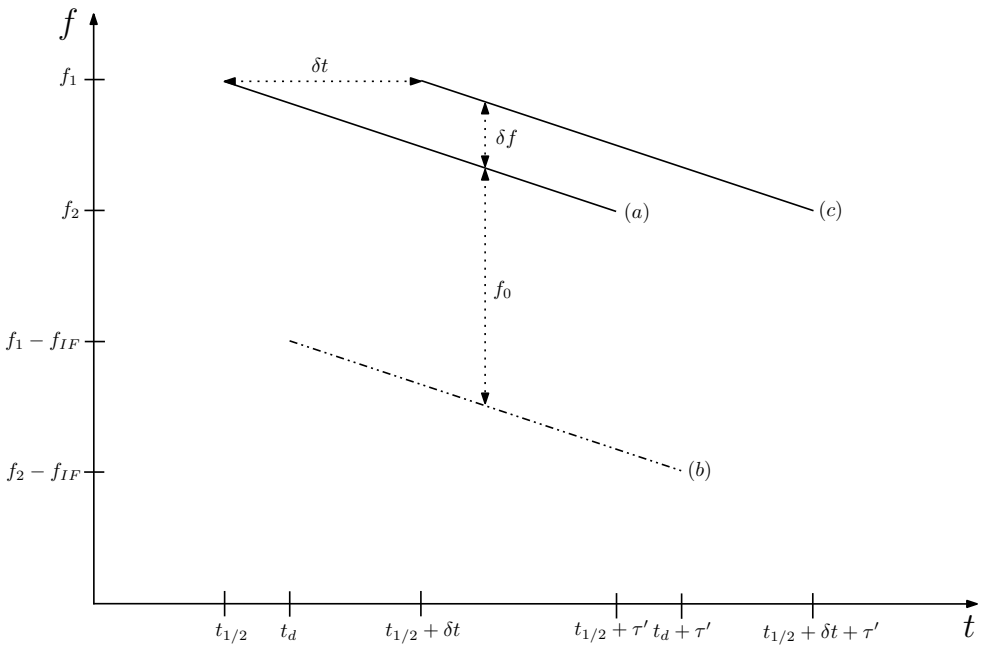

Figure 2.20: Received chirp from mean sea level in nadir (transmitted at $t_{1/2}$) at t_d (a) is mixed with a corresponding deramping chirp (b). The deramped chirp has a frequency offset f_{IF}, and a new signal with frequency f_0 is formed. Received chirp δt later (c). Adapted from Chelton et al. (2001).

To achieve acceptable signal-to-noise ratio (SNR) when the pulse is very short, the transmitted power must be unpractically large (Chelton et al., 2001). Therefore a pulse of longer duration is transmitted, but is analyzed as a short pulse. This technique is known as pulse compression. A signal with a linear frequency shift ΔF with duration τ' is transmitted. This pulse is called a chirp, and can be passed through a dispersive filter, giving a time delay. The time delay increases linearly with frequency, thus compressing the chirp to a pulse duration τ, by delaying the early part of the chirp more than the last. As the start frequency of the chirp is higher than the stop frequency, the product is a new signal with shorter duration and larger power.

We now consider the ideal condition with a backscattered signal from one facet on a flat sea surface. The received chirp is enhanced and mixed with a deramping chirp onboard the satellite, see Figure 2.20. The deramping chirp is, with the exception of its intermediate frequency f_{IF}, identical to the transmitted pulse, and must be made at the exact same time as the chirp reflected from the sea surface is received by the satellite. The time delay t_d of the deramping chirp is determined by an adaptive tracking unit (ATU) in the altimeter electronics.

A new signal with frequency f_0 is formed when the signals are mixed (Chelton et al., 2001):

$$f_0 = f_{IF} - Q(t_d - t_{1/2}), \tag{2.108}$$

where $Q = (f_1 - f_2)/\tau' = \Delta F/\tau'$. Furthermore, observing Figure 2.20 we see that the frequency shift of the deramped signal becomes:

$$\delta f = Q\delta t. \tag{2.109}$$

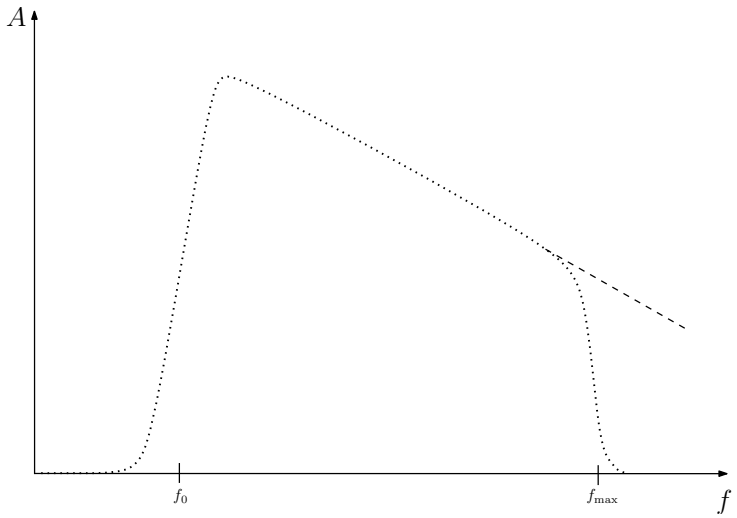

Figure 2.21: Schematic of the discrete sampling of the returned waveform in the frequency domain. The number of samples is not shown in this figure; it is only shown that discrete samplings are made (dotted line). The frequency f_0 corresponds to the frequency of the deramped chirp, backscattered from mean sea level in nadir. Only the part of the waveform below $f_{\max}$ is used. The great decline of the curve for frequencies near $f_{\max}$ is a result of the anti-aliasing filter that is used. Adapted from Chelton et al. (2001).

The relationship in Eq. (2.109) is exploited as the signal is analyzed in the frequency domain, by a discrete Fourier transformation onboard the satellite, see Figure 2.21. For TOPEX/Poseidon, $\Delta F = 320$ MHz, and after the frequency domain analysis, an effective pulse duration of $\tau = \Delta F^{-1}$ =3.125 ns is found.

The smooth ramp shape of the waveform will become evident only after averaging multiple returns (Chelton et al., 2001). The time $t_{1/2}$ corresponds to frequency f_0. The discrete sampling interval $\delta t'$ can in principle be chosen arbitrarily, yet it is important to avoid aliasing effects due to frequencies above the Nyquist frequency, and, in practice, the signal is low-pass filtered.

2.5.3 SAR altimetry

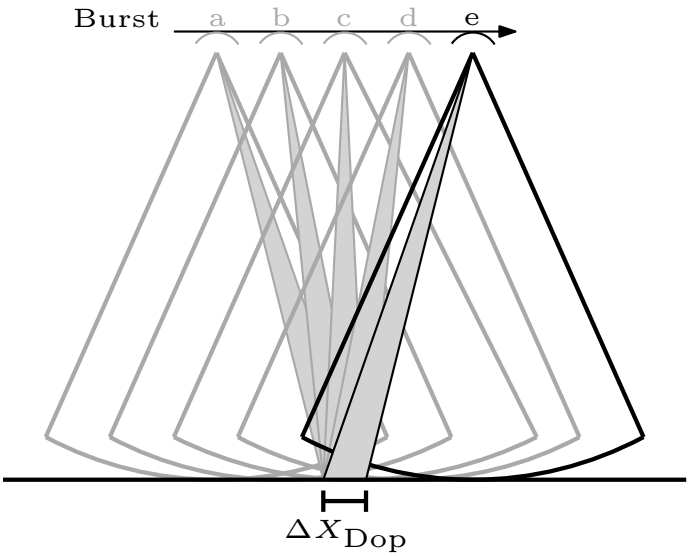

Figure 2.22: The principle of SAR altimetry. The schematic shows beams from five bursts a-e, which all illuminate the same small area on the surface. Adapted from Stenseng (2011).

The delay-Doppler or synthetic aperture radar (SAR) altimeter differs from the conventional pulse-limited systems in that multiple radar pulses are coherent within a number of pulses, known as a burst (Stenseng, 2011). Figure 2.22 illustrates the principle, where a small area on the surface, ΔX_{Dop}, is seen from five directions. The returned pulses are correlated, and the entire returned burst is processed simultaneously, giving higher return power, smaller footprints, and self-noise reduction.

The SAR altimeter considers smaller along-track slices of the pulse-limited altimeter footprint, but emits far more pulses, such that effectively the same footprint as the pulse-limited altimeter is covered, but with increased resolution, see Figure 2.23. The same pulse compression technique as described in Section 2.5.2 is used also for SAR altimetry.

The result of a small along-track footprint and multiple looks is a waveform with a steep leading edge, a fast-decaying trailing edge, and a response much stronger at the peak power when compared with conventional altimetry (Stenseng, 2011), see Figure 2.24.

The ESA CryoSat-2 (CS2) mission, launched on April 8th 2010, is the first new-generation altimetry satellite carrying a SAR altimeter (ESA and MSSL-UCL,

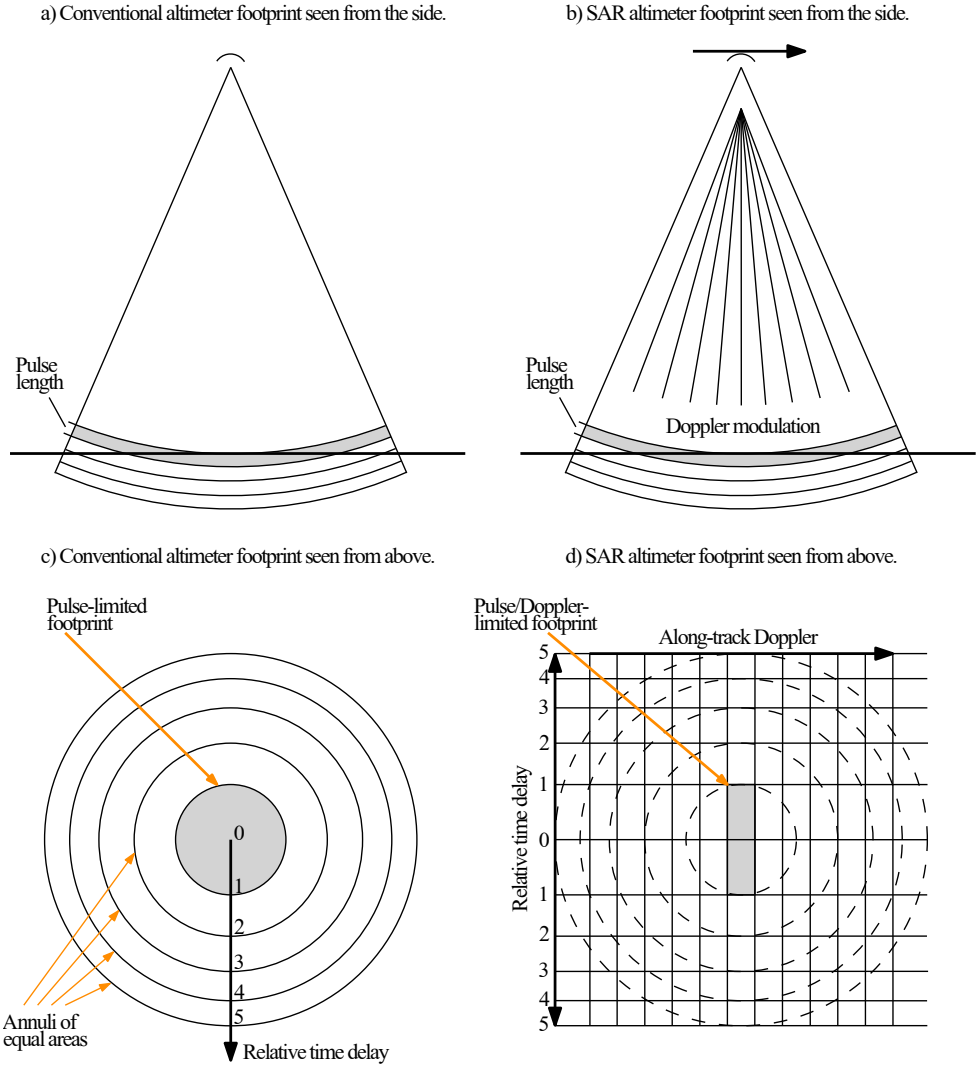

Figure 2.23: Schematic showing the footprint geometry of the conventional pulse-limited altimeter and the SAR altimeter. Adapted from Stenseng (2011).

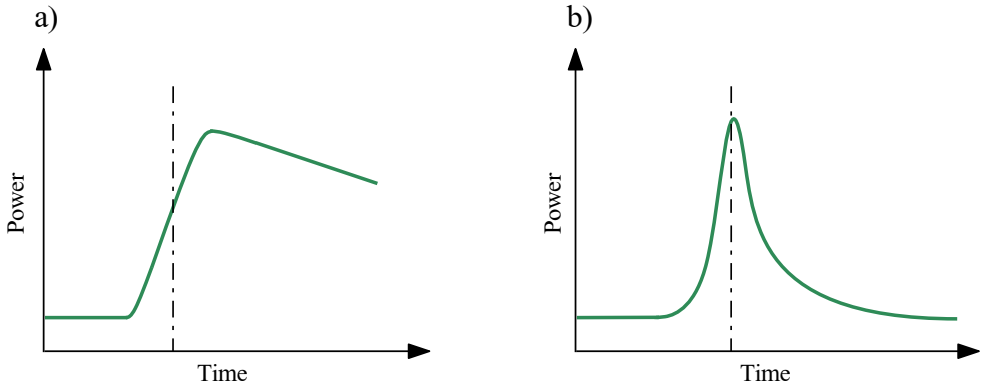

Figure 2.24: Schematic showing the idealized shape of (a) a conventional altimeter echo, and (b) a SAR altimeter echo. The vertical dashed lines correspond to the position related to the surface, cf. Figure 2.19. Note that the return power from the SAR echo is more than 10 dB stronger than from the conventional altimetry echo. Adapted from Stenseng (2011).

2012), see Table 2.5. The SAR altimeter onboard CryoSat-2 emits 18,000 pulses per second and has a ground speed of 6800 ms^{-1}; thus, the satellite moves 0.38 m between pulses, much less than half of the antenna diameter (Wingham et al., 2006). The high sampling rate allows for collocating the pulses, forming a bigger synthetic antenna. The two-way travel time of a single pulse is 5.3 ms. To avoid emitting new pulses at the same time as previous ones are received, the pulses are emitted through short bursts less than the two-way travel time, typically 64 pulses in one burst. The collocation of all radar echoes over the burst interval forms a synthetic antenna with a diameter of 48 m.

Due to its geodetic orbit configuration, CS2 has a high spatial resolution, with a groundtrack spacing of 5-7 km at high latitudes, see Figure 2.25. CS2 carries a synthetic aperture interferometric radar altimeter (SIRAL) using a single Ku band frequency of 13.575 GHz, which can operate in synthetic aperture radar (SAR) mode, SAR interferometric (SARIn) mode, as well as conventional low resolution (LR) modes.

CS2 uses a geographical mode mask to decide which mode to operate in (ESA and MSSL-UCL, 2012), see Figure 2.26. CS2 is in LR mode (LRM) over flat surfaces and the open ocean, where it operates as a conventional altimeter with an almost circular footprint. The SAR mode improves the along-track resolution to ~300 m, and is typically used over sea ice. Over regions with significant topography, CS2 operates in SARIn mode, which also has an along-track resolution of ~300 m. In addition, the altimeter measures the phase difference of the backscattered signal at

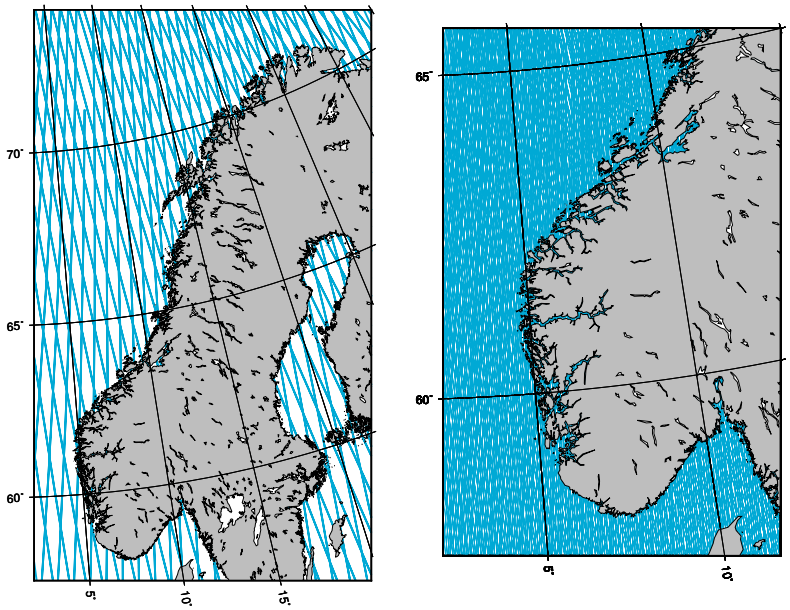

Figure 2.25: Theoretical CS2 tracks in the Norwegian coastal zone; one 30-day subcycle (left), and a whole 369-day cycle (right). See also Figure 2.17.

two antennas, from which the position of any backscattered point may be derived. Thus, the SARIn mode may help discriminating and mitigating land contamination signals from off-nadir land targets (e.g., steep cliffs) (Armitage and Davidson, 2014; Abulaitijiang et al., 2015).

The next SAR altimetry mission has already begun with the launch of ESA's Sentinel-3A satellite on February 16, 2016. It is part of the European Commission's Corpernicus environmental monitoring program. The Sentinel-3 mission is based on two identical satellites placed in an interleaved orbit for optimal spatial coverage (Table 2.5 and Figure 2.17), and will continue the time series started with ERS-1 in 1991. The SAR Radar Altimeter (SRAL) onboard the Sentinel satellites is a dual-frequency type operating at Ku and C bands, and in LR and SAR modes. As with CS2, a geographical mode mask is used to determine the SRAL operating mode.

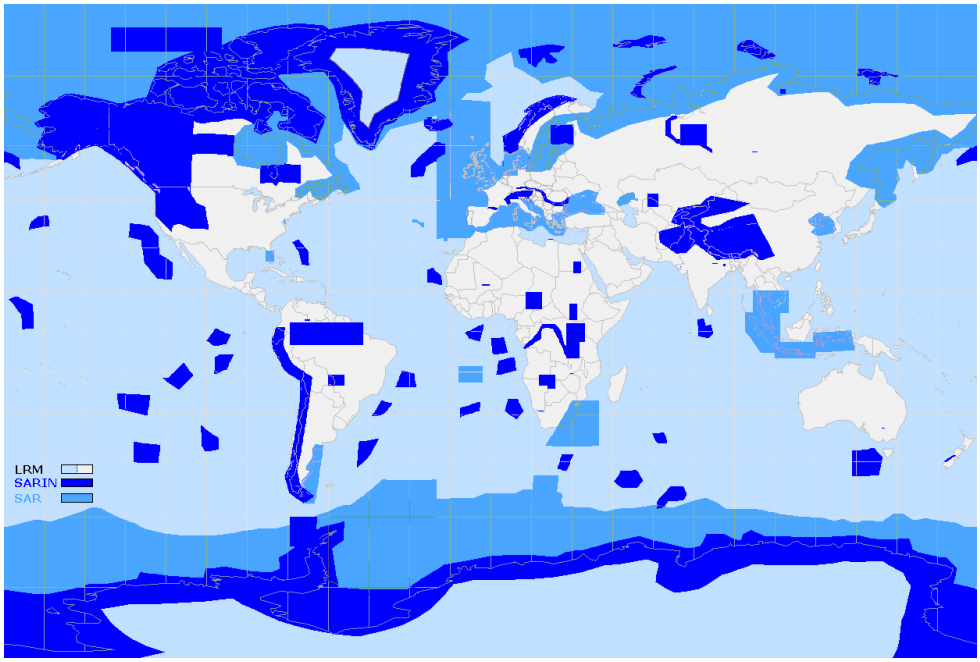

Figure 2.26: An example of a CS2 geographical mode mask. It has changed throughout time according to user needs, with the most recent version 3.8 released in March 2016. Taken from ESA and MSSL-UCL (2012)

2.5.4 Retracking

There exist different analytical functions that may be used for waveform tracking, and several methods for fitting these to the form of the radar echo (Gommenginger et al., 2011). The returned waveform from open sea is characterized by the ramp function (e.g., Figure 2.24). The actual tracking is done by identifying the half-effect point in the leading edge of the radar pulse. The ramp function can be described analytically by the Brown model (Chelton et al., 2001). From the somewhat complicated shape of the Brown model, several physical parameters (including the sea surface height) may be derived by comparing true (averaged) waveforms with a theoretical curve.

The shape of the returned waveform depends on the surface it is reflected from, and will depart considerably from the typical ramp shape if, e.g., the target contains land areas, which often is the case in coastal altimetry (Gommenginger et al., 2011). Returned waveforms from coastal and land areas are characterized by several isolated peaks, and the standard analytical Brown model cannot be used. In addition, the SAR waveform is significantly different from the conventional altimeter waveform (Stenseng, 2011). Consequently, alternative waveform analysis methods must be used, known as retrackers. A vast amount of retrackers exist, and they are classified in two categories; physical and empirical retrackers (Jain, 2015).

The SAMOSA3 physical retracker uses the Brown approach to analytically describe the returned waveform from the SAR altimetry footprint (Jain, 2015). Because it is a physical retracker, other parameters than the sea surface height can be determined from it, e.g., significant wave height and antenna mispointing.

Empirical retrackers do not take the physics of the reflected waveform into account (Jain, 2015). They can either be based on fitting of empirical functions, typically developed over many years of empirical observations and practical experiences, or use waveform statistics to determine the retracking point. In this thesis the latter type of empirical retrackers have been used, as they form an important research area at DTU Space, by which the experimental CS2 data used in **Paper D** and **Paper E** were supplied. The empirical retrackers only give the range, but provide a sea surface height estimate for all kinds of waveforms and are computationally efficient. A study by Villadsen et al. (2016) shows that empirical retrackers perform as well as physical retrackers if only the sea surface height is wanted.

The range is determined by finding the point in time when the signal from the surface in nadir was observed. The waveform is received in a number of bins, where each bin contains a power value corresponding to a certain distance from the satellite

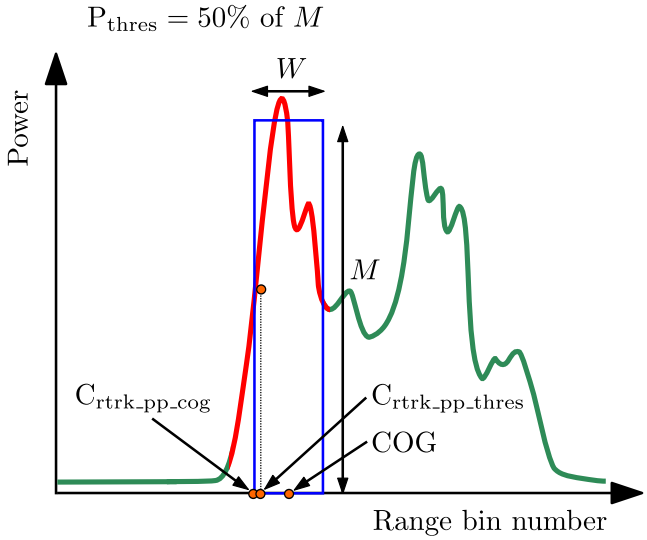

Figure 2.27: Schematic showing the Narrow Primary Peak COG and Threshold retrackers. COG is the center of gravity of the primary peak (red part of curve), $C_{rtrk\_pp\_cog}$ is the retracked position for the COG retracker, and $C_{rtrk\_pp\_thres}$ is the retracked position for the Threshold retracker. Modified from Jain (2015).

(Chelton et al., 2001). CS2 SAR waveforms have 128 bins with a bin width of 23.42 cm, corresponding to a range window of ~30 m (Villadsen et al., 2016).

In **Paper D**, the simple threshold retracker is used (Nielsen et al., 2015). It is an extension of the Offset Center of Gravity (OCOG) retracker, which draws a rectangle width around the center of gravity of the waveform (Jain, 2015). The magnitude M and width W of the rectangle is computed from the different bin power levels. The simple threshold retracker uses a threshold percentage (80%) of M. The retracking position is determined by interpolation between adjoining bins where the threshold value is first reached on the leading edge of the waveform. The simple threshold retracker works on the complete waveform.

In **Paper E**, the Narrow Primary Peak Threshold retracker (NPPT) is used. It is similar to the simple threshold retracker, but only the primary peak of the waveform is considered, see Figure 2.27. The primary peak is the first high peak including the leading edge of the radar pulse, containing most of the reflections from nadir (Jain, 2015). As coastal waveforms may be complex and contain multiple peaks due to reflections from other sufaces than the ocean, considering only the primary peak of the waveform will give the most precise information about the sea surface.

The primary peak COG retracker is much like the traditional COG retracker, but only power levels P_i of the bins in the primary peak, N_{pp} are considered (Jain, 2015). The magnitude of the rectangle is given by

$$M = \sqrt{\frac{\sum_{i=1}^{N_{pp}} P_i^4}{\sum_{i=1}^{N_{pp}} P_i^2}}, \tag{2.110}$$

and its width

$$W = \frac{\left(\sum_{i=1}^{N_{pp}} P_i^2\right)^2}{\sum_{i=1}^{N_{pp}} P_i^4}. \tag{2.111}$$

The COG is given by

$$\mathrm{COG} = \frac{\sum_{i=1}^{N_{pp}} iP_i^2}{\sum_{i=1}^{N_{pp}} P_i^2}, \tag{2.112}$$

and

$$\mathrm{C}_{\mathrm{rtrk\_pp\_cog}} = \mathrm{COG} - \frac{W}{2}. \tag{2.113}$$

The NPPT uses Eq. (2.110) and identifies the first bin location where the power of the bin exceeds an optimal 50% threshold percentage (Jain, 2015),

$$P_{\mathrm{thres}} = 0.5M. \tag{2.114}$$

The first bin where the power is greater than P_{thres} is found through a loop, and $\mathrm{C}_{\mathrm{rtrk\_pp\_thres}}$ is obtained by interpolation between this first bin and the preceding bin (Jain, 2015).

Today, many altimetry data sets contain data from more than one retracker, working in parallel over all areas (Gommenginger et al., 2011). This enables the user to choose the best determined range depending on the reflecting surface. Most of the radar returns form the open sea are of the Brown type, while in the coastal zone, the radar pulses tend to vary between multiple types. Choosing a retracking algorithm in an adaptive way introduces new challenges as the different mathematical functions include systematic effects that can give constant biases between range observations based on different algorithms.

2.5.5 Mean dynamic topography from altimetry

Eqs. (2.93) and (2.94) are quite simplified. A number of corrections must be applied to R in order to achieve the geometrical distance between the satellite and Earth's surface. Some concern the behavior of the radar pulse on its journey through the

atmosphere, while other concern local wind and wave conditions (known as the sea state), and yet other geophysical signals (Andersen and Scharroo, 2011). Several of these corrections need special attention in the coastal zone.

According to Andersen and Scharroo (2011), the corrections may be divided into two groups:

1. Range corrections, which concern the change of radar propagation speed and the actual scattering surface of the radar pulse.
2. Geophysical corrections, which adjust the observed sea surface due to time-variable effects such as tides and atmospheric pressure.

Eq. (2.93) would have sufficed if the atmosphere was replaced by perfect vacuum, and the distribution of ocean waves was adequately known. The existence of dry gases, water vapor, as well as free electrons in the atmosphere decelerates the speed of the radar pulse, increasing the length of the observed range, giving an ocean surface that is too low, if these effects are not accounted for (Chelton et al., 2001). The corrections that aims to model the refraction and delay of the radar signal in the atmosphere, are usually divided into three components:

1. The dry tropospheric correction (ΔR_{dry}), considering dry gases (mainly oxygen and nitrogen). The refractivity for the dry part of the troposphere depends on the air pressure at sea level, which is typically obtained from meteorological models.
2. The wet tropospheric correction (ΔR_{wet}), considering water vapor. The correction can be estimated from measurements with a microwave radiometer onboard the altimetry satellite, or from a meteorological model, with the correction based on the radiometer being preferred, because it is considered more accurate.
3. The ionospheric correction (ΔR_{iono}) takes the existence of free electrons in the upper layers of the atmosphere into account. Due to the ionospheric delay being dispersive, it will vary depending on which frequency band is used. The correction may be computed for the primary Ku band, if, e.g. a Ku and C dual-frequency altimeter is used. Alternatively, the ionospheric correction may be computed from models.

The wave distribution, as well as the scattering of the radar pulse by the sea surface, is not gaussian; wave troughs reflect more of the signal back to the satellite, than wave crests, which gives rise to a bias (Chelton et al., 2001). It is a result of three interrelated effects; an EM bias physically related to the distribution of specular facets, a skewness bias due to the use of a median tracker when it is the mean which

is desired, and an instrument bias related to the specific tracker. The total bias is related to the local sea state, and is therefore known as the sea-state bias (ΔR_{ssb}).

The corrected range $R_{\mathrm{corrected}}$ is related to the observed range $R = R_{\mathrm{obs}}$ through

$$R_{\mathrm{corrected}} = R_{\mathrm{obs}} - \Delta R_{\mathrm{dry}} - \Delta R_{\mathrm{wet}} - \Delta R_{\mathrm{iono}} - \Delta R_{\mathrm{ssb}}. \tag{2.115}$$

The ellipsoidal height of the sea surface, SSH, is given by:

$$\mathrm{SSH} = h - R_{\mathrm{corrected}} = h - \left(R_{\mathrm{obs}} - \Delta R_{\mathrm{dry}} - \Delta R_{\mathrm{wet}} - \Delta R_{\mathrm{iono}} - \Delta R_{\mathrm{ssb}}\right). \tag{2.116}$$

All observations must be related to the same reference system (Andersen and Scharroo, 2011). Most altimetry products are processed in the ITRF. Typically, altimeter observations refer to the TOPEX ellipsoid, but CryoSat-2 uses WGS84 as standard (ESA and MSSL-UCL, 2012) (Table 2.1). In addition, one must consider how the tides have been treated (Section 2.2.2) in the product. Typically, altimetry observations are given in the MT system.

The main focus of satellite altimetry is the study of dynamical sea surface signals related to oceanographic processes, normally on the submeter scale (Andersen and Scharroo, 2011). In order to isolate these signals, the dominant geophysical signals due to the geoid, the tides, and the dynamic atmosphere must be removed. Consequently, the actual sea surface height is a combination of the mentioned geophysical signals and the dynamic ocean topography (DOT), such that

$$\mathrm{DOT} = \mathrm{SSH} - N + \Delta R_{\mathrm{tides}} + \Delta R_{\mathrm{atm}}. \tag{2.117}$$

Note that these corrections are actual geophysical signals, but here they act as corrections to the observed range.

A summary of all range and geophysical corrections is shown in Table 2.6. For each correction, several models exist, and the international science community decides and updates its standards continuously. Most range and geophysical corrections need special attention in the coastal zone; either because the signal is much larger there, or the correction less accurate.

Local observations of the SSH where the geoid has been removed, will rarely present a zero time mean (Andersen and Scharroo, 2011). This is due to the DOT having both a steady-state and a time-variable component. The steady-state component is the mean dynamic topography (MDT), which reflects the steric expansion of sea water (volume changes of sea water due to changing temperatures and salinities), as well as ocean currents in geostrophic balance (Section 2.6). Depending on the application, either the geoid or the MSS may be removed from the SSH. If we want to study large-scale ocean currents, the geoid must be removed, see Eq. (2.117).

Table 2.6: Typical mean and standard deviation (σ,) values of all time-variable corrections which must be applied to the sea surface height observed by the satellite altimeter. The values are computed from six years of Jason-1 data. The geoid correction is presumed to have negligible time variability, and is therefore not shown in this table. Taken from Andersen and Scharroo (2011).

	Mean (cm)	Time-variable deep ocean (σ) (cm)	Time-variable coast (σ) (cm)
Dry troposphere	-231	0-2	0-2
Wet troposphere	-16	5-6	5-8
Ionosphere	-8	2-5	2-5
Sea-state bias	-5	1-4	2-5
Tidal corrections	$\sim$ 0-2	0-80	0-500
Dynamic atmosphere	$\sim$ 0-2	5-15	5-15

From the MDT derived by altimetry, geostrophic surface currents can be derived (Section 2.6.4).

In most regions, the ocean tide (OT) amounts to more than 80% of the SSH signal variability (Andersen and Scharroo, 2011). In addition to the dominating OT signal, the tidal correction comprises corrections due to several smaller tidal signals; ocean tide loading (OTL), solid earth tides (SET), and the pole tide (PT). The sum of these corrections may be written as follows:

$$\Delta R_{\mathrm{tides}} = \Delta R_{\mathrm{OT}} + \Delta R_{\mathrm{OTL}} + \Delta R_{\mathrm{SET}} + \Delta R_{\mathrm{PT}}. \tag{2.118}$$

The satellite altimeter observes the total geocentric (elastic) tidal forces, which is the sum of OT, OTL, and SET. This contrasts with tide gauges on the ground, which only observe the OT and PT.

Determining the OT has dramatically improved since the launch of TOPEX/Poseidon, and now global OT models have an accuracy of about 1-2 cm (Andersen and Scharroo, 2011). However, the tidal correction needs special attention in the coastal zone, where both OT height and complexity increases. In some cases, errors exceed 20 cm in those areas, or the correction is not provided at all. A local modeling of the OT in the coastal zone may be rewarding, which is the subject of **Paper D**. Solid earth tides and pole tides, however, are unaffected by the coastal zones, and may be modeled with the usual accuracy.

As a first approximation, the response of the sea surface to air pressure is like an inverted barometer; it rises when pressure is low, and sinks when pressure is high

(Pugh and Woodworth, 2014). A change in air pressure of 1 hPa (= 1 mbar) gives a change in sea surface of around 1 cm. The correction for atmospheric variation is typically divided into a low-frequency contribution (periods longer than 20 days), and a high-frequency contribution (periods shorter than 20 days).

For the modeling of the low-frequency contribution, the classic inverted barometer correction is used, taking into account the assumed hydrostatic response of the ocean to changes in atmospheric pressure (Andersen and Scharroo, 2011). The instantaneous correction can be directly computed from the surface pressure, in centimeters:

$$\Delta R_{\mathrm{atm}}^{\mathrm{ib}} \approx 0.99484(P_0 - P_{\mathrm{ref}}), \tag{2.119}$$

where P_0 may be derived from the dry tropospheric correction. P_{ref} is the global mean reference pressure; traditionally it has had a value of 1013.3 hPa. However, the mean global pressure is not equal to the mean pressure above the ocean, which is closer to 1011 hPa. The global mean pressure is not constant either, but has an annual amplitude of around 0.6 hPa. If a correction taking this variation into account is used, we get a better correction for the low-frequency contribution. The correction for the low-frequency contribution should be combined with a high-frequency contribution (short-periodic changes in air pressure and wind effects), normally available from a model.

2.6 Ocean dynamics

2.6.1 Ocean and atmosphere

The Sun, together with Earth's rotation, ultimately drive the ocean currents (Vallis, 2012). The Sun supplies the energy needed to keep the currents in motion. However, the amount of energy that is received by the Earth is unevenly distributed on its surface: it is lower in the polar regions, and higher at the equator, see Figure 2.28. Also, as the Earth's spin axis is tilted by 23.45°, the amount of received energy will vary seasonally, see Figure 2.29. This differential distribution of heat happens through winds (75%) and ocean currents (25%); thus it sets both atmosphere and ocean in motion. The wind is caused by differences in atmospheric pressure, because air moves from higher to lower pressure, see Figure 2.30. The atmosphere and the ocean have different characteristics, and respond at different time scales. The atmosphere responds quickly to any disturbance it is subject to, while the ocean responds much slower, supplying some of its energy back to the atmosphere, and distributing the rest by circulation. However, even if the ocean dampens climate

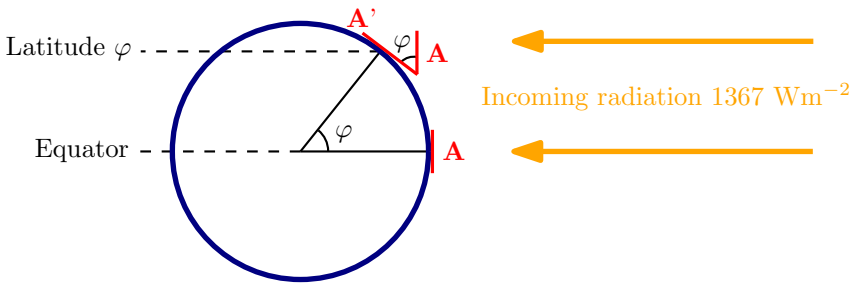

Figure 2.28: The same amount of incoming solar radiation is distributed over a larger area **A′** at higher latitudes φ. Adapted from Vallis (2012).

variations, the effects will be returned to the atmosphere some decades or hundreds of years later.

Salinity is the concentration of dissolved salts in the ocean water (Stewart, 2008). Although salinity varies spatially due to the aforementioned reasons, the ratio among various dissolved salts remains practically constant. Salinity has been difficult to define and measure accurately enough. The current definition of salinity, called the Practical Salinity Scale of 1978, defines salinity in terms of a conductivity ratio, and renders salinity, S, dimensionless. The salinity distribution of the ocean tends to be zonal, with less salty water near the equator and in polar regions, and the saltiest water at mid-latitudes, where evaporation is high. The general range of ocean salinities is between 32 and 37, but may locally be lower or higher.

Temperature is important for many physical processes, some of which can be used to define an absolute temperature T (in unit Kelvin, K) (Stewart, 2008). Absolute temperature measurements are used to define a practical temperature scale, where the temperature scale in Kelvin is related to another known temperature scale in Celsius by $T[^\circ\mathrm{C}] = T[\mathrm{K}-273.15]$. The temperature distribution of the ocean also tends to be zonal, with the warmest water near the equator, and the coldest water near the poles. Ocean temperature ranges from -2°C to 30°C, with local variations exceeding this range.

Pressure in the ocean, denoted p, is a function of depth, density, and gravity (Stewart, 2008). The SI unit of pressure is Pascal (Pa), but oceanographers often use the unit bar, or, rather, mbar, where 1 mbar = 1 hPa. Pressure is often used as a vertical coordinate instead of depth, and pressure in dbars ≈ depth in meters. Conductivity and temperature are often measured digitally as a function of pressure, using CTDs. They are electronic instruments measuring conductivity, temperature, and depth, and recording the measurements digitally. CTDs are a collection of sensors, usually

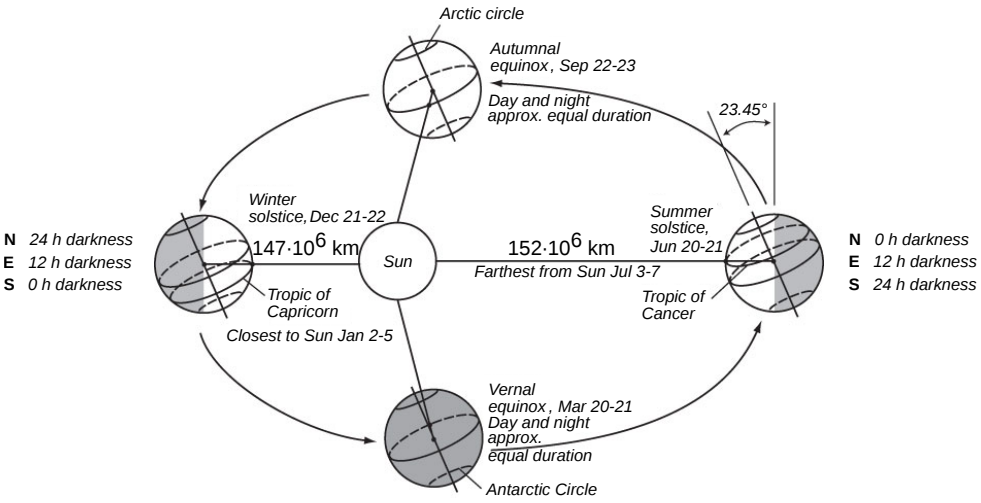

Figure 2.29: Earth's orbit around the Sun is slightly elliptical; thus, the closest approach to the Sun occurs in January, and the farthest distance occurs in July. Due to the eccentricity, maximum insolation averaged over Earth's surface occurs in January. Due to the inclination of Earth's rotation axis, maximum insolation at any point outside the tropics occurs in June in the Northern Hemisphere, and in December in the Southern Hemisphere. Thus, in this figure, the winter and summer solstices apply to the Northern Hemisphere. Adapted from Stewart (2008).

lowered from ships. CTD may also be measured on drifters and sub-surface floats, such as the ARGO system.

The density, ρ (in $\mathrm{kg \cdot m^{-3}}$, or $\mathrm{g \cdot cm^{-3}}$), of sea water is a function of temperature, salinity, and pressure (Stewart, 2008). It increases with increasing salinity and pressure, and decreases with increasing temperature. Density is rarely measured, rather, we compute density from measurements of temperature, conductivity (salinity), and pressure, using the equation of state of sea water. The equation of state, $\rho = f(T, S, p)$, is an equation that empirically relates density to temperature, salinity, and pressure, and consists of three polynomials with 41 constants.

When surface water cools, density increases, and the water sinks to a depth governed by its density relative to the density of the deeper water (Vallis, 2012). Next, the water is transported to other parts of the ocean by the aid of currents, at all times staying above denser water and below less dense water. Interior ocean currents depend on the pressure distribution, which depends on the density variations of the ocean interior. Thus, to follow water movement within the ocean, we must know the ocean's interior density distribution.

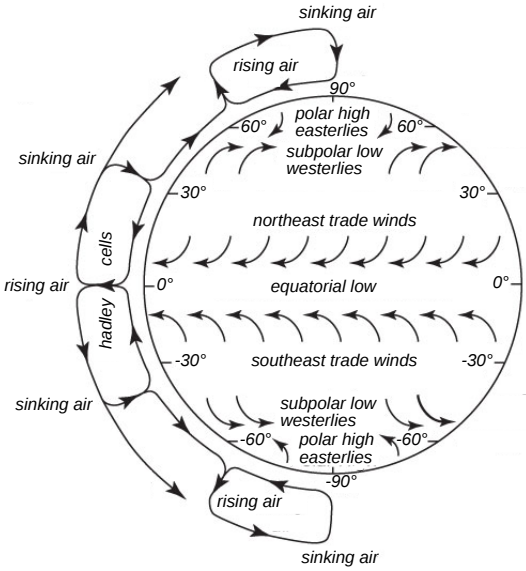

Figure 2.30: Schematic of the atmospheric circulation. The sun warms the ocean in the tropics, transferring heat from the ocean to the atmosphere through the evaporation of sea water. When the water vapor condenses and falls down as rain, heat is released. Adapted from Stewart (2008).

The large-scale ocean circulation comprises basin-wide wind-driven circulating water masses known as gyres, as well as other quasi-horizontal currents, and a meridional overturning circulation (Vallis, 2012). In addition come mesoscale (50 to 300 km) eddies, containing around 50% of the kinetic energy of the ocean, the ocean's weather analogue. In a nutshell:

- Gyres are mainly wind-driven, and due to meridional variations of zonal winds.
- Wind stress affects the upper few tens of meters of the ocean, where it induces a perpendicular Ekman flow; consequently, the ocean surface slopes and gives rise to a geostrophic flow.
- All the main gyres have intense western boundary currents, caused by the latitudinal variation of the Coriolis force.
- The meridional overturning circulation is due to buoyancy effects, i.e., the sinking of dense water at high latitudes. To keep the MOC in motion, both mixing (warming of water at low latitudes) and wind (strong westerlies in the Antarctic Circumpolar Current) bring the deep water back up to the surface.

2.6.2 Equations of motion

Ocean dynamics concerns how the ocean reacts to internal and external forces, and is commonly described by Newtonian fluid mechanics (Vallis, 2006). The equation of motion for a fluid forms a basic description of ocean dynamics. Even though classical solid and fluid media are governed by the same physical laws (of Newton and thermodynamics), their equations look differently. To be able to describe fluid flow, we exploit the theory of conservation of mass, energy and momentum, which amount to five equations: the thermodynamic equation (1), the continuity equation (1), and the Navier-Stokes equation (3, in x, y, and z directions).

If the equation of state of a fluid not only involves density and pressure, but also temperature (cf. Section 2.6.1), the thermodynamic equation is necessary to secure the conservation of energy and obtain a closed system of equations, see Vallis (2006) for more details.

Within classical mechanics, mass is conserved, and normally it is not needed to formulate a separate equation describing the effect. Within fluid dynamics it is different, as fluids flow in and out of regions and the fluid density may change (Vallis, 2006). Therefore, we need an equation explicitly describing the mass flow. The continuity equation can be formulated as follows:

$$\frac{\partial \rho}{\partial t} + \nabla \cdot \rho \mathbf{u} = 0, \tag{2.120}$$

where $\mathbf{u}$ is the fluid velocity $\mathbf{u} = \mathbf{u}(\mathbf{x},t)$, and $\mathbf{x}$, t are the position vector and time, respectively.

Ocean currents are assumed to be incompressible except when describing the property of sound (Stewart, 2008). The density is assumed to be constant except in the case when it is multiplied with gravity. This approximation is known as the Boussinesq approximation. For an incompressible fluid, $\rho = \text{const.}$ (where the given density of the fluid does not change), Eq. (2.120) simplifies to:

$$\nabla \cdot \mathbf{u} = 0. \tag{2.121}$$

The Navier-Stokes equation has its origin in Newton's second law, $(\Sigma)\mathbf{F} = m\mathbf{a}$, which in fluid mechanics is commonly expressed as (Vallis, 2006)

$$\rho \mathbf{a} = \mathbf{f}, \tag{2.122}$$

where the acceleration is written on the left-hand side, and we consider the force density $\mathbf{f}$ in $\mathrm{N/m^3}$, as well as $m \to \rho$.

There are three main contributors to $\mathbf{f}$; pressure force $\mathbf{f}_\mathrm{P}$ due to the spatially varying pressure around the fluid element (where the fluid element is an infinitesimal part of the fluid), gravity $\mathbf{f}_\mathrm{G}$, and friction $\mathbf{f}_\mathrm{V}$ due to the viscosity of the fluid (Vallis, 2006). Thus Eq. (2.122) can be written as

$$\rho\mathbf{a} = \mathbf{f}_\mathrm{P} + \mathbf{f}_\mathrm{G} + \mathbf{f}_\mathrm{V}, \tag{2.123}$$

where

$$\begin{aligned} \mathbf{f}_\mathrm{P} &= -\nabla p, \\ \mathbf{f}_\mathrm{G} &= \rho\mathbf{g}, \\ \mathbf{f}_\mathrm{V} &= \nu\nabla^2\mathbf{u}, \end{aligned} \tag{2.124}$$

where $\mathbf{g} = [0,0,g_z]^T$, $\nu = \mu/\rho$ is the kinematic viscosity, and μ is the molecular viscosity.

As a fluid is typically characterized by its velocity field $\mathbf{u} = \mathbf{u}(\mathbf{x},t)$, we express the acceleration $\mathbf{a}$ as the derivative of the fluid velocity (Vallis, 2006). Thereby, we must relate a fluid element's acceleration to the derivative of the velocity field at a given point within the fluid. This connection is termed the total derivative,

$$\mathbf{a} = \frac{\mathrm{D}\mathbf{u}}{\mathrm{D}t} = \frac{\partial\mathbf{u}}{\partial t} + (\mathbf{u}\cdot\nabla)\,\mathbf{u}. \tag{2.125}$$

Taking Eq. (2.125) into account, Eq. (2.123) can be written out as

$$\frac{\mathrm{D}\mathbf{u}}{\mathrm{D}t} = -\frac{1}{\rho}\nabla p + \mathbf{g} + \nu\nabla^2\mathbf{u}. \tag{2.126}$$

Eq. (2.126) incorporates two additional forces, namely the Coriolis and centrifugal forces, both of which arise as a consequence of Earth's rotation (Vallis, 2012). The centrifugal force is an apparent force pulling a rotating body away from the rotation axis, caused by the body's inertia. The Coriolis force causes a deflection of moving bodies, as seen in a rotating reference system. If this rotating system is Earth, the Coriolis force causes clockwise deflection (with respect to the direction of motion) in the Northern Hemisphere, and counter-clockwise in the Southern Hemisphere. The relationship between an inertial reference system I, and a rotating system R (assuming a constant angular velocity ω) can be expressed as (Vallis, 2006)

$$\left(\frac{\mathrm{d}\mathbf{v}_I}{\mathrm{d}t}\right)_R = \left(\frac{\mathrm{d}\mathbf{v}_R}{\mathrm{d}t}\right)_I - 2\omega\times\mathbf{v}_R - \omega\times(\omega\times\mathbf{r}), \tag{2.127}$$

where $\mathbf{v}_R$ and $\mathbf{v}_I$ are relative and inertial velocities, respectively. The term on the left-hand side is the rate of change of the relative velocity observed in the rotating

system, while the first term on the right-hand side is the rate of change of the inertial velocity observed in the inertial system. The second and third terms on the right-hand side (signs inclusive) are the Coriolis and centrifugal forces per unit mass. Usually these terms are written on the left-hand side of the equation and the terms $+2\omega \times \mathbf{v}_R$ and $+\omega \times (\omega \times \mathbf{r})$ are called the Coriolis and centrifugal accelerations, respectively. We note that there is no Coriolis force acting on a body at rest in the rotating system.

Eq. (2.126) is a non-linear partial differential equation. The equations of motion of a fluid developed from a simple first-order differential equation for velocity (Newton's second law) into a non-linear partial differential equation that is nearly impossible to solve (Stewart, 2008). Within fluid dynamics, several boundary conditions are considered, e.g., that there is no velocity perpendicular to a boundary (i.e., no flow through the boundary), and that there is no flow parallel to a solid boundary (no-slip condition; near a solid surface the fluid's velocity with respect to the surface equals zero). Even when boundary conditions are introduced, the equations are challenging to solve. If we consider viscosity, no exact solution exists to this day. When neglecting friction, some exact solutions exist. Because the equations are so difficult to solve, they are usually simplified. Analytical solutions may be found for very simplified versions of the equations and may be used to study ocean processes, including waves. Solutions for ocean currents including realistic coastal areas with bathymetry can only be achieved by numerical computations.

2.6.3 Numerical ocean models

Numerical ocean models attempt to simulate the ocean as realistically as possible (Stewart, 2008). The computer effort needed to run such models is considerable, and several approximations and discretizations must be made to the initially challenging continuous equations describing ocean dynamics. Numerical ocean models have several areas of use. They may be used in scientific applications, e.g., to study changes due to altering one of the model parameters or decide which approximations hold. Further, they are useful for interpolation and allows a dynamically consistent interpretation in areas where actual observations are scarce. Another decisive application of numerical ocean models lies within prediction or forecasting. There will never be a one-model-fits-all ocean model covering all kinds of ocean dynamics. One important reason is that ocean dynamics spans temporal scales from seconds to centuries and spatial scales from meters to kilometers. Instead, application-dependent requirements need to be set.

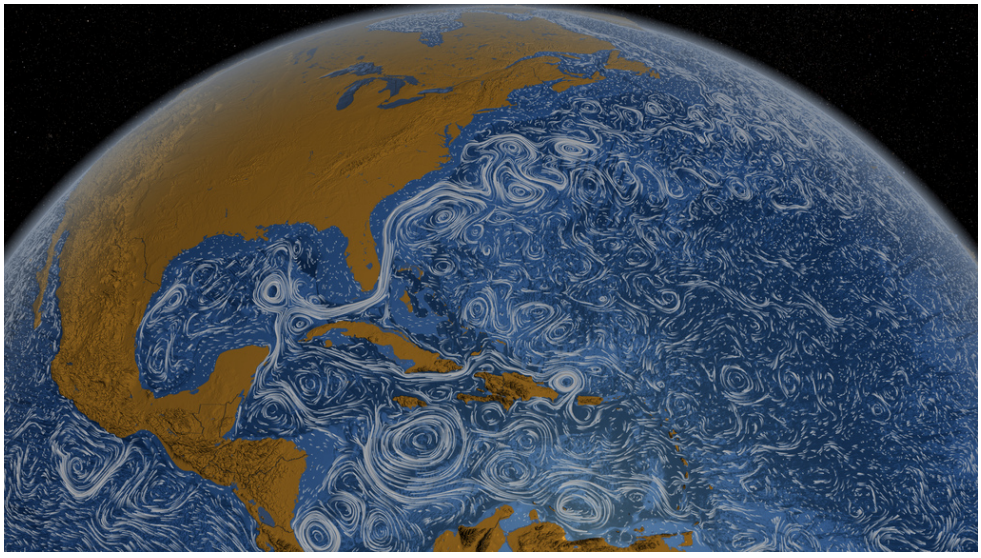

Figure 2.31: Still view of NASA's Perpetual Ocean ocean flow visualization, based on the ECCO model, taken from `http://www.nasa.gov/topics/earth/features/perpetual-ocean.html`. Additional stills and videos are available at their web page.

As mentioned, numerical ocean models solve approximations of the equations of motion, and the fluid is assumed to be incompressible. In addition come the following important physical approximations (Stewart, 2008):

- The Boussinesq approximation; ocean density variations are small (less than 3%), thus the density ρ is replaced with $\rho_0 \approx 1035\,\mathrm{kgm}^{-3}$ except in terms involving gravity g. This results in a Boussinesq approximation in the horizontal equations of motion only. In essence, the Boussinesq approximation implies that because density variations are small, their effect on the mass of the fluid is negligible, but not their effect on the weight of the fluid (mass multiplied with gravity).
- Hydrostatic approximation; the hydrostatic approximation holds when vertical accelerations are small compared to gravity. Since the width of the ocean is much larger than its depth, this approximations often holds.

Considering the approximations above, a mathematical description of the ocean circulation is given by a set of seven equations, known as the primitive equations:

- 3 equations represent the time derivative of horizontal and vertical velocity (equations of motion).

- 1 equation represents the conservation of mass (continuity equation).
- 2 equations represent the rate of change of temperature and salinity with time.
- 1 equation to compute density from salinity and temperature (equation of state).

Ocean general circulation models based on the above equations are often termed "Primitive Equation Models". Examples of such models are the Parallel Ocean Program Model (POP), the Miami Isopycnic Coordinate Ocean Model (MICOM), the Hybrid Coordinate Ocean Model (HYCOM), the Ocean Circulation and Climate Advanced Modelling (OCCAM) global model, the Estimating the Circulation and Climate of the Ocean (ECCO) ocean model, the MIT/Liverpool model, and the Regional Oceanic Modeling System (ROMS), see Figure 2.31. These models are quite computationally intensive and complex, but, in return, provide an extensive nowcasting and forecasting of the ocean's development in time.

Numerical ocean models give the part of the SSH that arises from the ocean's circulation, i.e., sea level relative to an implicit geopotential surface. Thus, an average of such heights over a given time period will be equivalent to MDT (Section 2.5.5).

2.6.4 Geostrophic currents

We have seen that ocean currents are a result of fluid motion due to internal pressure and Coriolis forces, external gravity force and friction. Near the ocean surface, friction is almost exclusively due to steady winds pushing the water (Vallis, 2012). This horizontal, wind-driven boundary layer is only a few tens of meters thick and is called the Ekman layer, after Swedish oceanographer V. W. Ekman.

Although the ocean surface is exposed to steady winds, the ocean current velocity will not increase infinitely with time (Stewart, 2008). Starting from an ocean at rest and no wind, an increasing wind will force the water to start moving (due to wind stress). The water will accelerate until a constant velocity is reached, and when it does, the net force acting on the water will be zero and we will have a force balance. The force needed to oppose the current flow is mainly due to friction. However, the Coriolis force also affects the force balance, aiming to deflect the flow. F. Nansen observed that ice bergs would tend to flow at an angle of $20°$ - $40°$ to the wind direction, and argued that the three forces wind stress **W**, friction **F**, and the Coriolis force **C** were important constituents of this effect, see Figure 2.32. Not only must friction be in the opposite direction of the flow velocity, but the Coriolis force must be perpendicular to the flow, and the forces must balance for a steady flow, i.e., $\mathbf{W} + \mathbf{F} + \mathbf{C} = 0$.

Ekman did the theoretical study on Nansen's observations, and formulated the equations of motion in zonal (east-west) and meridional (north-south) directions, termed u and v, respectively, assuming a steady, homogeneous, horizontal flow on a rotating Earth, and with constant Eddy viscosity A_z, which is a parametrization of the mixing of momentum. Assuming a north-blowing wind, the solutions to the Ekman equations are (Stewart, 2008)

$$u = V_0 \exp(az) \cos(\pi/4 + az), \tag{2.128}$$

$$v = V_0 \exp(az) \sin(\pi/4 + az), \tag{2.129}$$

with constants

$$V_0 = \frac{T}{\sqrt{\rho_w^2 f A_z}}, \tag{2.130}$$

$$a = \sqrt{\frac{f}{2A_z}}, \tag{2.131}$$

where V_0 is the velocity at the sea surface, and T is the wind stress. At the sea surface, $z = 0$, and we get

$$u(0) = V_0 \cos(\pi/4), \tag{2.132}$$

$$v(0) = V_0 \sin(\pi/4). \tag{2.133}$$

We observe that in the Northern Hemisphere, the surface current is $45°$ to the right of the wind. In the Southern Hemisphere, the surface current is $45°$ to the left of the wind. This angle increases with increasing depth. Further, the current velocity decays exponentially with depth. Thus we get the famous Ekman spiral, describing near-surface current flow, see Figure 2.33.

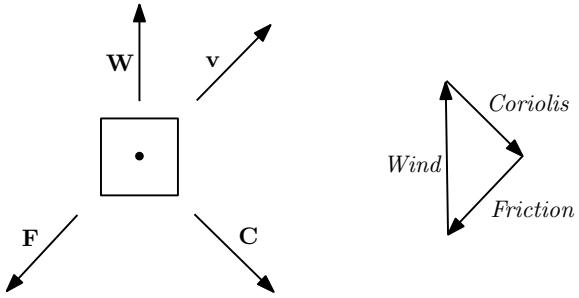

Figure 2.32: Steady flow **v** of an ice berg on a rotating Earth due to the balance of wind stress **W**, friction **F**, and the Coriolis **C** forces acting on it while a steady wind blows. Adapted from Stewart (2008).

Summarizing, stress initiates an Ekman current with increasing velocity until we have a force balance between wind stress and the Coriolis force and the velocity is constant (Vallis, 2012). If we now consider flow below the Ekman layer, or, rather, a flow not affected by wind stress, another force balance becomes prominent. It is a balance between the pressure gradient force and the Coriolis force, known as geostrophic balance.

Conceptually, the way a flow reaches geostrophic balance is very similar to the way Ekman balance occurs in Figure 2.32. We begin with assuming there is a horizontal pressure gradient force $\mathbf{P}$ present in a fluid, generating a flow from higher to lower pressure, see Figure 2.34. As the fluid is set in motion on a rotating Earth, it is deflected by the Coriolis force $\mathbf{C}$. When these forces are in equilibrium, the fluid's flow direction $\mathbf{v}$ is perpendicular to both Coriolis and pressure gradient forces. Geostrophic currents flow clockwise around high-pressure centers and counter-clockwise around low-pressure centers in the Northern Hemisphere. On spatial scales of several tens of kilometers and temporal scales of several days, ocean flow is largely in geostrophic balance.

Assuming an ocean at rest, the pressure field of the ocean practically equals the hydrostatic pressure (Stewart, 2008). However, it is not easy to measure pressure directly, since small changes in depth give large changes in pressure. Pressure may therefore be computed from other observables, such as the weight and density of the water column above the point of interest. The volume, and thereby the density, depends on temperature, conductivity, and, to a lesser degree, on pressure itself (since water is considerably incompressible). Density is computed by the conventional

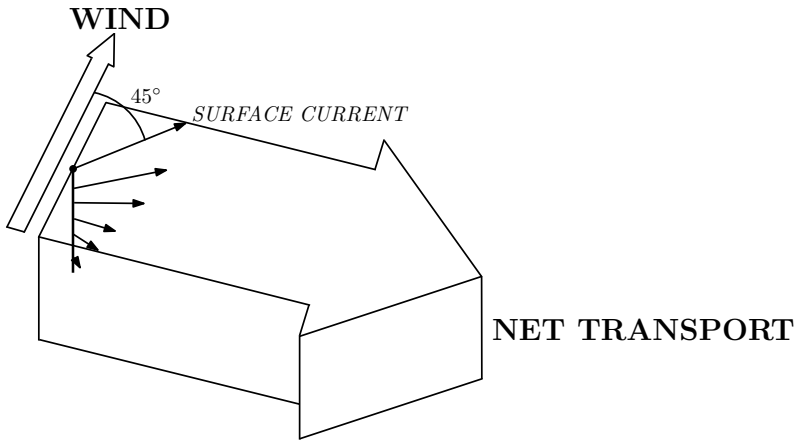

Figure 2.33: Schematic Ekman spiral in the Northern Hemisphere. Adapted from Vallis (2012).

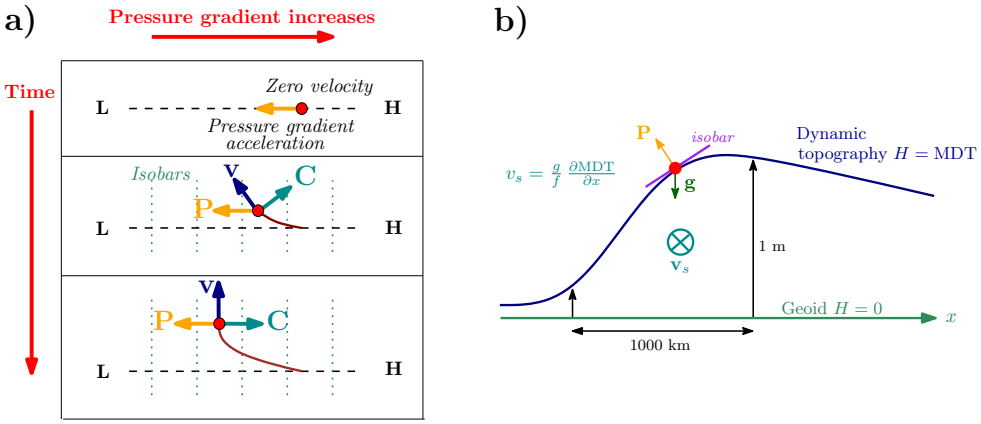

Figure 2.34: Schematic showing (a) how a geostrophic flow **v** is initiated by a force balance between the pressure gradient force **P** and the Coriolis force **C**, and (b) how geostrophic surface currents are directly related to the slope of the sea surface above the geoid. Both gravity **g** and the pressure gradient **P** affect the point of interest. In the Northern Hemisphere, geostrophic balance is achieved if the corresponding flow $\mathbf{v}_s$ is directed into the page. Adapted from Segar (2012) and Stewart (2008).

equation of state, $\rho = f(T, S, p)$. Next, the pressure at any depth h is determined from the hydrostatic equation:

$$p = \int_{-h}^{0} g(\varphi, z)\rho(z)\, \mathrm{d}z, \tag{2.134}$$

where g is gravity and φ is the geodetic latitude.

When considering geostrophic flow, we neglect non-linear terms as well as friction in the equations of motion (Stewart, 2008). This simplification is reasonable, since the dominating horizontal forces are the horizontal pressure gradient force and the Coriolis force, balancing within a few parts per thousand for space and time dimensions larger than 50 km and a few days, respectively. In the vertical, the only important balance is hydrostatic. Thus, the geostrophic equations may be written as follows:

$$\frac{\partial p}{\partial y} = -\rho f u, \tag{2.135}$$

$$\frac{\partial p}{\partial x} = \rho f v, \tag{2.136}$$

$$\frac{\partial p}{\partial z} = \rho g(\varphi, z), \tag{2.137}$$

where, as before, v is the meridional component, u is the zonal component, and $f = 2\omega \sin\varphi \approx 10^{-4}$ is the Coriolis parameter. Using Eq. (2.134), the geostrophic equations may be reformulated as follows:

$$u = -\frac{1}{f\rho}\frac{\partial p}{\partial y}, \tag{2.138}$$

$$v = \frac{1}{f\rho}\frac{\partial p}{\partial x}, \tag{2.139}$$

$$p = p_0 + \int_{-h}^{H} g(\varphi, z)\rho(z)\, \mathrm{d}z, \tag{2.140}$$

where p_0 is the atmospheric pressure at a level surface $z = 0$ (usually the geoid) below the sea surface, and H is the height of the sea surface above the geoid, i.e., the dynamic ocean topography.

Further, using the Boussinesq approximation, and substituting the vertical geostrophic component into the horizontal components, yields:

$$u = \overbrace{-\frac{1}{f\rho}\frac{\partial}{\partial y}\int_{-h}^{H} g(\varphi, z)\rho(z)\, \mathrm{d}z}^{u_d} - \overbrace{\frac{g}{f}\frac{\partial H}{\partial y}}^{u_s}, \tag{2.141}$$

$$v = \overbrace{\frac{1}{f\rho}\frac{\partial}{\partial x}\int_{-h}^{H} g(\varphi, z)\rho(z)\, \mathrm{d}z}^{v_d} + \overbrace{\frac{g}{f}\frac{\partial H}{\partial x}}^{v_s}, \tag{2.142}$$

where the geostrophic currents have been divided into a deeper current u_d, v_d dependent on density structure, and a surface current u_s, v_s. We observe that the surface geostrophic currents are dependent on the slope of the sea surface, see Figure 2.34. The slope of the MDT, as measured by altimetry (Section 2.5.5), will give surface geostrophic currents, which, in terms of geodetic coordinates, can be formulated as:

$$u_s = -\frac{g}{fR}\frac{\partial H}{\partial \varphi}, \tag{2.143}$$

$$v_s = \frac{g}{fR\cos\varphi}\frac{\partial H}{\partial \lambda}, \tag{2.144}$$

where R is Earth's mean radius.

What we have so far is that wind stress causes an Ekman flow in the uppermost part of the ocean, which, in turn, causes the sea surface to slope, inducing a geostrophic

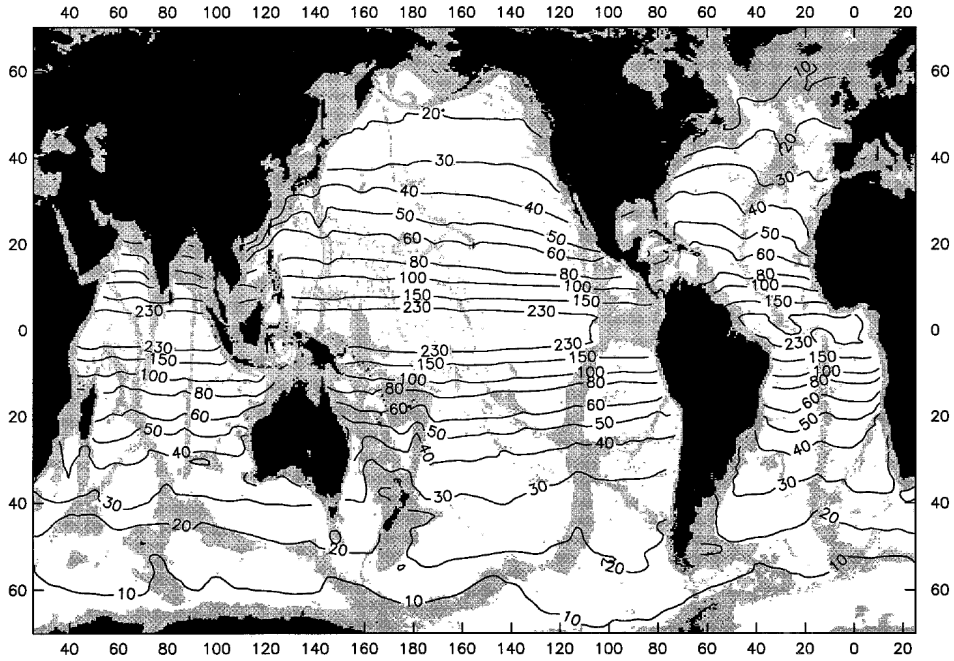

Figure 2.35: Global $1° \times 1°$ map of the baroclinic Rossby radius of deformation in km. Taken from Chelton et al. (1998).

flow that drives the major ocean circulation patterns. The reason why wind stress can produce large-scale oceanic circulation is that only a small change in the slope of the sea surface is needed in order to induce a considerable current flow (Stewart, 2008). If we suppose that the sea surface varies with only $\Delta H = 1\ \mathrm{m}$ across a distance of around $L = 1000\ \mathrm{km}$ (a slope that is measurable by satellite altimeters in space, see Section 2.5), the magnitude of the current that is produced is

$$u_s \approx \frac{g}{f}\frac{\Delta H}{L} = \frac{9.8}{10^{-4}}\frac{1}{10^6} \approx 10\ \mathrm{cms}^{-1}, \tag{2.145}$$

which is a significant and measurable current velocity. In fact, the typical dynamic topography varies between $\pm 1\ \mathrm{m}$, which is one part-per-hundred of the geoid variation (see Figure 1.3).

In the beginning of this section, it was mentioned that the geostrophic balance is relevant on spatial scales of several tens of kilometers and temporal scales of several days. We have seen that the geostrophic flow is not in the direction of the pressure gradient, but rather at right angles to it, along contours of constant pressure. This, however, does not happen instantly in time, but rather the flow will initially be di-

rected toward the pressure gradient, and as the velocity increases, the Coriolis force will increasingly deflect the velocity vector until it is perpendicular to the pressure gradient. Then we have geostrophic equilibrium. The distance traveled to reach this equilibrium is known as the Rossby radius of deformation (Rossby, 1938). In other words, the Rossby radius is the length scale at which geostrophic currents become important. Generally, for a one-layered ocean, the Rossby radius is large >1000 km, and not suitable for small-scale geostrophic flows. If we consider a more realistic baroclinic, two-layer stratified ocean instead, with, e.g., relatively warm water lying over colder (and denser) water, we get a baroclinic Rossby radius of

$$R = \frac{\sqrt{g'h}}{f}, \tag{2.146}$$

where g' is the reduced gravity $g' = g\delta\rho/\rho$, $\delta\rho$ is the density difference between the two layers, and h is the thickness of the upper layer. The Rossby radius of deformation is thus reduced to about 1/50 of its original value (Rossby, 1938). We also note that Eq. (2.146) includes the Coriolis parameter and thus varies with latitude, which was studied in detail by Chelton et al. (1998), see Figure 2.35. Note that for the study area of this research, the baroclinic Rossby radius is < 10 km. This spatial scale is far less than that of any satellite-based geoid, suggesting the use of a higher-resolution regional geoid model instead.

2.6.5 Mean dynamic topography from hydrography

Until the MDT could be determined by satellite altimetry, the only way to describe the general ocean circulation was through hydrographic measurements of temperature and salinity from ships (Pugh and Woodworth, 2014). Returning to Section 2.6.4, the first terms in the geostrophic eqs. (2.141), (2.142), represent the deeper geostrophic flow. We know that density varies with depth, and so they form the baroclinic component of the flow. To compute them, we must turn to hydrographic measurements and use the equation of state. Pressure is then computed by Eq. (2.140), but in order to do this, we need to know the pressure at the reference surface z =0. It is impossible to measure pressure on the geoid surface, but we can measure the distance between two surfaces of constant pressure, thus the relative deeper geostrophic current may be computed.

In oceanography, calculation of pressure gradients is done along geopotential surfaces (Stewart, 2008). For example, the geoid is a level surface of Earth's gravity field, and a surface of constant potential. The work required to move a mass m a vertical distance z is mgz. The change of potential per unit mass is gz. Geopotential

surfaces are not at fixed heights in the atmosphere since gravity is not constant, and therefore the geopotential meter Z was introduced,

$$Z = \frac{\Phi}{9.80}, \qquad \Phi = \int_0^z g \, \mathrm{d}z, \tag{2.147}$$

where Φ is the geopotential. The geopotential meter is defined analogous to the dynamic height in geodesy, see Section 2.4.4.

The steric height is the distance a column of water between depth z_1 and z_2 would rise if temperature and salinity were changed from their standard values (T =0° C, S =35) to the observed ones (Stewart, 2008). The weight of the water remains the same during the expansion, so Δp remains the same. Thus it is the distance between two surfaces of constant pressure:

$$h(z_1, z_2) = \int_{z_1}^{z_2} \delta(T, S, p) \rho_0 \, \mathrm{d}z, \tag{2.148}$$

where ρ_0 is a reference density and $\delta(T, S, p)$ the specific volume anomaly:

$$\delta(T, S, p) = \frac{1}{\rho} - \frac{1}{\rho_0} = \frac{1}{\rho(T, S, p)} - \frac{1}{\rho(0, 35, p)} \approx \frac{\rho_0 - \rho(T, S, p)}{\rho_0^2}, \tag{2.149}$$

where ρ and ρ_0 are determined from the equation of state. The geopotential anomaly between two surfaces of constant pressure is

$$\Delta\Phi = \int_{p_1}^{p_2} \delta(T, S, p) \, \mathrm{d}p. \tag{2.150}$$

The geostrophic surface currents are then proportional to the gradients of the geopotential anomaly (or the steric height) (Stewart, 2008). At any point in the ocean the dynamic height relative to a given pressure surface can be computed. However, we need a reference surface with known pressure in order to perform the integration in the above equation. Deep ocean observations have revealed that, at depths of 1000 to 2000 km (≈1000 to 2000 dbar), the ocean flow is mostly barotropic. This means that a level surface at 2000 km can be treated as a level of no motion; there is no pressure gradient, thus we have a surface of constant pressure, and $u, v = 0$. Geostrophic currents may then be computed relative to a level of no motion. However, if we know the currents at some level, e.g., the surface geostrophic currents from satellite altimetry, it is better to compute geostrophic currents at depth relative to this level.

2.6.6 In situ observation of ocean currents

Both Lagrangian and Eulerian methods exist for observing ocean currents (Stewart, 2008). Lagrangian methods measure the position of a water parcel, while Eulearian methods measure the flow velocity past a fixed point.

Lagrangian observation of ocean currents is done with the aid of:

- Surface drifters, computing a time-mean of the current velocity over some traveled distance divided by the specified time period. Typically the positioning of the drifters is done by satellite systems like ARGOS or GNSS. Errors are due to the drifter failing to follow the expected flow along a parcel of water (due to, e.g., wind), drifter positioning error, and the sampling error (as drifters tend to go towards convergent zones.
- Sub-surface floats, where the widely used ARGO floats are the best examples, see Figure 2.36. The float positions alter between the ocean surface and some preset depth, usually of about 1 km. They stay below the surface for some 10 days, and then rise to the surface. While rising, they measure profiles of salinity and temperature as a function of pressure, and when they reach the surface, the data are relayed to the shore via the ARGOS system.
- Tracers for measuring the deep ocean currents. These are molecules (e.g., the chemical tracer tritium) not normally present in the water parcel, and are tracked by measuring their concentration in water samples collected in hydrographic surveys.

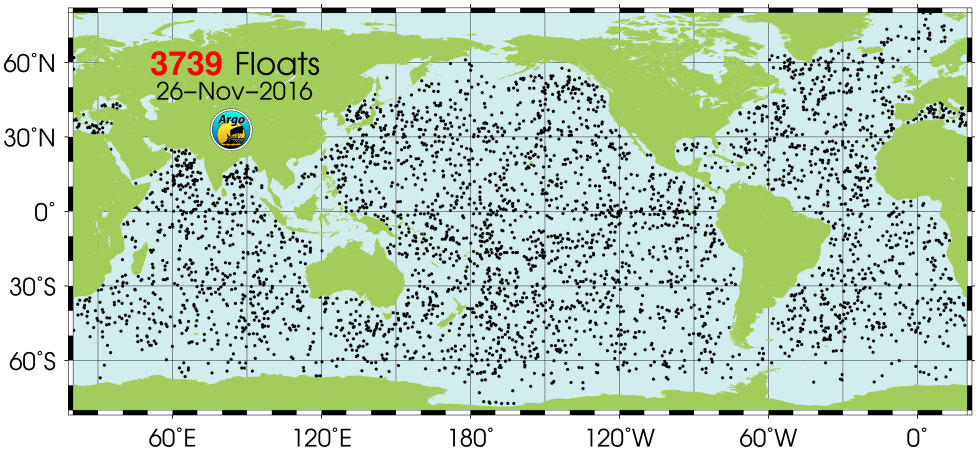

Figure 2.36: Distribution of ARGO floats as of November 26, 2016. Taken from `http://www.argo.ucsd.edu/`.

Eulerian observation of ocean currents is usually done by instruments moored (anchored by wire) to the sea floor, where the mooring is kept straight by some kind of float. The instruments may be current meters or CTDs, attached to the wire at multiple depths. The moorings are deployed and recovered by ships, and are usually operative for a few months to over a year. Unfortunately, moorings are quite expensive, and are easily destroyed, e.g., when strong currents affect the floats.

Chapter 3

Results and discussion

3.1 Regional geoids based on GOCE

In **Paper A**, two of the fifth release (R5) of GOCE satellite-only GGMs, TIM5 and DIR5, were combined with the already existing NMA2014 regional geoid model for Norway using the filter-combined approach with the Gaussian mean kernel (Section 2.3). NMA2014 is based on the fourth-release GOCE DIR4 GGM and was computed using the Wong and Gore kernel modification (Wong and Gore, 1969), with a linear transition of the weighting between spherical harmonic degrees 130 and 140. Eight filter-combined solutions were computed for filter radii between 40 and 110 km at 10 km intervals, and validated externally in terms of standard deviations of differences to a set of 1,344 GNSS/leveling points. An optimal filter radius of 80 km was found for both TIM5+NMA2014 and DIR5+NMA2014, see Figure 3.1. Table 3.1 shows the validation results. Effectively "replacing" DIR4 with TIM5/DIR5 in NMA2014 reduces the standard deviation of differences to GNSS/leveling from 3.5 cm to 3.1 cm. The improvement due to the advent of GOCE is seen by comparison with the pre-GOCE EGM2008 GGM at 4.6 cm.

The Gaussian kernel is a basic way of weighting terrestrial and satellite data, as it does not take the data quality into account. **Paper F** extends the investigation of the filter-combined approach to regional geoid enhancement. Several regional geoid models were computed by applying different kernel modifications for the optimal combination of GOCE and terrestrial gravity data. In this study the DIR5 and GOCO05s R5 GGMs were used, and the terrestrial information was still represented by NMA2014. In addition to the Wong and Gore and Gaussian deterministic kernels, the stochastically optimal Wenzel kernel (Eq. (2.77)) was used. In addition, a few older pre-GRACE and pre-GOCE geoid models, as well as the recent European geoid model EGG2015 were included in the validation with GNSS/leveling.

The spectral combination technique requires knowledge of the error degree variances of both the GGM and the terrestrial data. It is further assumed that both data sets have homogeneous and isotropic error characteristics, and that the errors of both

Table 3.1: Validation of different geoid models with respect to GNSS/leveling data in Norway. The pure GOCE DIR5 and TIM5 geoid model results are shown to quantify the omission error due to their limited spatial resolution. All modified solutions are combinations of either TIM5, DIR5 or GOCO05s with NMA2014. Results from **Paper A** and **Paper F** are combined in this table, bearing in mind that a slightly smaller subset of the original 1,344 GNSS/leveling points was used in the latter analysis.

Geoid model	type of modification	$\hat{\sigma}$ (cm)
	Paper A	
TIM5	–	28.23
DIR5	–	27.37
EGM2008	–	4.64
NMA2014	–	3.49
TIM5	Gauss (80 km)	3.07
DIR5	Gauss (80 km)	3.07
	Paper F	
NKG96	–	8.48
NKG2004	–	5.91
EGG2015	–	3.43
NMA2014	–	3.41
DIR5	Gauss (80 km)	2.98
DIR5	mbm (2.0 mGal)	2.93
DIR5	mbm (1.0 mGal)	2.94
DIR5	mbm (0.2 mGal)	3.10
DIR5	Wong and Gore	3.11
GOCO05s	Gauss (80 km)	3.00
GOCO05s	mbm (2.0 mGal)	2.94
GOCO05s	mbm (1.0 mGal)	3.01
GOCO05s	mbm (0.2 mGal)	3.12

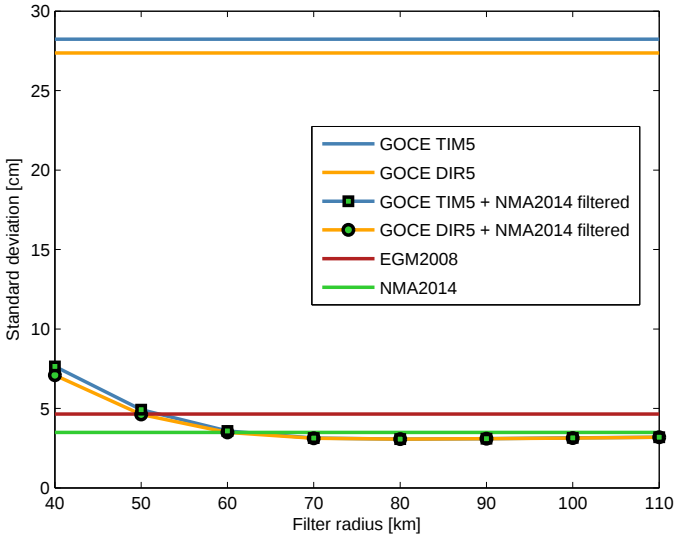

Figure 3.1: Validation of pure and combined geoid models using varying filter radii, by comparison with observed geoid heights at 1,344 GNSS/leveling benchmarks in Norway.

are uncorrelated. Realistic error descriptions for the terrestrial data are unfortunately often not available. In **Paper F**, the error of NMA2014 was approximated by the error covariance function of EGG2008 (noting that, as EGG2008 and NMA2014 are already combined models, the assumption of no correlation is not strictly met). The error degree variances of the GOCE GGMs were obtained by scaling the m-block approximated (Gerlach and Fecher, 2012) error variance-covariance matrix (mbm) to fit the average variance in the region of interest.

Figure 3.2 shows the cumulative geoid height errors for a selection of the geoid models, which reflect their formal errors. Table 3.1 shows the empirical errors in the form of validation results to GNSS/leveling. Although the different stochastically filtered GOCE-based geoids vary only slightly around 3 cm, there is a tendency that filter-combinations that put more weight on GOCE than on the terrestrial gravity data are the best. Considering the older geoid models, the results show that GRACE and GOCE have substantially improved the geoid over the last decade, with a drop from 8.5 cm (pre-GRACE) to about 3 cm (GOCE) in terms of standard deviations of differences to GNSS/leveling. However, part of the improvement is also due to upgraded terrestrial databases. The formal geoid errors are lower and show larger variations depending on the filter-combination method than the empirical errors from the GNSS/leveling validation, which suggests that the empirical error is

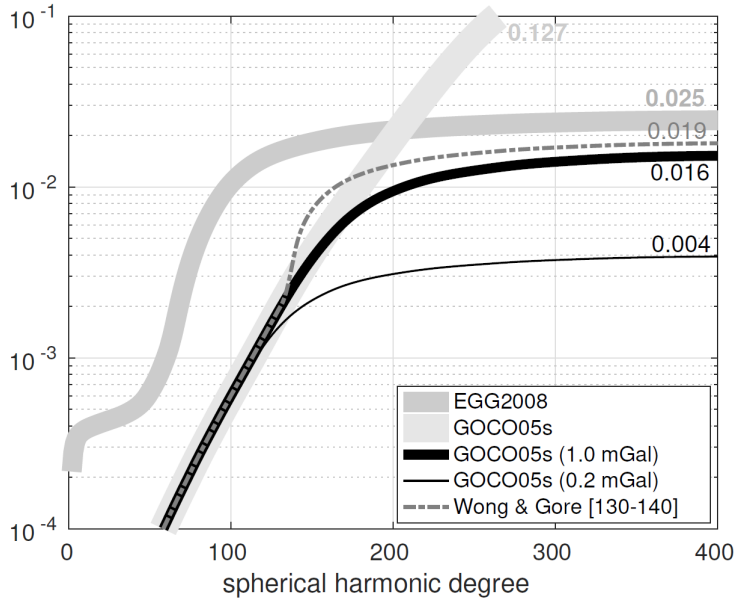

Figure 3.2: Cumulative geoid height errors for different geoid solutions in units of m.

dominated by the quality of the GNSS/leveling data. Our formal error budget indicates that EGG2015 has been optimized to a different validation data set than the Norwegian one. EGG2015 assumes a rather optimistic terrestrial data error of 0.2 mGal, whereas for the Norwegian data set, an error of around 2.0 mGal seems more realistic.

3.2 Geodetic MDT and geostrophic surface currents

Paper A is a benchmark study which compared geodetic and ocean MDTs pointwise using a suite of regional geoid models, altimetry data sets, numerical ocean models, as well as TG data. The analysis concerned point values because the study focused on TGs and along-track altimetry data (which are point values). Instead of interpolating along-track altimetry to the TGs, altimetry observations "close to" the TGs were chosen, but still within the altimetry track. Two altimetry sites per TG were chosen by plotting each TG and nearby altimetry tracks, and choosing sites where all tracks cross, thus containing observations from all altimetry products (at VIKE, only one such altimetry site could be found). All model grids used were interpolated to the TG and altimetry sites. The data sets are summarized in Table 3.2, and the TG and altimetry sites are shown in Figure 3.3.

Table 3.2: Overview of data sets used in **Paper A**, **Paper D** and **Paper E**. TIM5 and DIR5 are combined with the DIR4-based NMA2014. TG data have been obtained from PSMSL (Section 2.4.6) and the Norwegian Mapping Authority (NMA).

Paper	Data set	Coverage	Time Period	Note
		Geoid		
A	TIM5	Regional	–	Gauss (80 km)
	DIR5	Regional	–	Gauss (80 km)
	NMA2014	Regional	–	Based on DIR4
	EGM2008	Global	–	
E	NMA2014	Regional	–	Based on DIR5
	NKG2015	Regional	–	
	EGG2015	Regional	–	
		TG		
A	PSMSL and NMA	19 TGs	1996-2000	Annual/hourly, NN1954 Annual/hourly, NN2000
D	NMA	22 TGs	2010-2014	10-minute, relative
E	PSMSL	19 TGs	2012-2015	Monthly, NN2000
		Altimetry		
A	Jason-2	21 sites	1996-2000	Only south of 66°N
	PISTACH Red3	21 sites	1996-2000	Only south of 66°N
	PISTACH Ocean3	21 sites	1996-2000	Only south of 66°N
	Envisat	37 sites	1996-2000	
	CTOH	37 sites	1996-2000	
	DTU13MSS	Global	1993-2012	
D	CryoSat-2	45 km around TG	2010-2014	SARIn
	SARAL/AltiKa	Tracks 85 and 360	2013-2016	
	Envisat	Tracks 775 and 390	2010-2012	Phase C
	Jason-2	Tracks 163 and 246	2010-2016	
	DTU15MSS	Global	1993-2014	
E	CryoSat-2	Regional	2012-2015	LRM, SAR, SARIn
		Ocean		
A	Nemo12	Global	1996-2000	
	NemoQ	Global	1996-2000	
	L-MITf	Global	1996-2000	
	L-MITc	Global	1996-2000	
	OCCAM12	Global	1996-2000	
	POLCOMS	Regional	1996-2000	Only south of 65°N
E	NorKyst800	Regional	2012-2015	

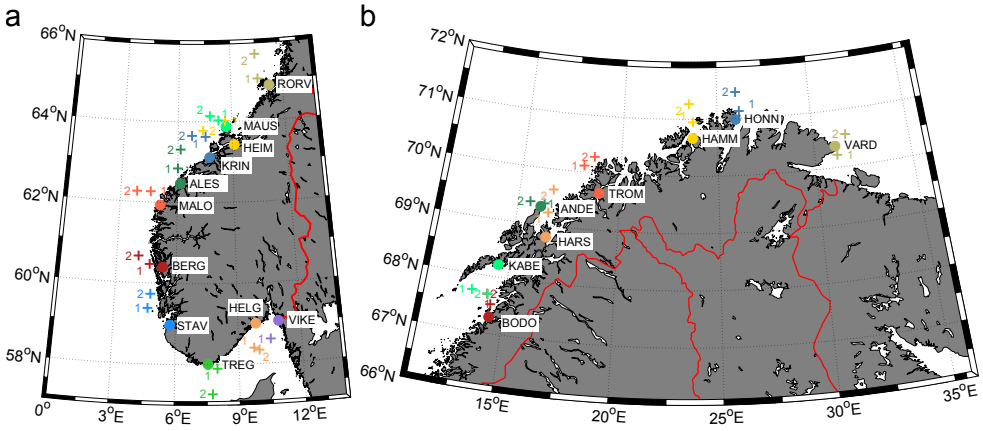

Figure 3.3: TG MSL (dots) and altimetric MSS (plus signs) (a) south of 66°N and (b) north of 66°N.

We find that geodetic and ocean MDTs agree on the ~3-7 cm level at the TGs, and on the ~5-11 cm level at the altimetry sites. Figure 3.4 shows ocean and geodetic MDT profiles at the TGs, where we observe a characteristic pattern of a 10 cm rise of MDT towards Kabelvåg, a flattening towards Stavanger, and another 10 cm rise towards Viker. Considering the TG geodetic MDTs, where the ellipsoidal height of MSL is derived using the alternative approach (Section 2.4.6), results improve when using data based on the new national height system NN2000.

Figure 3.5 shows Taylor diagrams, where the best-performing ocean MDT based on Nemo12 was chosen as reference model against which all other MDTs were compared. They nicely summarize the results. The pointwise monomission altimetry products (Jason-2 and Envisat) give results comparable with the multimission DTU13MSS grid on the ~5 cm level. However, the coastal altimetry products (Jason-2/PISTACH and Envisat/CTOH) generally do not offer an improvement over the conventional products they are based on. In general, geodetic MDTs correlate with the Nemo12 ocean model on a similar level as the other ocean models, suggesting a convergence of approaches.

Furthermore, error estimates for both geodetic and ocean MDTs were derived, relating the empirical standard deviation of the MDT budget (Eq. (1.2)) to the MDT error budget (Eq. (1.3)). Depending on whether or not we assume equal error contributions from ocean MDT, ellipsoidal height of MSS/MSL, and geoid, we get the following error estimates:

- Ocean MDT: ≤5 cm

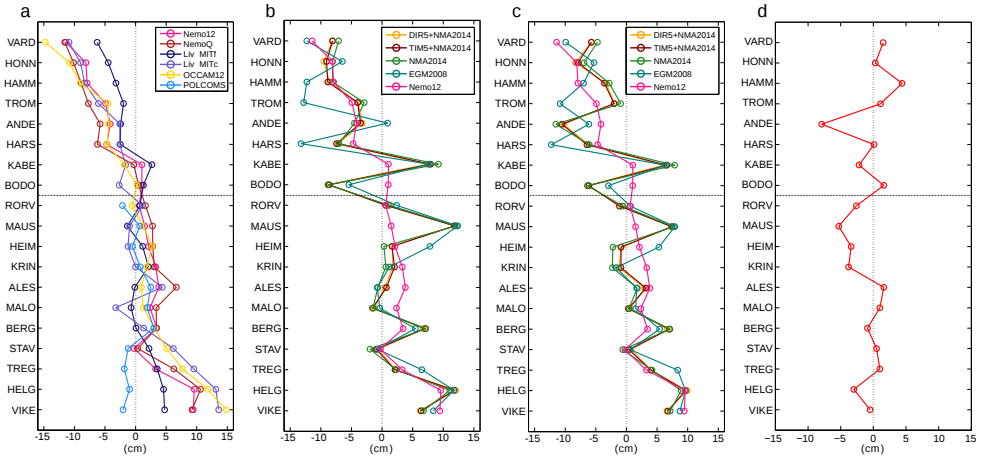

Figure 3.4: TG MDT profiles: (a) ocean, (b) geodetic, using NN1954-originated ellipsoidal heights of MSL, (c) geodetic, using NN2000-originated ellipsoidal heights of MSL, and (d) the difference between NN1954-originated and NN2000-originated MDT. In Figures 3.4b and 3.4c, Nemo12 is included. The horizontal dashed line denotes 66°N. In all cases, the profile mean has been removed.

- Altimetric MSS: $\leq$7 cm
- TG MSL: $\leq$3 cm
- Geoid: $\leq$4 cm

The results of **Paper A** are shown to be statistically significant. From Figure 3.5b we can infer signal standard deviations of the altimetric MDTs of $\sim$7 cm, which together with our altimetry error estimates gives a signal-to-noise ratio (SNR) of 1-3. At the TGs (Figure 3.5a), the signal standard deviation is $\sim$6 cm, which together with the TG error estimates again gives a SNR of 1-3. In addition, the correlations in Figure 3.5 are significant on the 99% level, as confirmed by a correlation significance test.

Paper D can be seen as an interlude between **Paper A** and **Paper E**. It evaluates the performance of new-generation SAR altimetry in the Norwegian coastal zone, where CS2 delivers new coastal altimetry data over areas previously uncovered by conventional altimetry. Relative sea level observed by CS2 in a 45×45 km area

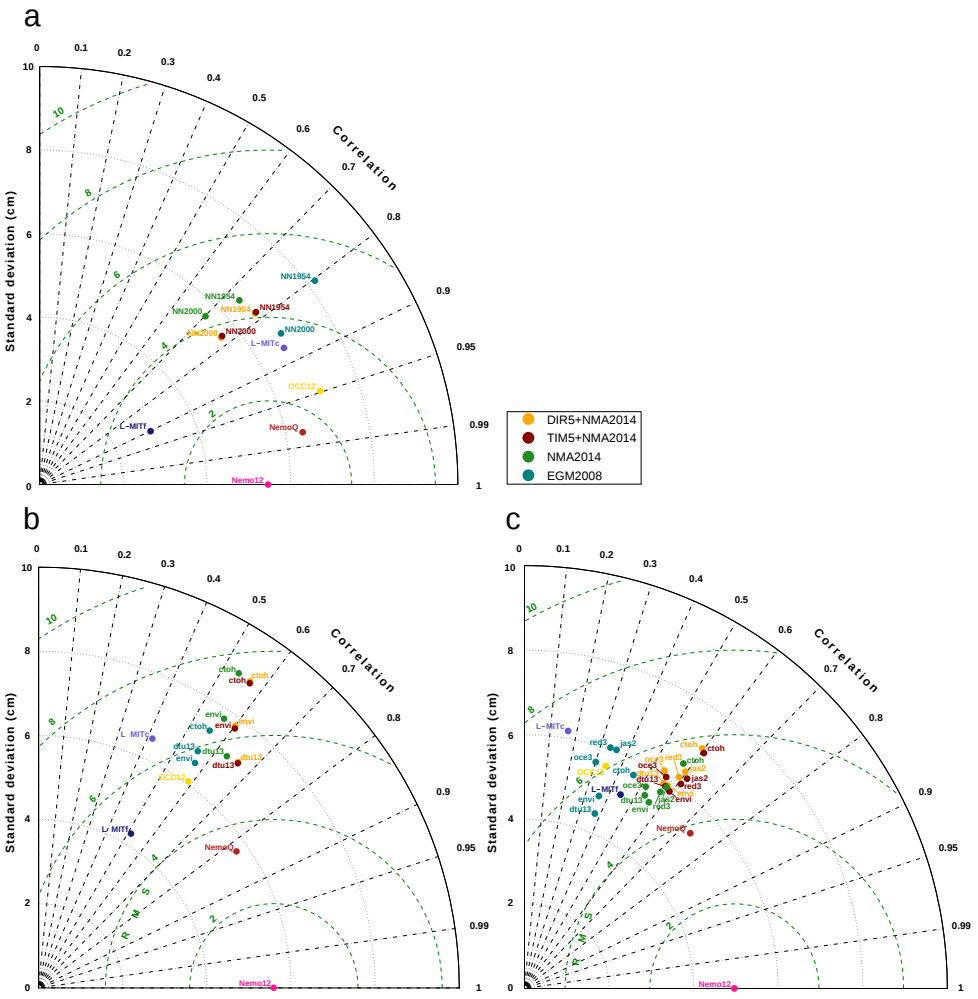

Figure 3.5: Taylor diagram intercomparison of geodetic and ocean MDTs for TGs (a) along the entire Norwegian coast, altimetric MSS sites (b) along the entire Norwegian coast, and (c) south of 66°N. To ease readability, labels for the geoid models incorporated in the geodetic MDTs have been left out of the diagrams, but can be found in the legend.

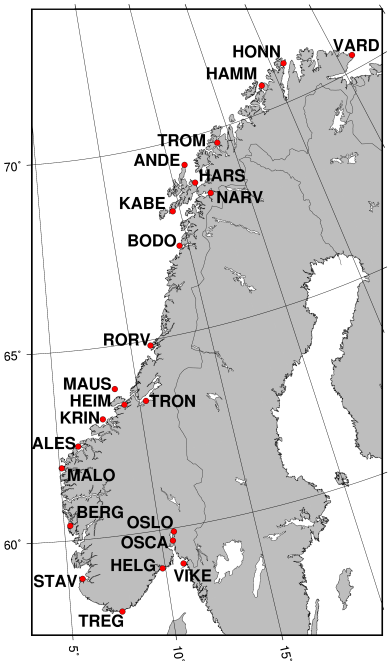

Figure 3.6: TGs on the Norwegian mainland used in **Paper D**, with the exception of NARV, which was left out due to few altimeter observations.

around each TG was compared with TG observations with a high 10-minute temporal resolution. The data sets used in this study are listed in Table 3.2, and the 23 TGs on the Norwegian mainland shown in Figure 3.6. Generally, CS2 agrees well with the TGs. We observe larger standard deviations of differences at TGs well inside fjords with relatively few CS2 observations (~20 cm or more), and smaller differences at TGs close to the open ocean with dense CS2 observations (~7 cm). When replacing the standard ocean tide and atmospheric corrections with local corrections derived from ocean tide predictions and pressure observations, we observe a 2-5 cm improvement in standard deviations of differences at 19 out of 22 TGs. In terms of standard deviations of differences to the STAV TG, CS2 shows an improvement of ~3 cm over conventional altimeters.

Paper E is a natural extension of **Paper A**, and builds upon the experiences with CS2 in **Paper D**. Table 3.2 summarizes the data sets that are used in this study; three new GOCE-based regional geoid models NKG2015, EGG2015, and NMA2014 (now an updated version of NMA2014 based on DIR5) as well as CS2 data were used to determine coastal MDT surfaces ($\mathrm{C2}_{\mathrm{NKG}}$, $\mathrm{C2}_{\mathrm{EGG}}$, and $\mathrm{C2}_{\mathrm{NMA}}$) and associated geostrophic surface currents. In turn, these were compared with TG MDT

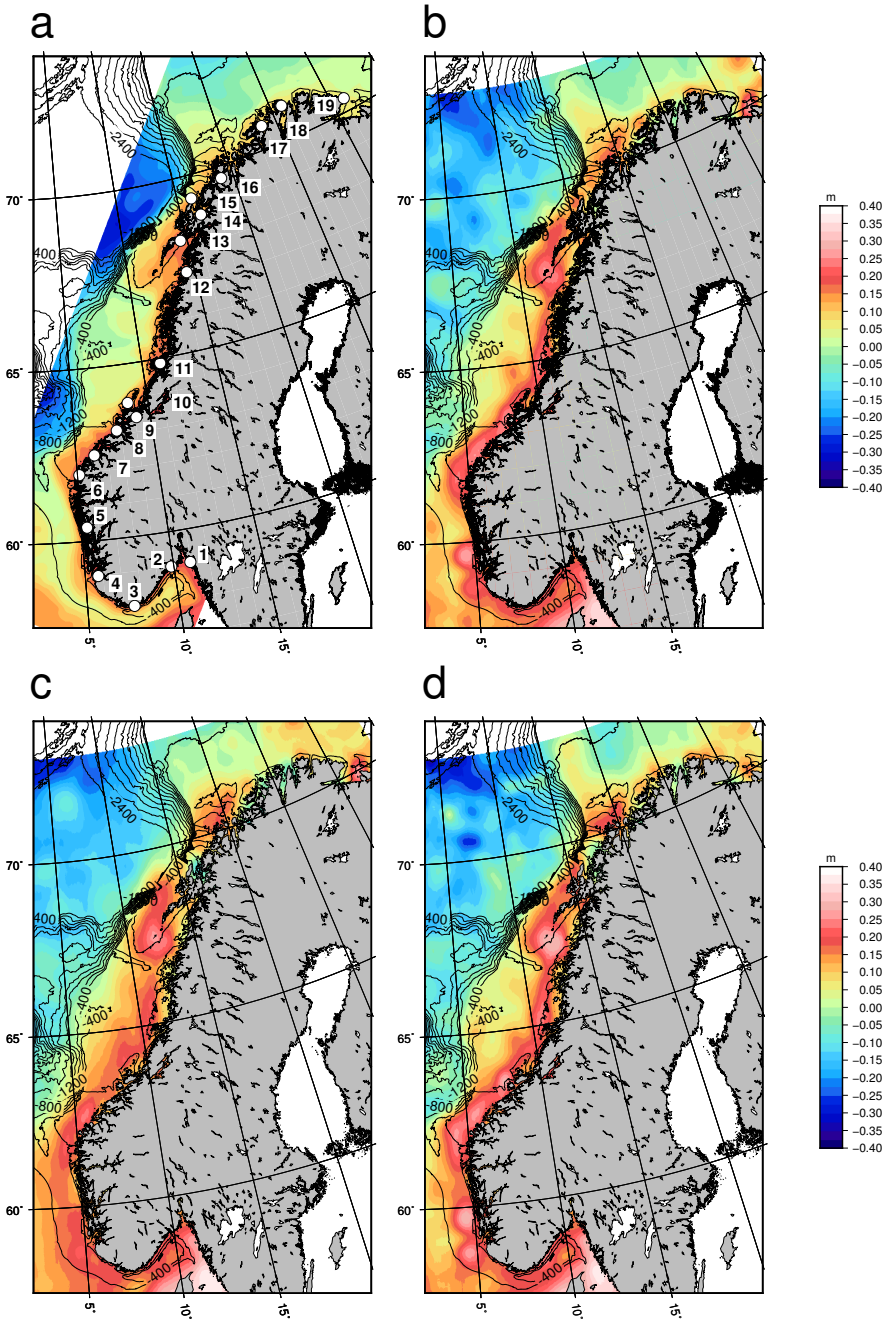

Figure 3.7: Coastal MDTs in Norway; (a) ocean, based on NorKyst800 and geodetic, based on (b) $C2_{NKG}$, (c) $C2_{EGG}$, and (d) $C2_{NMA}$. The mean value has been removed in all cases. The TGs considered in **Paper E** are shown in (a), for which a code is given in Figure 3.8. In all (a-d), 400 m isobaths from the 2014 General Bathymetric Charts of the Oceans (GEBCO) (Weatherall et al., 2015) grid are shown.

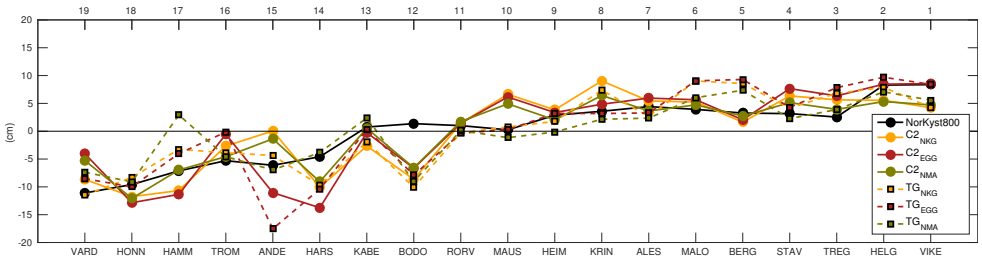

Figure 3.8: Tide-gauge MDT profiles using geodetic and ocean estimates, arranged from north to south. For all profiles the mean value has been removed. TG codes and IDs are given on the bottom and top x-axis, respectively.

estimates and the independent high-resolution numerical ocean model NorKyst800. The coastal MDTs are shown in Figure 3.7, where we observe that the CS2 MDTs are generally consistent with NorKyst800. The general pattern of the Norwegian Sea circulation (Figure 1.2) is evident in all MDTs; we can trace the NwASC northward and observe its branching at the BSO around 72°N, as well as the NCC originating in the Baltic Sea around 58°N flowing northwards along the coast all the way to its final destination in the Barents Sea.

$\mathrm{C2_{NKG}}$ and $\mathrm{C2_{NMA}}$ show standard deviations of differences of ~6 cm to NorKyst800, while the $\mathrm{C2_{EGG}}$ shows a slightly larger difference of ~8 cm. All the geodetic MDTs have areas along the coast where the MDT shows smaller values than expected. The most striking coastal features of $\mathrm{C2_{EGG}}$ and $\mathrm{C2_{NMA}}$ are MDT lows seen in the area between the Lofoten-Vesterålen area and Senja island, roughly at 69°N, between 15-20°E. The lows are at slightly different locations. These features are much less visible in $\mathrm{C2_{NKG}}$, which suggests that they are related to the geoid and not CS2.

Figure 3.8 shows the ocean and geodetic MDT profiles at the TGs. Much in accordance with the findings in **Paper A**, the profile obtained from the ocean MDT is smoother compared to the geodetic MDT profiles obtained from TGs and CS2. The same general pattern of a 10 cm rise towards Kabelvåg, a flattening towards Stavanger, and another 10 cm rise towards Viker can be observed. Moreover, we observe the largest differences in the Lofoten-Vesterålen area. The CS2 MDTs agree on the ~3-5 cm level with both TG and ocean MDTs. Figure 3.8 also reveals a polarization of TG and CS2 MDTs at some sites, which can hint on whether the observed discrepancy to NorKyst800 is due to errors in the geoid or in the CS2 observations. For example, at HONN, MAUS, and STAV, the TG MDTs agree more with NorKyst800 than the CS2 MDTs, while the converse holds true at BERG. The first case suggests that the CS2 MDTs are off due to errors in the CS2 observations

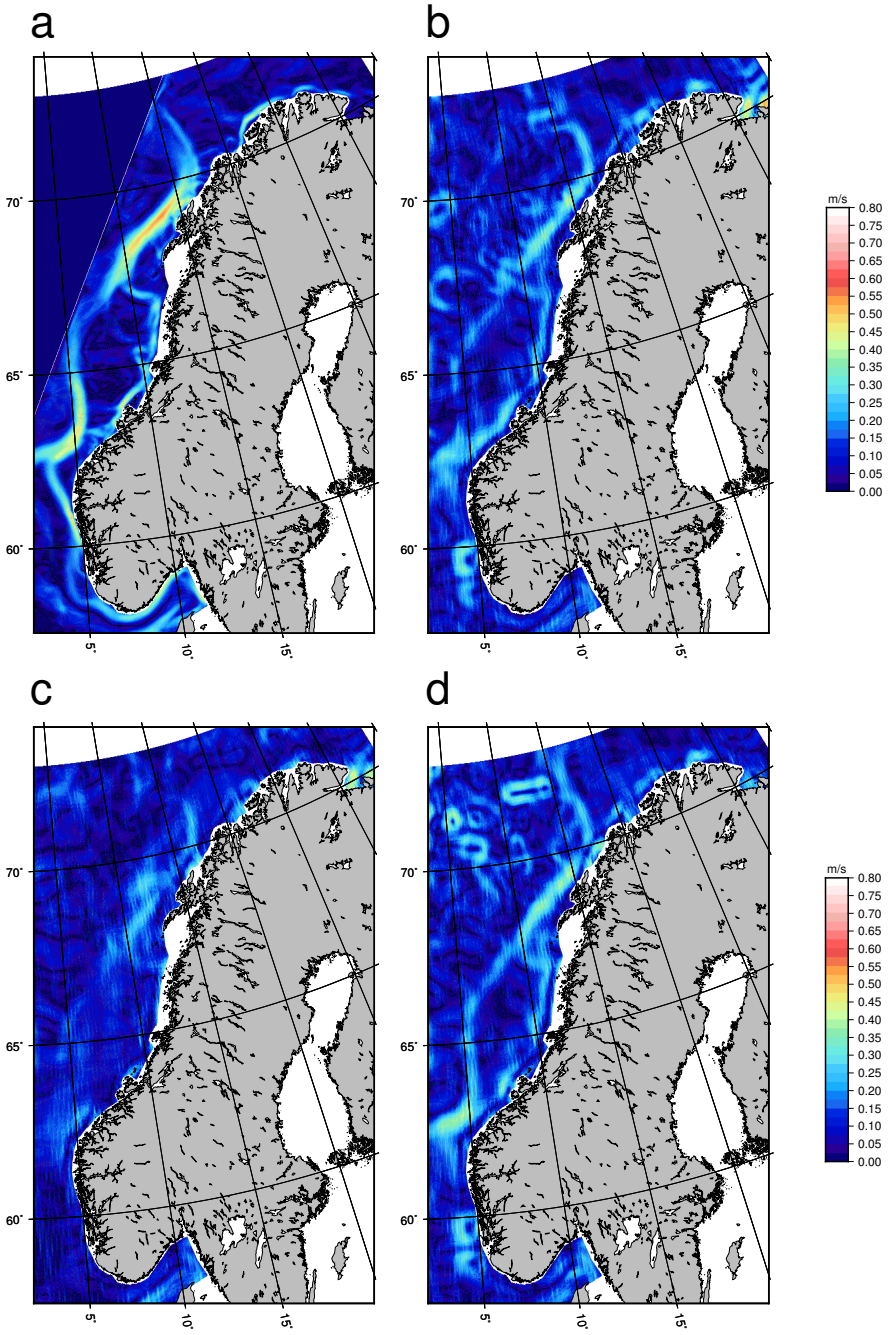

Figure 3.9: Geostrophic ocean surface currents derived from (a) NorKyst800, (b) $C2_{NKG}$, (c) $C2_{EGG}$, and (d) $C2_{NMA}$. Areas not relevant to the geostrophic assumption, at the coast or inside fjords, have been masked out.

and rather than geoid errors, while the latter case suggests there could be an error in the ellipsoidal height of MSL. Notably, at BODO, all geodetic MDTs show a ∼10 cm disagreement with NorKyst800, which suggests there could be a geoid-related error.

Figure 3.9 shows the geostrophic velocity fields, derived by applying Eqs. (2.143) and (2.144) to all MDTs. Prior to the differentiation, the MDTs were filtered using a Gaussian kernel with a filter with of 12 km. The general pattern of the Norwegian Sea circulation is evident in NorKyst800, $\mathrm{C2_{NKG}}$, and $\mathrm{C2_{NMA}}$. We can trace the NwASC northward and observe its branching at the BSO, as well as the hot spots at Svinøy around 62.5°N and the Lofoten-Vesterålen area, and continuing towards its final destination in the Barents Sea. We observe the strongest currents in NorKyst800, which is highly correlated with the bathymetry. $\mathrm{C2_{NMA}}$ and $\mathrm{C2_{NKG}}$ both show reasonable current patterns and reveal the NCC, albeit the less visible narrow jet along the south-eastern coast. Apart from the Lofoten-Vesterålen hot spot, the circulation pattern is more or less absent in $\mathrm{C2_{EGG}}$.

3.3 Comparison of methods for regional geoid computation

LSC and the more modern RBF approaches offer a higher degree of versatility and data adaptation possibility than the classical Stokes approach. **Paper C** presents a theoretical and numerical comparison of the three methods, demonstrating their equivalence. It does not present new theory, but is a first attempt to compare the three methods both theoretically and numerically in a unified framework. The theoretical equivalence of Stokes's formula, LSC, and RBFs was reviewed in the global case, where it was seen that the SKs are equivalent with the covariance function of LSC in the theoretical limit case where the distribution of SKs becomes continuous. Their theoretical equivalence was also investigated in regional applications, where the Stokes integration is restricted to a spherical cap around the computation point (Section 2.3.4). de Min (1995) has shown that if LSC is not applied globally, its result will be different from Stokes's formula, because an unwanted extrapolation outside the cap takes place. If the cross-covariance function is modified by introducing the Molodensky truncation coefficients,

$$\bar{\mathrm{C}}_{Pi}^{Ng} = \sum_{n=2}^{\infty} \frac{R}{2\gamma} \left[\frac{2}{n-1} - Q_n(\psi_0) \right] c_n^g P_n(\cos\psi_{Pi}), \tag{3.1}$$

LSC and Stokes's formula are again equal. As SKs are equivalent to LSC, they have to be modified correspondingly to give equal results as Stokes's formula. The

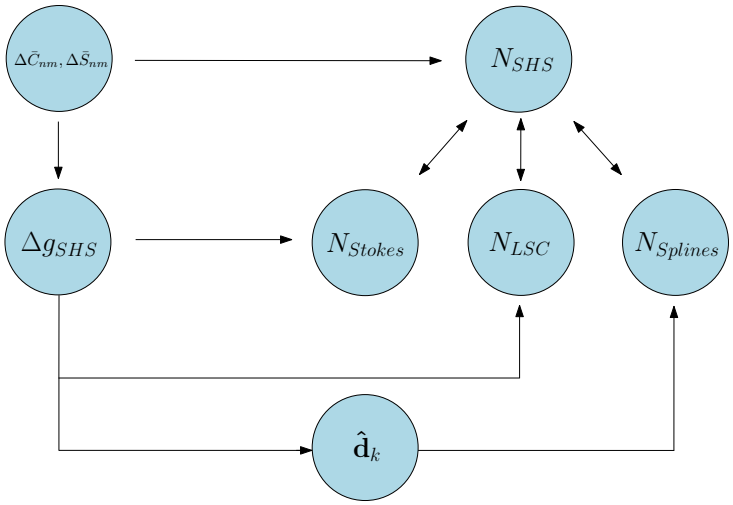

Figure 3.10: Schematic of the closed-loop simulation. Stokes's formula, LSC, and SKs are compared with a reference solution, to which they all should be equal. Thereby, we check not only whether the methods are internally consistent, but also whether the methods are actually correct.

Molodensky truncation coefficients were introduced in the SKs in the synthesis step (Eq. (2.66)). Then, the elements of $\mathbf{A}^N$ are given as follows,

$$A_{Pk}^N = \sum_{n=2}^{\infty} \sqrt{2n+1}/(4\pi R^2)\lambda_n^N \left[1 - \frac{n-1}{2} Q_n(\psi_0)\right] B_n^{SK} P_n\left(\cos\psi_{Pk}\right). \qquad (3.2)$$

For more details regarding the theoretical equivalence of the methods, the reader is referred to **Paper C**.

Paper C also includes a few numerical examples. SKs, LSC, and Stokes's formula were compared in a closed-loop environment using synthetic data, see Figure 3.10. Both noise-free synthetic observations (in the form of gravity anomalies Δg) and the true validation geoid were computed by spherical harmonic synthesis using the EGM2008 GGM. To simulate the remove-compute-restore technique, the synthesis was performed for degrees $251 \leq n \leq 2190$, assuming that the long wavelength part of the gravity signal has been removed using a GOCE-based GGM. The Molodensky truncation coefficents were also introduced in the spherical harmonic validation geoid, such that it is equivalent to the geoids computed by the regional methods, which are restricted to a spherical cap with radius ψ_0. For practical computational reasons, the input and output resolutions were set to 5 arcmin, which corresponds to the maximum resolution of EGM2008. The integration cap was set to $\psi_0 = 1^\circ$.

Two regions were considered, the North Sea coastal region of East Frisia, with smooth topography, as well as the mountainous Alpine region, with rough topography. Geoid heights by Stokes's formula were computed using Eq. (2.69), implemented according to Eq. (2.47) using the closed formula for computing Stokes kernel. Geoid heights by LSC were computed using Eq. (3.1) and Eq. (2.57). Considering the SKs, dimensionless spline coefficients were estimated using Eq. (2.63) with Eq. (2.65) and $\mathbf{R} = \mathbf{I}$. Subsequently, the spline coefficients were used to compute geoid heights using Eq. (2.66) with Eq. (3.2). The SKs were developed to degree 2190, corresponding to the maximum resolution of the observations (5 arcmin).

At the 5 arcmin resolution, all methods agree within 2 $\times 10^{-2}$ mm to 5.9 mm in the target areas. The largest RMS differences were obtained with Stokes's formula, suggesting the error could be due to the discretization of Stokes's formula. This was confirmed by setting up the closed-loop simulation at the 2.5 arcmin resolution, where all methods agree within 6 $\times 10^{-2}$ mm to 2.4 mm. Furthermore, because EGM2008 does not contain signal at resolutions beyond 5 arcmin, the discretization error is attributed to the Stokes function and not the gravity data. The Stokes function is evaluated only at each grid point of the input data, instead of evaluating its surface integral over the corresponding blocks. If the resolution increases and the block size decreases, the function value at the grid nodes gives an increasingly better representation of the surface integral.

Finally we investigated what role the number of SKs play in the equivalence of SKs with the other methods. Figure 3.11 shows the RMS difference between spherical harmonic synthesis and SKs for varying number of SKs in the Alpine target area. They have been computed from observations provided on the original 5 arcmin grid. The vertical dotted lines represent the number of observations corresponding to the 5 arcmin and 2.5 arcmin resolutions, while the horizontal dotted line represents the 1-m difference with respect to the spherical harmonic solution. The regularization parameter is kept constant, securing that the only variable in the test is the number of SKs.

We see that in practice, we do not need to reach the theoretical limit case for the SKs to correspond to LSC, as they tend to be identical already for moderate point densities. As we have placed the observations on a 5 arcmin grid, the SKs converge towards LSC when setting the number of SKs equal to the number of observations, because the number of observations is equal to their maximum signal resolution. Consequently there is nothing to gain from increasing the number of SKs beyond 5 arcmin, as seen in Figure 3.11. Our numerical examples thus suggest that the RBF method is similar to spherical harmonics or LSC in case the number of SKs

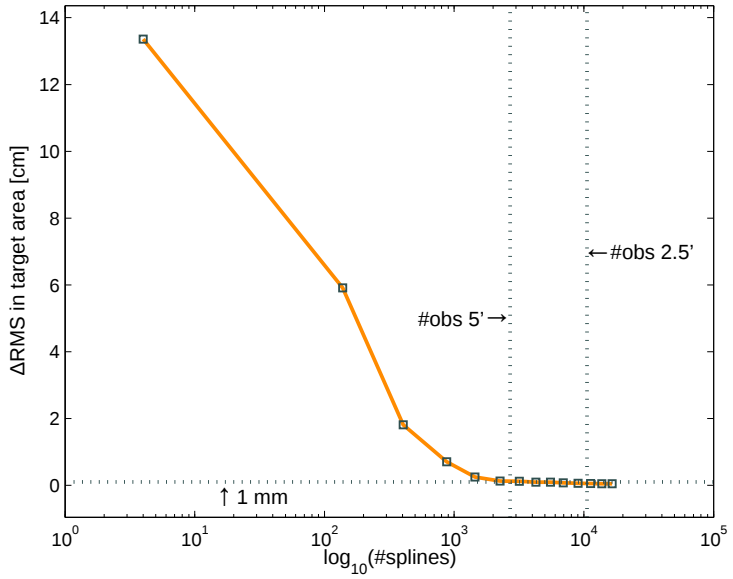

Figure 3.11: Difference between SHS and SKs for varying number of SKs in the Alpine target area, with the regularization parameter kept constant. The signal resolution is 5 arcmin.

corresponds to the signal resolution of the data, independent of the number of observations. By contrast, the size of the auto-covariance matrix to be inverted in LSC corresponds directly to the number of observations and is independent of the signal resolution.

3.4 Temporal variations of the gravity field in Norway

Paper B addresses temporal gravity variations in Norway by compiling and analyzing all FG5 AG observations between 1993 and 2014 at 21 gravity sites in Norway. As the main component of secular vertical land motion in Fennoscandia is due to GIA, we explore to what extent the Norwegian AG observations are applicable for GIA studies. In addition, refined gravitational corrections due to ocean tide loading, non-tidal ocean loading, as well as atmospheric and global hydrological mass variations were computed. Secular gravity trends using both standard ($\dot{g}_0$) and refined ($\dot{g}$) corrections were compared with modeled gravity rates ($\dot{g}_M$) based on a GIA model.

The Norwegian AG network is shown in Figure 3.12, together with a recent GIA model. It should be noted that this Fennoscandian GIA pattern is not strictly correct

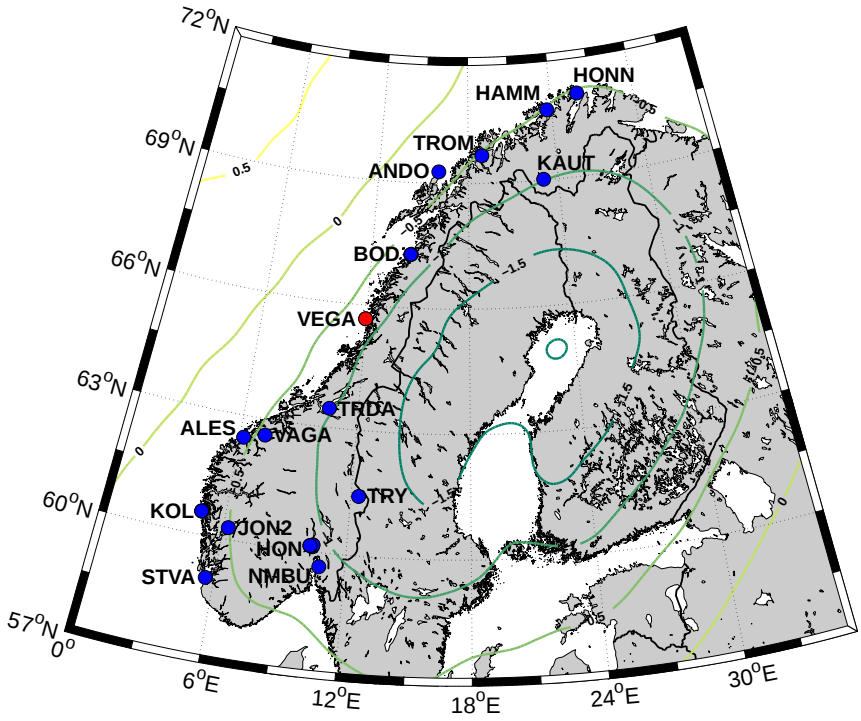

Figure 3.12: AG sites in Norway. Blue sites have been observed more than once. The contour lines show modeled gravity rates (μGal yr^{-1}) from the preliminary NKG2016GIA_prel0306 GIA model; note that while this method of computing $\dot{g}$ is occasionally seen in the literature, it is not strictly correct (P.-A. Olsson and H. Steffen, personal communication, 2016), see text for details.

(P.-A. Olsson and H. Steffen, personal communication, 2016). This is because the gravity rate has been computed with the direct attraction term of Green's function for gravity represented as an internal series (Olsson et al., 2012). Thereby it is assumed that the observation site is located below the attracting masses, giving the direct attraction from the sea with a wrong sign (compare Figure 3.12 herein with Figure 4 of Olsson et al. (2012)). If instead an external series is used for the direct attraction term, a more correct pattern is obtained, see Figure 5 of Olsson et al. (2012), but they recommend to rather compute $\dot{g}$ from height rates of change $\dot{h}$ and a fixed relation between them.

All the FG5-226 observations (~180) were consistently reprocessed using the g9 software (Micro-g LaCoste, 2012), where we aspired to use campaigns from roughly the same time of the year to reduce seasonal effects (e.g., the influence of surface snow cover on gravity). To minimize computational biases, a common processing scheme was adopted, ensuring consistency with respect to model and setup parameters (official site coordinates, polar coordinates, etc.). The Rb frequency standard has been calibrated (compared with a stable reference signal) throughout, and the frequency value closest in time to each observation was used. All gravity gradients measured by NMBU were recomputed and adopted as official gradients. In addition, AG observations by other agencies and FG5 instruments were carefully included into the data set with updated uncertainties.

In addition, refined gravitational corrections due to ocean tide loading (OTL), non-tidal ocean loading (NTL), as well as atmospheric (ATM) and global hydrological (GH) mass variations were computed. The majority of the Norwegian AG sites are located within 2 km of the coast, and may be strongly influenced by OTL and NTL. Standard g9 processing considers OTL only, and uses a global OT model. The spatial resolution of the OT model is gradually refined towards the observation point. A web-service called the OTL provider (`http://holt.oso.chalmers.se/loading/`) does the same gradual refinement, but also checks whether the new grid cell is on land or on sea. A further refinement of the OTL effect was achieved by an in-house software where a higher-resolution coastline is used and an option to replace the OT model with local TG observations. NTL is also computed by the in-house software, by considering actual minus predicted sea level at the nearest TG. For a suite of OT models we identified corrections (OTL+NTL) that reduce the AG set to set scatter the most. Choosing a best-performing model is challenging, as their performance depends on the gravity site, but the NAO99b and FES2012 OT models in combination with a more accurate coastline perform best at 9 out of 14 sites.

If the gravity observation has been reduced for the time-variable tidal and polar motion components, it remains influenced by atmosphere and hydrology. AG observations are typically not corrected for hydrology (Timmen, 2010), but standard g9

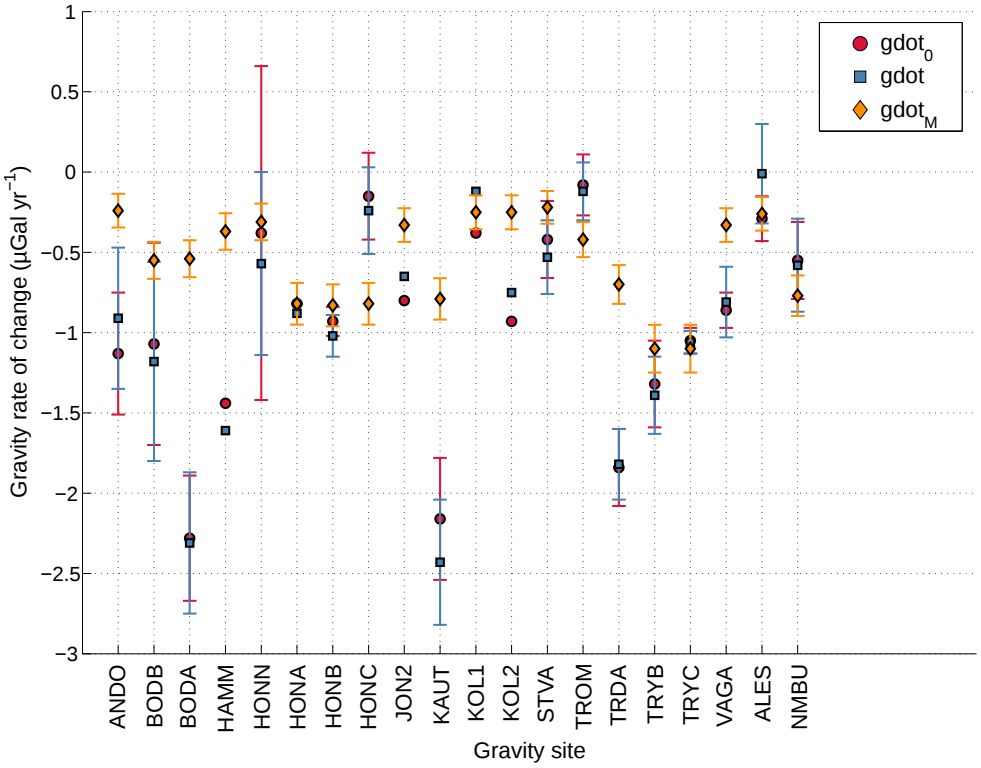

Figure 3.13: Linear rates of change in gravity. $\dot{g}_0$ and $\dot{g}$ are empirical linear gravity rates based on standard and refined gravity corrections, respectively. $\dot{g}_M$ are modeled rates using a recent empirical land uplift model together with a theoretical relation between the gravity and height rate of change for GIA.

processing includes the single-admittance ATM correction, $\Delta g_{\mathrm{ATM}} = A(P_0 - P_n)$, where $A = 0.30\ \mu\mathrm{Gal/hPa}$ is the conventional admittance factor, P_0 is in situ pressure as observed by the FG5 barometer, and P_n is the nominal barometric pressure in accordance with DIN Standard #5450. A refined ATM or GH effect is typically computed by incorporating attraction and load from zones of increasing distance to the gravity site. This is implemented in the novel MATLAB® tool mGlobe (Mikolaj et al., 2016), which was used here. mGlobe relies on global meteorological and hydrological models, but does not include local hydrology because it is not captured by the latter models.

Next, secular gravity trends using both standard and refined corrections were compared with modeled gravity rates based on a GIA model. The modeled gravity rates were computed using $\dot{h}$ from a recent empirical absolute land uplift model (given in ITRF2008) of the NMA, based on a combination of GNSS and leveling (O. Vestøl,

personal communication, 2015), together with a recent modeled relation between gravity and height rates of change $\left(\dot{g}/\dot{h}\right)_M$ of -0.163 $\mu\mathrm{Gal\ mm^{-1}}$ for GIA (Olsson et al., 2015). The uncertainty of $\left(\dot{g}/\dot{h}\right)_M$ was taken to be 0.016 $\mu\mathrm{Gal\ mm^{-1}}$ (H. Steffen, personal communication, 2016), and the uncertainties of $\dot{h}$ were determined as a sum of the observation error and systematic errors due to the reference frame. In turn, the uncertainties of $\dot{g}_M$ were determined by formal error propagation.

Figure 3.13 shows the linear gravity rates $\dot{g}_0$, $\dot{g}$, and $\dot{g}_M$ for all gravity sites, computed by ordinary linear regression (OLR) without weights. With the exception of HONC and TROM, the observed gravity rates are larger than the modeled ones, particularly BODA, KAUT, and TRDA. $\dot{g}$ performs better than $\dot{g}_0$ at 9 out of 20 gravity sites. For the remaining sites, the refined gravity corrections give no significant improvement or even degrade the trend.

Based on the results presented in Figure 3.13, a subset of reliable rates was formed, where a reliable rate is defined as within the uncertainty of $\dot{g}_M$. Thereby, an agreement of $\dot{g}_0$ or $\dot{g}$ with $\dot{g}_M$ gives us confidence in that the empirical rates mainly reflect GIA. The subset contains empirical gravity rates from 10 sites, namely BODB, HONN, HONA, HONB, KOL1, STVA, TRYB, TRYC, ALES, and NMBU. These rates were used in the following comparison of gravity and height rates of change.

The considerable variation in the uncertainties of the empirical gravity rates suggests a weighted linear regression (WLR) approach rather than OLR. This poses a challenge, however, as it is not possible to derive reliable uncertainties for HONA and KOL1, which are only based on two observations. Due to the large error estimates at HONA and KOL1, we investigated both WLR and OLR approaches.

Figure 3.14 shows gravity versus height rates of change using the standard gravity rates $\dot{g}_0$, which yields a WLR of $\dot{g}_0 = -0.135\,(\pm0.100) - 0.142\dot{h}\,(\pm0.018)$ $\mu\mathrm{Gal\ yr^{-1}}$ and an OLR of $\dot{g}_0 = -0.175\,(\pm0.137) - 0.143\dot{h}\,(\pm0.032)$ $\mu\mathrm{Gal\ yr^{-1}}$. Using $\dot{g}$, Figure 3.15 shows a WLR of $\dot{g} = -0.210\,(\pm0.183) - 0.133\dot{h}\,(\pm0.030)$ $\mu\mathrm{Gal\ yr^{-1}}$ and an OLR of $\dot{g} = -0.097\,(\pm0.196) - 0.167\dot{h}\,(\pm0.045)$ $\mu\mathrm{Gal\ yr^{-1}}$. We first note that WLR and OLR based on $\dot{g}_0$ are quite similar, while WLR and OLR based on $\dot{g}$ differ considerably. Considering the constant terms and their relatively large uncertainties, only OLR based on $\dot{g}$ is statistically equal to zero. The regression slopes based on OLR ($\left(\dot{g}/\dot{h}\right)_0 = -0.143\,(\pm0.032)$ $\mu\mathrm{Gal\ mm^{-1}}$, $\left(\dot{g}/\dot{h}\right) = -0.167(\pm0.045)$ $\mu\mathrm{Gal\ mm^{-1}}$) and WLR ($\left(\dot{g}/\dot{h}\right)_0 = -0.142\,(\pm0.018)$ $\mu\mathrm{Gal\ mm^{-1}}$, $\left(\dot{g}/\dot{h}\right) = -0.133\,(\pm0.030)$ $\mu\mathrm{Gal\ mm^{-1}}$) are all in agreement with $\left(\dot{g}/\dot{h}\right)_M$ and the reported range. However, in general, $\dot{g}$ gives a more uncertain regression than $\dot{g}_0$.

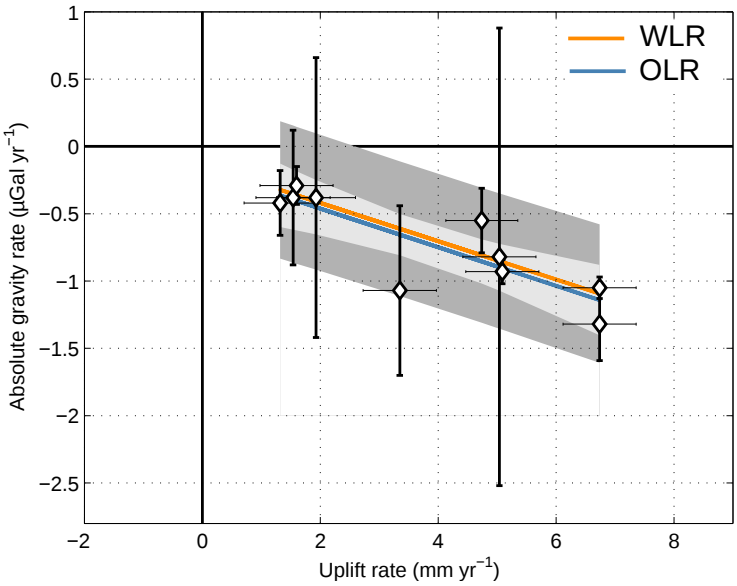

Figure 3.14: Gravity versus height rates of change based on standard gravity rates $\dot{g}_0$. Height rates given in ITRF2008. The white diamonds denote the gravity site, with vertical (gravity) and horizontal (height) error bars reflecting the respective uncertainties. The solid orange line shows the WLR, with the dark gray area showing its 95% confidence interval. The solid blue line shows the OLR, with the light gray area showing its 95% confidence interval.

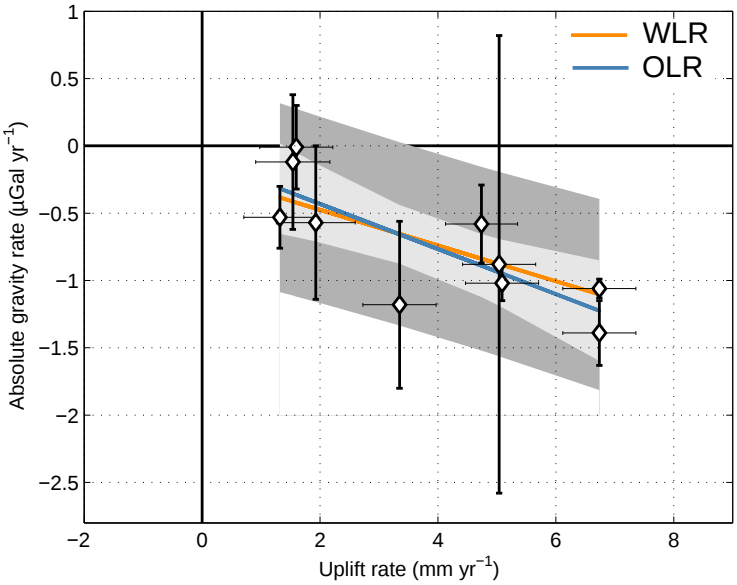

Figure 3.15: Same as Figure 3.14, but based on refined gravity rates $\dot{g}$.

3.5 Limitations of the research

From **Paper A** it becomes clear that the geoid models used give somewhat contradictory results, which we try to expand upon by considering the different data sources of the models. The GOCE R5 filter-combined models offer an improvement over NMA2014 and EGM2008 in comparison with GNSS/leveling (Section 3.1), but the geodetic MDTs based on EGM2008 outperform the NMA2014-based geoids on average. This could be owing to the different quality of terrestrial gravity data over land and ocean. NMA2014 is largely based on terrestrial gravity information over the oceans, and undetected systematics in shipborne gravity may degrade its quality over the ocean. EGM2008, on the other hand, relies heavily on altimetry-derived gravity, and should be less affected. We note that the dependence of EGM2008 on altimetry might eliminate short-scale MDT signal in the geodetic MDT, which would lead to the EGM2008-based geodetic MDTs being more similar to the smooth ocean MDTs.

Our findings in **Paper E** further nuances the picture, as the geodetic MDT surfaces determined using three different regional geoid models show different patterns depending on the geoid. All three geoid models NKG2015, NMA2014, and EGG2015 are based on GOCE R5 GGMs, with some variation in the terrestrial gravity data sets. NKG2015 and NMA2014 are mostly free of altimetry-derived gravity, while

EGG2015 relies heavily on altimetry-derived gravity, much like EGM2008. Here, the geodetic MDTs based on NKG2015 and NMA2014 outperform those based on EGG2015, both as a CS2 MDT surface and as TG MDT. $\mathrm{C2}_{\mathrm{EGG}}$ performs worse in comparison with NorKyst800, and the finer details of the Norwegian Sea circulation are missing. All CS2 MDTs show different artifacts along the coast, where the MDT lows could in part be due to geoid determination issues related to data weigthing and interpolation because of the lack of marine gravity data.

The bottom line regarding the geodetic MDTs is that even though we get a notable improvement with the inclusion of the latest GOCE data, there is still room for improving the marine geoid in the Norwegian coastal zone. Although it is clear that terrestrial gravity data are important for the geodetic MDT, it is not possible to reach unanimous conclusions regarding the inclusion of altimetry-derived gravity or inaccurate shipborne gravity. It is important to remember that the regional geoids are tuned to fit validation data on land, where also the bulk of gravimetric observations are found, and might not necessarily be the best option for describing the short-scale marine gravity field off the coast.

The TG geodetic MDTs in this thesis are based on derived ellipsoidal heights of MSL. Although we see an improvement when using data from the new Norwegian height system, the error analysis and interpretation of results are significantly more challenging when the TG MDTs are dependent on the height system.

For the determination of CS2 MDTs in particular, the geographical mode mask poses another challenge (Figure 2.26). The border between the SARIn mode and LRM/SAR modes along the Norwegian coast often coincides with the NCC, requiring special attention when combining CS2 data from the different modes. In addition, the CS2 observations are more sparse exactly at this border, and more uncertain. This is seen in particular along the south-eastern coast of Norway, where the border between SARIn and SAR modes coincides with the narrow jet of the NCC, making it highly dependent on the CS2 data weighting and interpolation methods. The jet is not a distinct feature in the current CS2 MDTs.

The CS2 observations are based on novel SARIn processing and crude data editing. Only ~60% of the raw CS2 data (omitting points on land) are used in **Paper E**. This not only suggests that a considerable amount of valid data points did not pass the editing, but also reveals that the CS2 targets along the Norwegian coast are generally noisy. Also, a large amount of CS2 observations inside fjords do not have a valid ocean tide (OT) correction, as they are outside the coverage of the standard global OT model. These observations have been disregarded in **Paper E**, but could be included in the future by considering local ocean tide corrections (**Paper D**).

Our comparison of regional geoid computation methods in **Paper C** is a synthetic closed-loop simulation which only serves the direct comparison of SKs, LSC and Stokes's formula in a regional application. It is not possible to reach general conclusions regarding the performance or practical implementation of the individual methods, as computation requirements of all three methods must be fulfilled at the same time, where Stokes's formula poses the strictest requirements. One of the main advantages of RBFs is the possibility to use more RBFs where the signal is rough, and less where the signal is smoother (also, the maximum degree of the expansion of the RBFs can be adapted accordingly). This advantage cannot be assessed by the numerical examples in **Paper C**. Another advantage of RBFs and LSC is that the input data can be irregularly distributed, while our numerical implementation of Stokes's formula requires regularly distributed data. In addition, **Paper C** does not compare the formal errors of the three methods.

In **Paper B** we identify some limitations in our refined modeling of ATM and GH gravitational effects through mGlobe, partly due to using a coarse orography rather than a DEM in the local zone, and partly due to approximating in-situ pressure observations at sites where these were not available. A further obvious limitation is that local hydrology is completely left out, when it is predominantely the local hydrology in the local zone which is expected to impact on the observations. The GLDAS/NOAH global hydrological model explicitly does not include the effect of groundwater variations, these have not been considered neither globally nor locally. Regressions based on two gravity campaigns only, i.e., HAMM, HONA, JON2, KOL1 and KOL2 are inherently uncertain, and although HONA and KOL1 present reasonable trends, they are obviously not reliable. Because of the larger gravity rate uncertainties that were estimated for HONA and KOL1, the WLR is similar to a linear regression where both are left out. Thus, the WLR underlines the difficulty of using these rates. This consolidates the need for extending the gravity time series, but this depends on funding and operator availability.

Figure 3.12 shows that the majority of the Norwegian AG sites are located along the coast, relatively close to the zero-line of present GIA-induced rebound in Fennoscandia. Consequently, at these sites, the signal we aim to describe (GIA) is weak, and other site-specific unmodeled processes or observation noise may dominate the rates. For almost all gravity rates of the reliable subset, $\dot{g}_0$ agrees more with $\dot{g}_M$ than $\dot{g}$. This suggests that $\dot{g}_M$ is not an optimal choice for assessing the refined corrections. Rather, our refined gravity rates mainly impact sites where GIA is not the dominant signal, which suggests that a refined modeling is meaningful at sites that are affected by various unmodeled or insufficiently modeled effects.

Regarding the discussion of the empirical and modeled gravity trends in **Paper B**, some of the Norwegian AG sites and observations have known limitations which

did not make it into the final paper, but are worth mentioning here. At TROM, a tunnel was built beneath the gravity site between 2005 and 2008, severly impacting the time series. Subsequent observations have been corrected by a rough estimate of the gravity shift due to the excavation, i.e., -20.27 ± 3.59 $\mu\mathrm{Gal}$, and are therefore quite uncertain. In later years, we observe a gravity increase at HONC which does not show up as a corresponding height decrease in the co-located GNSS observations. This suggests some kind of mass redistribution going on at this gravity site, which, until known, renders the HONC rate unreliable. We suspect something similar for the TRDA 1995.666/1998.474 campaigns as they give large values that strongly constrain the time series. The home site of FG5-226, NMBU, seems to be relatively stable, although there have been some disturbances. Due to the establishment of a calibration line in the neighboring surveying laboratory at the university between 2005-2006, a concrete beam was constructed stretching into the gravity laboratory and situated directly above the gravimeter. We have modeled the attraction of the beam to 3.00 ± 0.25 $\mu\mathrm{Gal}$, where the uncertainty was found by varying the beam density between 2200 and 2600 $\mathrm{kg\ m^{-3}}$. This gravity decrease has been applied to the 2004.609 and 2005.605 campaigns, rendering them more uncertain. As mentioned in the above, it remains a question what underlies the anomalous rates at ANDO, BODA/BODB, KAUT, and VAGA. These sites have not been visited more than 4-5 times, but we consider them quite stable. Furthermore, when comparing rates that are expected to be similar (KOL1/KOL2, TRYB/TRYC), they show discrepancies of ~0.5 $\mu\mathrm{Gal\ yr^{-1}}$, pointing in favor of observation uncertainties or small-scale geophysical processes. The continued observation of these sites is expected to shed more light on these questions.

BODA/BODB, TRYB/TRYC, KOL1/KOL2, HONA/HONB/HONC are groups of gravity sites which, at times, have been visited more or less simultaneously, thus allowing their combination. As pointed out by Timmen et al. (2015), however, individual gravity trends should be reliable before any combination of them is considered. Consequently, only TRYB/TRYC remains a possible combination candidate, cf. **Paper B** Table 5. The combined TRYB/TRYC trend (24 observations) yields -1.06 ± 0.12 $\mu\mathrm{Gal\ yr^{-1}}$ (using refined corrections), equal to the stand-alone TRYC trend (17 observations) and slightly more uncertain. This suggests the TRYB series might not yet be suitable for combination with TRYC, as it is based on few observations in comparison with TRYC, and strongly constrained by the more uncertain adopted campaigns of the early-to-mid 1990s.

Chapter 4

Conclusions, recommendations, and outlook

4.1 Conclusions

This thesis has revolved around the question of whether recent developments within geodesy can improve our understanding of sea level, dynamics, and gravity field in the Norwegian coastal zone. In a nutshell the answer is positive. We draw the following conclusions for the new GOCE-based regional geoid models:

- GRACE and GOCE have substantially improved the geoid over the last decade, with a drop from 8.5 cm (pre-GRACE) through 4.6 cm (GRACE) to $\sim$3 cm (GOCE) in terms of standard deviations of differences to GNSS/leveling.
- Part of the improvement is also due to upgraded terrestrial gravity databases.
- Although the different stochastically filtered GOCE-based geoids vary only slightly around 3 cm, there is a tendency that filter-combinations that put more weight on GOCE than on the terrestrial gravity data are the best.
- The formal geoid errors are lower and show larger variations depending on the filter-combination method than the empirical errors from the GNSS/leveling validation, which suggests that the empirical error is dominated by the quality of the GNSS/leveling data.
- Our formal geoid error budget indicates that EGG2015 has been optimized to a different validation data set than the Norwegian one. EGG2015 assumes a rather optimistic terrestrial data error of 0.2 mGal, whereas for the Norwegian data set, an error of around 2.0 mGal seems more realistic.

As for the geodetic MDT and associated ocean currents in the Norwegian coastal zone,

- geodetic and ocean MDTs agree on the ~3-7 cm level at the tide gauges, and on the ~5-11 cm level on the altimetry sites.
- The contributions to the error budget are estimated as follows:
  - Ocean MDT: ≤5 cm
  - Altimetric MSS: ≤7 cm
  - TG MSL: ≤3 cm
  - Geoid: ≤4 cm
- For most TGs, better absolute sea-level observations are obtained using the new national height system, NN2000. However, we stress the importance of directly observing ellipsoidal heights at TGs by GNSS, thus ruling out possible distortions from leveling and geoid errors.
- Geodetic MDTs correlate with the Nemo12 ocean model on a similar level as the other ocean models, suggesting a convergence of approaches.
- The coastal altimetry products generally do not offer an improvement over the conventional products they are based on.
- CS2 provides observations of SSH in areas previously not monitored by conventional altimetry.
- In comparison with 10-minute sea level observations at 22 TGs, we observe larger standard deviations of differences at TGs well inside fjords with relatively few CS2 observations (~20 cm or more), and smaller differences at TGs close to the open ocean with dense CS2 observations (~7 cm).
- When replacing the standard ocean tide and atmospheric corrections with local corrections derived from ocean tide predictions and pressure observations, we observe a 2-5 cm improvement in standard deviations of differences at 19 out of 22 TGs.
- At the TGs, the CS2 MDTs agree on the ~3-5 cm level with both TG and ocean MDTs.
- The CS2 MDT surfaces based on NKG2015 and NMA2014 show standard deviations of differences of ~6 cm to NorKyst800, while the CS2 MDT surface based on EGG2015 shows a slightly larger difference of ~8 cm.
- The general pattern of the Norwegian Sea circulation is evident in the CS2 MDTs, but variations are seen depending on the geoid.

- The NCC is revealed in the geostrophic current patterns of the CS2 MDTs based on NKG2015 and NMA2014.
- The CS2 MDT surfaces use recent regional geoid models which are all based on GOCE R5 GGMs; the observed variation emphasizes the importance of terrestrial gravity information for the geodetic MDT.
- Considering the geoid contribution to the MDT budget, and recognizing the substantial contribution of GOCE, still, short-scale geoid structures not covered by GOCE are of high relevance for coastal areas.
- The quality of regional geoid models is higher on land than over the ocean, which may be due to the fact that geoid models are often tuned to fit validation data on land, and due to the data situation.

Our comparison of regional geoid computation methods shows that

- Stokes's formula, LSC and RBFs using the SK are theoretically equivalent methods in the global case.
- LSC and SKs need a modification to provide the same results as Stokes's formula in regional applications, where the Stokes integration is restricted to a spherical cap around the computation point.
- The methods are also equal in practice, as shown in numerical examples. At the 5 arcmin resolution, all methods agree within $2{\times}10^{-2}$ mm to 5.9 mm in the target areas, where the largest RMS differences are due to the discretization of Stokes's formula.
- At the 2.5 arcmin resolution, all methods agree within $6{\times}10^{-2}$ mm to 2.4 mm.
- Little is gained by using more SKs than the corresponding resolution of the observations, as there is hardly any signal variability between the original grid nodes. Thus, the SKs are dependent on the signal resolution rather than the number of observations.
- The opposite holds true for LSC, as the size of the auto-covariance matrix to be inverted corresponds to the number of observations, independent of the signal resolution.
- Although we have demonstrated that the three methods give equal results in applications, we stress that the modification of LSC and SKs is not a general necessity when applying these methods; however, it is critical in direct comparison with Stokes's formula.

This research has also contributed to a better understanding of different effects that affect temporal gravity changes in Fennoscandia, and provides new independent gravity rates based on AG.

- All Norwegian FG5 AG observations 1993-2014 have been compiled and analyzed, raw observations consistently reprocessed, and adopted observations carefully incorporated into the data set with updated uncertainties.
- Gravity rates based on a refined modeling of OTL, NTL, ATM, and GH gravitational effects mainly impact sites where GIA is not the dominant signal.
- This suggests that a refined modeling is meaningful at sites that are affected by various unmodeled or insufficiently modeled effects.
- Compared to the modeled gravity rates, the refined gravity rates agree better than standard rates at 9 out of 20 sites. This reveals the need for further improvement of refined corrections as well as consideration of unmodeled effects.
- From a subset of 10 rates mainly reflecting GIA, estimated gravity-to-height rate of change ratios are within $-0.133\,(\pm 0.030)$ to $-0.167\,(\pm 0.045)$ $\mu\mathrm{Gal}\ \mathrm{mm}^{-1}$, in agreement with previous estimates (-0.154 to $-0.217\,\mu\mathrm{Gal}\,\mathrm{mm}^{-1}$)
- Regressions of the gravity-to-height rate of change ratio based on refined gravity rates are slightly more uncertain than those based on the standard rates.
- WLR reveals the challenge of incorporating rates based on few observations, and other sites with a sufficient number of campaigns show artifacts which are yet to be explained.
- This emphasizes the need for extending the gravity time series at all sites.

4.2 Recommendations and outlook

The benchmark study shows a fair agreement between geodetic and oceanographic estimates of MDT and coastal ocean currents. The employed data sets do, however, not allow deriving lower bounds for the error estimates of the individual components, which would be necessary to further investigate remaining discrepancies. For example, geodetic MDTs do in general show higher variability than oceanographic ones. It remains unclear to what extent this must be attributed to noise of the geodetic observations or an important signal which is not represented in the ocean models. More precise answers to these questions would obviously be of high relevance for oceanographers and geodesists.

In the future, more research is necessary on the short spatial scales of the marine and coastal gravity field. The NMA has recently established a gravimetric test field in the Norwegian coastal area of Sunnmøre (roughly bounded by 62°-62.5°N and 5°-6.2°E), where a large amount of new terrestrial, shipborne and airborne gravity data have been collected, and almost 30 intermediate tide gauges have been installed (O. C. D. Omang, personal communication, 2016). It is therefore a good candidate for the study of the short spatial scales of the geoid. From an optimized local geoid model, with formal and empirical error estimates, and an altimetric MSS or other absolute sea level information, a thorough signal and error assessment of the coastal gravity field, MSS, and MDT could be derived. By taking the signal characteristics of the test field into account, i.e., the smoothness properties of MSS, MDT, and geoid, the results could then be transferred to other areas in the Nordic Seas with a less favorable data situation.

For the Norwegian coastal zone in general, gravity data are sparse in a small coastal gap between terrestrial and marine gravity observations. Such gravity observation gaps could be filled efficiently with airborne gravimetry in a future regional geoid realization with particular focus on the coastal zone (Jiang and Wang, 2016). Alternatively, SSHs as determined from ships equipped with GNSS (and possibly an inertial navigation system) can be used to fill gaps directly at the coast and inside fjords (Reinking et al., 2012). Shipborne SSHs with GNSS could also be used for validation of coastal altimetry, and even regional geoid models (Lavrov et al., 2015).

The continued application of SAR altimetry is an obvious next step in improving the MDT budget. **Paper D** gave a first comparison of CS2 and TG data along the Norwegian coast. The study shows an improvement of standard deviations of differences in the order of 25-50% between TG and CS2 altimetry in comparison conventional systems (Envisat, Jason-2, SARAL/AltiKa). Further improvement was seen when the standard altimetric geophysical correction was replaced with locally predicted tides and pressure data. The tide and sea level web service of the NMA has the possibility to spatially interpolate ocean tides using nearby TGs and ROMS. This gives the opportunity to remediate all CS2 observations near the coast and inside fjords that do not have a valid ocean tide correction, and improve existing corrections. After early initiatives like CTOH or PISTACH (validated in **Paper A**), several initiatives have recently tested new altimetry standards and developed a set of optimized retrackers and corrections for different satellite missions. These are available, e.g., through the PEACHI project of CNES (Valladeau et al., 2015), ESA's Grid Processing-On-Demand service SARvatore (`http://gpod.eo.esa.int`) or through the different altimetry databases (AVISO, RADS, etc.). Updated gridded products such as the DTU15MSS (Andersen et al., 2015) have become available. These altimetry products, in addition to experimental retrackers if made available, are natural candidates for future validation studies.

In case of experimental altimetry data, these are often provided as-is, with no editing or quality assessment. This was the case of the experimentally retracked data used in **Paper E**, provided by the DTU Space retracker system. The present editing is quite crude, and a more elaborate and robust statistical editing of the data may remediate a larger amount of valid observations. For example, Nielsen et al. (2015) present a more sophisticated method for outlier detection, employing a statistical mixture distribution to describe the observation noise.

Due to the use of derived ellipsoidal height of MSL, the error budget is complicated. In general, an observed quantity is cleaner than a derived quantity, and with this in mind we recommend that MSL at all Norwegian TGs should be observed directly by GNSS. Although the Norwegian HRCS is of quite good quality due to the large amount of GNSS/leveling points, the leveling accuracy is worse along the coast, especially where height transfers over fjords have been made (O. Vestøl, personal communication, 2014). Furthermore, GNSS-determined ellipsoidal height of MSL would provide a nice control and validation of the HRCS at the coast. For Norway, the easiest place to start would be to measure the difference between antenna reference point and TG zero at the TGs that are already equipped with a GNSS receiver. In addition, campaign measurements of TGBMs could be performed. Filmer (2014) explores the potential of MDT models to identify and detect blunders in coastal leveling. This of course requires the blunder to be larger than the MDT uncertainty, but could be interesting to investigate for the Norwegian leveling data in and around fjords and on islands.

With better knowledge of the quality of the leveling-based height system, and increased quality of the available regional geoid models, the question whether a future height system should be based on the geoid rather than on leveling is timely, and possibilities for and consequences of a geoid-based height system for Norway should be subject to future studies.

With new and more accurate geodetic observations the global ocean models will be too coarse, and only high-resolution coastal numerical ocean models should be considered for validation purposes (Lin et al., 2015). Furthermore, the closer we get to the shore, away from the cross-shelf region, the geostrophic assumption will break down, as the underlying physics controlling circulations and tilts of sea level is fundamentally different. Lin et al. (2015) explore the Pacific coastal alongshore momentum balance of wind stress, friction and density, all contributing to the coastal tilt of sea level. A similar investigation along the Norwegian coast could be interesting. In addition, other independent means for validating the geodetic results, such as drifters, moorings, and volume transport estimates should be considered in the future.

What remains an important issue for solving ill-conditioned linear inverse problems by Tikhonov regularization (as applied in **Paper C**), is the determination of the regularization parameter α. It may be considered a weight, balancing the contribution of observations and prior information to the solution. If it is too large, the solution is over-regularized, or smoothed too much. If it is too small, no physically meaningful solution is obtained. Many existing algorithms for the determination of α are computationally intensive, requiring numerous solutions for a range of α. In addition, the failure of the algorithms to provide a unique α is problematic. Such ambiguity gives rise to questions about how important the choice of α is, and whether a best α exists. For applications within regional gravity modeling in particular, there have been attempts to compare different common approaches to determining α, resulting in the recommendation of different algorithms depending on the base function used (Naeimi et al., 2015). An interesting next step within this topic would be to explore the applicability of general and computationally efficient approaches to determine α in regional gravity modeling, i.e., where no assumption on the regularization matrix is made (Mead and Renaut, 2009; Renaut et al., 2010).

One of the advantages of LSC is the estimation of formal errors. In the comparison of different geoid computation methods of **Paper C**, there is no comparison of the formal errors of the different methods, which would be a natural next step within this topic.

The quality of terrestrial gravity data is not necessarily constant over the area of interest. This gives rise to the question as to whether the Stokes approach is a viable option in future regional geoid computation with demands of centimeter or even sub-centimeter accuracy, as a single weighting scheme for the whole area is used, i.e., the modified Stokes function. Thus, the Stokes approach will always be a compromise between the subareas with highest and lowest terrestrial data quality. LSC or spherical RBFs allow taking the spatial variations in data quality into account, and may give better results. **Paper C** is a simulation study where this versatility of LSC or RBFs cannot be assessed. A comparison of the methods using real data is a natural next step in future studies.

In 1990, the Nordic Geodetic Commission (NKG) began establishing a geodetic network for monitoring crustal deformations and sea-level changes in Fennoscandia and Svalbard. The subset of presented gravity values in **Paper B** mainly reflecting GIA will serve as a Norwegian contribution to the Fennoscandian AG project of the Working Group on Geodynamics of the NKG, which aims to combine all Fennoscandian AG data in a joint analysis on postglacial gravity change for the region. We expect the subset to be augmented with additional sites in the future, as they become suitable for GIA studies through improved corrections for remaining geophysical effects and/or additional observations.

The obvious next step in the refined modeling of gravitational effects is the inclusion of local hydrology. This, unfortunately, was outside the scope of the current research. Local hydrology can be described by considering groundwater variations. The GLDAS/NOAH model employed here does not include groundwater, but other global models could be tested, e.g., a GRACE-based model which includes groundwater. However, the smallest spatial scales of groundwater variations can only be unveiled through measurements of groundwater level directly at the AG site during each campaign. This, in turn, is limited by the infrastructure at the AG site, and in Norway only a few sites include a bore hole for measuring the groundwater level. A different approach could be to test the regional HBV hydrological model for Norway, run by the Norwegian Water Resources and Energy Directorate (NVE). It has a spatial resolution of 1 km^2 and provides groundwater volume values. Using the Bouguer-plate approximation, the groundwater volume change could be transformed to gravity change (Timmen, 2010). With the HBV model, groundwater variations in the past are also available, such that the 1993-2014 AG data set could still be considered.

References

Abulaitijiang A, Andersen OB, Stenseng L (2015) Coastal sea level from inland CryoSat-2 interferometric SAR altimetry. Geophys Res Lett 42(6):1841–1847, DOI 10.1002/2015GL063131

Albertella A, Rummel R (2014) GOCE geoid, mean dynamic topography and geostrophic velocities. Tech. Rep. CGE Report 6, Centre of Geodetic Earth System Research, München

Amjadiparvar B, Rangelova E, Sideris MG (2016) The GBVP approach for vertical datum unification: recent results in North America. J Geod 90(1):45–63, DOI 10.1007/s00190-015-0855-8

Andersen OB, Scharroo R (2011) Range and Geophysical Corrections in Coastal Regions: And Implications for Mean Sea Surface Determination. In: Vignudelli S, Kostianoy AG, Cipollini P, Benveniste J (eds) Coastal Altimetry, Springer, pp 103–145, DOI 10.1007/978-3-642-12796-0_5

Andersen OB, Knudsen P, Stenseng L (2015) The DTU13 MSS (Mean Sea Surface) and MDT (Mean Dynamic Topography) from 20 Years of Satellite Altimetry. In: IAG Symposia, Springer Berlin Heidelberg, Berlin, Heidelberg, pp 1–10, DOI 10.1007/1345_2015_182

Armitage TWK, Davidson MWJ (2014) Using the Interferometric Capabilities of the ESA CryoSat-2 Mission to Improve the Accuracy of Sea Ice Freeboard Retrievals. IEEE Trans Geosci Remote 52(1):529–536, DOI 10.1109/TGRS.2013.2242082

Bentel K (2013) Regional gravity modeling in spherical radial basis functions – on the role of the basis function and the combination of different observation types. PhD thesis, Norwegian University of Life Sciences

Bingham RJ, Haines K, Lea DJ (2014) How well can we measure the ocean's mean dynamic topography from space? J Geophys Res Oceans 119(6):3336–3356, DOI 10.1002/2013JC009354

Blakely RJ (1996) Potential Theory in Gravity & Magnetic Applications. Cambridge University Press, Cambridge

Breili K (2009) Investigations of surface loads of the Earth — geometrical deformations and gravity changes. PhD thesis, Norwegian University of Life Sciences

Brockmann JM, Zehentner N, Höck E, Pail R, Loth I, Mayer-Gürr T, Schuh WD (2014) EGM_TIM_RL05: An independent geoid with centimeter accuracy purely based on the GOCE mission. Geophys Res Lett 41, DOI 10.1002/2014GL061904

Bruinsma SL, Förste C, Abrikosov O, Marty JC, Rio MH, Mulet S, Bonvalot S (2013) The new ESA satellite-only gravity field model via the direct approach. Geophys Res Lett 40, DOI 10.1002/grl.50716

Chafik L, Nilsson J, Skagseth Ø, Lundberg P (2015) On the flow of Atlantic water and temperature anomalies in the Nordic Seas toward the Arctic Ocean. J Geophys Res Oceans 120:7897–7918, DOI 10.1002/2015JC011012

Chelton DB, deSzoeke RA, Schlax MG, Naggar KE, Siwertz N (1998) Geographical variability of the First Baroclinic Rossby Radius of Deformation. J Phys Oceanogr 28:433–460, DOI 10.1175/1520-0485(1998)028<0433:GVOTFB>2.0.CO;2

Chelton DB, Ries JC, Haines BJ, Fu LL, Callahan PS (2001) Satellite Altimetry. In: Fu LL, Cazenave A (eds) Satellite Altimetry and Earth Sciences — A Handbook of Techniques and Applications, Academic Press, San Diego, California., pp 1–131, DOI 10.1016/S0074-6142(01)80146-7

Collilieux X, Altamimi Z, Argus DF, Boucher C, Dermanis A, Haines BJ, Herring TA, Kreemer CW, Lemoine FG, Ma C, MacMillan DS, Mäkinen J, Métivier L, Ries J, Teferle FN, Wu X (2014) External Evaluation of the Terrestrial Reference Frame: Report of the Task Force of the IAG Sub-commission 1.2. In: Rizos C, Willis P (eds) Earth on the Edge: Science for a Sustainable Planet: Proceedings of the IAG General Assembly, Melbourne, Australia, June 28 - July 2, 2011, Springer, Berlin, Heidelberg, pp 197–202, DOI 10.1007/978-3-642-37222-3_25

Crossley D, Hinderer J, Riccardi U (2013) The measurement of surface gravity. Rep Prog Phys 76, DOI 10.1088/0034-4885/76/4/046101

Denker H (2013) Regional gravity field modeling: Theory and practical results. In: Xu G (ed) Sciences of Geodesy – II, Springer, Berlin, pp 185–191, DOI 10.1007/978-3-642-28000-9_5

Drinkwater MR, Floberghagen R, Haagmans R, Muzi D, Popescu A (2003) GOCE: ESA's First Earth Explorer Core Mission. In: Beutler G, Drinkwater MR, Rummel R, Von Steiger R (eds) Earth Gravity Field from Space — From

Sensors to Earth Sciences: Proceedings of an ISSI Workshop 11–15 March 2002, Bern, Switzerland, Springer Netherlands, Dordrecht, pp 419–432, DOI 10.1007/978-94-017-1333-7_36

Eicker A (2008) Gravity field refinement by radial basis functions from in-situ satellite data. Dissertation, University of Bonn

ESA and MSSL-UCL (2012) CryoSat Product Handbook. ESA and Mullard Space Science Laboratory - University College London

Featherstone WE (2008) GNSS-based heighting in Australia: Current, emerging, and future issues. J Spatial Sci 53(2):115–133, DOI 10.1080/14498596.2008.9635153

Featherstone WE, Filmer MS (2012) The north-south tilt in the Australian Height Datum is explained by the ocean's mean dynamic topography. J Geophys Res Oceans 117(C08035), DOI 10.1002/2012JC007974

Featherstone WE, Kuhn M (2006) Height systems and vertical datums: A review in the Australian context. J Spatial Sci 51(1):21–41, DOI 10.1080/14498596.2006.9635062

Filmer MS (2014) Using models of the ocean's mean dynamic topography to identify errors in coastal geodetic leveling. Mar Geod 37:47–64, DOI 10.1080/01490419.2013.868383

Freeden W, Gervens T, Schreiner M (1998) Constructive Approximation on the Sphere, with Applications in Geomathematics. Clarendon Press, Oxford

Gerlach C, Fecher T (2012) Approximations of the GOCE error variance-covariance matrix for least-squares estimation of height datum offsets. J Geod Sci 2(4):247–256, DOI 10.2478/v10156-011-0049-0

Gerlach C, Rummel R (2013) Global height system unification with GOCE: a simulation study on the indirect bias term in the GBVP. J Geod 87(1):57–67, DOI 10.1007/s00190-012-0579-y

Gommenginger C, Thibaut P, Fenoglio-Marc L, Quartly G, Deng X, Gomez Enri J, Challenor P, Gao Y (2011) Retracking altimeter waveforms near the coasts. In: Vignudelli S, Kostianoy AG, Cipollini P, Benveniste J (eds) Coastal Altimetry, Springer, pp 61–101, DOI 10.1007/978-3-642-12796-0_4

Haagmans R, de Min E, von Gelderen M (1993) Fast evaluation of convolution integrals on the sphere using 1D FFT, and a comparison with existing methods for Stokes's integral. Man Geod 18:227–241

Hansen PC, O'Leary DP (1993) The Use of the L-curve in the Regularization of Discrete Ill-posed Problems. SIAM J Sci Comput 14:1487–1503, DOI 10.1137/0914086

Hattermann T, Isachsen PE, von Appen WJ, Albretsen J, Sundfjord A (2016) Eddy-driven recirculation of Atlantic Water in Fram Strait. Geophys Res Lett 43(7):3406–3414, DOI 10.1002/2016GL068323

Hofmann-Wellenhof B, Moritz H (2006) Physical geodesy, second ed. Springer, Wien

Jain M (2015) Improved sea level determination in the Arctic regions through development of tolerant altimetry retracking. PhD thesis, DTU Space, Technical University of Denmark, Copenhagen

Jekeli C (1981) Alternative methods to smooth the Earth's gravity field. Tech. Rep. 327, Dept. of Geodetic Science and Surveying, Ohio State University, Columbus

Jekeli C (2005) Spline representations of functions on a sphere for geopotential modeling. Tech. Rep. 475, Dept. of Civil and Environmental Engineering and Geodetic Science, Ohio State University, Columbus

Jiang T, Wang YM (2016) On the spectral combination of satellite gravity model, terrestrial and airborne gravity data for local gravimetric geoid computation. J Geod 90(12):1405–1418, DOI 10.1007/s00190-016-0932-7

Johannessen JA, Raj RP, Nilsen JEØ, Pripp T, Knudsen P, Counillon F, Stammer D, Bertino L, Andersen OB, Serra N, Koldunov N (2014) Toward Improved Estimation of the Dynamic Topography and Ocean Circulation in the High Latitude and Arctic Ocean: The Importance of GOCE. Surv Geophys 35(3):661–679, DOI 10.1007/s10712-013-9270-y

Lavrov D, Even-Tzur G, Reinking J (2015) Extraction of geoid heights from shipborne GNSS measurements along the Weser River in northern Germany. J Geod Sci 5(1):148–155, DOI 10.1515/jogs-2015-0014

Li X, Crowley JW, Holmes SA, Wang YM (2016) The contribution of the GRAV-D airborne gravity to geoid determination in the Great Lakes region. Geophys Res Lett 43(9):4358–4365, DOI 10.1002/2016GL068374

Lieb V, Schmidt M, Dettmering D, Börger K (2016) Combination of various observation techniques for regional modeling of the gravity field. J Geophys Res Solid Earth 121:3825–3845, DOI 10.1002/2015JB012586

Lin H, Thompson KR, Huang J, Véronneau M (2015) Tilt of mean sea level along the Pacific coasts of North America and Japan. J Geophys Res Oceans 120:6815–6828, DOI 10.1002/2015JC010920

Liu X (2008) Global gravity field recovery from satellite-to-satellite tracking data with the acceleration approach. PhD thesis, Technical University of Delft

Lysaker DI, Omang OCD, Pettersen BR, Solheim D (2007) Quasigeoid evaluation with improved levelled height data for Norway. J Geod 81(9):617–627, DOI 10.1007/s00190-006-0129-6

Mayer-Gürr T, et al. (2015) The new combined satellite only model GOCO05s. Paper presented at the European Geosciences Union General Assembly, Vienna, Austria, April 12–17

Mead JL, Renaut RA (2009) A Newton root-finding algorithm for estimating the regularization parameter for solving ill-conditioned least squares problems. Inverse Probl 25(2), DOI 10.1088/0266-5611/25/2/025002

Meissl P (1971) A study of covariance functions related to the Earth's disturbing potential. Tech. Rep. 151, Dept. of Geodetic Science, Ohio State University, Columbus

Micro-g LaCoste (2012) g9 User's Manual, April 2012 version. Lafayette, Colorado, USA.

Mikolaj M, Meurers B, Güntner A (2016) Modelling of global mass effects in hydrology, atmosphere and oceans on surface gravity. Comp Geosci 93:12–20, DOI 10.1016/j.cageo.2016.04.014

Milne GA, Davis JL, Mitrovica JX, Scherneck HG, Johansson JM, Vermeer M, Koivula H (2001) Space-Geodetic Constraints on Glacial Isostatic Adjustment in Fennoscandia. Science 291(5512):2381–2385, DOI 10.1126/science.1057022

de Min E (1995) A comparison of Stokes' numerical integration and collocation, and a new combination technique. Bull Géod 69:223–232, DOI 10.1007/BF00806734

Moritz H (1980) Advanced physical geodesy. Wichmann, Karlsruhe

Naeimi M (2013) Inversion of satellite gravity data using spherical radial base functions. Dissertation, Deutsche Geodätische Kommission Reihe C, Nr. 711

Naeimi M, Flury J, Brieden P (2015) On the regularization of regional gravity field solutions in spherical radial base functions. Geophys J Int 202:1041–1053, DOI 10.1093/gji/ggv210

NASA Earth System Sciences Committee (1988) Earth system science: A closer view. Tech. rep., National Aeronautics and Space Administration, Washington D. C.

Niebauer TM, Sasagawa GS, Faller JE, Hilt R, Klopping F (1995) A new generation of absolute gravimeters. Metrologia 32(3):159–180, DOI 10.1088/0026-1394/32/3/004

Nielsen K, Stenseng L, Andersen OB, Villadsen H, Knudsen P (2015) Validation of CryoSat-2 SAR mode based lake levels. Remote Sens Environ 171:162–170, DOI 10.1016/j.rse.2015.10.023

Olsson PA, Ågren J, Scherneck HG (2012) Modelling of the GIA-induced surface gravity change over Fennoscandia. J Geodyn 61:12–22, DOI 10.1016/j.jog.2012.06.011

Olsson PA, Milne G, Scherneck HG, Ågren J (2015) The relation between gravity rate of change and vertical displacement in previously glaciated areas. J Geodyn 83:76–84, DOI 10.1016/j.jog.2014.09.011

Orvik KA, Skagseth Ø, Mork M (2001) Atlantic inflow to the Nordic Seas: Current structure and volume fluxes from moored current meters, VM-ADCP and SeaSoar-CTD observations, 1995-1999. Deep Sea Res 19:937 – 957, DOI 10.1016/S0967-0637(00)00038-8

Paul M (1973) A method of evaluating the truncation error coefficients for geoidal height. Bull Géod 47:413–425

Pavlis NK, Holmes SA, Kenyon SC, Factor JK (2012) The development and evaluation of the Earth Gravitational Model 2008 (EGM2008). J Geophys Res Solid Earth 117:B04,406, DOI 10.1029/2011JB008916

Plag HP, Pearlman M (eds) (2009) Global Geodetic Observing System: Meeting the Requirements of a Global Society on a Changing Planet in 2020. Springer, DOI 10.1007/978-3-642-02687-4

Pugh D, Woodworth PL (2014) Sea-Level Science: Understanding Tides, Surges, Tsunamis and Mean Sea-Level Changes. Cambridge University Press, Cambridge

Ray RD, Egbert GD, Erofeeva SY (2011) Tide predictions in shelf and coastal waters: Status and prospects. In: Vignudelli S, Kostianoy AG, Cipollini P, Benveniste J (eds) Coastal Altimetry, Springer, pp 191–216, DOI 10.1007/978-3-642-12796-0_8

Reigber C, Balmino G, Schwintzer P, Biancale R, Bode A, Lemoine JM, König R, Loyer S, Neumayer H, Marty JC, Barthelmes F, Perosanz F, Zhu SY (2002) A high-quality global gravity field model from CHAMP GPS tracking data and accelerometry (EIGEN-1S). Geophys Res Lett 29(14), DOI 10.1029/2002GL015064

Reinking J, Härting A, Bastos L (2012) Determination of sea surface height from moving ships with dynamic corrections. J Geod Sci 2(3):172–187, DOI 10.2478/v10156-011-0038-3

Renaut RA, Hnětynková I, Mead J (2010) Regularization parameter estimation for large-scale Tikhonov regularization using a priori information. Comput Stat Data An 54(12):3430 – 3445, DOI 10.1016/j.csda.2009.05.026

Reuter R (1982) Über Integralformeln der Einheitssphäre und harmonische Splinefunktionen. Dissertation, Veröffentlichungen des Geodätischen Instituts, RWTH Aachen

Rhines P, Häkkinen S, Josey SA (2008) Is Oceanic Heat Transport Significant in the Climate System? In: Dickson RR, Meincke J, Rhines P (eds) Arctic-Subarctic Ocean Fluxes, Springer, pp 87–109, DOI 10.1007/978-1-4020-6774-7_5

Rossby CG (1938) On the mutual adjustment of pressure and velocity distributions in certain simple current systems. J Mar Res 2:239–263

Rothacher M (2002) Estimation of Station Heights with GPS. In: Drewes H, Dodson AH, Fortes LPS, Sánchez L, Sandoval P (eds) Vertical Reference Systems: IAG Symposium Cartagena, Colombia, February 20–23, 2001, Springer, Berlin, Heidelberg, pp 81–90, DOI 10.1007/978-3-662-04683-8_17

Rülke A, Liebsch G, Sacher M, Schäfer U, Schirmer U, Ihde J (2012) Unification of European height system realizations. J Geod Sci 2(4):343–354, DOI 10.2478/v10156-011-0048-1

Rummel R (2012) Height unification using GOCE. J Geod Sci 2(4):355–362, DOI 10.2478/v10156-011-0047-2

Rummel R, Pail R (2011) Erdmessung Teil 3, Vorlesungsskriptum. Institut für Astronomische und Physikalische Geodäsie, Technische Universität München

Rummel R, Rothacher M, Beutler G (2005) Integrated Global Geodetic Observing System (IGGOS) — science rationale. J Geodyn 40:357 – 362, DOI 10.1016/j.jog.2005.06.003

Rummel R, Gruber T, Ihde J, Liebsch G, Rülke A, Schäfer U, Sideris MG, Rangelova E, Woodworth PL, Hughes C, Gerlach C (2015) Height System

Unification with GOCE. Summary and Final Report of STSE-GOCE+. Tech. rep., European Space Agency, Noordwijk

Sansò F, Sideris MG (eds) (2013) Geoid Determination: Theory and Methods. Lecture Notes in Earth System Sciences, Springer, Berlin

Santamaría-Gómez A, Gravelle M, Collilieux X, Guichard M, Martín Míguez B, Tiphaneau P, Wöppelmann G (2012) Mitigating the effects of vertical land motion in tide gauge records using a state-of-the-art GPS velocity field. Global Planet Change 98-99:6–17, DOI 10.1016/j.globplacha.2012.07.007

Sasaki H, Nonaka M, Masumoto Y, Sasai Y, Uehara H, Sakuma H (2008) An Eddy-Resolving Hindcast Simulation of the Quasiglobal Ocean from 1950 to 2003 on the Earth Simulator. In: Hamilton K, Ohfuchi W (eds) High Resolution Numerical Modelling of the Atmosphere and Ocean, Springer, New York, NY, pp 157–185, DOI 10.1007/978-0-387-49791-4_10

Scharroo R, Bonekamp H, Ponsard C, Parisot F, von Engeln A, Tahtadjiev M, de Vriendt K, Montagner F (2016) Jason continuity of services: continuing the Jason altimeter data records as Copernicus Sentinel-6. Ocean Sci 12:471–479, DOI 10.5194/os-12-471-2016

Schmidt M (2001) Grundprinzipien der Wavelet-Analyse und Anwendungen in der Geodäsie. Shaker Verlag, Aachen

Seeber G (2003) Satellite Geodesy, second ed. Walter de Gruyter, Berlin

Segar DA (2012) Introduction to Ocean Sciences, third ed. Available from `http://www.reefimages.com/oceans/oceans.html`.

Simpson MJR, Nilsen JEØ, Ravndal OR, Breili K, Sande H, Kierulf HP, Jansen E, Carson M, Vestøl O (2015) Sea Level Change for Norway: Past and Present Observations and Projections to 2100. Tech. Rep. 1, Norwegian Centre for Climate Services, Oslo, Norway

Skagseth Ø, Furevik T, Ingvaldsen R, Loeng H, Mork KA, Orvik KA, Ozhigin V (2008) Volume and Heat Transports to the Arctic Ocean Via the Norwegian and Barents Seas. In: Dickson RR, Meincke J, Rhines P (eds) Arctic-Subarctic Ocean Fluxes, Springer, pp 45–64, DOI 10.1007/978-1-4020-6774-7_3

Skagseth Ø, Drinkwater KF, Terrile E (2011) Wind- and buoyancy-induced transport of the Norwegian Coastal Current in the Barents Sea. J Geophys Res Oceans 116:C08,007, DOI 10.1029/2011JC006996

Sneeuw N (2000) A semi-analytical approach to gravity field analysis from satellite observations. Dissertation, Deutsche Geodätische Kommission Reihe C, Nr. 527

Šprlák M (2010) Generalized geoidal estimators for deterministic modifications of spherical Stokes function. Contr Geophys Geod 40(1):45–64, DOI 10.2478/v10126-010-0003-7

Šprlák M, Gerlach C, Omang OCD, Pettersen BR (2012) Validation of GOCE global gravity field models using terrestrial gravity data in Norway. J Geod Sci 2(2):134–143, DOI 10.2478/v10156-011-0030-y

Steffen H, Wu P (2011) Glacial isostatic adjustment in Fennoscandia - A review of data and modeling. J Geodyn 52:169–204, DOI 10.1016/j.jog.2011.03.002

Stenseng L (2011) Polar Remote Sensing by CryoSat-type Radar Altimetry. PhD thesis, DTU Space, Technical University of Denmark, Copenhagen

Stewart RH (2008) Introduction to Physical Oceanography. Dept. of Oceanography, Texas A & M University, College Station, Texas

Stokes GG (1849) On the variation of gravity on the surface of the Earth. Trans Cambridge Phil Soc 8:672–695

Tapley BD, Kim MC (2001) Applications to Geodesy. In: Fu LL, Cazenave A (eds) Satellite Altimetry and Earth Sciences — A Handbook of Techniques and Applications, Academic Press, San Diego, California., pp 371–406, DOI 10.1016/S0074-6142(01)80155-8

Tapley BD, Bettadpur S, Watkins M, Reigber C (2004) The gravity recovery and climate experiment: Mission overview and early results. Geophys Res Lett 31(9), DOI 10.1029/2004GL019920

Tarbuck EJ, Lutgens FK (2015) Earth Science, fourteenth ed. Pearson

Tegedor J, Øvstedal O, Vigen E (2014) Precise orbit determination and point positioning using GPS, Glonass, Galileo and BeiDou. J Geod Sci 4(1):65–73, DOI 10.2478/jogs-2014-0008

Tikhonov AN (1963) Regularization of incorrectly posed problems. Soviet Math Dokl 4:1624–1627

Timmen L (2010) Absolute and Relative Gravimetry. In: Xu G (ed) Sciences of Geodesy - I: Advances and Future Directions, Springer Berlin Heidelberg, Berlin, Heidelberg, pp 1–48, DOI 10.1007/978-3-642-11741-1_1

Timmen L, Engfeldt A, Scherneck HG (2015) Observed secular gravity trend at Onsala station with the FG5 gravimeter from Hannover. J Geod Sci 5:1–8, DOI 10.1515/jogs-2015-0001

Torge W, Müller J (2012) Geodesy, fourth ed. De Gruyter, Berlin

Valladeau G, Thibaut P, Picard B, Poisson JC, Tran N, Picot N, Guillot A (2015) Using SARAL/AltiKa to Improve Ka-band Altimeter Measurements for Coastal Zones, Hydrology and Ice: The PEACHI Prototype. Mar Geod 38:124–142, DOI 10.1080/01490419.2015.1020176

Vallis GK (2006) Atmospheric and Oceanic Fluid Dynamics. Cambridge University Press, Cambridge

Vallis GK (2012) Climate and the Oceans. Princeton University Press, Princeton, New Jersey

Van Camp M, de Viron O, Avouac JP (2016) Separating climate-induced mass transfers and instrumental effects from tectonic signal in repeated absolute gravity measurements. Geophys Res Lett 43:4313–4320, DOI 10.1002/2016GL068648

Verron J, Sengenes P, Lambin J, Noubel J, Steunou N, Guillot A, Picot N, Coutin-Faye S, Sharma R, Gairola RM, Raghava Murthy DVA, Richman JG, Griffin D, Pascual A, Rémy F, Gupta PK (2015) The SARAL/AltiKa Altimetry Satellite Mission. Mar Geod 38:2–21, DOI 10.1080/01490419.2014.1000471

Vignudelli S, Kostianoy AG, Cipollini P, Benveniste J (eds) (2011) Coastal Altimetry. Springer, DOI 10.1007/978-3-642-12796-0

Villadsen H, Deng X, Andersen OB, Stenseng L, Nielsen K, Knudsen P (2016) Improved inland water levels from SAR altimetry using novel empirical and physical retrackers. J Hydrol 537:234 –247, DOI 10.1016/j.jhydrol.2016.03.051

Weatherall P, Marks KM, Jakobsson M, Schmidt T, Tani S, Arndt JE, Rovere M, Chayes D, Ferrini V, Wigley R (2015) A new digital bathymetric model of the world's oceans. Earth Space Sci 2:331–345, DOI 10.1002/2015SEA000107

Wenzel HG (1981) Zur Geoidbestimmung durch Kombination von Schwereanomalien und einem Kugelfunktionsmodell mit Hilfe von Integralformeln. Z Verm 3:102–111

Wenzel HG (1982) Least Squares Spectral Combination Using Integral Kernels. In: Proceedings of the IAG General Meeting, Tokyo, Japan, May 7–15, 1982, Springer, Berlin, Heidelberg, pp 438–453

Wichiencharoen C (1984) A comparison of gravimetric undulations computed by the modified Molodensky truncation method and the method of least squares spectral combination by optimal integral kernels. Bull Géod 58(4):494–509, DOI 10.1007/BF02523696

Wingham DJ, Francis CR, Baker S, Bouzinac C, Brockley D, Cullen R, de Chateau-Thierry P, Laxon SW, Mallow U, Mavrocordatos C, Phalippou L, Ratier G, Rey L, Rostan F, Viau P, Wallis DW (2006) CryoSat: A mission to determine the fluctuations in Earth's land and marine ice fields. Adv Space Res 37:841–871, DOI 10.1016/j.asr.2005.07.027

Wittwer T (2009) Regional gravity field modelling with radial basis functions. PhD thesis, Technical University of Delft

Wong L, Gore R (1969) Accuracy of Geoid Heights from Modified Stokes Kernels. Geophys J Royal Astron Soc 18(1):81–91, DOI 10.1111/j.1365-246X.1969.tb00264.x

Woodworth PL, Hughes CW, Bingham RJ, Gruber T (2012) Towards worldwide height system unification using ocean information. J Geod Sci 2(4):302–318, DOI 10.2478/v10156-012-0004-8

Woodworth PL, Wöppelmann G, Marcos M, Gravelle M, Bingley RM (2017) Why we must tie satellite positioning to tide gauge data. Eos 98, DOI 10.1029/2017EO064037

Wöppelmann G, Marcos M (2016) Vertical land motion as a key to understanding sea level change and variability. Rev Geophys 54, DOI 10.1002/2015RG000502

Wunsch C, Stammer D (1998) Satellite Altimetry, the Marine Geoid, and the Oceanic General Circulation. Annu Rev Earth Planet Sci 26(1):219–253, DOI 10.1146/annurev.earth.26.1.219

Yi W (2012) The Earth's gravity field from GOCE. Dissertation, Institut für Astronomische und Physikalische Geodäsie, Technische Universität München

Errata

Location	Before	Now	Type
pp 1	Weddel	Weddell	Typo
pp 2	...is influenced, among other factors, by variations...	...is influenced, among other factors, by winds, variations...	Specification
pp 6	One outcome of a model run is the part of the SSH...	One outcome of a model run is the SSH...	Clarification
pp 9	...by Eq. (1.1) is analogue to...	...by Eq. (1.1) is the ocean analogue to...	Clarification
pp 20	continous	continuous	Typo
pp 23	$U(r,\theta) = \frac{GM}{R} \sum_{n=0}^{\infty} \left(\frac{R}{r}\right)^{n+1} \bar{C}_{n0} \bar{P}_{n0}(\cos\theta) + \frac{1}{2}\omega^2 r^2 (\sin\theta)^2$	$U(r,\theta) = \frac{GM}{R} \sum_{n=0}^{\infty} \left(\frac{R}{r}\right)^{n+1} \bar{C}^N_{n0} \bar{P}_{n0}(\cos\theta) + \frac{1}{2}\omega^2 r^2 (\sin\theta)^2$	Typo
pp 24	the the	the	Typo
pp 27	The increased precision... have	The increased precision... has	Typo
pp 28	...by relative gravity measurements...	...by relative gravity measurements (see below)...	Clarification
pp 32	Magnitude	Order of magnitude	Clarification
pp 35	...has opened up for a range...	...opened up a range...	Clarification
pp 44	$A^g_{kk} = \sum_{n=2}^{\infty} \sqrt{2n+1}/(4\pi R^2) \lambda^g_n B^{SK}_n P_n(\cos\psi_{Pk})$	$A^g_{kq} = \sum_{n=2}^{\infty} \sqrt{2n+1}/(4\pi R^2) \lambda^g_n B^{SK}_n P_n\left(\cos\psi_{kq}\right)$	Typo
pp 45	$\lambda^N_n = GM/R\gamma$	$\lambda^N_n = GM/(R\gamma)$	Typo
pp 57	Most important, perhaps, is..	Most important is...	Clarification
pp 61	The flattening can give rise...	The Earth flattening can give rise...	Clarification
pp 62	..., such that the orbital plane rotated eastwards...	..., such that the orbital plane rotates eastwards...	Typo
pp 64	...is the radar diameter.	...is the radar antenna diameter.	Clarification
pp 79	..., which is the sum of OT and OTL.	..., which is the sum of OT, OTL, and SET.	Specification
pp 79	..., which only observe the OT.	..., which only observe the OT and PT.	Specification
pp 81	...less salty water near the equator, ...	...less salty water near the equator and in polar regions, ...	Specification
pp 82	appply	apply	Typo
pp 88	oocen	ocean	Typo
pp 102	Two altimetry sites per TG was chosen by	Two altimetry sites per TG were chosen by	Typo
pp 102	All grids were...	All model grids used were...	Clarification
pp 116	...OTL provider does...	...OTL provider (`http://holt.oso.chalmers.se/loading/`) does...	Clarification
pp 118	...for all gravity sites.	...for all gravity sites, computed by ordinary linear regression (OLR) without weights.	Clarification
pp 118	...rather than the ordinary linear regression (OLR) without weights.	...(WLR) approach rather than OLR.	Clarification
pp 125	...upgraded terrestrial databases.	...upgraded terrestrial gravity databases.	Clarification
pp 126	...the ~5-11 cm on the...	...the ~5-11 cm level on the...	Typo
pp 126	...in areas previously uncovered by altimetry.	...in areas previousy not monitored by conventional altimetry	Clarification
pp 128	The refined gravity rates agree better...	Compared to the modeled gravity rates, the refined...	Clarification
pp 128	Regressions based...	Regressions of the gravity-to-height rate of change ratio based...	Clarification
pp 128	...or valuable signal...	...or an important signal...	Clarification
pp 129	...an agreement in the order of 25-50% of...	...an improvement of standard deviations of differences in the order of 25-50% between...	Clarification
pp 132	...comprise a well...	...include a bore hole...	Clarification
pp 132	hydrolocial	hydrological	Typo

List of papers

Peer-reviewed publications:

A **Ophaug, V.**, Breili, K., and Gerlach, C.
A comparative assessment of coastal mean dynamic topography in Norway by geodetic and ocean approaches
J. Geophys. Res. Oceans (**2015**), 120, 7807-7826,
doi: 10.1002/2015JC011145.

B **Ophaug, V.**, Breili, K., Gerlach, C., Gjevestad, J. G. O., Lysaker, D. I., Omang, O. C. D., and Pettersen, B. R.
Absolute gravity observations in Norway (1993-2014) for glacial isostatic adjustment studies: The influence of gravitational loading effects on secular gravity trends
J. Geodyn. (**2016**), 102, 83-94, doi: 10.1016/j.jog.2016.09.001.

C **Ophaug, V.**, and Gerlach, C.
On the equivalence of spherical splines with least-squares collocation and Stokes's formula for regional geoid computation
J. Geod. (**2016**, under review).

D Idžanović, M., **Ophaug, V.**, and Andersen, O. B.
Coastal sea level from CryoSat-2 SAR altimetry in Norway
Adv. Space Res. (**2016**, under review).

E Idžanović, M., **Ophaug, V.**, and Andersen, O. B.
The Norwegian Coastal Current observed by CryoSat-2 and GOCE
Geophys. Res. Lett. (**2017**, submitted).

F Gerlach, C., and **Ophaug, V.**
Accuracy of Regional Geoid Modelling with GOCE
In: Gravity, Geoid and Height Systems: Proceedings of the IAG Symposium GGHS2016, September 19-23, 2016 (**2016**, submitted).

Paper A

AGU PUBLICATIONS

JGR

Journal of Geophysical Research: Oceans

RESEARCH ARTICLE

10.1002/2015JC011145

A comparative assessment of coastal mean dynamic topography in Norway by geodetic and ocean approaches

Vegard Ophaug[1], Kristian Breili[1,2], and Christian Gerlach[1,3]

[1]Department of Mathematical Sciences and Technology, Norwegian University of Life Sciences (NMBU), Ås, Norway, [2]Geodetic Institute, Norwegian Mapping Authority, Hønefoss, Norway, [3]Commission of Geodesy and Glaciology, Bavarian Academy of Sciences and Humanities, Munich, Germany

Key Points:
- First comprehensive validation of coastal MDT by geodetic and ocean approaches in Norway
- Along the Norwegian coast, geodetic and ocean MDTs agree on the 3–11 cm level
- Dedicated coastal altimetry products generally do not offer improvements over conventional products

Supporting Information:
- Supporting Information S1
- Supporting Information S2
- Supporting Information S3

Correspondence to:
V. Ophaug,
vegard.ophaug@nmbu.no

Citation:
Ophaug, V., K. Breili, and C. Gerlach (2015), A comparative assessment of coastal mean dynamic topography in Norway by geodetic and ocean approaches, *J. Geophys. Res. Oceans*, *120*, 7807–7826, doi:10.1002/2015JC011145.

Received 15 JUL 2015
Accepted 3 NOV 2015
Accepted article online 5 NOV 2015
Published online 12 DEC 2015

Abstract The ocean's mean dynamic topography (MDT) is the surface representation of ocean circulation. It may be determined by the ocean approach, using numerical ocean circulation models, or by the geodetic approach, where MDT is the height of the mean sea surface (MSS), or mean sea level (MSL), above the geoid. Using new geoid models, geodetic MDT profiles based on tide gauges, dedicated coastal altimetry products, and conventional altimetry are compared with six ocean MDT estimates independent of geodetic data. Emphasis is put on the determination of high-resolution geoid models, combining ESA's fifth release (R5) of GOCE satellite-only global gravity models (GGMs) with a regional geoid model for Norway by a filtering technique. Differences between MDT profiles along the Norwegian coast together with Taylor diagrams confirm that geodetic and ocean MDTs agree on the ∼3–7 cm level at the tide gauges, and on the ∼5–11 cm level at the altimetry sites. Some geodetic MDTs correlate more with the best-performing ocean MDT than do other ocean MDTs, suggesting a convergence of the methods. While the GOCE R5 geoids are shown to be more accurate over land, they do not necessarily show the best agreement over the ocean. Pointwise monomission altimetry products give results comparable with the multimission DTU13MSS grid on the ∼5 cm level. However, dedicated coastal altimetry products generally do not offer an improvement over conventional altimetry along the Norwegian coast.

1. Introduction

The mean dynamic topography (MDT) is the height of the time-mean sea surface above the geoid. Its slope reveals the magnitude and direction of ocean surface geostrophic currents; hence, it is a surface representation of the ocean's mean circulation. Historically, oceanographers have determined the global ocean circulation by means of hydrographic measurements of temperature and salinity (in situ data) from ships [*Pugh and Woodworth*, 2014]. Today, the oceanographic MDT is determined from numerical ocean models, which employ a set of dynamical equations and are driven by in situ data sets, meteorological wind and air pressure information, and hydrological information. This may be termed the *ocean approach* to MDT computation.

A precise geoid model in combination with observations of the mean sea surface (MSS) by means of satellite altimetry allows a *geodetic approach* to determine the MDT. Altimetric observations yield ellipsoidal heights of the MSS. With geoid heights above the same ellipsoid, the MDT may be derived through a purely geometrical approach based on geodetic observations. The same principle can be applied if ellipsoidal heights of mean sea level (MSL), as observed by tide gauges connected to a geodetic reference frame, are available.

The rapid development of geodetic measurement techniques and models has rendered them sufficiently accurate to complement and validate traditional oceanographic results. The European Space Agency (ESA) gravimetric satellite mission Gravity and steady-state Ocean Circulation Explorer (GOCE) [*Drinkwater et al.*, 2003] provides a global geoid with unprecedented detail and has significantly improved geodetic MDT determination. Presently, ocean and geodetic MDTs show an average agreement on subdecimetric level, with better agreement in the open ocean than along coastlines [e.g., *Bingham et al.*, 2011; *Albertella et al.*, 2012; *Griesel et al.*, 2012; *Johannessen et al.*, 2014; *Higginson et al.*, 2015; *Hughes et al.*, 2015; *Woodworth et al.*, 2015].

The circulation of the Norwegian Sea incorporates a poleward transport of warm surface water from the North Atlantic Ocean (Norwegian Atlantic Current) as well as the Baltic Sea (Norwegian Coastal Current), with implications for the Norwegian coastal ecosystem [e.g., *Mork and Skagseth*, 2010; *Skagseth et al*., 2011]. This heat transport maintains a relatively mild climate in northwest Europe, as well as North Atlantic Deep Water formation, sustaining the Atlantic Meridional Overturning Circulation [*Rhines et al*., 2008]. Consequently, a quantitative understanding of ocean circulation variability at northern high latitudes is crucial to environmental and climate-related studies.

Coastal ocean dynamics has gained recent interest due to its importance for shipping, fishery, coastal ecosystem processes, other on-shore and offshore activities, and sea-level rise [*Pugh and Woodworth*, 2014]. In geodesy, coastal MDT remains an important implement for height system unification, wherein a precise geoid represents the reference surface for heights [*Rummel*, 2012]. However, the coastal zone presents a multitude of challenges regarding geoid and MDT computation. Both geodetic and ocean approaches to MDT computation show irregularities close to the coast [e.g., *Woodworth et al*., 2012; *Featherstone and Filmer*, 2012; *Filmer*, 2014]. Land contaminates coastal altimetry observations [e.g., *Gommenginger et al*., 2011] and tide-gauge observations are affected by vertical land motion [e.g., *Pugh and Woodworth*, 2014]. Tides become more complex along the coast, and global tide models loose validity there [e.g., *Ray et al*., 2011]. It is generally challenging to make observations from land, open sea, and coast consistent with each other [e.g., *Woodworth et al*., 2012]. Only a few numerical ocean models and selected coastal altimetry products have been developed for pilot studies or for specific areas. The Norwegian coast adds further complications, due to the many islands, mountains, and deep, narrow fjords.

A thorough validation of the quality of coastal products, specifically for the Norwegian coast, does not exist. The main goal of this work is to explore the level of agreement between novel geodetic and recent ocean MDT estimates along the Norwegian coast. A secondary goal is to assess whether geodetic MDTs using new GOCE geoid models offer an improvement over existing models. Finally, we investigate whether two dedicated coastal altimetry products perform better than the pure altimetry observations they are based on, and how pointwise altimetry compares with a state-of-the-art global gridded altimetry product.

Three fundamental vertical reference surfaces (or vertical datums) are considered in geodesy: the reference ellipsoid, the geoid, and the quasigeoid. While the reference ellipsoid is a vertical reference for nonphysical heights, the geoid and quasigeoid are vertical references for physical heights (orthometric and normal heights, respectively), incorporating gravity. The distinction between the geoid and the quasigeoid is not important in this work, as the geoid and the quasigeoid coincide over the oceans, with assumed negligible differences at the coast. However, all geoid models in this work are strictly quasigeoids, in the form of quasigeoid heights (better known as *height anomalies* in geodesy).

Geodetic MDTs have been determined using four quasigeoid models (see Table 6), two of which have been determined specifically for this work by a filtering approach, combining a regional quasigeoid model for Norway with the fifth release (R5) of ESA's GOCE satellite-only global gravity models (GGMs). The remaining two are the original Norwegian regional quasigeoid model and a quasigeoid model based on the GGM EGM2008.

Both tide-gauge and altimetry observations have been employed in this work. We aim to compare coastal geodetic MDTs based on these different observational methods. We have selected six ocean MDTs independent of geodetic data, primarily for validating our geodetic MDTs, but also to reveal their consistency along the coast. Section 2 describes the data sets in detail, with focus on data consistency. In section 3, we make a comparison of geodetic and ocean MDTs, before discussing the results in section 4. Conclusions are presented in section 5.

2. Data and Methods

2.1. Geodetic Approach

2.1.1. Regional Quasigeoids Based on GOCE

We investigate the performance of regional quasigeoids based on GOCE R5 GGMs, specifically the TIM5 and DIR5 models, based on the time-wise [*Brockmann et al*., 2014] and direct [*Bruinsma et al*., 2013] approaches,

Table 1. Validation of Best Combined and Pure Quasigeoid Models

Quasigeoid Model	$\hat{\sigma}$ (cm)
TIM5 + NMA2014 filtered @ 80 km	3.07
DIR5 + NMA2014 filtered @ 80 km	3.07
NMA2014	3.49
EGM2008[a]	4.64
GOCE TIM5[b]	28.23
GOCE DIR5[b]	27.37

[a]Developed to d/o 2190.
[b]Developed to d/o 280 (TIM5) and 300 (DIR5), and including omission errors.

respectively. These GGMs are given as sets of spherical harmonic coefficients to degree and order (d/o) 280 (TIM5) and 300 (DIR5), thus limited to a spatial resolution of ∼80–100 km, and with an accuracy of ∼1–4 cm (at d/o 220) [*Gruber*, 2014]. As the smallest spatial scales of the gravity field are not resolved, an omission error of ∼30 cm is introduced, if the GGMs are used alone [e.g., *Haines et al*., 2011]. This is demonstrated in Table 1, described below. Such an omission error is not negligible for our detailed studies of MDT along the Norwegian coast. Computing a regional gravimetric quasigeoid using the new GGMs in combination with terrestrial gravity data would be the optimal solution to this problem; this, however, is a time-consuming and computationally intensive task outside the scope of this work.

Instead, we have increased the resolution of the GGMs by combining them with the latest regional quasigeoid model for Norway, NMA2014, provided by the Norwegian Mapping Authority (NMA) (O. C. D. Omang, personal communication, 2014). It is based on the remove-compute-restore method [e.g., *Denker*, 2013], and the Wong and Gore kernel modification of Stokes's formula [*Wong and Gore*, 1969], evaluated by the 2-D multiband spherical FFT method [e.g., *Sideris*, 2013]. The DIR4 GGM was used as a global reference model. The Wong and Gore degree of modification is 140, with a linear transition from degree 130 to 140 to reduce edge effects, reflecting the best agreement in comparison with GNSS/leveling based on trial runs [e.g., *Forsberg and Featherstone*, 1998; *Omang and Forsberg*, 2002]. Consequently, above d/o 140, NMA2014 is solely based on terrestrial data. Bearing in mind that GOCE delivers accuracy improvements mainly in the medium wavelengths between d/o 100 and 200 in Norway [e.g., *Šprlák et al*., 2015], we expect an improvement in the accuracy of our combined quasigeoid model.

As NMA2014 is given on a regular grid with $0.01^\circ \times 0.02^\circ$ spacing, within an area delimited by $53^\circ \leq \varphi \leq 77.99^\circ$, and $-15^\circ \leq \lambda \leq 40^\circ$, GOCE TIM5 and DIR5 height anomalies have been computed on the NMA2014 grid points by spherical harmonic synthesis (SHS). Height anomalies are defined as $\zeta = T/\gamma$ [*Hofmann-Wellenhof and Moritz*, 2005, equation (8–26)], where T is the disturbing potential on Earth's surface, and γ is the normal gravity acceleration on the telluroid (an approximation of Earth's surface). Naturally, we have neither ellipsoidal nor normal heights for each NMA2014 grid point; instead, we have used topographic heights (excluding bathymetry) from the global ACE2 $30'' \times 30''$ digital elevation model [*Berry et al*., 2010], bilinearly interpolated to the NMA2014 grid points. ACE2 topographic heights are a fusion of orthometric height data from the Shuttle Radar Topography Mission (SRTM) and altimetry (ERS-1, ERS-2, and Envisat). For our purposes, these heights are assumed to be a sufficient approximation to normal heights. The effect of this approximation was investigated by initially computing height anomalies using topographic heights from ACE2, then adding them to the topographic heights, yielding approximated ellipsoidal heights, before finally computing height anomalies using both approximated normal and ellipsoidal heights. The difference between computed height anomalies using the simple approach (based on approximated normal heights only), and the more rigorous two-step approach (based on both approximated normal and ellipsoidal heights), was found to be insignificant at the mm level. Therefore, we used the simple approach for quasigeoid computation by SHS. Finally, we also considered the GGM EGM2008 [*Pavlis et al*., 2012], given as a set of spherical harmonic coefficients to d/o 2190, corresponding to a spatial resolution of 5 arc min. The EGM2008 quasigeoid was computed by SHS to its maximum d/o in the same manner as the TIM5 and DIR5 GGMs (Table 1).

Closely following the approach of *Rülke et al*. [2012], the TIM5 and DIR5 quasigeoids were low-pass filtered using the Gaussian mean kernel [*Jekeli*, 1981, equation (61)], and NMA2014 high-pass filtered with the complementary filter. Filtering was done by a convolution in the spatial domain, evaluated by the 1D-FFT method of *Haagmans et al*. [1993]. We used an integration radius of 4°, ensuring filter weights close to zero at the domain edges. Ultimately, the filtered quasigeoids were added, giving combined quasigeoids TIM5+NMA2014 and DIR5+NMA2014, delimited by $57^\circ \leq \varphi \leq 73.99^\circ$ and $-11^\circ \leq \lambda \leq 36^\circ$. Eight filter-combined solutions were computed for filter radii between 40 and 110 km at 10 km intervals, and validated externally by comparison with observed height anomalies, determined at sites observed both by GNSS and

Table 2. Tide Gauges in Our Work

Tide Gauge	Code	φ (°)	λ (°)
Vardø	VARD	70.375	31.104
Honningsvåg	HONN	70.980	25.973
Hammerfest	HAMM	70.665	23.683
Tromsø	TROM	69.647	18.961
Andenes	ANDE	69.326	16.135
Harstad	HARS	68.801	16.548
Kabelvåg	KABE	68.213	14.482
Bodø	BODO	67.288	14.391
Rørvik	RORV	64.860	11.230
Mausund[a]	MAUS	63.869	8.666
Heimsjø	HEIM	63.425	9.102
Kristiansund	KRIN	63.114	7.734
Ålesund	ALES	62.469	6.152
Måløy	MALO	61.934	5.113
Bergen	BERG	60.398	5.321
Stavanger	STAV	58.974	5.730
Tregde	TREG	58.006	7.555
Helgeroa	HELG	58.995	9.856
Viker	VIKE	59.036	10.950

[a]Mausund is not part of the PSMSL database.

leveling. For this, we have used a set of 1344 GNSS/leveling points in Norway, provided by NMA (Omang, personal communication, 2014). We acknowledge that the Gaussian kernel is a basic way of weighting terrestrial and satellite data, because it does not take data quality into account. Better results may be obtained using a stochastic kernel, weighting the data more correctly.

Table 1 shows validation results from pure and combined quasigeoids, in the form of standard deviations of differences between modeled and observed height anomalies. A greater filter radius means that more of the regional quasigeoid is incorporated into the combined model. We found an optimum filter radius of 80 km for both TIM5+NMA2014 and DIR5+NMA2014, where the combined quasigeoids perform better than NMA2014. In addition to the four high-resolution quasigeoids used in this work, the pure GOCE DIR5 and TIM5 model results are shown in Table 1, to quantify the omission error.

All height anomalies in this work refer to the GRS80 ellipsoid, with a semimajor axis of 6,378,137 m and an inverse flattening of 1/298.2572 (and practically equal to the WGS84 ellipsoid). With regard to the treatment of the permanent tides, we have decided to standardize all our data sets in the mean tide (MT) system, which retains the permanent tide effects from external bodies (mainly the Sun and the Moon). As the quasigeoids are given in the conventional tide free system (TF, where direct and indirect effects of the Sun and the Moon are removed), they were converted to the MT system using *Ekman* [1989, equation (17)].

Jayne [2006] as well as *Woodworth et al.* [2015] underline the importance of not mixing altimetry-derived gravity information in a quasigeoid model for MDT estimation purposes, as some of the dynamic topography will blend into the quasigeoid model, corrupting the MDT estimate when combined with the ocean's time-mean surface from altimetry or tide gauges. In this respect, there is a considerable difference between NMA2014 and EGM2008. EGM2008 incorporates a 5′×5′ gravity anomaly data set, which relies heavily on altimetry-derived gravity information over the oceans. Only a small amount of altimetry-derived gravity data are included in NMA2014, in areas sparsely covered with shipborne and airborne gravity data, more than ∼500 km off the Norwegian coast (Omang, personal communication, 2014). Therefore, we regard NMA2014 as a purely gravimetric quasigeoid for our purposes. The distributions of terrestrial and altimetry-derived gravity data in NMA2014 are provided in supporting information Figures S1 and S2.

2.1.2. Tide-Gauge MSL

The Norwegian tide-gauge network comprises 24 tide gauges. Not all have been considered in our work. We have omitted the tide gauge in Ny-Ålesund due to its location on the Svalbard archipelago in the Arctic Ocean, outside our study area. Also, we have not considered the tide gauges in Oslo, Oscarsborg, Trondheim, and Narvik, located well inside fjords not covered by the coastal altimetry data. At these tide gauges, complex local dynamics not resolved by the ocean models are expected to considerably contribute to observed MSL, thus unnecessarily complicating our comparative assessment. Consequently, we have included MSL observations from 19 tide gauges along the Norwegian coast (Table 2 and Figure 1), averaged over the epoch 1996–2000 inclusive, so as to be in the same epoch as the ocean models.

With the exception of the tide gauge in Mausund, we have used annual values of MSL from the Permanent Service for Mean Sea Level (PSMSL) [*Holgate et al.*, 2013] at http://www.psmsl.org/data/obtaining/. Mausund was recently transferred to the official Norwegian tide-gauge network, which is maintained by NMA. Mausund data are not yet available at PSMSL, but its inclusion is planned (A. Voldsund, NMA, personal communication, 2015). In this work, we have used hourly MSL values for Mausund from the NMA database, averaged to monthly values. These values are given in the former national height system, NN1954.

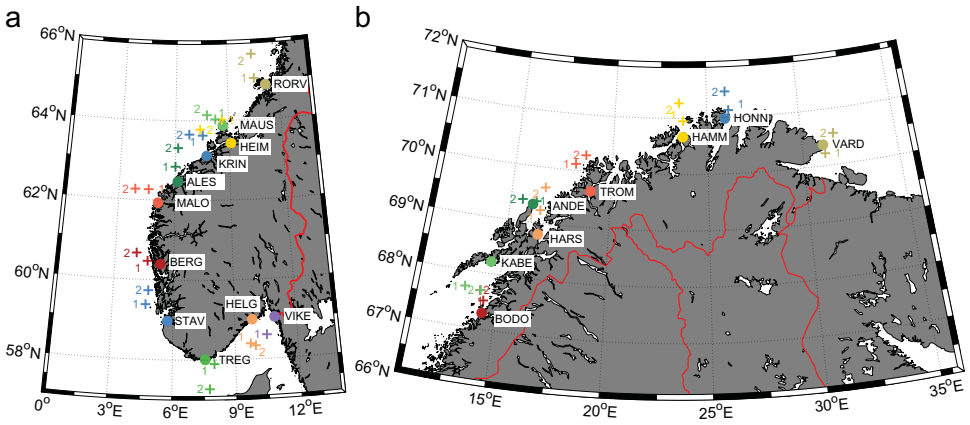

Figure 1. Tide-gauge MSL (dots) and altimetric MSS (plus signs) (a) south of 66°N and (b) north of 66°N.

Horizontal tide-gauge coordinates have been obtained using the tide and sea level web service of the NMA at http://www.kartverket.no/en/sehavniva/(with an uncertainty of ∼30 m) and have been compared with the cruder ones at PSMSL (with an uncertainty of ∼100 m), discovering no significant difference.

All PSMSL data in this work are within the Revised Local Reference (RLR) data subset, meaning that MSL is given relative to a tide-gauge benchmark (TGBM) at each tide gauge. Ideally, the absolute height of MSL should be determined directly by Global Navigation Satellite Systems (GNSS), either continuously or by precise campaign measurements at the tide gauge itself or a nearby benchmark with a leveled connection to a TGBM. By these approaches, the vertical uncertainty is within ∼1–2 cm [*Rothacher*, 2002].

Unfortunately, none of the TGBMs in our work have been observed by GNSS with sufficient accuracy. Some of the tide gauges have GNSS receivers mounted on them, but lack the necessary connection between the antenna reference point and the tide gauge zero, because they were installed with the aim of monitoring relative vertical site displacements only.

A solution for the interim is to derive ellipsoidal heights of MSL by using a height reference conversion surface (HRCS). This surface is typically a geoid fitted to benchmarks with known heights both in the national height system by means of leveling, and ellipsoidal heights h observed by GNSS, enabling the conversion of heights H in the national height system into ellipsoidal ones by the simple relation:

$$h = H + \mathrm{HRCS}. \tag{1}$$

We have used the Norwegian height reference surface HREF [*Solheim*, 2000], necessarily aggravating the total error budget due to possible errors in the quasigeoid on which the conversion surface is based, errors from GNSS/leveling benchmark interpolation, as well as errors in the national leveling network [*Featherstone*, 2008]. *Mysen* [2014] derived a formal HREF uncertainty map using least squares collocation, covering Norway south of 65°N, with coastal uncertainties ranging from ∼1 to ∼3 cm. Although they conclude that these uncertainties may be too optimistic, and uncertainties for Northern Norway have yet to be estimated, we reckon these as best present estimates for error budgeting purposes.

Currently, Norway is in the process of changing its height system. The former spheroidal-orthometric height system of Norway, NN1954, refers to a benchmark close to the tide gauge in Tregde, and was based on an adjustment of MSL determined at seven tide gauges along the coast [*Lysaker et al*., 2007]. The new normal height system, NN2000, refers to the Normaal Amsterdams Peil, and is based on a common Nordic adjustment with reference epoch 2000.0, taking vertical land motion [*Vestøl*, 2006; *Ågren and Svensson*, 2007] into account. Further deviations of NN2000 from NN1954 are due to different treatment of the permanent tides, which will be discussed below. *Featherstone and Filmer* [2012] showed that a tilt in the Australian Height

Datum, a height system established in a similar manner as NN1954, constrained to MSL at multiple tide gauges, was almost completely due to neglecting MDT effects at these tide gauges. NN2000, on the other hand, should be free of any MDT effects. In order to explore whether possible artifacts in the height systems significantly affect final MDT estimates, tide-gauge MSL was computed using both the former NN1954-constrained conversion surface HREF2008a, as well as the current NN2000-constrained conversion surface HREF2014c.

For all tide gauges except Mausund, the ellipsoidal heights of the TGBMs were computed according to equation (1) (using either NN1954-related or NN2000-related quantities *H* and HRCS). Next, the ellipsoidal height of MSL was computed by subtracting the height difference between TGBM and MSL (given by the RLR) from the ellipsoidal height of the TGBM.

For Mausund, the ellipsoidal height of MSL could be computed without going via the TGBM, using equation (1) as well as NN1954-related quantities *H* and HRCS. The height of MSL in NN1954 was transferred to NN2000 by forming a height difference between NN1954 and NN2000 at Mausund TGBM, and adding it to MSL.

The standard deviation of the differences between derived ellipsoidal heights of MSL using either NN1954 heights with HREF2008a or NN2000 heights with HREF2014c, amounts to 2.8 cm, with discrepancies ranging from −7.9 cm (Andenes) to 4.4 cm (Hammerfest) (Figure 2d).

HREF is derived from ellipsoidal heights given in the TF system. Therefore, ellipsoidal heights of MSL derived from HREF are also given in the TF system, and we converted them to the MT system using *Petit and Luzum* [2010, equation (7.14a)]. This latitude-dependent conversion ranges from ∼−7 cm in Southern Norway, to ∼−10 cm in Northern Norway. The ellipsoidal heights of MSL refer to the GRS80 ellipsoid.

MSL was corrected for the ocean's inverted barometer (IB) response (static atmospheric loading effect) using *Wunsch and Stammer* [1997, equation (1)], and local monthly sea level pressure data obtained from the eKlima database of the Norwegian Meteorological Institute at http://eklima.met.no, with respect to a reference value of 1011.4 mbar [*Woodworth et al*., 2012]. The mean distance between tide gauge and pressure data sites is ∼16 km, and the IB correction ranges from −47 to +4 mm.

Furthermore, a correction for the nodal tide, a long-period (18.61 years) astronomical tide, was applied to the MSL values using *Woodworth* [2012, equation (1), scaled by 0.44 according to *Pugh and Woodworth*, 2014]. For our range of latitudes, the nodal tide correction varies between ∼7 and ∼10 mm.

2.1.3. Altimetric MSS

We have employed six satellite altimetry data sets in this work; two basic monomission Envisat and Jason-2 data sets, three dedicated coastal products based on Envisat and Jason-2, and one multimission gridded product.

Dedicated coastal along-track monomission data have been produced by the Centre de Topographie des Océans et de l'Hydrosphère (CTOH) [*Roblou et al*., 2011], and the Collecte Localisation Satellites (CLS) through the Prototype Innovant de Système de Traitement pour l'Altimétrie Côtière et l'Hydrologie (PISTACH) project [*Mercier et al*., 2008], funded by the Centre National d'Etudes Spaciales (CNES). Both are distributed through the Archivage, Validation et Interprétation de données des Satellites Océanographiques (AVISO) project at http://www.aviso.altimetry.fr.

Processed on a regional basis using the X-TRACK software [*Roblou et al*., 2011], we have used the Envisat CTOH product covering the entire Norwegian coast. It is based on a two-step procedure. First, Geophysical Data Record (GDR) sea surface heights (SSH) have been analyzed applying stricter data validity criteria than normal. If a sudden change in a single range correction term occurs, it implies that the whole altimeter measurement is flagged as erroneous. This first step causes considerable data rejection, which, in a second step, is remedied by data recovery using correction terms interpolated from the valid data. Finally, the SSH values are resampled to reference tracks, producing 1 Hz observations at the same points for each cycle, with ∼6 km spacing between the points.

In order to assess whether coastal tuning of Envisat data gives better results along the Norwegian coast, we have also used standard along-track Envisat RA-2 GDR version 2.1 data provided by the European Space Agency (ESA) and downloaded from ESA's Earth Online portal at http://earth.esa.int. Corrections were applied due to an anomaly identified in the flight time delay calibration factor (PTR), estimated as part of the Envisat RA-2 GDR v2.1 reprocessing. The anomalies have a significant effect on mean sea level trend

estimates but are not crucial for the mean sea level itself [*Ollivier and Guibbaud*, 2012]. No PTR corrections are applied in the Envisat CTOH product (CTOH Team, personal communication, 2015). Only the Envisat GDR and CTOH cycles 10–92 were considered, which implies preclusion of the Envisat geodetic mission (cycles 93–113). The Envisat GDR data have a similar along-track spatial resolution as the Envisat CTOH-product (∼6 km), but the observations were not resampled to reference tracks. For the remainder of this work, standard Envisat GDR data will simply be referred to as Envisat, and Envisat CTOH as CTOH.

In addition to the two Envisat-based altimetry products described above, we have considered three products based on Jason-2 observations: one basic Jason-2 product and two PISTACH products. PISTACH is dedicated to the reprocessing of 20 Hz (∼300 m) Jason-2 I-GDR data along coasts and over inland waters, and covers all oceans. Due to the orbit configuration of Jason-2, PISTACH is limited to areas south of 66°N. It employs retracking [*Gommenginger et al*., 2011] schemes, which restrict the analysis window to consider only the coastal waveform gates contaminated by land effects, and filters the waveforms. Again, in order to assess the retracked Jason-2 data, we have used the standard Jason-2 Ku band corrected range measurement with no retracking applied, together with the Red3 and Ocean3 retrackers, dedicated to reduce instrumental noise and improve coastal approach, respectively. Our analysis of the PISTACH data revealed a shift in the sea surface heights around 1 September 2012. Data after this epoch were transformed to the initial mean level by estimating a step function at this epoch by least squares adjustment. We used all Jason-2 PISTACH data available at the time of writing, i.e., cycles 1–228, covering the 2008–2014 period. For the remainder of this work, standard Jason-2 I-GDR data will simply be referred to as Jason-2, and the PISTACH trackers Ocean3 and Red3 will be termed Ocean3 and Red3, respectively.

In general, we have employed standard range and geophysical corrections (ionosphere, troposphere, dynamic atmosphere, sea-state bias, and tides) as provided in the (I-)GDR files. However, there are some exceptions: The wet tropospheric corrections based on radiometer observations have been replaced by ECMWF model corrections within about 50 km of the coastline (which practically includes all MSS sites). In addition, the ionospheric corrections were subject to special attention. For Envisat observations prior to the S-band failure at 17 January 2008, and passing the editing criteria recommended in the Envisat User Manual [*Soussi et al*., 2009], smoothed ionospheric corrections calculated by combining range measurements on the Ku and S bands were used. For other epochs, corrections computed from global ionospheric maps (GIM) were used. We followed a similar approach for the Jason-2 and Ocean3 ranges, while GIMs were used for all Red3 and CTOH ranges. Parametric sea-state bias corrections were applied to all sets of ranges except for Red3, as sea-state bias corrections are presently only available for ocean trackers. For ocean tidal corrections, a mix of models have been used due to different processing standards. The CTOH sea surface heights have been corrected using the FES2012 model, while the FES2004 model was used for the Envisat and Jason-2 data. A third model, GOT4.7, was applied to the Jason-2/PISTACH trackers. Table 3 gives an overview of the applied corrections.

We have chosen 37 MSS sites along the Norwegian coast (Tables 4 and 5 and Figure 1). The MSS sites were chosen using a semiautonomous script, by consecutively plotting each tide gauge and nearby altimetry tracks, and choosing sites where all tracks cross, thus containing observations from all altimetry products. Because only the CTOH data were resampled to reference tracks, we included all sea surface heights within a spherical distance of 5 km from each MSS site (roughly corresponding to an altimetry footprint). To sufficiently represent the Norwegian coast, and also to increase confidence in the MSS observations, we have striven to find two MSS sites per tide gauge fulfilling the above criterion, which was possible for all tide gauges but Viker. The average distances between MSS sites and the coast, and between MSS sites and the associated tide gauges, are 23.1 and 54.1 km, respectively.

To explore whether the chosen MSS sites experience similar temporal variations as the tide gauges, the correlation of the altimetry time series with the associated tide-gauge time series was computed for each MSS site. Also, formal accuracies of the MSS observations were computed from the along-track observation variability. Envisat and CTOH observations have an average standard deviation of ∼1 cm (Tables 4 and 5), with slightly improved numbers south of 66°N (Table 5). On the whole, CTOH presents the lower standard deviation of the two. Observations from Jason-2, Ocean3, and Red3 have an average standard deviation of ∼0.5 cm (Table 5), but here the pure Jason-2 observation accuracy is better than the retrackers. The average correlation of altimetric MSS with tide-gauge MSL is higher north of 66°N, where Envisat on average correlates slightly better (0.74) than CTOH (0.70) (Table 4). Correlation deteriorates for the data south of 66°N, but

Table 3. Applied Range and Geophysical Corrections

Correction	Envisat	CTOH	Jason-2	Ocean3	Red3	DTU13MSS
Dry	ECMWF	ECMWF	ECMWF	ECMWF	ECMWF	ECMWF
Wet	Composite	Radiometer	Composite	Composite	Composite	Radiometer
Iono	IFC+GIM[a]	GIM	IFC+GIM	IFC+GIM	GIM	IFC
LF[b]	IB w/ECMWF	IB w/ECMWF	IB w/ECMWF	IB w/ECMWF	IB w/ECMWF	MOG2D_IB
HF[c]	MOG2D	MOG2D	MOG2D	MOG2D	MOG2D	MOG2D
Sea-State Bias	Non-param	Non-param	Non-param	Non-param	No SSB	Non-param
Ocean Tide	FES2004	FES2012	FES2004	GOT4.7	GOT4.7	GOT4.7
Solid Earth Tide	CT[d]	CT[d]	CT[d]	CT[d]	CT[d]	CT[d]
Pole Tide	*Wahr* [1985]	*Wahr* [1985]	*Wahr* [1985]	*Wahr* [1985]	*Wahr* [1985]	*Wahr* [1985]
Range bias (m)	0.433	0.433	0.174	0.174	0.174	
Cycles	10–92	10–92	1–228	1–228	1–228	
Period	2002–2010	2002–2010	2008–2014	2008–2014	2008–2014	1993–2012

[a]IFC: ionospheric-free combination; GIM: global ionosphere map.
[b]Low-frequency contribution with periods > 20 days.
[c]High-frequency contribution with periods < 20 days.
[d]CT: tidal potential from *Cartwright and Tayler* [1971] and *Cartwright and Edden* [1973].

still Envisat correlates better (0.57) than CTOH (0.53) (Table 5). Jason-2 observations have an average correlation of 0.52, similar to Envisat and CTOH. Furthermore, the Ocean3 and Red3 average correlations (0.39 and 0.32, respectively) are notably lower than the other altimetry data.

Temporal means of observed SSH were formed, where SSH is the difference between the ellipsoidal height of the spacecraft and the observed range between altimeter and sea surface, corrected for atmospheric and sea surface scattering effects as well as tides and atmospheric loading. Consequently, SSH is automatically given in the MT system. In accordance with the standardization of MSL (section 2.1.2), all altimetry observations were first adjusted to the mean epoch (1998.5) of the 1996–2000 period covered by the ocean models (section 2.2). This was done by applying corrections for regional sea level change,

$$\mathrm{SSH}_{1998.5}(t) = \mathrm{SSH}(t) + \beta(1998.5 - t), \tag{2}$$

where $\mathrm{SSH}_{1998.5}(t)$ is the sea surface height observed at epoch t (SSH(t)), transformed back to the mean epoch (1998.5). The local sea level rate (β) was estimated by using records from the associated tide gauges. We have chosen to use tide-gauge records instead of altimetry data because suitable multimission time series are restricted to areas south of 66°N. In addition, regional altimetric sea level rates are quite uncertain (*Prandi et al*. [2012] adopt a total error of 1.3 mm/yr [90% confidence interval] for the Arctic Ocean), especially in the coastal zone. We used monthly tide-gauge records from the PSMSL (see section 2.1.2). Relative sea level rates were estimated by fitting equation (3) to the tide-gauge records by least squares adjustment:

Table 4. MSS Observations From Altimetry North of 66°N (1996–2000)[a]

Site	φ (°)	λ (°)	d_{TG}	d_c	$\hat{\sigma}^{envi}$	$\hat{\sigma}^{ctoh}$	r_{TG}^{envi}	r_{TG}^{ctoh}
$VARD_1$	70.219	31.168	12.9	8.6	1.2	0.9	0.59	0.75
$VARD_2$	70.561	31.711	34.1	28.0	0.9	0.8	0.70	0.60
$HONN_1$	71.127	26.181	17.6	5.2	1.1	1.0	0.73	0.54
$HONN_2$	71.461	26.021	53.3	33.3	0.8	0.8	0.75	0.73
$HAMM_1$	70.948	23.699	31.3	2.9	1.0	0.8	0.80	0.73
$HAMM_2$	71.266	23.481	67.2	26.3	0.7	0.7	0.70	0.60
$TROM_1$	70.280	18.610	71.5	8.4	1.3	1.4	0.70	0.61
$TROM_2$	70.112	18.114	61.1	12.0	0.8	0.8	0.85	0.77
$ANDE_1$	69.383	16.305	9.6	8.5	0.9	1.0	0.79	0.74
$ANDE_2$	69.391	15.598	23.2	16.9	0.7	1.0	0.87	0.63
$HARS_1$	69.232	16.535	48.2	4.0	1.1	1.1	0.78	0.78
$HARS_2$	69.642	16.683	94.1	25.6	0.8	0.8	0.82	0.75
$KABE_1$	67.723	13.435	70.4	24.5	1.5	0.9	0.63	0.67
$KABE_2$	67.686	14.185	60.5	8.9	1.3	1.1	0.74	0.76
$BODO_1$	67.511	14.380	25.4	3.8	1.8	1.4	0.74	0.70
$BODO_2$	67.685	14.173	45.7	9.4	1.3	1.1	0.72	0.76

[a]Chosen MSS observation sites contain Envisat and CTOH data. d_{TG} is the distance (in km) to the associated tide gauge, d_c is the distance (in km) to the coastline. $\hat{\sigma}$ is the estimated accuracy computed from the along-track altimetry data (in cm), and r_{TG} is the correlation of the altimetry data time series with the associated tide-gauge time series.

Table 5. MSS Observations From Altimetry South of 66°N (1996–2000)[a]

Site	φ (°)	λ (°)	d_{TG}	d_c	$\hat{\sigma}^{envi}$	$\hat{\sigma}^{ctoh}$	$\hat{\sigma}^{Jas2}$	$\hat{\sigma}^{oce3}$	$\hat{\sigma}^{red3}$	r_{TG}^{envi}	r_{TG}^{ctoh}	r_{TG}^{jas2}	r_{TG}^{oce3}	r_{TG}^{red3}
RORV$_1$	65.029	10.579	36.2	4.7	0.9	0.8	0.6	0.6	0.6	0.85	0.67	0.67	0.57	0.46
RORV$_2$	65.639	10.474	93.9	36.4	0.7	0.8	0.5	0.5	0.5	0.62	0.49	0.56	0.37	0.19
MAUS$_1$	64.031	8.249	27.2	20.7	1.2	0.9	0.5	0.6	0.6	0.56	0.50	0.34	0.22	0.16
MAUS$_2$	64.138	7.775	52.9	44.1	1.1	1.0	0.4	0.5	0.5	0.50	0.53	0.37	0.25	0.12
HEIM$_1$	64.017	8.620	70.2	9.9	0.9	0.8	0.5	0.6	0.6	0.79	0.80	0.80	0.71	0.64
HEIM$_2$	63.778	7.382	93.9	38.7	0.9	0.9	0.4	0.5	0.5	0.55	0.54	0.62	0.35	0.20
KRIN$_1$	63.625	7.522	58.0	20.5	1.1	1.0	0.5	0.6	0.5	0.56	0.64	0.59	0.47	0.33
KRIN$_2$	63.652	6.768	77.0	52.8	0.9	0.8	0.4	0.5	0.4	0.61	0.56	0.56	0.28	0.07
ALES$_1$	62.846	6.015	42.6	12.4	1.1	1.1	0.6	0.6	0.6	0.73	0.81	0.64	0.55	0.49
ALES$_2$	63.312	6.150	94.0	50.5	0.8	0.8	0.4	0.4	0.4	0.68	0.54	0.54	0.30	0.30
MALO$_1$	62.266	4.591	45.9	27.5	0.8	0.8	0.5	0.6	0.6	0.65	0.64	0.66	0.45	0.43
MALO$_2$	62.266	3.868	74.8	63.5	0.7	0.8	0.4	0.5	0.5	0.58	0.67	0.52	0.24	0.24
BERG$_1$	60.470	4.669	36.7	8.9	0.9	0.9	0.5	0.6	0.6	0.66	0.61	0.60	0.45	0.45
BERG$_2$	60.667	4.095	73.6	33.0	0.5	0.8	0.5	0.6	0.6	0.44	0.25	0.42	0.34	0.24
STAV$_1$	59.384	4.640	77.2	14.8	0.8	0.9	0.6	0.6	0.6	0.43	0.41	0.51	0.46	0.39
STAV$_2$	59.734	4.753	101.4	18.2	1.4	0.9	0.6	0.6	0.6	0.55	0.38	0.54	0.46	0.43
TREG$_1$	57.898	7.992	28.5	16.3	1.3	1.2	0.7	0.7	0.8	0.48	0.52	0.50	0.45	0.48
TREG$_2$	57.271	7.762	83.0	49.9	1.0	1.0	0.7	0.7	0.7	0.53	0.47	0.45	0.39	0.38
HELG$_1$	58.394	9.734	67.4	43.2	1.0	0.9	0.6	0.7	0.6	0.37	0.33	0.34	0.33	0.23
HELG$_2$	58.340	9.978	73.4	58.0	1.4	1.1	0.5	0.6	0.5	0.30	0.32	0.33	0.24	0.18
VIKE$_1$	58.602	10.534	54.1	29.4	1.0	1.1	0.6	0.7	0.7	0.53	0.47	0.41	0.33	0.28

[a]Chosen MSS observation sites contain Envisat/CTOH and Jason-2/PISTACH data. d_{TG} is the distance (in km) to the associated tide gauge, d_c is the distance (in km) to the coastline. $\hat{\sigma}$ is the estimated accuracy computed from the along-track altimetry data (in cm), and r_{TG} is the correlation of the altimetry data time series with the associated tide-gauge time series.

$$z(t) = \alpha + \beta \cdot t + A_1 \sin(2\pi t - \varphi_1) + A_2 \sin(2\pi t/18.6 - \varphi_2), \quad (3)$$

where $z(t)$ is tide-gauge observation at epoch t, α is the intersect of the model, A_1, φ_1 are the amplitude and phase of the annual periodic variation, and A_2, φ_2 are the amplitude and phase of the nodal periodic variation [*Baart et al.*, 2012]. At most stations, the rate was estimated from a record covering the 1983–2013 period, but due to significant data gaps and short time series, the rates at Andenes and Mausund were estimated for the 1992–2013 period. As tide gauges provide relative observations of sea level, estimated rates need to be corrected for vertical land motion before they can be used to correct geocentric sea surface heights observed by altimetry. This was done by estimating vertical land motion from time series recorded at nearby permanent GNSS stations [*Kierulf et al.*, 2013].

With sea surface heights referenced to the mean epoch, cycle averages ($\overline{\mathrm{SSH}}_{1998.5}$) were formed, and the mean sea surface was estimated by fitting equation (4) to the series of cycle averages (35 days for Envisat and 10 days for Jason-2):

$$\overline{\mathrm{SSH}}_{1998.5}(t) = \mathrm{MSS}_{1998.5} + A_1 \sin(2\pi t - \varphi_1), \quad (4)$$

where the annual term was included in order to reduce the variance of the adjustment and by that improve the possibility of detecting outliers. We note that ellipsoidal heights of MSS from Envisat refer to the WGS84 ellipsoid, likewise the Envisat-originated CTOH data. Jason-2/PISTACH, on the other hand gives MSS values above the TOPEX ellipsoid (with a semimajor axis of 6,378,136.3 m, and an inverse flattening of 1/298.25765). The ellipsoidal heights referenced to the TOPEX ellipsoid were transformed to WGS84 by first transforming the heights to Cartesian coordinates and then back to ellipsoidal heights above the WGS84 ellipsoid. The transformations were realized by standard formulas [e.g., *Hofmann-Wellenhof et al.*, 2001, chapter 10].

Finally, in addition to the five monomission along-track data sets, we have considered the Technical University of Denmark (DTU) multimission MSS model DTU13MSS [*Andersen et al.*, 2013], available at ftp://ftp.space.dtu.dk/pub/DTU13/. It is given on a global $1' \times 1'$ grid and is a development of the former DNSC08 MSS model [*Andersen and Knudsen*, 2009], with standard range corrections applied (Table 3). DTU13MSS is averaged over the period 1993–2012 and offers an increased amount of retracked coastal satellite altimetry data, data from the Jason-1 geodetic mission, as well as a combination of ERS-1/ERS-2/Envisat and Cryosat-2 altimetry data in the northern high latitudes. DTU13MSS is also referred to the TOPEX ellipsoid and was referenced to WGS84 by computing an average difference of 0.686 m between regional geoids synthesized

with WGS84 and TOPEX ellipsoidal parameters, and subtracting this difference from the MSS values. DTU13MSS was adjusted to the 1996–2000 period using equation (2).

2.1.4. Geodetic MDT

Determining the geodetic MDT is closely related to the method of combining GNSS and leveling on land, cf. equation (1):

$$\mathrm{MDT} = h - \zeta, \tag{5}$$

where h is the ellipsoidal height of MSS or MSL at altimetry or tide-gauge sites, respectively, and ζ is the height anomaly, all referring to the same reference ellipsoid.

Height anomalies from the four quasigeoid model grids (Table 6) were linearly interpolated to the altimetry and tide-gauge sites (Tables 2, 4, and 5) by nearest neighbor, before subtraction by equation (5).

2.2. Ocean Approach

The geodetic MDT estimates were validated using numerical ocean models independent of geodetic data (as opposed to assimilated models incorporating geodetic data). Such models employ forcings in the form of in situ hydrographic data sets (salinities and temperatures) and meteorological information, where the MDT reflects the mean dynamical response of the ocean model to these forcings, determined by the equations of motion. In this work, six numerical ocean models have been used (Table 6).

Five of the ocean models were provided by the National Oceanography Centre (C. W. Hughes, personal communication, 2014). In particular, there are two Nemo (Nucleus for European Modelling of the Ocean) ORCA [*Madec*, 2008] model integrations, one at a resolution of $1/4^\circ$ (NemoQ), and one at a resolution of $1/12^\circ$ (Nemo12). Then come two Liverpool University implementations of the Massachusetts Institute of Technology (MIT) global ocean circulation model [*Marshall et al*., 1997a, 1997b], assimilating hydrographic information provided by the UK Met Office [*Smith and Murphy*, 2007]; one in a coarse form (L-MITc), with a global resolution of 1°, and a finer version (L-MITf) with an increased resolution of $1/5^\circ \times 1/6^\circ$ in the North Atlantic. Finally, there is the Ocean Circulation and Climate Advanced Modeling (OCCAM) $1/12^\circ$ global ocean circulation model [*Marsh et al*., 2009]. The ocean models incorporate a climatology for their initiation, as well as wind and atmospheric forcing from meteorological reanalyses. All models are averaged over the period 1996–2000 inclusive, which set the standardization epoch for all data sets.

The five mentioned ocean models have their primary application in deep ocean studies, rather than in studies of the coastal zone, and their spatial resolutions are insufficient to resolve many coastal processes (e.g., river runoff) [*Woodworth et al*., 2012]. Therefore, we have also considered the Proudman Oceanographic Laboratory Coastal Modelling System (POLCOMS) coastal model [*Holt and James*, 2001], distributed by the British Oceanographic Data Centre at http://www.bodc.ac.uk. Yearly model runs were averaged over the 1996–2000 period. With a $1/9^\circ \times 1/6^\circ$ resolution, this model is used for studies of continental shelf processes, and takes river runoff into account. Regrettably, the model does not cover the entire Norwegian coast (see Table 6) but has been included in the analysis for tide-gauge and altimetry sites south of 65°N.

As part of earlier work, the global ocean models provided to us have been resampled to common $1/4^\circ \times 1/4^\circ$ grids by nearest-neighbor linear interpolation to facilitate intercomparison studies (C. W. Hughes, personal communication, 2015). In the present work, these grids were further linearly interpolated to the altimetry and tide-gauge sites (Tables 2, 4, and 5) by nearest neighbor.

We investigated how the intermediate $1/4^\circ \times 1/4^\circ$ interpolation might affect the final MDT values by resampling POLCOMS in the same manner, and comparing values at the altimetry and tide-gauge sites with the ones directly interpolated from the native POLCOMS grid. The standard deviation of differences between native and resampled POLCOMS values was found to be $\sim$1 cm. This impacts the final results (Tables 7 and 8) on the submillimeter level; thus, we do not expect a significant error due to the intermediate interpolation.

We further compared linearly interpolated with bicubically interpolated ocean MDTs, and observed an improvement (reaching 9 mm with Nemo12) with the bicubically interpolated values at the altimetry sites. Simultaneously, however, a degradation was observed (reaching 12 mm, again with Nemo12) with the bicubically interpolated values at the tide gauges. Due to this ambiguity, we decided to retain the linearly interpolated values for all altimetry and tide-gauge sites.

Table 6. Model Grids Used in Our Work

Model	Coverage	Time Period	Grid Spacing (°) or d/o	Reference
Quasigeoid[a]				
TIM5+NMA2014	$57^\circ \le \varphi \le 73.99^\circ$ $-11^\circ \le \lambda \le 36^\circ$		0.01×0.02	This work
DIR5+NMA2014	$57^\circ \le \varphi \le 73.99^\circ$ $-11^\circ \le \lambda \le 36^\circ$		0.01×0.02	This work
NMA2014	$53^\circ \le \varphi \le 77.99^\circ$ $-15^\circ \le \lambda \le 40^\circ$		0.01×0.02	NMA
EGM2008	Global		2190	*Pavlis et al.* [2012]
MSS[b]				
DTU13MSS	Global	1993–2012	1/60×1/60	*Andersen and Knudsen* [2009], *Andersen et al.* [2013]
Ocean[c]				
Nemo12	Global	1996–2000	1/12×1/12	*Blaker et al.* [2015] ,
NemoQ	Global	1996–2000	1/4×1/4	*Madec* [2008]
L-MITf[d]	Global	1996–2000	1/5×1/6	*Marshall et al.* [1997a],
L-MITc	Global	1996–2000	1×1	*Marshall et al.* [1997b], *Smith and Murphy* [2007]
OCC12	Global	1996–2000	1/12×1/12	*Marsh et al.* [2009], *Webb et al.* [1997]
POLCOMS	$40.0556^\circ \le \varphi \le 64.8889^\circ$ $-19.9167^\circ \le \lambda \le 13^\circ$	1996–2000	1/9×1/6	*Holt and James* [2001]

[a]All quasigeoid models were equally arranged on the grid delimited by $57^\circ \le \varphi \le 73.99^\circ$, $-11^\circ \le \lambda \le 36^\circ$, and with $0.01^\circ \times 0.02^\circ$ spacing. Next, the geoid values were linearly interpolated to the altimetry and tide-gauge sites (Tables 2, 4, and 5) by nearest neighbor.
[b]DTU13MSS was linearly interpolated to the altimetry sites (Tables 4 and 5).
[c]All ocean models were linearly interpolated to the altimetry and tide-gauge sites (Tables 2, 4, and 5) by nearest neighbor.
[d]This grid spacing covers the North Atlantic, and gradually spreads to $1^\circ \times 1^\circ$ elsewhere.

Any ocean model including air pressure forcing was corrected for it before being provided to us (Hughes, personal communication, 2015). POLCOMS also includes an IB correction as described in section 2.1.2, with a reference pressure of 1012 mbar (J. T. Holt, personal communication, 2015). We used a simple approach to revert the interpolated $MDT_{POLCOMS}$ values. At each tide-gauge site with associated altimetry sites, the IB correction was subtracted. For this we used the single pressure value that was used to correct tide-gauge MSL.

3. Comparative Assessment

We have focused our analysis on the entire Norwegian coast, because it yields the most robust statistics. However, due to the limited spatial coverage of the Jason-2/PISTACH and POLCOMS data sets (sections 2.1.3 and 2.2), we also present results from the regions south and north of 66°N.

3.1. Tide-Gauge MDT

Table 7 shows standard deviations of differences between tide-gauge geodetic and ocean MDTs, using ellipsoidal heights of MSL determined from NN2000 and NN1954 data. We first note that geodetic and ocean MDTs agree on the ∼3–7 cm level. This is an encouraging observation, as similar studies for tide gauges along other coasts have shown an agreement between geodetic and ocean MDTs on the ∼6–14 cm level [e.g., *Woodworth et al.*, 2012, 2015]. *Higginson et al.* [2015] got an agreement between geodetic and ocean MDTs of 2.3 cm along the east coast of North America; however, this number resulted from mean geodetic and ocean MDTs based on 7 geoid models and 11 ocean models, respectively.

On average, NN2000-based geodetic MDTs score better than NN1954-based geodetic MDTs for all ocean models. The lowest standard deviations are found when geodetic MDTs are compared with MDT_{Nemo12}, and the highest when compared with $MDT_{L\text{-}MITc}$. The GOCE R5 models outperform NMA2014.

The along-shore tide-gauge geodetic and ocean MDT profiles are shown in Figure 2. All MDTs show similar general traits; MDT rises 10 cm from Vardø to Kabelvåg, then flattens out to Stavanger, and rises another 10 cm toward Viker. The geodetic profiles present a greater variation in MDT than the ocean models. The ocean profiles (Figure 2a) have an average standard deviation of 5.7 cm, while the average standard deviations of the NN1954-based and NN2000-based geodetic profiles (Figures 2b and 2c) are 7.0 and 5.9 cm, respectively. MDT_{Nemo12} is plotted together with the geodetic MDTs to allow for easier comparison, as it is

Table 7. Standard Deviations of Differences Between Tide-Gauge Geodetic and Ocean MDTs (cm)

	Nemo12	NemoQ	L-MITf	L-MITc	OCC12	POLCOMS[a]
Entire Coast						
NN2000 DIRS+NMA2014	3.8	4.1	4.2	4.9	4.9	
NN2000 TIMS+NMA2014	3.8	4.2	4.3	5.0	5.0	
NN2000 NMA2014	4.4	4.8	4.6	5.5	5.6	
NN2000 EGM2008	3.7	3.5	5.0	4.9	4.5	
NN1954 DIRS+NMA2014	4.2	4.5	5.2	5.4	5.2	
NN1954 TIMS+NMA2014	4.3	4.5	5.3	5.5	5.3	
NN1954 NMA2014	4.6	5.0	5.3	5.8	5.7	
NN1954 EGM2008	5.1	5.0	6.6	6.2	5.7	
North of 66°N						
NN2000 DIRS+NMA2014	5.1	5.1	4.0	5.4	5.9	
NN2000 TIMS+NMA2014	5.1	5.2	4.1	5.6	6.0	
NN2000 NMA2014	5.8	5.9	4.8	6.3	6.7	
NN2000 EGM2008	4.5	4.3	4.3	5.4	5.8	
NN1954 DIRS+NMA2014	4.7	5.0	4.3	4.7	5.5	
NN1954 TIMS+NMA2014	4.8	5.0	4.4	4.8	5.6	
NN1954 NMA2014	5.2	5.4	4.7	5.3	6.1	
NN1954 EGM2008	5.9	5.9	6.2	6.3	6.8	
South of 66°N						
NN2000 DIRS+NMA2014	2.8	2.7	3.7	4.6	3.8	4.2
NN2000 TIMS+NMA2014	2.8	2.7	3.7	4.7	3.9	4.2
NN2000 NMA2014	3.1	3.1	4.1	4.9	4.1	4.5
NN2000 EGM2008	3.1	2.9	3.5	4.7	3.4	4.8
NN1954 DIRS+NMA2014	4.0	4.2	4.8	6.2	5.2	5.1
NN1954 TIMS+NMA2014	4.0	4.3	4.9	6.2	5.2	5.1
NN1954 NMA2014	4.3	4.5	5.1	6.4	5.4	5.4
NN1954 EGM2008	4.3	4.4	4.7	6.3	5.0	5.7

[a]For POLCOMS, the analysis covers the Norwegian coast south of 65°N.

the best-performing ocean model. As concluded from Table 7, the general agreement between geodetic and ocean MDTs increases when using NN2000-based geodetic estimates. We further note that $MDT_{POLCOMS}$ performs on the same level as the remaining ocean MDTs, although it does not observe the 10 cm rise from Stavanger toward Viker.

3.2. Altimetric MDT

Table 8 shows standard deviations between altimetric geodetic and ocean MDTs. Geodetic and ocean MDTs agree on the ~5–11 cm level. To our knowledge, no comparisons of geodetic MDTs based on pointwise altimetry with pure ocean MDTs have been made. However, *Thompson et al.* [2009] compared zonal and meridional sections of ocean and geodetic (computed by subtracting a GRACE-based regional geoid model from an altimetric MSS product) MDT grids in the North Atlantic Ocean, and obtained an agreement

Table 8. Standard Deviations of Differences Between Altimetric Geodetic and Ocean MDTs (cm)

	Nemo12	NemoQ	L-MITf	L-MITc	OCC12		Nemo12	NemoQ	L-MITf	L-MITc	OCC12	POLCOMS[a]
Entire Coast						**South of 66°N**						
envi DIRS+NMA2014	6.4	7.1	8.2	8.7	7.3	envi DIRS+NMA2014	5.2	7.0	7.6	9.6	7.7	5.3
envi TIMS+NMA2014	6.3	7.1	8.2	8.8	7.3	envi TIMS+NMA2014	5.0	7.0	7.6	9.5	7.6	5.1
envi NMA2014	6.6	7.2	8.3	8.7	7.3	envi NMA2014	5.0	6.8	7.2	9.2	7.2	4.8
envi EGM2008	5.7	6.7	6.3	8.1	7.1	envi EGM2008	5.7	6.2	6.0	7.4	7.2	5.5
ctoh DIRS+NMA2014	7.4	8.1	9.3	9.9	8.6	ctoh DIRS+NMA2014	5.9	7.9	8.7	10.5	9.0	6.2
ctoh TIMS+NMA2014	7.4	8.1	9.3	9.9	8.6	ctoh TIMS+NMA2014	5.8	7.9	8.7	10.5	9.0	6.0
ctoh NMA2014	7.6	8.3	9.3	9.9	8.7	ctoh NMA2014	5.6	7.6	8.3	10.1	8.6	5.7
ctoh EGM2008	6.4	7.4	7.2	9.0	8.1	ctoh EGM2008	5.7	6.7	6.9	8.1	8.1	5.6
dtu13 DIRS+NMA2014	5.6	6.5	7.5	8.4	6.7	dtu13 DIRS+NMA2014	5.3	6.6	7.4	9.1	7.1	5.0
dtu13 TIMS+NMA2014	5.5	6.5	7.5	8.5	6.8	dtu13 TIMS+NMA2014	5.2	6.6	7.5	9.1	7.1	4.9
dtu13 NMA2014	5.7	6.5	7.5	8.4	6.7	dtu13 NMA2014	5.2	6.4	7.1	8.7	6.7	4.6
dtu13 EGM2008	6.1	7.1	6.4	8.6	7.6	dtu13 EGM2008	5.4	5.4	5.4	6.5	6.2	4.7
North of 66°N						jas2 DIRS+NMA2014	5.4	6.7	7.6	9.4	7.8	5.4
envi DIRS+NMA2014	7.2	7.3	7.5	7.8	7.0	jas2 TIMS+NMA2014	5.2	6.6	7.5	9.3	7.8	5.2
envi TIMS+NMA2014	7.3	7.3	7.5	7.9	7.0	jas2 NMA2014	5.2	6.4	7.2	9.0	7.4	4.9
envi NMA2014	7.8	7.8	7.9	8.4	7.6	jas2 EGM2008	6.5	6.4	6.6	7.6	7.8	6.1
envi EGM2008	5.2	5.8	6.8	6.1	5.0							
						oce3 DIRS+NMA2014	5.5	6.2	7.0	8.7	7.4	6.1
ctoh DIRS+NMA2014	8.8	8.6	8.7	9.3	8.4	oce3 TIMS+NMA2014	5.4	6.1	7.0	8.7	7.3	5.9
ctoh TIMS+NMA2014	8.8	8.7	8.8	9.4	8.5	oce3 NMA2014	5.3	5.9	6.6	8.3	7.0	5.7
ctoh NMA2014	9.4	9.2	9.3	10.0	9.1	oce3 EGM2008	6.4	5.7	5.7	6.7	7.2	6.7
ctoh EGM2008	6.7	7.0	7.8	7.6	6.4							
						red3 DIRS+NMA2014	5.3	5.4	6.3	8.1	6.6	6.3
dtu13 DIRS+NMA2014	6.0	6.4	7.1	7.3	6.3	red3 TIMS+NMA2014	5.1	5.3	6.3	8.0	6.5	6.1
dtu13 TIMS+NMA2014	6.1	6.4	7.1	7.3	6.4	red3 NMA2014	5.1	5.1	5.9	7.6	6.1	5.9
dtu13 NMA2014	6.5	6.8	7.3	7.8	6.9	red3 EGM2008	6.6	5.3	5.3	6.2	6.7	7.3
dtu13 EGM2008	4.8	5.8	7.2	6.5	5.3							

[a]For POLCOMS, the analysis covers the Norwegian coast south of 65°N.

of 8 cm between the grids. *Woodworth et al.* [2015] obtained an agreement of 6 cm between a geodetic MDT grid (computed by subtracting a DIR5-based geoid from an altimetric MSS product) and an assimilated MDT grid in the Mediterranean. They further conclude that ∼5 cm is a likely general level of agreement between altimetric geodetic and ocean MDT grids. This work shows that pointwise monomission coastal altimetry products give results comparable with the multimission DTU13MSS grid on the ∼5 cm level, which is encouraging.

As with the tide gauges, on average, we observe lowest standard deviations when comparing geodetic MDTs with MDT_{Nemo12}, and highest when comparing with $MDT_{L\text{-}MITc}$. As with the tide-gauge geodetic MDTs, we note that the GOCE R5 models outperform NMA2014. We further observe that $MDT_{POLCOMS}$ performs well, on the level of MDT_{Nemo12}. The poorest altimetry performance is delivered by CTOH, regardless of quasigeoid model.

Figure 3 shows the along-shore altimetric geodetic and ocean MDT profiles for the entire coast. Even though the pattern complexity has increased, it is still possible to infer the MDT rise from Vardø to Kabelvåg, as well as a flattening toward Heimsjø. A distinctive fall of MDT is observed by all MDT models toward Bergen 2. Another fall is observed by MDT_{Nemo12} and the geodetic MDTs from Tregde toward Helgeroa, which is not observed by the remaining ocean models.

In the cases where the distances between two associated MSS sites and the coast differ considerably (e.g., Rørvik 1 and Rørvik 2), so will their MDT value, because the MDT is higher toward the coast. This explains the zigzag pattern we observe when following the profile lines with their alternating order of sites closer to, respectively further off the coast (Figure 3a).

The ocean profiles (Figure 3a) present an average standard deviation of 4.9 cm, while the geodetic profiles (Figures 3b–3d) based on Envisat, CTOH, and DTU13MSS present larger values of 7.0, 8.1, and 6.5 cm, respectively.

The along-shore altimetric geodetic and ocean MDT profiles south of 66°N are shown in Figure 4, beginning at Rørvik 2. In Figure 4a, we see that the course of $MDT_{POLCOMS}$ observes the same fall from Tregde toward Helgeroa as MDT_{Nemo12} and the geodetic MDTs. The course of the Jason-2-based MDT profiles (Figures 4b–4d) generally agrees well with the Envisat-based MDT profiles south of 66°N.

3.3. Comparison of Taylor Diagrams

A Taylor diagram [*Taylor*, 2001] summarizes four model statistics in a single diagram. If we consider two models, the four statistics are the model standard deviations (σ_1, σ_2), their correlation R, and the centered

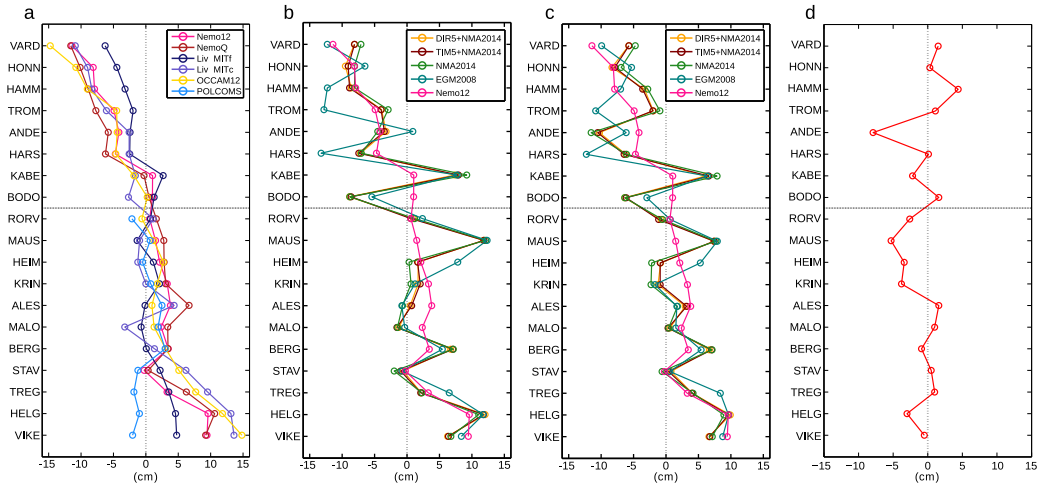

Figure 2. Tide-gauge MDT profiles: (a) ocean, (b) geodetic, using NN1954-originated ellipsoidal heights of MSL, (c) geodetic, using NN2000-originated ellipsoidal heights of MSL, and (d) the difference between NN1954-originated and NN2000-originated MDT. In Figures 2b and 2c, MDT_{Nemo12} is included. The horizontal dashed line denotes 66°N. In all cases, the profile mean has been removed.

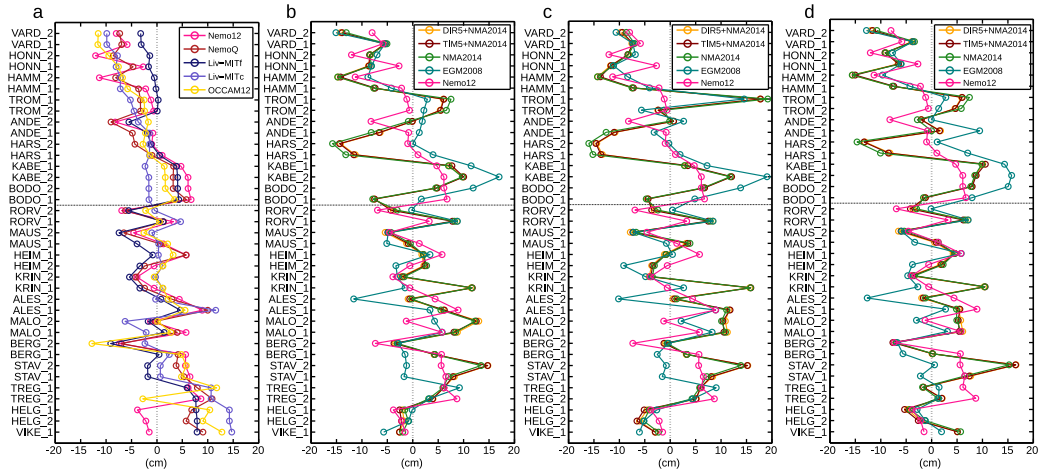

Figure 3. Altimetric MDT profiles along the entire Norwegian coast: (a) ocean, (b) geodetic, using Envisat, (c) geodetic, using CTOH, and (d) geodetic, using DTU13MSS. In Figures 3b–3d, MDT_{Nemo12} is included. The horizontal dashed line denotes 66°N. In all cases, the profile mean has been removed.

root-mean-square (RMS) difference between the models E', related by $E'^2=\sigma_1^2+\sigma_2^2-2\sigma_1\sigma_2 R$. This relation has an analogue in the cosine rule for triangles, which is exploited in the Taylor diagram. It allows for convenient model intercomparison and was applied to MDTs by *Bingham and Haines* [2006].

Figure 5 shows Taylor diagrams where MDT_{Nemo12} has been chosen as the reference model against which all other MDTs are compared. It was chosen because, on average, it is the best-performing ocean model. The model standard deviations are represented as radial distances from the origin, the centered RMS differences are proportional to the distances between reference and test models, and correlations are represented as the azimuthal angle. Consequently, the reference model has a correlation of one.

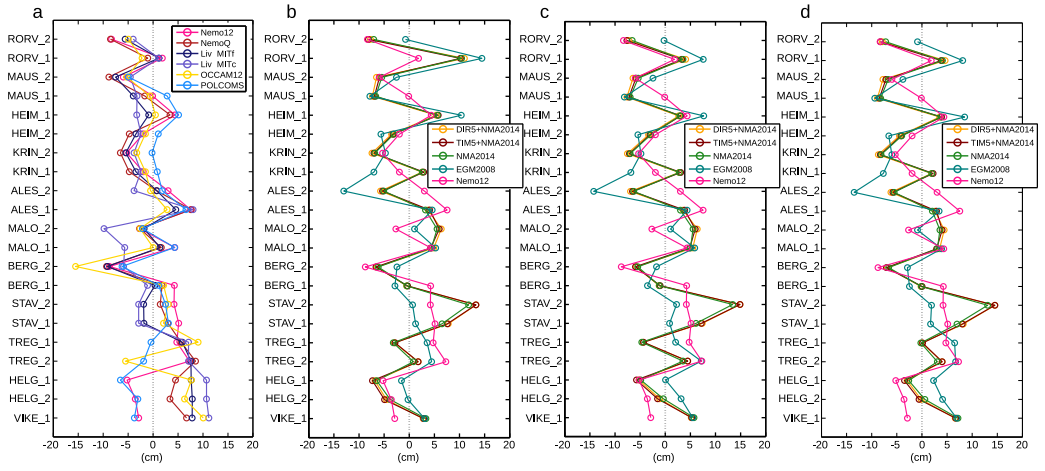

Figure 4. Altimetric MDT profiles along the Norwegian coast south of 66°N: (a) ocean, (b) geodetic, using Jason-2, (c) geodetic, using Ocean3, and (d) geodetic, using Red3. In Figures 4b–4d, MDT_{Nemo12} is included. In all cases, the profile mean has been removed.

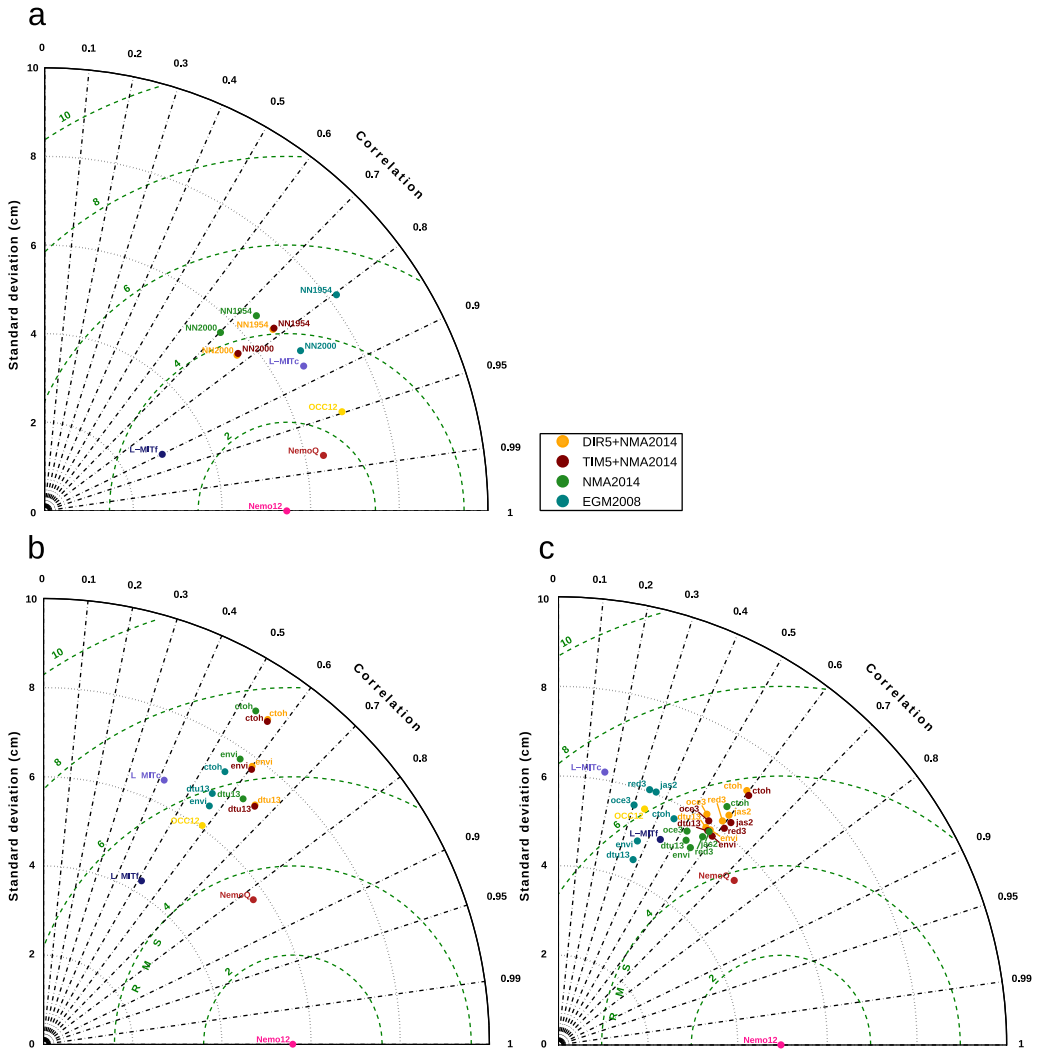

Figure 5. Taylor diagram intercomparison of geodetic and ocean MDTs for tide gauges (a) along the entire Norwegian coast, altimetric MSS sites (b) along the entire Norwegian coast, and (c) south of 66°N. To ease readability, labels for the geoid models incorporated in the geodetic MDTs have been left out of the diagrams; however, this information may be inferred from the legend.

Figure 5a shows the Taylor diagram for tide-gauge geodetic and ocean MDTs along the entire coast. As MDT_{NemoQ} is closely related to the reference model, it consequently has the lowest RMS difference and highest correlation. Geodetic MDTs based on EGM2008 have a higher correlation than the NMA2014-related MDTs, but generally the geodetic MDTs give quite similar results. Almost all MDTs but the NN1954-based geodetic MDTs lie within an RMS of 4 cm.

Figures 5b and 5c show results from the altimetric geodetic and ocean MDTs along the entire coast as well as south of 66°N. We observe that the ocean MDTs are more similar to MDT_{Nemo12} considering the entire

coast than south of 66°N. Furthermore, the signal standard deviations of the geodetic MDTs are lower south of 66°N than for the entire coast, suggesting that the geodetic MDTs are a little smoother in the south. This explains why the MDT values in Table 8 vary primarily by geodetic MDT north of 66°N, while varying primarily by ocean MDT south of 66°N.

4. Discussion

4.1. Error Budgeting and Significance of Results

Using the standard deviations of differences between geodetic and ocean MDTs (Tables 7 and 8) we derive error estimates for both. We relate the empirical standard deviation of differences, $s=\sqrt{\sum_{i=1}^{n}(\epsilon_i-\bar{\epsilon})^2/(n-1)}$, where $\epsilon=\mathrm{MDT}-(h-\zeta)$, to the formal error propagation $\sigma=\sqrt{\sigma_{\mathrm{MDT}}^2+\sigma_h^2+\sigma_\zeta^2}$. Here we take MDT to be the ocean model, h to be the ellipsoidal height of tide-gauge MSL or altimetric MSS, and ζ to be the height anomaly. Consequently, σ_{MDT}, σ_h, and σ_ζ are the error contributions from ocean model, ellipsoidal height, and quasigeoid model, respectively. By this approach, we assume that the individual components are uncorrelated, because they are derived from independent methods.

We turn to Table 1, and, assuming equal error contribution from quasigeoid, leveling and GNSS, derive an estimate $\sigma_\zeta \approx 2$ cm. This estimate is based on the NMA2014-related quasigeoids. We did not consider EGM2008 because we trace its worse performance to the slightly lower resolution compared to the NMA2014-related quasigeoids. Furthermore, we take $\sigma_h \approx 1$ cm, corresponding to the lower HREF error estimate of *Mysen* [2014]. Using these numbers together with the standard deviations s from Table 7 (entire coast, and NN2000), we get $\sigma_{\mathrm{MDT}} \approx 3-5$ cm, depending on the ocean model. Because σ_ζ is derived from an assumption of equal error contribution from quasigeoid, leveling, and GNSS, rather than from error propagation of the heterogeneous gravity data included in the quasigeoid model, we take it to be an optimistic estimate. Furthermore, the HREF error estimate σ_h is inherently optimistic due to different aspects of the estimation method of *Mysen* [2014]. Consequently, as we regard our estimates of σ_ζ and σ_h as optimistic, σ_{MDT} is a pessimistic estimate. Alternatively, assuming equal error contributions from σ_ζ, σ_h, and σ_{MDT}, we get $\sigma_{\mathrm{MDT}} \approx 2-3$ cm.

It is more challenging to assess the quasigeoid error off the coast. Therefore, we choose the more conservative estimate of $\sigma_\zeta \approx 3$ cm. We do not expect the ocean models to be more accurate at the tide gauges than at the altimetry sites (in fact, the opposite is more likely). Consequently we adopt $\sigma_{\mathrm{MDT}} \approx 2-5$ cm. Using these numbers together with the standard deviations s from Table 8 (entire coast, Nemo12), we get $\sigma_h \approx 1-7$ cm for the altimetric MSS. We have chosen Nemo12 because it shows the lowest s values, and larger values are attributed to σ_{MDT} and not σ_h. Alternatively, if we assume equal error contributions from σ_ζ, σ_h, and σ_{MDT}, we get $\sigma_{\mathrm{MDT}} \approx 3-4$ cm.

When summarizing the error estimates at the tide-gauge and altimetry sites, we conclude that $\sigma_\zeta \leq 4$ cm, $\sigma_{\mathrm{MDT}} \leq 5$ cm, and $\sigma_h \leq 7$ cm.

We further want to comment on the significance of our results. Looking at the Taylor diagram at the altimetry sites (Figure 5b), we see that the signal standard deviation of the geodetic MDTs is roughly 7 cm. From our altimetry error estimates, we derive an error standard deviation for the geodetic MDTs of 2–8 cm, which gives a signal-to-noise ratio (SNR) of 1–3. This suggests that our results at the altimetry sites are statistically significant. From Figure 5b, we also find a ∼60% correlation of the geodetic MDTs with $\mathrm{MDT}_{\mathrm{Nemo12}}$. This value proves actual correlation with a certainty of 99%, as confirmed by a correlation significance test. At the tide gauges (Figure 5a), the signal standard deviation of the geodetic MDTs is roughly 6 cm. The tide-gauge error estimates give an error standard deviation of 2–4 cm for the geodetic MDTs, again resulting in an SNR of 1–3. Furthermore, we observe an even higher ∼80% correlation of the geodetic MDTs with $\mathrm{MDT}_{\mathrm{Nemo12}}$ than at the altimetry sites. Thus, we consider our results statistically significant.

4.2. Tide-Gauge MDT

Considering the assessment of geodetic MDTs at Norwegian tide gauges, standard deviations of differences suggest an improvement when using data based on the new height system, NN2000. North of 66°N, improvement is less evident. We note a possible explanation for the worse fit of tide-gauge geodetic MDTs

north of 66°N. As mentioned, Norway is in the process of changing its height system from NN1954 to NN2000, and at the time of writing, no municipalities north of 66°N have initiated the change. Consequently, HREF2014c should not be considered a final HRCS for NN2000, and changes are expected in future versions (D. I. Lysaker, NMA, personal communication, 2015). As the largest discrepancies between NN1954 and NN2000 are found in Northern Norway, this might be part of the explanation. We thus expect that with the finalization of the height system change, better results will be obtained when using data based on the new height system, NN2000. Better still, using GNSS to directly observe ellipsoidal height of MSL at the tide gauges would eliminate this uncertainty altogether.

4.3. Altimetric MDT

Regarding the altimetry-based geodetic MDTs, we note that those based on DTU13MSS perform well in all regions. One of the reasons for the good performance of DTU13MSS could be that it contains an increased amount of altimetry observations from several altimeters, including the more recent Cryosat-2 mission. Another reason could be that it is a gridded product. Gridding will to some extent always imply an unwanted smoothing, as values at equally spaced grid points are estimated from irregularly distributed data through spatiotemporal interpolation. Thus, DTU13MSS may well be more similar to the ocean models, which are also smooth surfaces not only due to their initial model physics and grids but also due to resampling (section 2.2).

We should also mention that *Woodworth et al.* [2015] considered DTU10MSS rather than DTU13MSS in the Mediterranean, as the latter model showed more spatial differences than was expected from the few additional years of observations. Our analysis with DTU10MSS along the Norwegian coast, however, gave slightly worse results than with DTU13MSS, which suggests that DTU13MSS offers an improvement over DTU10MSS along the Norwegian coast.

In general, CTOH performance is poor, which is not easily explained. Part of the explanation may be that CTOH uses the radiometer for the wet tropospheric correction, while Envisat and Jason-2/PISTACH use a composite model, exchanging the radiometer for ECMWF data within 50 km of the coast. However, DTU13MSS also uses the radiometer for the wet tropospheric correction, which suggests that differences in the correction method (radiometer or ECMWF) are of minor importance.

The performance of Jason-2/PISTACH corresponds well with Envisat for all ocean models. On average, Ocean3 offers a slight improvement over Jason-2, and Red3 an improvement over Ocean3 (Red3 differs from Jason-2 and Ocean3 in that it uses GIM only for the ionospheric correction, and lacks correction for the sea-state bias). However, we conclude that improvements due to retracking are small compared with the differences observed between different quasigeoid models.

From the Taylor diagram intercomparison at the altimetry sites, we observe that geodetic MDTs based on both pointwise and gridded altimetry correlate more with MDT_{Nemo12} than do $MDT_{L\text{-}MITc}$, $MDT_{L\text{-}MITf}$, and MDT_{OCC12}, suggesting a convergence of the geodetic and ocean MDT approaches.

4.4. Characteristics of Coastal MDT in Norway

The tide-gauge and altimetric geodetic MDT profiles generally show a similar pattern (a 10 cm rise toward Kabelvåg, a flattening toward Stavanger, and another 10 cm rise toward Viker), although with some differences. In part, these differences result from the geographic location of the tide-gauge and altimetry sites (Figure 1).

At the tide gauges, the rise from Stavanger southward is evident in all ocean MDTs but $MDT_{POLCOMS}$ (Figure 2). This rise is confirmed by the geodetic MDTs regardless of quasigeoid model or height system, which suggests that the MDT along the southern coast is not well represented in $MDT_{POLCOMS}$. The general tendency of lower MDT values at the altimetry sites further off the coast is evident in all geodetic MDTs and MDT_{Nemo12}, but not in the remaining ocean MDTs (Figure 3). This suggests that the MDT characteristics along the southern coast of Norway are best described by MDT_{Nemo12} as opposed to the other ocean models.

If a tide gauge is located in a protected harbor, or in the vicinity of an estuary, observed MSL may include a steric contribution from river runoff and other coastal processes that the altimetry observations lack. All geodetic MDTs observe large variations in the Lofoten Basin (covered by Kabelvåg and Bodø) that are not

observed by the ocean MDTs. This, however, is an area of considerable dynamic activity in the form of maelstroms and eddies, and the ocean models are likely to have limited validity in this area.

In general, we observe more variability in the geodetic MDTs than in the ocean MDTs. This may be attributed to observation errors in the geodetic MDTs, but also to the smooth characteristics of the ocean models, which have their main application in the open ocean, resolving features at larger spatial scales. Generally, the spatial scale of MDT will depend on the temporal averaging period, as well as the length scale at which geostrophic currents (determined from the MDT inclination) become important. This length scale, known as the Rossby radius of deformation, depends on the Coriolis parameter, and thus varies with latitude (∼200 km close to the equator, ∼10 km at high latitudes). In addition, at the coast, ocean dynamic features not yet fully understood, exist at shorter scales than on the open ocean. Therefore, it is likely that part of the variability observed by geodetic observations comes from actual short-scale ocean dynamics not resolved by the general circulation models.

Consequently, we would expect $MDT_{POLCOMS}$, which takes shorter-scale coastal shelf processes into account, to show a better agreement with the geodetic MDTs than the other ocean MDTs. While scoring well at the altimetry sites, in close agreement with MDT_{Nemo12}, and corresponding well to the geodetic MDTs, it lags behind at the tide gauges.

It generally remains challenging to assess whether geodetic MDT variability is actual ocean signal or short spatial-scale errors in the geodetic observations.

4.5. Quasigeoid Performance

In order to assess the quasigeoid performance, we reconsider the data sources of the quasigeoid models. EGM2008 relies solely on GRACE data up to d/o 70 (∼285 km), and solely on terrestrial gravity information beyond d/o 120 (∼167 km) [*Pavlis et al*., 2012]. NMA2014 is purely based on terrestrial gravity data above d/o 140 (∼140 km), and GOCE DIR4 data below. The GOCE R5 models are dominated by GOCE data up to d/o ∼181 (∼110 km). This can be derived from the empirical relationship $n=1.45\times10^4/r$ between filter radius r and maximum SH degree n, as reported by *Zenner* [2006].

The GOCE R5 quasigeoids offer an improvement over NMA2014. This corresponds to our findings from GNSS/leveling (section 2.1.1). Considering the filter length, the improvement is related to the spectral band between d/o 140 and 180. On average, however, geodetic MDTs based on EGM2008 outperform the NMA2014-based quasigeoids. This contrasts the fact that EGM2008 performs worst in comparison with GNSS/leveling. This can be explained by the different quality of terrestrial gravity data over land and ocean. Undetected systematics in shipborne gravity may degrade the quality of the NMA2014-related quasigeoids over ocean, while EGM2008, which heavily relies on altimetry-derived gravity, is less affected. However, we cannot rule out the possibility that the dependence of EGM2008 on altimetry-derived gravity eliminates short-scale MDT signal in the geodetic MDT. Consequently, EGM2008-based geodetic MDTs are more similar to the smooth ocean MDTs, leading to smaller standard deviations of differences.

5. Conclusions

Returning to the goals of this work, we observe that along the Norwegian coast, geodetic and ocean MDTs agree on the ∼3–7 cm level at the tide gauges, and on the ∼5–11 cm level at the altimetry sites. In the Norwegian coastal area covered in this work, we quantify the ocean MDTs to contribute to the total error budget by 2–5 cm, while satellite altimetry and quasigeoid models contribute by less than 7 cm, respectively 4 cm. From the Taylor diagram intercomparison at the altimetry sites, we observe that geodetic MDTs based on both pointwise and gridded altimetry correlate with MDT_{Nemo12} on a similar level as the ocean models, suggesting a convergence of geodetic and ocean MDT approaches. The GOCE R5 quasigeoids offer an improvement over NMA2014. Over land, both models are superior to EGM2008, while the latter performs best over ocean areas. The dedicated coastal altimetry products generally do not offer an improvement over the conventional products they are based on. Pointwise monomission altimetry products give results comparable with the multimission DTU13MSS grid on the ∼5 cm level. Lacking ellipsoidal heights of MSL directly observed by GNSS, our tide-gauge geodetic MDT estimates rely on different height systems. For most sites, better results are obtained when using the new height system, NN2000. However, we stress the

importance of directly observing ellipsoidal heights of MSL at tide gauges by GNSS, thus ruling out possible distortions from leveling and quasigeoid errors.

Acknowledgments
We would like to thank O. C. D. Omang at the Norwegian Mapping Authority, for providing a set of GNSS/leveling points, the NMA2014 regional quasigeoid model for Norway, as well as valuable information regarding its determination. We further appreciate helpful comments from P. L. Woodworth at the National Oceanography Centre during the preparation of this paper. Thanks also go to C. W. Hughes at the National Oceanography Centre, for providing a suite of numerical ocean models. Taylor diagrams were created using G. Maze's MATLAB® script, at http://www.mathworks.com/matlabcentral/fileexchange/20559-taylor-diagram. Figure 1 was created using the M_Map package (http://www.eos.ubc.ca/~rich/map.html), with coastlines and political boundaries from the National Oceanic and Atmospheric Administration (http://www.ngdc.noaa.gov/mgg/shorelines/gshhs.html) and Natural Earth (http://www.naturalearthdata.com), respectively. The GGMs are available through the International Centre for Global Earth Models (ICGEM), at http://icgem.gfz-potsdam.de, and ACE2 is available at http://tethys.eaprs.cse.dmu.ac.uk/ACE2. Data used to produce Figures 2–5 and Tables 7–8 are available in the supporting information Tables S1 and S2. We further acknowledge the open data policies of the PSMSL, the Technical University of Denmark, the European Space Agency, the AVISO portal of CNES and CTOH, and MET Norway. This work is part of the Norwegian University of Life Science's GOCODYN project, supported by the Norwegian Research Council under project number 231017. Finally, we would like to thank Don Chambers and two anonymous reviewers for helpful comments that greatly improved the manuscript.

References

Ågren, J., and R. Svensson (2007), Postglacial land uplift model and system definition for the new Swedish height system RH2000, in *Reports in Geodesy and Geographical Information Systems*, 123 pp., Lantmäteriet, Gävle, Sweden.

Albertella, A., R. Savcenko, T. Janjić, R. Rummel, W. Bosch, and J. Schröter (2012), High resolution dynamic ocean topography in the Southern Ocean from GOCE, *Geophys. J. Int.*, *190*, 922–930, doi:10.1111/j.1365-246X.2012.05531.x.

Andersen, O. B., and P. Knudsen (2009), DNSC08 mean sea surface and mean dynamic topography models, *J. Geophys. Res.*, *114*, C11001, doi:10.1029/2008JC005179.

Andersen, O. B., L. Stenseng, and P. Knudsen (2013), The DTU13 global mean sea surface from 20 years of satellite altimetry, paper presented at the Ocean Surface Topography Science Team Meeting, Joint Office For Science Support (JOSS), Boulder, Colo., 8–11 Oct.

Baart, F., P. H. A. J. M. van Gelder, J. de Ronde, M. van Koningsveld, and B. Wouters (2012), The effect of the 18.6-year lunar nodal cycle on regional sea-level rise estimates, *J. Coastal Res.*, *28*(2), 511–516, doi:10.2112/JCOASTRES-D-11-00169.1.

Berry, P. A. M., R. G. Smith, and J. Benveniste (2010), ACE2: The New Global Digital Elevation Model, in *Gravity, Geoid and Earth Observation, Int. Assoc. Geod. Symp.*, vol. 135, edited by S. P. Mertikas, pp. 231–237, Springer, Berlin, doi:10.1007/978-3-642-10634-7_30.

Bingham, R. J., and K. Haines (2006), Mean dynamic topography: Intercomparisons and errors, *Philos. Trans. R. Soc. A*, *364*(1841), 903–916, doi:10.1098/rsta.2006.1745.

Bingham, R. J., P. Knudsen, O. Andersen, and R. Pail (2011), An initial estimate of the North Atlantic steady-state geostrophic circulation from GOCE, *Geophys. Res. Lett.*, *38*, L01606, doi:10.1029/2010GL045633.

Blaker, A. T., J. J.-M. Hirschi, G. McCarthy, B. Sinha, S. Taws, R. Marsh, A. Coward, and B. de Cuevas (2015), Historical analogues of the recent extreme minima observed in the Atlantic Meridional overturning circulation at 26°N, *Clim. Dyn.*, *44*, 457–473, doi:10.1007/s00382-014-2274-6.

Brockmann, J. M., N. Zehentner, E. Höck, R. Pail, I. Loth, T. Mayer-Gürr, and W.-D. Schuh (2014), EGM_TIM_RL05: An independent geoid with centimeter accuracy purely based on the GOCE mission, *Geophys. Res. Lett.*, *41*, 8089–8099, doi:10.1002/2014GL061904.

Bruinsma, S. L., C. Förste, O. Abrikosov, J.-C. Marty, M.-H. Rio, S. Mulet, and S. Bonvalot (2013), The new ESA satellite-only gravity field model via the direct approach, *Geophys. Res. Lett.*, *40*, 3607–3612, doi:10.1002/grl.50716.

Cartwright, D. E., and A. C. Edden (1973), Corrected tables of tidal harmonics, *Geophys. J. R. Astron. Soc.*, *23*(1), 45–73, doi:10.1111/j.1365-246X.1973.tb03420.x.

Cartwright, D. E., and R. J. Tayler (1971), New computations of the tide-generating potential, *Geophys. J. R. Astron. Soc.*, *33*(3), 253–264, doi:10.1111/j.1365-246X.1971.tb01803.x.

Denker, H. (2013), Regional gravity field modeling: Theory and practical results, in *Sciences of Geodesy – II*, edited by G. Xu, pp. 185–291, Springer, Berlin, doi:10.1007/978-3-642-28000-9_5.

Drinkwater, M. R., R. Floberghagen, R. Haagmans, D. Muzi, and A. Popescu (2003), GOCE: ESA's first Earth Explorer Core mission, in *Earth Gravity Field from Space — From Sensors to Earth Sciences, Space Sciences Series of ISSI*, edited by G. Beutler et al., pp. 419–432, Springer, Dordrecht, Netherlands, doi:10.1007/978-94-017-1333-7_36.

Ekman, M. (1989), Impacts of geodynamic phenomena on systems for height and gravity, *Bull. Geod.*, *63*, 281–296, doi:10.1007/BF02520477.

Featherstone, W. E. (2008), GNSS-based heighting in Australia: Current, emerging and future issues, *J. Spatial Sci.*, *53*(2), 115–133, doi:10.1080/14498596.2008.9635153.

Featherstone, W. E., and M. S. Filmer (2012), The north-south tilt in the Australian Height Datum is explained by the ocean's mean dynamic topography, *J. Geophys. Res.*, *117*, C08035, doi:10.1029/2012JC007974.

Filmer, M. S. (2014), Using models of the ocean's mean dynamic topography to identify errors in coastal geodetic levelling, *Mar. Geod.*, *37*, 47–64, doi:10.1080/01490419.2013.868383.

Forsberg, R., and W. Featherstone (1998), Geoids and cap sizes, in *Geodesy on the Move, Int. Assoc. Geod. Symp.*, vol. 119, edited by R. Forsberg et al., pp. 194–200, Springer, Berlin, doi:10.1007/978-3-642-72245-5_27.

Gommenginger, C., P. Thibaut, L. Fenoglio-Marc, G. Quartly, X. Deng, J. Gómez-Enri, P. Challenor, and Y. Gao (2011), Retracking altimeter waveforms near the coasts, in *Coastal Altimetry*, edited by S. Vignudelli et al., pp. 61–101, Springer, Berlin, doi:10.1007/978-3-642-12796-0_4.

Griesel, A., M. R. Mazloff, and S. T. Gille (2012), Mean dynamic topography in the Southern Ocean: Evaluating Antarctic Circumpolar Current transport, *J. Geophys. Res.*, *117*, C01020, doi:10.1029/2011JC007573.

Gruber, T. (2014), GOCE gravity field models—Overview and performance analysis, paper presented at the 5th International GOCE User Workshop, European Space Agency, Paris, 25–28 Nov., European Space Agency.

Haagmans, R., E. de Min, and M. von Gelderen (1993), Fast evaluation of convolution integrals on the sphere using 1D FFT, and a comparison with existing methods for Stokes's integral, *Manuscr. Geod.*, *18*, 227–241.

Haines, K., J. A. Johannessen, P. Knudsen, D. Lea, M.-H. Rio, L. Bertino, F. Davidson, and F. Hernandez (2011), An ocean modelling and assimilation guide to using GOCE geoid products, *Ocean Sci.*, *7*, 151–164, doi:10.5194/os-7-151-2011.

Higginson, S., K. R. Thompson, P. L. Woodworth, and C. W. Hughes (2015), The tilt of mean sea level along the east coast of North America, *Geophys. Res. Lett.*, 1471–1479, doi:10.1002/2015GL063186.

Hofmann-Wellenhof, B., and H. Moritz (2005), *Physical Geodesy*, Springer, Wien, Austria.

Hofmann-Wellenhof, B., H. Lichtenegger, and J. Collins (2001), *Global Positioning System: Theory and Practice*, Springer, Wien, Austria.

Holgate, S. J., A. Matthews, P. L. Woodworth, L. J. Rickards, M. E. Tamisiea, E. Bradshaw, P. R. Foden, K. M. Gordon, S. Jevrejeva, and J. Pugh (2013), New data systems and products at the Permanent Service for Mean Sea Level, *J. Coastal Res.*, *29*, 493–504, doi:10.2112/JCOASTRES-D-12-00175.1.

Holt, J. T., and I. D. James (2001), An s coordinate density evolving model of the northwest European continental shelf: 1. Model description and density structure, *J. Geophys. Res.*, *106*, 14,015–14,034, doi:10.1029/2000JC000304.

Hughes, C. W., R. J. Bingham, V. Roussenov, J. Williams, and P. L. Woodworth (2015), The effect of Mediterranean exchange flow on European time mean sea level, *Geophys. Res. Lett.*, *42*, 466–474, doi:10.1002/2014GL062654.

Jayne, S. R. (2006), Circulation of the North Atlantic Ocean from altimetry and the Gravity Recovery and Climate Experiment geoid, *J. Geophys. Res.*, *111*, C03005, doi:10.1029/2005JC003128.

Jekeli, C. (1981), Alternative methods to smooth the Earth's gravity field, *Tech. Rep. 327*, Dept. of Geod. Sci. and Surv., Ohio State Univ., Columbus.

Johannessen, J. A., et al. (2014), Toward improved estimation of the dynamic topography and ocean circulation in the high latitude and Arctic ocean: The importance of GOCE, *Surv. Geophys.*, *35*, 661–679, doi:10.1007/s10712-013-9270-y.

Kierulf, H. P., M. Ouassou, and M. J. R. Simpson (2013), A continuous velocity field for Norway, *J. Geod.*, *87*, 337–349, doi:10.1007/s00190-012-0603-2.
Lysaker, D. I., O. C. D. Omang, B. R. Pettersen, and D. Solheim (2007), Quasigeoid evaluation with improved levelled height data for Norway, *J. Geod.*, *81*, 617–627, doi:10.1007/s00190-006-0129-6.
Madec, G. (2008), *NEMO ocean engine, Note du Pole de modélisation*, vol. 27, pp. 1288–1619, Inst. Pierre-Simon Laplace, Paris, France.
Marsh, R., B. A. de Cuevas, A. C. Coward, J. Jacquin, J. J.-M. Hirschi, Y. Aksenov, A. J. G. Nurser, and S. A. Josey (2009), Recent changes in the North Atlantic circulation simulated with eddy-permitting and eddy-resolving ocean models, *Ocean Modell.*, *28*, 226–239, doi:10.1016/j.ocemod.2009.02.007.
Marshall J., C. Hill, L. Perelman, and A. Adcroft (1997a), Hydrostatic, quasi-hydrostatic, and nonhydrostatic ocean modelling, *J. Geophys. Res.*, *102*, 5733–5752, doi:10.1029/96JC02776.
Marshall J., A. Adcroft, C. Hill, L. Perelman, and C. Heisey (1997b), A finite-volume, incompressible Navier Stokes model for studies of the ocean on parallel computers, *J. Geophys. Res.*, *102*, 5753–5766, doi:10.1029/96JC02775.
Mercier, F., et al. (2008), Improved Jason-2 altimetry products for coastal zones and continental waters (PISTACH project), paper presented at the Ocean Surface Topography Science Team Meeting, National Aeronautics and Space Administration, National Oceanic and Atmospheric Administration, Centre national d'études spatiales, European Space Agency, Nice, 10–15 Nov, Nice, France.
Mork, K. A., and Ø. Skagseth (2010), A quantitative description of the Norwegian Atlantic Current by combining altimetry and hydrography, *Ocean Sci.*, *6*, 901–911, doi:10.5194/os-6-901-2010.
Mysen, E. (2014), On the computation of reliable formal uncertainties in the densification of GPS-levelling networks by least-squares collocation, *J. Geod.*, *88*, 917–926, doi:10.1007/s00190-014-0732-x.
Ollivier, A., and M. Guibbaud (2012), Envisat RA2/MWR reprocessing impact on ocean data, technical report ESA CLS.DOS/NT/12.064, Collect. Localisation Satell., Ramonville St-Agne, France.
Omang, O. C. D., and R. Forsberg (2002), The northern European geoid: A case study on long-wavelength geoid errors, *J. Geod.*, *76*, 369–380, doi:10.1007/s00190-002-0261-x.
Pavlis, N. K., S. A. Holmes, S. C. Kenyon, and J. K. Factor (2012), The development and evaluation of the Earth Gravitational Model 2008 (EGM2008), *J. Geophys. Res.*, *117*, B04406, doi:10.1029/2011JB008916.
Petit, G., and B. Luzum (eds.) (2010), IERS Conventions (2010), *IERS Tech. Note 36*, 179 pp., Verlag des Bundesamts für Kartographie und Geod., Frankfurt am Main, Germany.
Prandi, P., M. Ablain, A. Cazenave, and N. Picot (2012), A new estimation of mean sea level in the Arctic Ocean from satellite altimetry, *Mar. Geod.*, *35*(S1), 61–82, doi:10.1080/01490419.2012.718222.
Pugh, D., and P. L. Woodworth (2014), *Sea-Level Science: Understanding Tides, Surges, Tsunamis and Mean Sea-Level Changes*, Cambridge Univ. Press, Cambridge, U. K.
Ray, R. D., G. D. Egbert, and S. Y. Erofeeva (2011), Tide predictions in shelf and coastal waters: Status and prospects, in *Coastal Altimetry*, edited by S. Vignudelli et al., pp. 191–216, Springer, Berlin, doi:10.1007/978-3-642-12796-0_8.
Rhines, P., S. Häkkinen, and S. A. Josey (2008), Is oceanic heat transport significant in the climate system?, in *Arctic-Subarctic Ocean Fluxes*, edited by R. R. Dickson et al., pp. 87–109, Springer, Dordrecht, Netherlands, doi:10.1007/978-1-4020-6774-7_5.
Roblou, L., J. Lamouroux, J. Bouffard, F. Lyard, M. Le Hénaff, A. Lombard, P. Marsalaix, P. De Mey, and F. Birol (2011), Post-processing altimeter data toward coastal applications and integration into coastal models, in *Coastal Altimetry*, edited by S. Vignudelli et al., pp. 217–246, Springer, Berlin, doi:10.1007/978-3-642-12796-0_9.
Rothacher, M. (2002), Estimation of station heights with GPS, in *Vertical Reference Systems*, edited by H. Drewes et al., pp. 81–90, Springer, Berlin, doi:10.1007/978-3-662-04683-8_17.
Rülke, A., G. Liebsch, M. Sacher, U. Schäfer, U. Schirmer, and J. Ihde (2012), Unification of European height system realizations, *J. Geod. Sci.*, *2*, 343–354, doi:10.2478/v10156-012-0004-8.
Rummel, R. (2012), Height unification using GOCE, *J. Geod. Sci.*, *2*, 355–362, doi:10.2478/v10156-011-0047-2.
Sideris, M. G. (2013), Geoid Determination by FFT Techniques, in *Geoid Determination, Lecture Notes in Earth System Sciences*, edited by F. Sansò and M. G. Sideris, pp. 453–516, Springer, Berlin, doi:10.1007/978-3-540-74700-0_10.
Skagseth, Ø., K. F. Drinkwater, and E. Terrile (2011), Wind- and buoyancy-induced transport of the Norwegian Coastal Current in the Barents Sea, *J. Geophys. Res.*, *116*, C08007, doi:10.1029/2011JC006996.
Smith, D. M., and J. M. Murphy (2007), An objective ocean temperature and salinity analysis using covariances from a global climate model, *J. Geophys. Res.*, *112*, C02022, doi:10.1029/2005JC003172.
Solheim, D. (2000), New height reference surfaces for Norway, in *Report on the Symposium of the IAG Subcommission for Europe (EUREF) in Tromsø*, edited by J. A. Torres and H. Hornik, pp. 154–158, Verlag der Bayer. Akad. der Wiss., Munich, Germany, 22–24 June.
Soussi, B., M. Roca, D. Cotton, and P. Féménias (2009), *Envisat RA-2/MWR Level 2 User Manual*, version 1.3, 162 pp., European Space Agency, Noordwijk, Netherlands.
Šprlák, M., C. Gerlach, and B. R. Pettersen (2015), Validation of GOCE global gravitational field models in Norway, *Newton's Bull.*, *5*, 3–12, ISSN 1810-8555.
Taylor, K. (2001), Summarizing multiple aspects of model performance in a single diagram, *J. Geophys. Res.*, *106*, 7183–7192, doi:10.1029/2000JD900719.
Thompson, K. R., J. Huang, M. Véronneau, D. G. Wright, and Y. Lu (2009), Mean surface topography of the northwest Atlantic: Comparison of estimates based on satellite, terrestrial gravity, and oceanographic observations, *J. Geophys. Res.*, *114*, C07015, doi:10.1029/2008JC004859.
Vestøl, O. (2006), Determination of Postglacial Land Uplift in Fennoscandia from Leveling, Tide-gauges and Continuous GPS Stations using Least Squares Collocation, *J. Geod.*, *80*, 248–258, doi:10.1007/s00190-006-0063-7.
Wahr, J. M. (1985), Deformation induced by polar motion, *J. Geophys. Res.*, *90*, 9363–9368, doi:10.1029/JB090iB11p09363.
Webb, D. J., A. C. Coward, B. A. de Cuevas, and C. S. Gwilliam (1997), A multiprocessor ocean general circulation model using message passing, *J. Atmos. Oceanic Technol.*, *14*, 175–182, doi:10.1175/1520-0426(1997)014 < 0175:AMOGCM > 2.0.CO;2.
Wong, L., and R. Gore (1969), Accuracy of geoid heights from modified Stokes kernels, *Geophys. J. R. Astron. Soc.*, *18*, 81–91.
Woodworth, P. L. (2012), A note on the nodal tide in sea level records, *J. Coastal Res.*, *28*(2), 316–323, doi:10.2112/JCOASTRES-D-11A-00023.1.
Woodworth, P. L., C. Hughes, R. J. Bingham, and T. Gruber (2012), Towards worldwide height system unification using ocean information, *J. Geod. Sci.*, *2*, 302–318, doi:10.2478/v10156-012-0004-8.
Woodworth, P. L., M. Gravelle, M. Marcos, G. Wöppelmann, and C. W. Hughes (2015), The status of measurement of the Mediterranean mean dynamic topography by geodetic techniques, *J. Geod.*, *89*, 1–17, doi:10.1007/s00190-015-0817-1.
Wunsch, C., and D. Stammer (1997), Atmospheric loading and the oceanic "inverted barometer" effect, *Rev. Geophys.*, *35*, 79–107, doi:10.1029/96RG030337.
Zenner, L. (2006), Zeitliche Schwerefeldvariationen aus GRACE und Hydrologiemodellen, diploma thesis, Inst. für Astron. und Phys. Geod., Tech. Univ. München, Munich, Germany.

Paper B

Journal of Geodynamics 102 (2016) 83–94

Contents lists available at ScienceDirect

Journal of Geodynamics

journal homepage: http://www.elsevier.com/locate/jog

Absolute gravity observations in Norway (1993–2014) for glacial isostatic adjustment studies: The influence of gravitational loading effects on secular gravity trends

Vegard Ophaug[a,*], Kristian Breili[a,b], Christian Gerlach[a,c], Jon Glenn Omholt Gjevestad[a], Dagny Iren Lysaker[b], Ove Christian Dahl Omang[b], Bjørn Ragnvald Pettersen[a]

[a] Department of Mathematical Sciences and Technology, Norwegian University of Life Sciences (NMBU), Ås, Norway
[b] Geodetic Institute, Norwegian Mapping Authority, Hønefoss, Norway
[c] Commission of Geodesy and Glaciology, Bavarian Academy of Sciences and Humanities, Munich, Germany

ARTICLE INFO

Article history:
Received 16 April 2016
Received in revised form 4 August 2016
Accepted 10 September 2016
Available online 24 September 2016

Keywords:
Absolute gravity
Ocean tide loading
Non-tidal ocean loading
Atmospheric effect
Global hydrological effect
Time-variable gravity
Land uplift
Glacial isostatic adjustment
Gravity-to-height ratios

ABSTRACT

We have compiled and analyzed FG5 absolute gravity observations between 1993 and 2014 at 21 gravity sites in Norway, and explore to what extent these observations are applicable for glacial isostatic adjustment (GIA) studies. Where available, raw gravity observations are consistently reprocessed. Furthermore, refined gravitational corrections due to ocean tide loading and non-tidal ocean loading, as well as atmospheric and global hydrological mass variations are computed. Secular gravity trends are computed using both standard and refined corrections and subsequently compared with modeled gravity rates based on a GIA model. We find that the refined gravitational corrections mainly improve rates where GIA, according to model results, is not the dominating signal. Consequently, these rates may still be considered unreliable for constraining GIA models, which we trace to continued lack of a correction for the effect of local hydrology, shortcomings in our refined modeling of gravitational effects, and scarcity of observations. Finally, a subset of standard and refined gravity rates mainly reflecting GIA is used to estimate ratios between gravity and height rates of change by ordinary and weighted linear regression. Relations based on both standard and refined gravity rates are within the uncertainty of a recent modeled result.

1. Introduction

Gravimetry considers the observation or measurement of gravity. It may be spaceborne, air- and shipborne, or ground-based (terrestrial), where latter observations may be used to validate results from the first (e.g., Šprlák et al., 2015). Observing temporal gravity changes, and thus changes in the Earth's density distribution, gives insight into a range of geophysical phenomena, e.g., Earth tides, Chandler wobble, core, mantle and tectonic processes (Torge and Müller, 2012), sea-level change (e.g., Simpson et al., 2013), the hydrological cycle (e.g., Pálinkáš et al., 2012), and cryospheric mass variations (e.g., Breili and Rolstad, 2009; Arneitz et al., 2013). Long-term temporal gravity changes can be observed by repeated absolute gravimetry, with an accuracy of $\sim 0.5\,\mu\text{Gal}\,\text{yr}^{-1}$ (where $1\,\mu\text{Gal} = 10^{-8}\,\text{ms}^{-2}$) after 10 years of annual observations (Van Camp et al., 2016).

As opposed to space-geodetic observation techniques such as Global Navigation Satellite Systems (GNSS), absolute gravity (AG) is independent of the terrestrial reference frame, and may thus be used to assess it (e.g., Mazzotti et al., 2011; Collilieux et al., 2014). Furthermore, AG is particularly suitable for monitoring long-term vertical deformation (Van Camp et al., 2011) caused by, e.g., glacial isostatic adjustment (GIA) in North America (e.g., Lambert et al., 2006) and Fennoscandia (e.g., Steffen et al., 2009; Pettersen, 2011; Müller et al., 2012; Timmen et al., 2011, 2015; Nordman et al., 2014), alongside GNSS (e.g., Milne et al., 2001; Vestøl, 2006).

Sasagawa (1989) reviewed the required time span of gravity observations for determining a secular gravity trend with desired accuracy, given by

$$\sigma_{\dot{g}} = \frac{\sigma_g \sqrt{12}}{T\sqrt{N - \frac{1}{N}}}, \tag{1}$$

where $\sigma_{\dot{g}}$ is the trend uncertainty, σ_g is the uncertainty of individual gravity observations, T is the time in years, and N the number of observations. Eq. (1) assumes evenly distributed observations with known uncertainties and a true Gaussian distribution. Steffen

* Corresponding author.
E-mail address: vegard.ophaug@nmbu.no (V. Ophaug).

http://dx.doi.org/10.1016/j.jog.2016.09.001

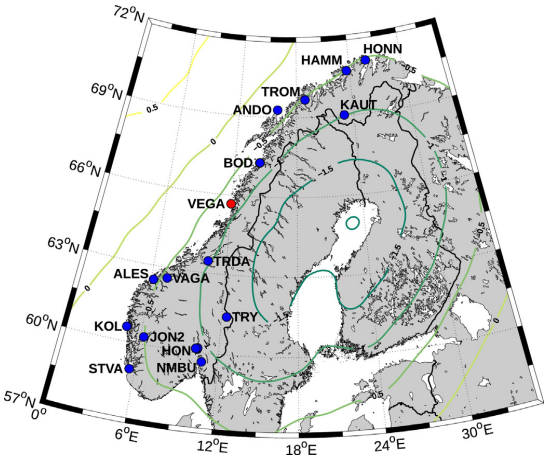

Fig. 1. AG sites in Norway. Blue sites have been observed more than once. The contour lines show modeled gravity rates (μGal yr^{-1}) from the preliminary NKG2016GIA_prel0306 GIA model (H. Steffen, personal communication, 2016). (For interpretation of the references to colour in this figure legend, the reader is referred to the web version of this article.)

and Wu (2011) further state that a secular gravity trend should be known within an uncertainty of ± 0.5 μGal yr^{-1} for crustal deformation studies, which, by Eq. (1), should be achieved by five to six years of annual gravity observations with $\sigma_g \approx 1-2$ μGal.

In 1990, the Nordic Geodetic Commission (NKG, http://www.nordicgeodeticcommission.com/) began establishing a geodetic network for monitoring crustal deformations and sea-level changes in Fennoscandia and Svalbard. As part of this initiative, the first AG observations with modern instruments were performed in Norway in 1991 and 1992 (Roland, 1998). Between 1991-1995, several AG campaigns were conducted in Fennoscandia and Svalbard (Roland, 1998).

Breili et al. (2010) established an AG reference frame for Norway including 16 gravity sites. Since then, it has been extended to include 21 sites, as shown in Fig. 1 and Table 1. Gravity sites marked in blue have been observed more than once, thus only VEGA is excluded from the set of candidates for trend computation. There exist single observations at a few other sites, but these are less likely to be revisited and are therefore not considered in our work. The observation time spans are ~5 years or longer for 18 of the 21 sites (Table 1). Unfortunately, some gravity sites show uneven observation distributions, with typically larger gaps between initial and later observations. Thus we interpret Eq. (1) as a best-case scenario for our data sets.

The present crustal movements of Fennoscandia are largely due to the viscoelastic process of GIA (or postglacial rebound), which has been monitored by geodetic techniques (e.g., Milne et al., 2001; Lidberg et al., 2010; Kierulf et al., 2014; Steffen and Wu, 2011). The GIA pattern of Fennoscandia is shown in Fig. 1.

This work presents results from two decades of AG observations in Norway, and an attempt is made to derive empirical secular gravity trends based on these data. Our main goal is to explore to what extent the gravity trends are applicable for GIA studies. A prerequisite for this goal is a homogenization of the gravity trends through a consistent analysis of the AG data. This is done by investigating to what extent the gravity trends reflect GIA or other geophysical processes. Ideally, careful reduction of other geophysical processes will ultimately give the pure GIA signal. Therefore, we compute refined ocean loading, atmospheric, and global hydrological effects on gravity, and explore how these affect the trends. Finally, the relation between gravity and height rates of change is investigated. The presented gravity values serve as a Norwegian contribution to the Fennoscandian AG project of the Working Group on Geodynamics of the NKG, which aims to combine all Fennoscandian AG data in a joint analysis on postglacial gravity change for the region.

Section 2 covers fundamentals of the AG processing scheme, where Sections 2.1 and 2.2 concern the refined modeling of ocean, atmospheric and hydrological effects on gravity. Secular gravity trends are computed in Section 3, and a subset of reliable trends are used for determining ratios between the rates of change of gravity and height. Results are discussed in Section 4, while Section 5 concludes the work with recommendations for future AG observations in Norway.

2. Processing absolute gravity

All AG observations in this work were made with the FG5 (Niebauer et al., 1995) absolute gravimeter, which has an accuracy of 1–2 μGal. It is ballistic, i.e., it applies the free-fall principle, where a test mass is dropped in vacuum. A laser interferometer and atomic clock are used to obtain time-distance pairs, and Newton's equations of motion are solved to obtain the acceleration. A typical observation campaign lasts 1–2 days, including several hourly gravity sets where a set consists of 50-100 drops of the test mass. With few exceptions, we have used observations made during the same season (between May and September), so as to reduce seasonal effects (e.g., the influence of surface snow cover during winter).

To minimize computational biases, we have adopted a common processing scheme for the data analysis, ensuring consistency with respect to model and setup parameters. All raw gravity observations have been reprocessed using the g9 software (Micro-g LaCoste, 2012), developed by Micro-g LaCoste and bundled with the instrument.

Vertical transfer of the measured gravity value is done using the vertical gravity gradient, which has been determined at each gravity site using the LaCoste & Romberg G-761 relative gravimeter, see Table 1. All AG observations in this work are given at a reference height of 120 cm, close to a point where the influence of the gradient uncertainty on the FG5 is almost zero (Timmen, 2010).

The most important time-variable components of the raw gravity value are reduced in the software by various models, i.e., variations due to solid Earth and ocean tides, polar motion, ocean loading, and atmospheric mass (Timmen, 2010). The atmospheric correction is determined by observed barometric pressure during the observations, which was done at all sites except Hammerfest in 2006.488, where the barometer failed, and pressure observations transferred from a nearby weather station were used instead (Breili et al., 2010). Corrections for polar motion were computed using final polar coordinates from the International Earth Rotation and Reference Systems Service (IERS), at http://datacenter.iers.org.

The bulk of observations presented here were made with the FG5-226 AG meter of the Norwegian University of Life Sciences (NMBU). The rubidium (Rb) frequency standard of the FG5-226 has been calibrated (i.e., compared with a stable reference signal) at convenience since its acquisition in April 2004, and on a regular basis using a portable Rb reference since the oscillator was replaced in May 2007. We have observed it to vary within a range of ~0.02 Hz (where 0.01 Hz roughly corresponds to 2 μGal). While Gitlein (2009) reports a linear drift of the FG5-220 Rb frequency, the FG5-226 Rb frequency development is non-linear, see Fig. 2. A stable frequency was observed with the original oscillator, while the frequency changed by ~−0.005 Hz during the first year after its replacement. Then it was stable within 0.002 Hz until a large

Table 1
Absolute gravity sites in Norway, gravity gradients, and observation spans.

Site	Code	φ (°)	λ (°)	H (m)	$\partial g/\partial H$[a] (μGal cm^{-1})	t_g[b] (yrs)	n_g[c]
Andøya	ANDO	69.278	16.009	370	−4.04 ± 0.01	6.0	5
Bodø Asylhaugen	BODB	67.288	14.434	68	−3.31 ± 0.01	4.0	4
Bodø Bankgata	BODA	67.280	14.395	13	−2.64 ± 0.02	5.1	4
Hammerfest	HAMM	70.662	23.676	17	−3.14 ± 0.01	4.0	2
Honningsvåg	HONN	70.977	25.965	20	−3.54 ± 0.01	4.9	5
Hønefoss AA	HONA	60.124	10.364	108	−2.23 ± 0.04	16.7	2
Hønefoss AB	HONB	60.167	10.389	604	−3.11 ± 0.02	16.7	4
Hønefoss AC	HONC	60.143	10.250	120	−2.80 ± 0.02	15.9	12
Jondal 2	JON2	60.286	6.246	52	−2.53 ± 0.03	9.0	2
Kautokeino	KAUT	69.022	23.020	388	−3.08 ± 0.01	4.9	5
Kollsnes 1	KOL1	60.559	4.836	10	−2.67 ± 0.01	7.7	2
Kollsnes 2	KOL2	60.557	4.828	3	−2.80 ± 0.02	7.7	2
Stavanger AA	STVA	59.018	5.599	55	−2.86 ± 0.08	15.2	7
Tromsø	TROM	69.663	18.940	103	−3.34 ± 0.01	15.9	8
Trondheim AA	TRDA	63.455	10.446	27	−2.95 ± 0.01	14.8	10
Trysil AB	TRYB	61.423	12.381	693	−3.85 ± 0.01	16.8	7
Trysil AC	TRYC	61.423	12.381	693	−3.85 ± 0.01	18.0	17
Vågstranda AA	VAGA	62.613	7.275	38	−3.03 ± 0.01	7.2	4
Vega	VEGA	65.673	11.964	12	−3.44 ± 0.01	–	1
Ålesund	ALES	62.476	6.199	145	−2.90 ± 0.01	7.0	5
Ås NMBU	NMBU	59.666	10.778	95	−2.94 ± 0.01	9.9	10

[a] Determined by repeated observations of the gravity difference between the floor marker and ∼1.4 m above it.
[b] Number of years.
[c] Number of campaigns.

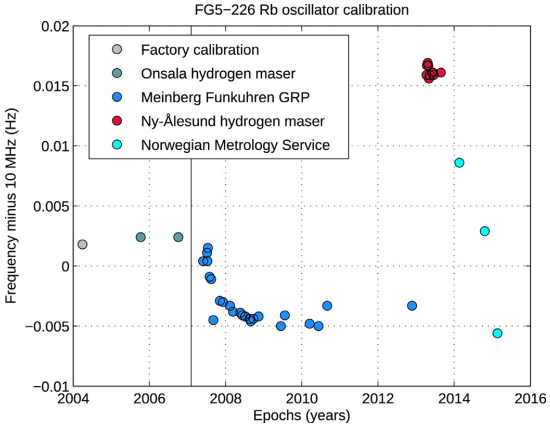

Fig. 2. Calibration of the FG5-226 Rb oscillator. The vertical bar denotes the oscillator replacement (May 2007).

frequency offset of ∼0.02 Hz was observed during the 2013 campaign in Ny-Ålesund in Svalbard. This large offset was due to a helium leakage from the co-located superconducting gravimeter which penetrated the Rb cell. Subsequent frequency calibrations indicate that it has slowly returned to the level prior to the helium contamination. Mäkinen et al. (2015) discuss the effect of helium contamination on Rb frequency references, and underline that large offsets are unproblematic as long as they are known and corrected for. For every observation epoch we have chosen to use the calibrated frequency value closest in time.

We have also used AG observations performed by other agencies and instruments, see Table 2. Raw observations by LM at TRYB, TRYC and VAGA in 2007 have been reprocessed using the above procedure. Observations by IfE and BKG, reported in Gitlein (2009), are given at 120 cm and 125 cm reference heights, respectively. Remaining observations by NOAA and BKG, reported in Roland (1998), are given at a reference height of 100 cm. When needed, the observations were transferred to the 120 cm reference height in two steps. First, the original gradient value was used to transfer gravity from the original reference height (100 or 125 cm) to the actual measurement height. In turn, the new gravity gradients presented in this work (Table 1) were used to transfer gravity from the actual measurement height to the new reference height of 120 cm.

The total uncertainty of an observed gravity value is composed of the gravity measurement precision σ_g, system errors σ_{SYS}, setup error σ_{SETUP}, and vertical transfer (gradient) error $\sigma_{\partial g/\partial H}$ (Niebauer et al., 1995). σ_{SYS} includes (i) instrumental errors (laser, clock, system model) and (ii) modeling errors (barometer, polar motion, Earth tide, ocean loading). Using formal error propagation and thereby assuming the error terms are uncorrelated, the total uncertainty σ_{tot} is given by

$$\sigma_{\mathrm{tot}} = \sqrt{\sigma_g^2 + \sigma_{\mathrm{SYS}}^2 + \sigma_{\mathrm{SETUP}}^2 + \left(\sigma_{\partial g/\partial H} \times H_{\mathrm{TRANS}}\right)^2}, \tag{2}$$

where H_{TRANS} is the difference between actual measurement height (top of the drop) and reference height. The measurement precision σ_g is the standard deviation of the mean of all sets, i.e., the set to set scatter σ_{SET} divided by the square root of the number of sets. We take $\sigma_{\mathrm{SYS}} \approx 1.6$ μGal as given in g9 by the manufacturer. Instead of the $\sigma_{\mathrm{SETUP}} = 1.0$ μGal estimate suggested in g9, however, we adopt the more conservative $\sigma_{\mathrm{SETUP}} = 1.6$ μGal estimate of Van Camp et al. (2005).

We investigated the stability of the FG5-226 by checking for time-variable instrument offsets, trends or drift. Fig. 3 shows the gravity time series using all sufficiently long FG5-226 gravity campaigns at its home site, NMBU. The mean gravity value has been subtracted from each observation, and the observations have been corrected for GIA using a recent modeled linear rate of change in gravity, $\dot{g}_M$, as described in Section 3. We observe the remaining secular gravity trend to be 0.0 ± 0.1 μGal yr^{-1} and insignificant. A similar conclusion can be drawn from Fig. 4, which shows the gravity time series using FG5-226 observations at all gravity sites where more than one observation is available. Here, the mean gravity value of each site has been removed from GIA-corrected site observations, giving several time series which are ultimately plotted in the same figure. Again we observe an insignificant remaining gravity trend of 0.1 ± 0.4 μGal yr^{-1}. Furthermore, we do not observe any nonlinear structure in neither Fig. 3 nor Fig. 4. We therefore conclude that the FG5-226 has no significant drift, which suggests it has been stable throughout the observation span of this work.

Table 2
FG5-generation of absolute gravimeters used in Norway 1993–2014.

Instrument	Agency	Reference
FG5-226 (2004–2014)	Norwegian University of Life Sciences (NMBU), Ås, Norway	This work
FG5-233 (2007)	Lantmäteriet (LM), Gävle, Sweden	
FG5-220 (2003–2007)	Institut für Erdmessung (IfE), Leibniz Universität Hannover, Germany	(Roland, 1998)
FG5-101 (1993–1998), FG5-301 (2003)	Bundesamt für Kartographie und Geodäsie (BKG), Frankfurt, Germany	(Gitlein, 2009)
FG5-102 (1993), FG5-111 (1995, 1997)	National Oceanic and Atmospheric Administration (NOAA), Silver Spring, Maryland, USA	G. Sasagawa, personal communication, 2005

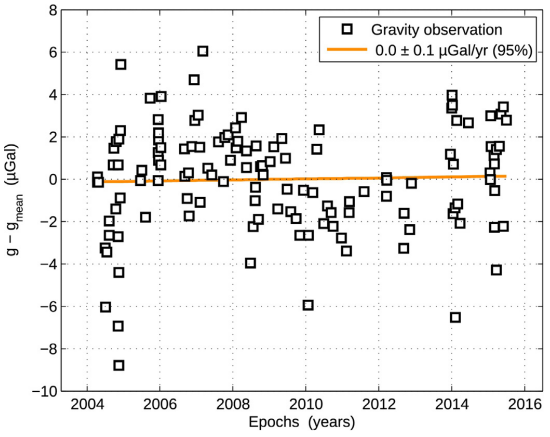

Fig. 3. Stability of the FG5-226 AG meter for the 2004–2015 period, as derived from all repeated gravity observations at NMBU. The gravity time series is reduced for the site-specific mean value and GIA trend, thus showing residual temporal variations including instrumental drift only.

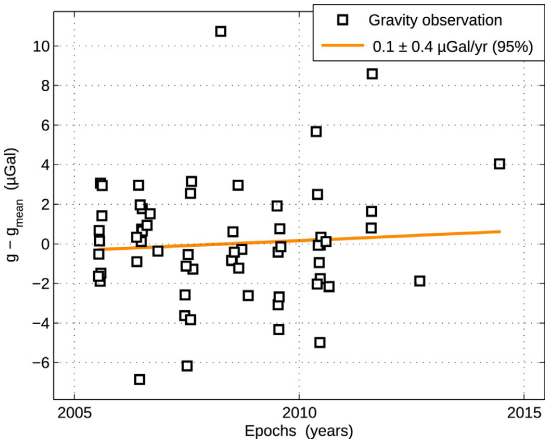

Fig. 4. Stability of the FG5-226 AG meter for the 2005–2014 period, as derived from repeated gravity observations at 20 different sites. The gravity time series of each station is reduced for the site-specific mean value and GIA trend, thus showing residual temporal variations including instrumental drift only.

Standard g9 gravity estimates g_0 and uncertainties are shown in the supplementary data Table S1.

2.1. Ocean loading effects

The majority of the AG sites in Norway are located within 2 km of the coast (see Fig. 1). It has been previously shown that these stations may be strongly influenced by ocean tide loading (OTL) (e.g., Lysaker et al., 2008; Breili, 2009; Breili et al., 2010). In addition, non-tidal variation of sea level due to low barometric pressure and strong winds may affect gravity (Olsson et al., 2009).

OTL and non-tidal loading (NTL) have different characteristics. Along the Norwegian coast, OTL may introduce deterministic semi-diurnal patterns with amplitudes of several µGal in time series of gravity (Lysaker et al., 2008). As a result, the variation of the set to set scatter of a gravity campaign may increase if appropriate OTL corrections are not applied. Furthermore, the campaign averages and derived secular trends may be biased (Timmen et al., 2015). This is particularly relevant for short campaigns not covering an integer multiple of the dominating tidal periods. NTL, on the other hand, is non-deterministic and non-periodic; hence, corrections must be computed from observations. As NTL may be close to constant during a campaign, its impact on gravity is difficult to infer from inspection of the set to set scatter alone.

In the following we investigate different OTL corrections and identify OTL models that are most successful in reducing the campaign set to set scatter (σ_{SET}).

In general, OTL corrections are easily computed from predetermined amplitude and phase coefficients for sinusoids with frequencies matching the major tidal constituents (Petit and Luzum, 2010, Ch. 7). The coefficients are computed by convolving global ocean tide (GOT) models with Green's functions formed by load Love numbers (Farrell, 1972), and are available through M.S. Bos and H.-G. Scherneck's Ocean tide loading provider at http://holt.oso.chalmers.se/loading/. This procedure is also implemented in g9, and for our standard gravity estimates (g_0, see Table S1), OTL was computed with the FES2004 GOT model (Lyard et al., 2006), with the exception of KAUT and TRYB/TRYC, where no OTL effect was computed due to their inland locations.

An important difference between g9 and the OTL provider is that the latter refines the spatial resolution of the GOT model gradually towards the observation point and checks whether new GOT cells are located on land or sea (Penna et al., 2008). g9 also refines the GOT model towards the observation point, but does no land/sea check of the new cells (O. Francis, personal communication, 2016).

With coefficients from the OTL provider we have explored a suite of GOT models, i.e., FES2004, CSR4.0 (Eanes, 1994), DTU10 (Cheng and Andersen, 2010), EOT11 (Savcenko and Bosch, 2011), GOT4.8 (Ray, 1999), NAO99b (Matsumoto et al., 2000), OSU12 (Fok et al., 2012), Schwiderski (Schwiderski, 1980), and TPXO7.2 (Egbert and Erofeeva, 2002). These models were chosen as they represent the latest release from each group available at the OTL provider.

Lysaker et al. (2008) showed that careful local modeling of the OTL correction (direct Newtonian and displacement of the observing point due to load) corresponded better with the OTL signal at selected high-latitude coastal stations in Norway than did the effect computed from GOT models. Thus for FES2012 (produced by Noveltis, Legos, and CLS Space Oceanography Division and distributed

Table 3
The gravitational and loading effects of a one-meter sea-level anomaly within 10 km of coastal gravity sites in Norway, and the amplitude of the M2 tidal constituent for the attraction component. All in μGal.

Code	Gravitation due to a 1 m sea-level anomaly	Loading due to a 1 m sea-level anomaly	Amplitude of M2 (attraction only)
ANDO	3.4	0.20	3.7
BODB	0.6	0.22	1.1
BODA	0.3	0.25	0.8
HAMM	3.1	0.13	3.0
HONN	6.4	0.28	5.9
JON2	4.8	0.16	1.5
KOL1	0.3	0.29	0.1
KOL2	0.5	0.30	0.2
STVA	1.5	0.26	0.2
TROM	1.4	0.14	1.6
TRDA	2.6	0.27	2.1
VAGA	4.2	0.21	3.2
VEGA	0.1	0.17	0.6
ALES	9.8	0.26	6.9

by Aviso, with support from CNES, at http://www.aviso.altimetry.fr) as well as NAO99b, we investigate OTL corrections as computed by an in-house software. The routines closely follow methods used by the OTL provider, although with two important distinctions.

First, we have used a higher-resolution coastline provided by the Norwegian Mapping Authority (NMA), with a level of detail corresponding to national maps in scale 1:50,000, and termed the N50 coastline hereafter. It is complete and includes all islands and reefs along the Norwegian coast with an area greater than 20,000 m^2.

Second, our software allows for choosing which regions are to be included in the convolution. We have used this functionality to investigate the effect of replacing the GOT model with predicted tides based on tide-gauge observations when computing the attraction from the tides in the local zone. The local zone is here defined as the area within 10 km of the gravity site. The method is a development of the one demonstrated by Lysaker et al. (2008). By this approach the gravitational effect of the local tides was modeled by (i) dividing the local zone into spherical sectors, (ii) assigning to each sector a uniform layer of water corresponding to sea level as observed by a local tide gauge, (iii) computing the attraction from each sector, (iv) eliminating sectors on land, and (v) add together the contributions from the individual ocean sectors.

The size of the spherical sectors was adjusted depending on the distance from the observation point, i.e., the length of the outer arc was set to 25, 50, and 200 m in the zones 0–500, 500–1000, and 1000–10,000 m from the observation point, respectively. Each sector was classified as land or ocean by comparing the sector midpoint coordinates with the N50 coastline.

In this work, NTL is the combined effect of gravitational attraction and loading of the seabed due to non-tidal variations in sea level. The gravitational attraction component was modeled by the above procedure, using spherical sectors with a water thickness equal to the difference between actual and predicted sea level as observed by a local tide gauge. For the loading components, we assumed that sea level responds like an inverted barometer (IB, static atmospheric loading effect). This implies that sea level variation due to changing atmospheric pressure does not induce any loading on the sea floor. Thus, before computing the loading effect, observed sea level was corrected for the IB effect using Wunsch and Stammer (1997, Eq. (1)).

We have computed refined OTL and NTL corrections at 14 coastal gravity sites in Norway (Table 3), with remaining sites excluded due to their inland locations. The gravitational and loading effects of a one-meter sea-level anomaly at the coastal gravity sites is shown in Table 3, where the actual gravitational effect may be found by scaling the one-meter effect with the actual sea-level anomaly.

We have used tide-gauge records from the NMA database, with a sampling rate of 10 minutes and all observations referring to present mean sea level (1996-2014 inclusive). Unfortunately, there are no tide gauges within the local zones of JON2, KOL1, KOL2, VEGA, and VAGA. For these sites, sea level was derived by applying site-specific scale factors and time delays to observations from the nearest tide gauge. The scale factors and time delays were obtained from the tide and sea-level web service of the NMA at http://www.kartverket.no/en/sehavniva/.

For each gravity site, we identify the ocean loading corrections that reduce σ_{SET} as much as possible, combining all OTL and NTL corrections. Table 4 shows the average percentage reduction in σ_{SET} for each site. We note that STVA and JON2 stand out with low reductions. For STVA, this is due to a weak OTL signal related to a M2 amphidromic point in the North Sea, giving a locally low tidal range (0.32 m between mean high and mean low tide). At JON2 the average is strongly influenced by the 2005.482 campaign, which has a low σ_{SET} of 1.2 μGal. When applied to this campaign, σ_{SET} increases for several OTL corrections, resulting in a negative reduction of σ_{SET}.

With few exceptions, the OTL corrections computed by g9 reduce σ_{SET} less than the corrections computed by the OTL provider or the in-house software. This also holds for FES2004 as used by both g9 and the OTL provider.

Table 4 suggests that N50 improves the fit between observations and models at several sites (e.g., NAO99b(N50) compared with NAO99b(OTLP), and FES2012(N50) compared with FES2004(OTLP)). Largest improvements are found at HONN and HAMM for NAO99b and FES2012, and at TRDA and VAGA for NAO99b. For these combinations, the N50 coastline reduces σ_{SET} by 7.5% to 22.5%. We expect coastline accuracy to have largest influence on gravity sites that are in immediate vicinity of the ocean. Indeed the sites showing the largest improvements are also among those closest to the ocean, e.g., HAMM and HONN (75 m).

For most stations we observe further improvement when the N50 coastline is combined with local tide-gauge observations. The change in reduced σ_{SET} ranges from −0.5% to 3.7% for NAO99b, and from 0% to 21.3% for FES2012. Both TRDA and JON2 are located inside fjords. Comparing NAO99b and FES2012 at these sites, the largest effect of introducing tide-gauge observations is seen for the latter, suggesting that FES2012 does not capture the tidal regime in these fjords.

Choosing a best-performing model is challenging, as their performance depends on the gravity site. Considering all models, NAO99b and FES2012 in combination with the N50 coastline perform best at 9 out of 14 sites.

Corrections from the OTL provider give the best results at BODA, VEGA, KOL1, JON2, and STVA, where all sites but JON2 have in common that the M2 amplitude of the attraction component is less than 1 μGal (see Table 3). This suggests that careful modeling of the local zone is important mainly at sites with a strong attraction component.

Table S1 shows the final ocean loading corrections for all coastal gravity campaigns, together with standard and refined set to set scatters and the chosen ocean loading model. As the standard gravity estimates from g9, g_0, have already been corrected for OTL (Δg^0_{OTL}), we present the change in OTL correction, i.e., $\delta g_{OTL} = \Delta g_{OTL} - \Delta g^0_{OTL}$, to ease the application of the refined OTL correction Δg_{OTL}. NTL is not treated in g9; hence, the complete correction is listed as Δg_{NTL}.

Typically, OTL and NTL contribute to a campaign gravity value by a few tenths of a μGal, although some corrections reach ∼2 μGal. The refined OTL correction ranges from −0.55 μGal (STVA 2006.855) to 1.81 μGal (ALES 2006.384), while the new NTL

Table 4
Average percentage reduction in set to set scatter (σ_{SET}) for each gravity site, obtained by applying OTL corrections from different models. Also includes NTL. Sites ordered along the coast from north to south. Only campaigns where raw data is available are included.

Code	FES2004 g[a]	FES2004 OTLP[b]	CSR4.0 OTLP	DTU10 OTLP	EOT11a OTLP	GOT4.8 OTLP	OSU12 OTLP	SCHW80 OTLP	TPXO7.2 OTLP	NAO99b OTLP	NAO99b N50[c]	TG+NAO99b N50	FES2012 N50	TG+FES2012 N50
HONN	25.5	34.4	20.9	35.6	35.7	34.1	35.2	37.8	35.0	31.8	57.3	61.0	58.7	60.9
HAMM	34.6	44.2	46.0	44.4	45.1	45.1	42.9	42.9	44.4	47.3	56.8	57.0	58.2	58.3
TROM	30.0	30.8	35.0	30.6	31.4	36.4	35.9	35.9	36.9	35.6	35.3	37.0	31.2	37.7
ANDO	53.9	62.2	55.3	62.8	63.3	62.5	63.3	58.7	62.5	63.9	63.7	64.3	62.2	63.3
BODA	36.1	39.6	34.9	39.7	39.4	38.7	39.5	39.9	38.3	39.4	38.7	38.8	39.5	39.5
BODB	45.1	50.0	47.9	50.5	50.1	50.9	50.9	50.8	49.6	51.3	51.2	51.4	50.0	50.3
VEGA	25.3	26.2	26.9	25.9	25.8	26.5	26.7	25.4	25.4	26.6	26.7	26.7	26.0	26.0
TRDA[d]	21.6	26.1	21.0	25.1	25.1	25.4	25.1	23.3	29.8	34.7	42.2	45.6	24.1	45.4
ALES	25.4	46.0	44.4	45.6	45.8	47.6	42.1	30.9	41.5	48.5	49.6	50.0	48.9	50.2
VAGA	32.4	39.3	27.9	39.0	39.4	34.1	35.1	32.6	36.4	36.4	47.0	47.5	40.7	47.3
KOL1	13.8	15.2	17.5	16.3	16.7	18.2	16.9	14.6	16.7	17.3	17.4	17.3	15.6	15.7
KOL2	32.9	40.0	37.8	39.4	40.4	39.5	40.1	33.7	40.6	42.6	43.2	43.1	41.9	42.2
JON2	9.3	3.8	3.4	3.1	4.0	16.5	10.3	12.0	19.6	18.7	14.2	15.4	−0.7	17.6
STVA	−0.2	1.0	4.8	2.0	2.5	2.4	2.5	2.1	2.7	4.1	4.7	4.2	1.6	1.8

[a] Original g9 OTL correction.
[b] OTL provider.
[c] In-house software with higher-resolution coastline.
[d] Not including the 2004.475 campaign.

correction ranges from −1.86 μGal (ALES 2003.715) to 1.04 μGal (ALES 2008.724).

2.2. Atmospheric and hydrological effects

Atmospheric density variations in time cause changes in the direct Newtonian gravitational attraction from the air mass around the gravimeter, as well as varying crustal and ocean surface deformation due to loading. Conventionally, local pressure and gravity variations are correlated with an admittance factor of $A = 0.30$ μ Gal/hPa, in accordance with IAG Resolution No. 9, 1983. This admittance factor is used in the correction Δg_{ATM} for atmospheric pressure implemented in g9, $\Delta g_{ATM} = A(P_o - P_n)$, where P_o is the in situ pressure as observed by the FG5 barometer, and $P_n = 1013.25\left(1 - 0.0065H/288.15\right)^{5.2559}$ is the nominal barometric pressure (H is the gravity site height in meters), in accordance with DIN Standard #5450. A more precise description of A allows it to vary in space and time, and depend on the total global mass distribution of the atmosphere. Typically, an improved atmospheric effect on gravity is computed by incorporating atmospheric mass attraction and load considering zones of increasing distance to the gravity site (Gitlein et al., 2013).

Having reduced the gravity value for the time-variable tidal, polar motion, and atmospheric mass components, it may remain strongly influenced by hydrological variations (Mikolaj et al., 2015). The effect of hydrology on the observed gravity value is usually not considered when processing absolute gravity observations (Timmen, 2010), and is not treated in g9.

For the computation of total atmospheric (ATM) and global hydrological (GH) effects on gravity we have tested the novel MATLAB® tool mGlobe (Mikolaj et al., 2016), developed at the German Research Centre for Geosciences (GFZ) in collaboration with the University of Vienna, obtained from https://github.com/emenems/mGlobe (M. Mikolaj, personal communication, 2015).

For the computation of the ATM effect, we have used 2D and 3D European Centre for Medium-Range Weather Forecasts (ECMWF) Interim Reanalysis (ERA Interim) data (Dee et al., 2011) as input model, obtained from http://apps.ecmwf.int/datasets/data/interim-full-daily. The temporal resolution was chosen to be six-hourly, and all data are given on 0.75°×0.75° grids, with a surface geopotential (orography) grid as height reference (where the height in meters is obtained by dividing the geopotential with 9.80665 ms^{-2}).

Using the coarse orography resolution of 0.75°×0.75° will often give large height discrepancies between actual gravity site height and orography height. This spatial deficiency, together with temporal deficiency (six-hourly), can be taken into account by considering the difference between pressure data from ERA Interim at orography height and actual in situ pressure at gravity site height. This difference in ATM effect, or residual effect ϵ, is then computed by the single admittance approach outlined in the above, i.e.,

$$\epsilon = -A\left(P^{site}_{in\ situ} - P^{oro}_{ERA}\right), \quad (3)$$

where A is the site-specific admittance factor. Gitlein (2009) estimated A at ANDO, BODB/BODA, HONN, KAUT, TROM, TRDA, TRYB/TRYC, ALES, and NMBU as well as a mean value of 0.32 μGal/hPa for Fennoscandia using ECMWF data. For the computation of Eq. (3) we used the site-specific A where available, and the mean value for Fennoscandia for the remaining sites.

We do not have actual in situ pressure measured by the FG5 barometer for the adopted gravity values (where we do not have raw data). Therefore, we obtained in situ pressure data for all gravity campaigns by cubic spline interpolation of six-hourly pressure data from nearby meteorological stations of the eKlima database of the Norwegian Meteorological Institute at http://eklima.met.no. The average distance between the meteorological station and the gravity site is ∼23 km.

We investigated the applicability of the interpolated in situ pressure values by comparing them with actual in situ pressure measured by the FG5 barometer where available (86 campaigns). Simulated single admittance ATM corrections were computed using interpolated in situ pressure and compared with those from g9. The mean difference between simulated and actual ATM correction is ∼0.4 μGal. In addition, we checked the pressure values of ERA Interim against the interpolated pressure values (for the same 86 campaigns and with ERA and eKlima pressure at equal height), and found a mean difference of ∼0.7 hPa, in agreement with previous comparisons of in situ and ECMWF pressure (Gitlein, 2009). We therefore conclude that the interpolated in situ pressure values are applicable.

For the computation of the GH effect, we have used the ACE2 30" × 30" digital elevation model (DEM) (Berry et al., 2010), as well as the Global Land Data Assimilation System (GLDAS) Version 2 NOAH (0.25°×0.25°) hydrological data (Rodell et al., 2004), downloaded through mGlobe. GLDAS has two versions, 2.0 and 2.1, covering the time periods 1948–2010 and 2000–2015, respectively. Where available, we have used the most recent

version. GLDAS/NOAH captures the contribution of global continental water storage to gravity variations by considering four soil moisture layers (0–10 cm 10–40 cm, 40–100 cm, and 100–200 cm) and snow (snow water equivalent); hence, it does not consider groundwater.

Although the IAG resolution (1983) recommends the removal of the mean atmosphere, this is not done in the current version of mGlobe, which computes effects with respect to an arbitrary reference (M. Mikolaj, personal communication, 2015). However, an absolute reference is not important here as we only consider temporal variations. Thus, we have computed long-term means of both ATM ($\bar{g}_{\mathrm{ATM}}^{\mathrm{ERA}}$) and GH ($\bar{g}_{\mathrm{GH}}^{\mathrm{GLDAS/NOAH}}$) effects and subtracted these from the short-term effects $g_{\mathrm{ATM}}^{\mathrm{ERA}}$ and $g_{\mathrm{GH}}^{\mathrm{GLDAS/NOAH}}$. For consistency, we have chosen the time period 2004-2009 inclusive for both mean ATM and GH effects. Fig. 5 shows the variation of mean ATM and GH effects at NMBU for the chosen epoch. The mean value at a given time step is computed using mGlobe output up to this time step only, i.e., it is computed in a cumulative fashion. We observe that the variation of the mean ATM effect stabilizes earlier than the mean GH effect, and by the end of the sixth year, both means vary by less than ~0.03 μGal, which is well within model uncertainties. Thus, we conclude that the chosen time period suffices as a stable long-term mean for all gravity sites in this work. Short-term ATM and GH effects were computed using six-hourly and daily resolutions, respectively, overlapping the gravity campaigns. For the ATM effect, overlapping values were subsequently interpolated to the actual time spans of the gravity campaigns.

The correction for the GH effect was computed according to

$$\Delta g_{\mathrm{GH}} = -\left(g_{\mathrm{GH}}^{\mathrm{GLDAS/NOAH}} - \bar{g}_{\mathrm{GH}}^{\mathrm{GLDAS/NOAH}}\right). \tag{4}$$

Computing the ATM correction is slightly more laborious. First, the 2004–2009 long-term mean $\bar{\epsilon}$ of the residual effect (Eq. (3)), was computed. Second, there will be a bias β between the ATM correction referring to the long-term mean pressure using ERA Interim, $\bar{P}_{\mathrm{ERA}}^{04-09}$, and the standard ATM correction referring to nominal pressure P_n. To ease comparison and facilitate the computation of the difference between standard and refined corrections, we computed β at orography height according to

$$\beta = 0.3\left(P_n - \bar{P}_{\mathrm{ERA}}^{04-09}\right). \tag{5}$$

Finally, the correction for the ATM effect was computed by

$$\Delta g_{\mathrm{ATM}} = -\left[\left(g_{\mathrm{ATM}}^{\mathrm{ERA}} - \bar{g}_{\mathrm{ATM}}^{\mathrm{ERA}}\right) + \left(\epsilon - \bar{\epsilon}\right) + \beta\right]. \tag{6}$$

Table S1 shows ATM and GH corrections for all gravity campaigns. As was the case for ocean loading, the standard gravity estimates from g9, g_0, have already been corrected for the ATM effect ($\Delta g_{\mathrm{ATM}}^0$), and we present the change in ATM correction, i.e., $\delta g_{\mathrm{ATM}} = \Delta g_{\mathrm{ATM}} - \Delta g_{\mathrm{ATM}}^0$. Hydrology is not treated in g9; hence, we list the complete correction Δg_{GH}.

The refined ATM correction ranges from −1.9 μGal (TRYC 2003.723) to 1.1 μGal (e.g., HONN 2007.507), which is in the same order as the refined ATM corrections of Gitlein (2009). The GH correction ranges from −1.5 μGal (TRYB 2008.254) to 1.7 μGal (TRYC 2006.614), corresponding to previous studies (e.g., Pálinkáš et al., 2012; Mikolaj et al., 2015).

3. Secular gravity trends and gravity-to-height ratios

Table 5 shows secular gravity trends for each observation site. The rates $\dot{g}_0$ and $\dot{g}$ were computed by fitting a linear trend using ordinary least-squares regression (OLR, without weights) to the gravity data sets g_0 and g of Table S1, respectively. The percentage change $\Delta_{\dot{g}}$ of $\dot{g}$ with respect to $\dot{g}_0$ has been computed, as well as statistics (for sites with more than two observations) in the form of coefficients of determination for both $\dot{g}_0$ and $\dot{g}$, and the 95% confidence interval for $\dot{g}$. The coefficient of determination was computed according to $R^2 = 1 - SSR/SST \in [0, 1]$, where SSR and SST are the residual and total sum of squares, respectively.

R^2 indicates how well the linear model fits the gravity data, and will increase as the model fit to the data improves. R_0^2 and R^2 denote the coefficient of determination for the standard gravity estimates g_0 and the refined estimates g, respectively. Looking at Table 5, we note that both R_0^2 and R^2 reveal both good and bad linear model fits. R^2 gives a better fit to the linear model than R_0^2 at nine sites. 95% confidence intervals shows a significantly negative trend at six sites.

In order to assess our empirical gravity rates, a modeled gravity rate, $\dot{g}_M$, was computed using height rates of change $\dot{h}$ from a recent empirical absolute land uplift model (given in ITRF2008) of the NMA, based on a combination of GNSS and leveling (O. Vestøl, personal communication, 2015), together with a recent modeled relation between gravity and height rates of change $\left(\dot{g}/\dot{h}\right)_M$ of −0.163 μGal mm^{-1} for GIA (Olsson et al., 2015) (Table 5). It is generally challenging to quantify the uncertainty of $\left(\dot{g}/\dot{h}\right)_M$, as it incorporates uncertainties of both the ice and Earth models used. However, Olsson et al. (2015) computed $\left(\dot{g}/\dot{h}\right)_M$ for Fennoscandia using six Earth models with varying upper mantle viscosities (their Table 3), giving a maximum difference of 0.008 μGal mm^{-1}. We adopted this model spread multiplied by two as an uncertainty estimate for $\left(\dot{g}/\dot{h}\right)_M$, yielding 0.016 μGal mm^{-1} (H. Steffen, personal communication, 2016). The uncertainties of $\dot{h}$ were determined as a sum of the observation error and systematic errors due to origin drift along the three directions (0.5 mm yr^{-1}) and scale error (0.3 mm yr^{-1}) of the reference frame (Collilieux et al., 2014). In turn, the uncertainties of $\dot{g}_M$ were computed by formal error propagation.

Considering $\dot{g}_M$ as a "true" reference, $\Delta_{\dot{g}}$ indicates that $\dot{g}$ performs better than $\dot{g}_0$ at nine gravity sites. For the remaining sites, the refined gravity corrections give no significant improvement or even degrade the trend. We note that these results are similar to the results of Gitlein (2009), where refined ATM corrections were estimated and found to improve the gravity rates at 6 out of 11 sites, with no observed improvement on average. We also note that in some cases, although the linear model fit degrades, the rate itself is improved.

Similar conclusions can be drawn from Fig. 6, which shows the linear gravity rates $\dot{g}_0$, $\dot{g}$, and $\dot{g}_M$ for all gravity sites. With the exception of HONC and TROM, the observed gravity rates are larger than the modeled ones, particularly BODA, KAUT, and TRDA.

Combining linear rates of change in gravity and height gives a convenient means for interpreting the physical processes underlying vertical crustal deformation, and is the only way to distinguish a gravity change due to vertical deformation from gravity change due to mass redistribution (de Linage et al., 2007). The relation between gravity and height rates of change due to GIA in Fennoscandia has been subject to extensive research, and the proportionality constant between gravity and height rates of change determined within the range of −0.154 to −0.217 μGal mm^{-1} (e.g.,Wahr et al., 1995; Ekman and Mäkinen, 1996; Gitlein, 2009; Pettersen, 2011; Olsson et al., 2015).

Based on the results presented in Fig. 6, we formed a subset of reliable rates, where a reliable rate is defined as within the uncertainty of $\dot{g}_M$. In other words, an agreement of $\dot{g}_0$ or $\dot{g}$ with $\dot{g}_M$ gives us confidence in that the empirical rates mainly reflect GIA. The subset contains empirical gravity rates from 10 sites, namely BODB, HONN, HONA, HONB, KOL1, STVA, TRYB, TRYC, ALES, and NMBU. These rates have been used for the following comparison of gravity and height rates of change.

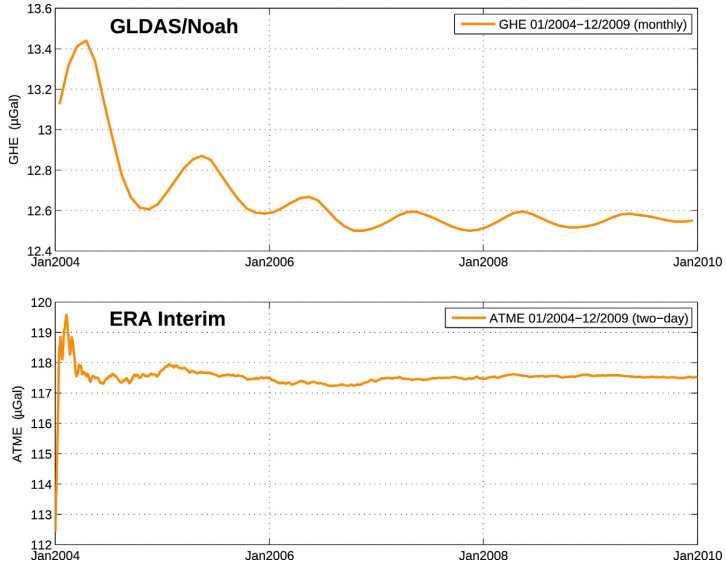

Fig. 5. Variation of mean ATM and GH effect at NMBU 2004–2009, as computed with mGlobe. The mean value at a given time step is computed cumulatively, using mGlobe output up to this time step only.

Fig. 6 and Table 5 reveal a considerable variation in the uncertainties of the empirical gravity rates, suggesting a weighted linear regression (WLR) approach for the estimation of gravity versus height rates of change. It is not possible to derive uncertainties for the gravity rates at HONA and KOL1, as they are based on two observations only. We approximated these uncertainties by plugging an average of both campaign uncertainties ($\overline{\sigma}_{\text{tot}}$) as well as their time span into Eq. (1). This gives uncertainties of $\sigma_{\dot{g}} \approx 0.5\,\mu\text{Gal yr}^{-1}$ and $\sigma_{\dot{g}} \approx 1.7\,\mu\text{Gal yr}^{-1}$ for HONA and KOL1, respectively. Eq. (1) must be taken as a rough uncertainty estimate when only two observations are used, and we consider the uncertainty estimate of KOL1 unrealistically large. Therefore, we decided to use both OLR and WLR approaches.

Fig. 7 shows gravity versus height rates of change using the standard gravity rates $\dot{g}_0$, which yields a WLR of $\dot{g}_0 = -0.135\,(\pm 0.100) - 0.142\dot{h}\,(\pm 0.018)\,\mu\text{Gal yr}^{-1}$ and an OLR of $\dot{g}_0 = -0.175\,(\pm 0.137) - 0.143\dot{h}\,(\pm 0.032)\,\mu\text{Gal yr}^{-1}$. Using $\dot{g}$, Fig. 8 shows a WLR of $\dot{g} = -0.210\,(\pm 0.183) - 0.133\dot{h}\,(\pm 0.030)\,\mu\text{Gal yr}^{-1}$ and an OLR of $\dot{g} = -0.097\,(\pm 0.196) - 0.167\dot{h}\,(\pm 0.045)\,\mu\text{Gal yr}^{-1}$. We first note that WLR and OLR based on $\dot{g}_0$ are quite similar, while WLR and OLR based on $\dot{g}$ differ considerably. Considering the constant terms and their relatively large uncertainties, only OLR based on $\dot{g}$ is statistically equal to zero. The regression slopes based on OLR $\left(\left(\dot{g}/\dot{h}\right)_0 = -0.143\,(\pm 0.032)\,\mu\text{Gal mm}^{-1}\right.$, $\left.\left(\dot{g}/\dot{h}\right) = -0.167(\pm 0.045)\,\mu\text{Gal mm}^{-1}\right)$ and WLR $\left(\left(\dot{g}/\dot{h}\right)_0 = -0.142\,(\pm 0.018)\right.$ $\left.\mu\text{Gal mm}^{-1},\ \left(\dot{g}/\dot{h}\right) = -0.133\,(\pm 0.030)\,\mu\text{Gal mm}^{-1}\right)$ are all in

Table 5
Linear rates of change in gravity and height.

Code	$\dot{g}_0$ (μGal yr^{-1})	R_0^2	$\dot{g}$ (μGal yr^{-1})	R^2	Cl$_{\dot{g}}$ [L U][a] (μGal yr^{-1})	$\dot{g}_M$ (μGal yr^{-1})	$\Delta_{\dot{g}}$[b] (%)	$\dot{h}$[c] (mm yr^{-1})
ANDO	−1.13 ± 0.38	74.2	−0.91 ± 0.44	58.7	[−2.32 0.49]	−0.24 ± 0.11	19.5	1.47 ± 0.63
BODB	−1.06 ± 0.63	59.0	−1.18 ± 0.62	64.4	[−3.46 1.49]	−0.55 ± 0.12	−11.0	3.35 ± 0.62
BODA	−2.28 ± 0.39	94.6	−2.31 ± 0.44	93.3	[−4.19 − 0.43]	−0.54 ± 0.12	1.4	3.33 ± 0.62
HAMM	−1.44		−1.61			−0.37 ± 0.11	11.9	2.26 ± 0.66
HONN	−0.38 ± 1.04	4.2	−0.57 ± 0.57	24.7	[−2.39 1.26]	−0.31 ± 0.11	−49.9	1.93 ± 0.67
HONA	−0.82		−0.88			−0.82 ± 0.13	−7.3	5.04 ± 0.62
HONB	−0.93 ± 0.09	98.2	−1.02 ± 0.13	96.8	[−1.58 − 0.45]	−0.83 ± 0.13	−9.4	5.09 ± 0.62
HONC	−0.15 ± 0.27	2.9	−0.24 ± 0.27	7.3	[−0.84 0.36]	−0.82 ± 0.13	−62.8	5.01 ± 0.62
JON2	−0.80		−0.65			−0.33 ± 0.11	19.1	2.03 ± 0.61
KAUT	−2.16 ± 0.38	91.7	−2.43 ± 0.39	92.6	[−3.68 − 1.17]	−0.79 ± 0.13	−12.2	4.84 ± 0.63
KOL1	−0.38		−0.12			−0.25 ± 0.11	67.8	1.54 ± 0.63
KOL2	−0.93		−0.75			−0.25 ± 0.11	19.7	1.54 ± 0.63
STVA	−0.42 ± 0.24	37.6	−0.53 ± 0.23	50.7	[−1.13 0.07]	−0.22 ± 0.10	−27.6	1.32 ± 0.61
TROM	−0.08 ± 0.19	2.8	−0.12 ± 0.18	6.3	[−0.57 0.33]	−0.42 ± 0.11	−50.0	2.59 ± 0.62
TRDA	−1.84 ± 0.24	87.9	−1.82 ± 0.22	89.3	[−2.33 − 1.31]	−0.70 ± 0.12	1.1	4.28 ± 0.61
TRYB	−1.32 ± 0.27	82.4	−1.39 ± 0.24	87.2	[−2.01 − 0.78]	−1.10 ± 0.15	−4.8	6.74 ± 0.62
TRYC	−1.05 ± 0.08	91.5	−1.06 ± 0.07	93.3	[−1.22 − 0.90]	−1.10 ± 0.15	−1.0	6.74 ± 0.62
VAGA	−0.86 ± 0.11	96.7	−0.81 ± 0.22	86.6	[−1.77 0.16]	−0.33 ± 0.11	5.7	2.03 ± 0.61
ALES	−0.29 ± 0.14	60.7	−0.01 ± 0.31	0.0	[−0.99 0.97]	−0.26 ± 0.10	96.3	1.60 ± 0.62
NMBU	−0.55 ± 0.24	39.1	−0.58 ± 0.29	33.1	[−1.26 0.09]	−0.77 ± 0.13	−5.5	4.74 ± 0.61

[a] Lower (L) and upper (U) limits of the 95% confidence interval for $\dot{g}$.
[b] Change of $\dot{g}$ with respect to $\dot{g}_0$.
[c] From the NMA empirical land uplift model, given in ITRF2008.

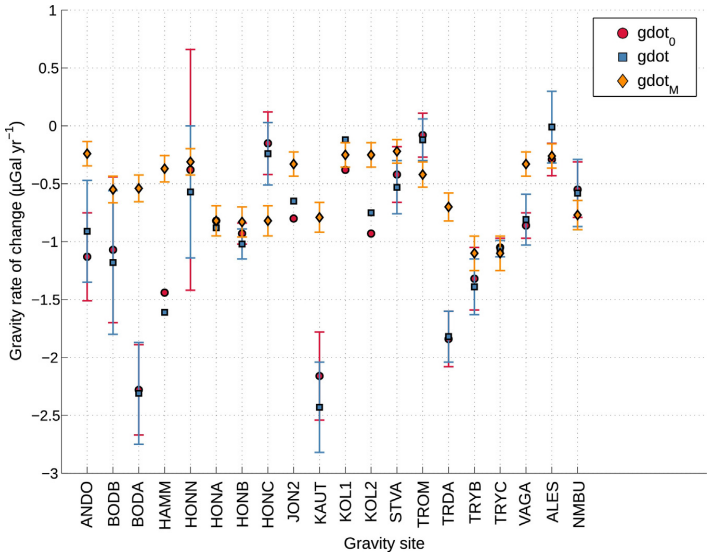

Fig. 6. Linear rates of change in gravity. $\dot{g}_0$ and $\dot{g}$ are empirical linear gravity rates based on standard and refined gravity corrections, respectively. $\dot{g}_M$ are modeled rates using a recent empirical land uplift model together with a theoretical relation between the gravity and height rate of change for GIA.

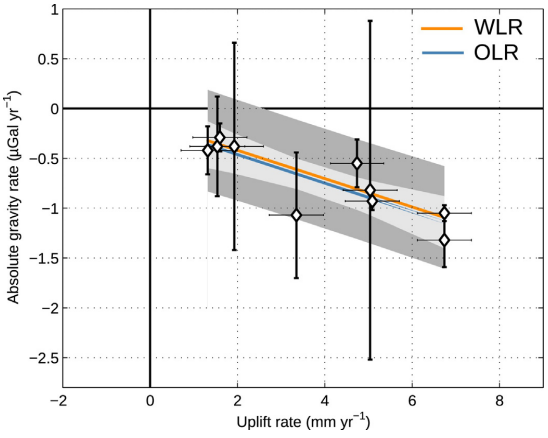

Fig. 7. Gravity versus height rates of change based on standard gravity rates $\dot{g}_0$. Height rates given in ITRF2008. The white diamonds denote the gravity site, with vertical (gravity) and horizontal (height) error bars reflecting the respective uncertainties. The solid orange line shows the WLR, with the dark gray area showing its 95% confidence interval. The solid blue line shows the OLR, with the light gray area showing its 95% confidence interval. (For interpretation of the references to colour in this figure legend, the reader is referred to the web version of this article.)

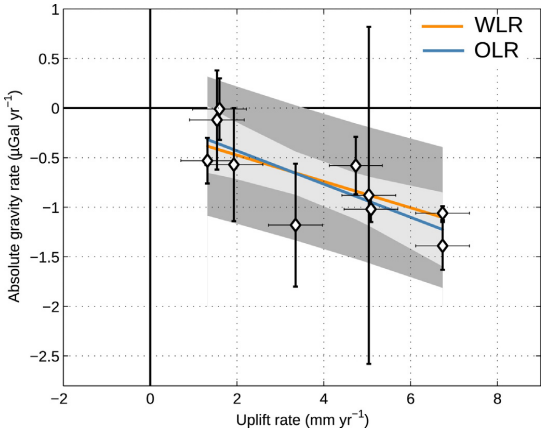

Fig. 8. Same as Fig. 7, but based on refined gravity rates $\dot{g}$.

agreement with $\left(\dot{g}/\dot{h}\right)_M$ and the reported range. However, in general, $\dot{g}$ gives a more uncertain regression than $\dot{g}_0$.

4. Discussion

There are limitations in our refined modeling of ATM and GH gravitational effects. We expect an ATM modeling inaccuracy due to using the coarse orography rather than a DEM in the local zone. In turn, the residual effect needs in-situ pressure observations which were not available for all campaigns, further limiting the accuracy.

For the GH effect, an obvious limitation is that the local zone is completely left out, when it is predominantly the local hydrology in the local zone which is expected to impact on the observations (e.g., Virtanen et al., 2006; Leirião et al., 2009). Further, as GLDAS/NOAH explicitly does not include the effect of groundwater variations, these have not been considered neither globally nor locally. Groundwater variations may lead to gravity changes in the order of ∼6–7 μGal depending on local topography and ground porosity (Breili and Pettersen, 2009), and may dominate our considered effects.

Regressions based on two gravity campaigns only, i.e., HAMM, HONA, JON2, KOL1 and KOL2 are inherently uncertain, and although HONA and KOL1 present reasonable trends, they are obviously not in agreement with the needed number of observations as prescribed by Eq. (1). Because of the larger gravity rate uncertainties at HONA and KOL1, the WLR is similar to a linear regression where

both are left out. Thus, the WLR underlines the difficulty of using these rates.

Fig. 1 shows that the majority of the Norwegian AG sites are located along the coast, relatively close to the zero-line of present GIA-induced rebound in Fennoscandia. Consequently, at these sites, the signal we aim to describe (GIA) is weak, and other site-specific unmodeled processes or observation noise may dominate the rates.

Although the main component of vertical land movement in Fennoscandia is GIA, smaller elastic processes (present-day changes due to, e.g., local tectonics or melting glaciers) may also give rise to vertical deformations. For example, by observing a misfit between observed uplift (using tide gauges, leveling, GPS, and gravity) and a GIA model, Fjeldskaar et al. (2000) found a weak tectonic uplift in the order of $\sim$1 mm yr^{-1} in addition to the uplift due to GIA in large parts of Norway. Other results confirm this misfit between GIA model and observations in the Norwegian area between 65°N and 68°N (e.g., Olesen et al., 2013; Kierulf et al., 2014), suggesting that this area might not be primarily affected by GIA, but other geophysical processes. Therefore, the Norwegian data set alone is insufficient for extensive GIA modeling in Fennoscandia, a topic which is left to the NKG joint analysis on postglacial gravity change, considering observations in the entire region.

Bearing the above considerations in mind, we return to our assessment of the refined gravitational corrections (Section 3). Here we consider a reliable secular gravity trend as one in agreement with $\dot{g}_M$, i.e., a GIA model. Thus, if the rate at a gravity site agrees well with $\dot{g}_M$ it is reasonable to believe that the vertical displacement of that site is dominated by GIA. For almost all gravity rates of the reliable subset chosen in Section 3, $\dot{g}_0$ agrees more with $\dot{g}_M$ than does $\dot{g}$. In other words, the refined gravitational corrections do not offer an improvement of the reliable rates, which might be expected, as the refined corrections mainly impact gravity sites that are not dominated by GIA. At sites that are still affected by residual signals caused by other geophysical processes than GIA, refined and additional modeling is needed. Exceptions are TRYC and NMBU; however, at these sites $\dot{g}_0$ and $\dot{g}$ are quite similar.

Consequently, $\dot{g}_M$ might not be the optimal choice for assessing the refined corrections, as an agreement with $\dot{g}_M$ occurs at sites where GIA already is the dominant signal. At sites where $\dot{g}$ and $\dot{g}_0$ depart from $\dot{g}_M$ (e.g., ANDO, BODA, HAMM, KAUT, and TRDA), the signal is possibly dominated by other processes (e.g., tectonics, groundwater). Heck and Mälzer (1983) investigate $\left(\dot{g}/\dot{h}\right)$ for tectonic processes using leveled heights and relative gravimetry, giving a linear regression of $\sim$−1.5 μGal mm^{-1}. Thus, if we consider a tectonic uplift of $\sim$1 mm yr^{-1}, the resulting gravity change could be 1 − 2 μGal yr^{-1}. Furthermore, de Linage et al. (2009) explore the variability of $\left(\dot{g}/\dot{h}\right)$ due to different surface loads, and report that $\left(\dot{g}/\dot{h}\right)$ is quite sensitive to local masses, where smaller surface load sizes give larger absolute values of $\left(\dot{g}/\dot{h}\right)$. For example, they give a mean ratio of $\sim$−0.87 μGal mm^{-1} over continents due to hydrological loading.

We stress, however, that it remains to be verified whether the observed deviations from $\dot{g}_M$ are due to the geophysical processes discussed herein. In addition to other geophysical processes, the misfit between GIA model and observations may be explained by errors in the GIA model or observation errors (GNSS, leveling, and AG).

The stability and accuracy of AG meters are usually assessed by AG intercomparisons, which have shown systematic biases between different instruments. Pettersen et al. (2010) computed gravity differences for two instruments measuring simultaneously at a site using a suite of gravimeters used in Fennoscandia 2003–2006, and obtained an rms error of ±3 μGal. The European Comparison of Absolute Gravimeters (ECAG) in 2007 (Francis et al., 2010) showed an agreement of ±2 μGal between 20 instruments, while ECAG 2011 showed an agreement of ±3.1 μGal between 22 instruments (Francis et al., 2013). The first North American comparison of 9 gravimeters showed an agreement of ±1.6 μGal (Schmerge et al., 2012). While differences that are larger than the observation uncertainties may indicate a possible systematic error, it is uncertain to which extent these differences are reproducible or stable in time. Consequently we did not consider applying an instrumental offset to our data set.

5. Conclusions

We have compiled and analyzed all Norwegian FG5 AG observations from the 1993–2014 period, with an aim of exploring the applicability of these data for GIA studies. Raw observations have been reprocessed using a common scheme, ensuring consistency with respect to model and setup parameters. Adopted observations by other instruments or agencies have been carefully incorporated in the data set, with updated uncertainties.

To improve the separation of the different gravity rate signal contributors, we have investigated whether it is possible to improve the corrections for geophysical processes other than GIA. Using a suite of GOT models, we have compared standard OTL corrections with results from a web service and an in-house software incorporating the higher-resolution coastline N50 as well as tide-gauge observations. Furthermore, we have tested the novel mGlobe tool for the computation of ATM and GH effects. Refined OTL, NTL, ATM, and GH corrections have all been applied to the standard gravity values to form refined gravity values.

Secular gravity trends based on both standard and refined corrections have been computed. These, in turn, have been compared with modeled rates based on a recent empirical land uplift model and theoretical relation between the gravity and height rate of change for GIA. The refined gravity rates mainly impact sites where GIA is not the dominant signal. This suggests that a refined modeling is meaningful at sites that are still affected by various unmodeled or insufficiently modeled effects. Compared to the modeled gravity rates, the refined gravity rates agree better than standard rates at 9 out of 20 sites. This reveals the need for further improvement of the refined corrections as well as the consideration of remaining unmodeled effects. We have not considered the effect of local hydrology in this work. Although seasonal variations will have less of an impact on the rates with time, we conclude it should be taken into account if possible (e.g., by monitoring groundwater variations).

Based on a subset of gravity trends mainly reflecting GIA, we have computed empirical estimates of the ratio between gravity and height rates of change using both standard and refined gravity corrections. The WLR gives $\dot{g}_0 = -0.135\,(\pm 0.100) - 0.142\dot{h}\,(\pm 0.018)$ μGal yr^{-1} and $\dot{g} = -0.210\,(\pm 0.183) - 0.133\dot{h}\,(\pm 0.030)$ μGal yr^{-1}, respectively. The OLR gives $\dot{g}_0 = -0.175\,(\pm 0.137) - 0.143\dot{h}\,(\pm 0.032)$ μGal yr^{-1} and $\dot{g} = -0.097\,(\pm 0.196) - 0.167\dot{h}\,(\pm 0.045)$ μGal yr^{-1}, respectively. The regression slopes are within −0.133 (±0.030) to −0.167 (±0.045) μGal mm^{-1}, in agreement with previous empirical and theoretical estimates. Therefore, this subset of the Norwegian data may well be embedded in the planned NKG joint analysis on postglacial gravity change, which will consider data from the entire region. We expect the subset to be augmented with additional sites in the future, as they become suitable for GIA studies through improved corrections for remaining geophysical effects and/or additional observations.

Finally, the WLR reveals the challenge of incorporating gravity rates that are based on few observations, emphasizing the need for extending the gravity time series. Both past and future observation of the AG reference frame in Norway is dependent on funding

and operator availability. Consequently, the sampling interval and number of observations at each gravity site is variable. Some of the longer time series rely on quite few observations. We therefore conclude that although the Norwegian AG data set should be applicable for further studies, extending the observation time series is decisive for improving the gravity rates, and is expected to reveal new and beneficial information at all gravity sites.

Acknowledgements

We would like to thank Andreas Engfeldt, Are Jo Næss, Per-Anders Olsson, and Glenn Sasagawa for contributions to Norwegian AG campaigns 1997–2010. Olav Vestøl at the NMA provided land uplift data. The open data policies of ECMWF and MET Norway are acknowledged, as well as NMA, BKG, IfE, and NOAA for having coordinated and made AG observations in Norway 1993–2007. Observation sites in this work are maintained and provided by Andøya Space Center, the Geological Survey of Norway, Gravitude AS, NMA, NMBU, and Statoil ASA. Finally, we are grateful for the constructive comments of the Editor and two anonymous reviewers that considerably improved the manuscript.

Appendix A. Supplementary data

Supplementary data associated with this article can be found, in the online version, at http://dx.doi.org/10.1016/j.jog.2016.09.001.

References

Arneitz, P., Meurers, B., Ruess, D., Ullrich, C., Abermann, J., Kuhn, M., 2013. Gravity effect of glacial ablation in the Eastern Alps – observation and modeling. Cryosphere 7, 491–498.

Berry, P.A.M., Smith, R.G., Benveniste, J., 2010. ACE2: the new global digital elevation model. In: Mertikas, S.P. (Ed.), Gravity, Geoid and Earth Observation, International Association of Geodesy Symposia 135. Springer, Berlin, pp. 231–237.

Breili, K., Pettersen, B.R., 2009. Effects of surface snow cover on gravimetric observations. J. Geodyn. 48, 16–22.

Breili, K., Rolstad, C., 2009. Ground-based gravimetry for measuring small spatial-scale mass changes on glaciers. Ann. Glaciol. 50, 141–147.

Breili, K., Gjevestad, J.G., Lysaker, D.I., Omang, O.C.D., Pettersen, B.R., 2010. Absolute gravity values in Norway. Norsk Geografisk Tidsskrift 64, 79–84.

Breili, K., 2009. Ocean tide loading at elevated coastal gravity stations. Kart og Plan 69, 151–164.

Cheng, Y., Andersen, O.B., 2010. Improvement in global ocean tide model in shallow water regions. In: Poster Presented at the Ocean Surface Topography Science Team Meeting, Lisbon, October 18–22.

Collilieux, X., Altamimi, Z., Argus, D.F., Boucher, C., Dermanis, A., Haines, B.J., Herring, T.A., Kreemer, C.W., Lemoine, F.G., Ma, C., MacMillan, D.S., Mäkinen, J., Métivier, L., Ries, J., Teferle, F.N., Wu, X.,2014. Ch. External Evaluation of the Terrestrial Reference Frame: Report of the Task Force of the IAG Sub-commission 1.2. In: Earth on the Edge: Science for a Sustainable Planet: Proceedings of the IAG General Assembly, Melbourne, Australia, June 28-July 2, 2011. Springer, Berlin, Heidelberg, pp. 197–202.

de Linage, C., Hinderer, J., Rogister, Y., 2007. A search for the ratio between gravity variation and vertical displacement due to a surface load. Geophys. J. Int. 171 (3), 986–994.

de Linage, C., Hinderer, J., Boy, J.-P., 2009. Variability of the gravity-to-height ratio due to surface loads. Pure Appl. Geophys. 166, 1217–1245.

Dee, D.P., Uppala, S.M., Simmons, A.J., Berrisford, P., Poli, P., Kobayashi, S., Andrae, U., Balmaseda, M.A., Balsamo, G., Bauer, P., Bechtold, P., Beljaars, A.C.M., van de Berg, L., Bidlot, J., Bormann, N., Delsol, C., Dragani, R., Fuentes, M., Geer, A.J., Haimberger, L., Healy, S.B., Hersbach, H., Hólm, E.V., Isaksen, L., Kållberg, P., Khler, M., Matricardi, M., McNally, A.P., Monge-Sanz, B.M., Morcrette, J.-J., Park, B.-K., Peubey, C., de Rosnay, P., Tavolato, C., Thpaut, J.-N., Vitart, F., 2011. The ERA-Interim reanalysis: configuration and performance of the data assimilation system. Quart. J. R. Met. Soc. 137 (656), 553–597.

Eanes, R.J., 1994. Diurnal and semidiurnal tides from TOPEX/POSEIDON altimetry (abstract). Eos Trans. AGU 75, 16. In: Spring Meeting Suppl, p. 108.

Egbert, G.D., Erofeeva, S.Y., 2002. Efficient inverse modeling of barotropic ocean tides. J. Atmos. Oceanic Technol. 19 (2), 183–204.

Ekman, M., Mäkinen, J., 1996. Recent postglacial rebound, gravity change and mantle flow in Fennoscandia. Geophys. J. Int. 126 (1), 229–234.

Farrell, W.E., 1972. Deformation of the Earth by surface loads. Rev. Geophys. 10 (3), 761–797.

Fjeldskaar, W., Lindholm, C., Dehls, J.F., Fjeldskaar, I., 2000. Postglacial uplift, neotectonics and seismicity in Fennoscandia. Quat. Sci. Rev. 19 (14–15), 1413–1422.

Fok, H.S., Shum, C.K., Yi, Y., Iz, H.B., Matsumoto, K., 2012. Improved coastal ocean tide modeling using satellite altimetry. In: Poster Presented at the 20 Years of Progress in Radar Altimetry Symposium, Venice, September 24–29.

Francis, O., Dam, T., Germak, A., Amalvict, M., Bayer, R., Bilker-Koivula, M., Calvo, M., D'Agostino, G.-C., Dell'Acqua, T., Engfeldt, A., Faccia, R., Falk, R., Gitlein, O., Fernandez, M., Gjevestad, J., Hinderer, J., Jones, D., Kostelecky, J., Le Moigne, N., Luck, B., Mäkinen, J., Mclaughlin, D., Olszak, T., Olsson, P.-A., Pachuta, A., Palinkas, V., Pettersen, B., Pujol, R., Prutkin, I., Quagliotti, D., Reudink, R., Rothleitner, C., Ruess, D., Shen, C., Smith, V., Svitlov, S., Timmen, L., Ulrich, C., Van Camp, M., Walo, J., Wang, L., Wilmes, H., Xing, L.,2010. Results of the European Comparison of Absolute Gravimeters in Walferdange (Luxembourg) of November. In: Gravity, Geoid and Earth Observation: IAG Commission 2: Gravity Field, Chania, Crete, Greece, 23–27 June 2008. Springer, Berlin, Heidelberg, pp. 31–35.

Francis, O., Baumann, H., Volarik, T., Rothleitner, C., Klein, G., Seil, M., Dando, N., Tracey, R., Ullrich, C., Castelein, S., Hua, H., Kang, W., Chongyang, S., Songbo, X., Hongbo, T., Zhengyuan, L., Plinks, V., Kostelecký, J., Mäkinen, J., Näränen, J., Merlet, S., Farah, T., Guerlin, C., Santos, F.P.D., Moigne, N.L., Champollion, C., Deville, S., Timmen, L., Falk, R., Wilmes, H., Iacovone, D., Baccaro, F., Germak, A., Biolcati, E., Krynski, J., Sekowski, M., Olszak, T., Pachuta, A., Agren, J., Engfeldt, A., Reudink, R., Inacio, P., McLaughlin, D., Shannon, G., Eckl, M., Wilkins, T., van Westrum, D., Billson, R., 2013. The European Comparison of Absolute Gravimeters 2011 (ECAG-2011) in Walferdange, Luxembourg: results and recommendations. Metrologia 50 (3), 257–268.

Gitlein, O., Timmen, L., Müller, J., 2013. Modeling of atmospheric gravity effects for high-precision observations. Int. J. Geosci. 4, 33344.

Gitlein, O., 2009. Absolutgravimetrische Bestimmung der Fennoskandischen Landhebung mit dem FG5-220, Ph.D. thesis. Leibniz Universität Hannover.

Heck, B., Mälzer, H., 1983. Determination of vertical recent crustal movements by levelling and gravity data. In: Vyskočil, P.A.M.W., Green, R. (Eds.), Recent Crustal Movements, 1982. Vol. 20 of Developments in Geotectonics. Elsevier, pp. 251–264.

Kierulf, H.P., Steffen, H., Simpson, M.J.R., Lidberg, M., Wu, P., Wang, H., 2014. A GPS velocity field for Fennoscandia and a consistent comparison to glacial isostatic adjustment models. J. Geophys. Res. 119 (8), 6613–6629.

Lambert, A., Courtier, N., James, T., 2006. Long-term monitoring by absolute gravimetry: tides to postglacial rebound. J. Geodyn. 41 (1-3), 307–317.

Leirião, S., He, X., Christiansen, L., Andersen, O.B., Bauer-Gottwein, P., 2009. Calculation of the temporal gravity variation from spatially variable water storage change in soils and aquifers. J. Hydrol. 365 (3–4), 302–309.

Lidberg, M., Johansson, J.M., Scherneck, H.-G., Milne, G., 2010. Recent results based on continuous GPS observations of the GIA process in Fennoscandia from BIFROST. J. Geodyn. 50, 8–18.

Lyard, F., Lefevre, F., Letellier, T., Francis, O., 2006. Modelling the global ocean tides: modern insights from FES2004. Ocean Dyn. 56 (5), 394–415.

Lysaker, D.I., Breili, K., Pettersen, B.R., 2008. The gravitational effect of ocean tide loading at high latitude coastal stations in Norway. J. Geod. 82 (9), 569–583.

Mäkinen, J., Virtanen, H., Bilker-Koivula, M., Ruotsalainen, H., Näränen, J., Raja-Halli, A., 2015. The Effect of Helium Emissions by a Superconducting Gravimeter on the Rubidium Frequency Standards of Absolute Gravimeters. Springer, Berlin, Heidelberg, pp. 1–6.

Müller, J., Naeimi, M., Gitlein, O., Timmen, L., Denker, H., 2012. A land uplift model in Fennoscandia combining GRACE and absolute gravimetry data. Phys. Chem. Earth, Parts ABC 53-54, 54–60.

Matsumoto, K., Takanezawa, T., Ooe, M., 2000. Ocean tide models developed by assimilating TOPEX/POSEIDON altimeter data into hydrodynamical model: a global model and a regional model around Japan. J. Oceanogr. 56 (5), 567–581.

Mazzotti, S., Lambert, A., Henton, J., James, T.S., Courtier, N., 2011. Absolute gravity calibration of GPS velocities and glacial isostatic adjustment in mid-continent North America. Geophys. Res. Lett. 38 (24.).

Micro-g LaCoste, 2012. g9 User's Manual, April 2012 version. Micro-g LaCoste, Lafayette, Colorado, USA.

Mikolaj, M., Meurers, B., Mojzeš, M., 2015. The reduction of hydrology-induced gravity variations at sites with insufficient hydrological instrumentation. Stud. Geophys. Geod. 59 (3), 424–437.

Mikolaj, M., Meurers, B., Güntner, A., 2016. Modelling of global mass effects in hydrology, atmosphere and oceans on surface gravity. Comp. Geosci. 93, 12–20.

Milne, G.A., Davis, J.L., Mitrovica, J.X., Scherneck, H.-G., Johansson, J.M., Vermeer, M., Koivula, H., 2001. Space-geodetic constraints on glacial isostatic adjustment in Fennoscandia. Science 291 (5512), 2381–2385.

Niebauer, T.M., Sasagawa, G.S., Faller, J.E., Hilt, R., Klopping, F., 1995. A new generation of absolute gravimeters. Metrologia 32 (3), 159–180.

Nordman, M., Poutanen, M., Kairus, A., Virtanen, J., 2014. Using the Nordic Geodetic Observing System for land uplift studies. Solid Earth 5 (2), 673–681.

Olesen, O., Kierulf, H.P., Brönner, M., Dalsegg, E., Fredin, O., Solbakk, T., 2013. Deep weathering, neotectonics and strandflat formation in Nordland, northern Norway. Norwegian J. Geol. 93 (3-4), 189–213.

Olsson, P.-A., Scherneck, H.-G., Ågren, J., 2009. Effects on gravity from non-tidal sea level variations in the Baltic Sea. J. Geodyn. 48 (3-5), 151–156.

Olsson, P.-A., Milne, G., Scherneck, H.-G., Ågren, J., 2015. The relation between gravity rate of change and vertical displacement in previously glaciated areas. J. Geodyn. 83, 76–84.

Pálinkáš, V., Lederer, M., Kostelecký, J., Šimek, J., Mojzeš, M., Ferianc, D., Csapó, G., 2012. Analysis of the repeated absolute gravity measurements in the Czech Republic, Slovakia and Hungary from the period 1991–2010 considering instrumental and hydrological effects. J. Geod. 87 (1), 29–42.

Penna, N.T., Bos, M.S., Baker, T.F., Scherneck, H.-G., 2008. Assessing the accuracy of predicted ocean tide loading displacement values. J. Geod. 82 (12), 893–907.

Petit, G., Luzum, B.e., 2010. IERS Conventions (2010) Tech. rep. International Earth Rotation and Reference Systems Service (IERS), Frankfurt am Main, tech. Note 36, 179 pp.

Pettersen, B.R., Bilker-Koivula, M., Breili, K., Engfeldt, A., Falk, R., Gitlein, O., Gjevestad, J.G.O., Hoppe, W., Lysaker, D.I., Mäkinen, J., Omang, O.C.D., Reinhold, A., Timmen, L., 2010. An accuracy assessment of absolute gravimetric observations in Fennoscandia. Nordic J. Surv. Real Estate Res. 7, 7–14.

Pettersen, B.R., 2011. The Postglacial Rebound Signal of Fennoscandia Observed by Absolute Gravimetry, GPS, and Tide Gauges. Int. J. Geophys, Article ID 957329.

Ray, R.D., 1999. A global ocean tide model from Topex/Poseidon altimetry: GOT99.2. Tech. rep. National Aeronautics and Space Administration (NASA), tech. Memo. 209478.

Rodell, M., Houser, P.R., Jambor, U., Gottschalck, J., Mitchell, K., Meng, C.-J., Arsenault, K., Cosgrove, B., Radakovich, J., Bosilovich, M., Entin, J.K., Walker, J.P., Lohmann, D., Toll, D., 2004. The global land data assimilation system. Bull. Am. Meteor. Soc. 85 (3), 381–394.

Roland, E., 1998. Absolutt tyngdemåling i Fennoskandia og Svalbard (Absolute gravity measurements in Fennoscandia and Svalbard), Tech. rep. Norwegian Mapping Authority, internal project report (in Norwegian), 21 pp.

Sasagawa, G., 1989. Validation and application of an absolute gravity meter in California, Ph.D. thesis. University of California, San Diego.

Savcenko, R., Bosch, W., 2011. EOT11a – a new tide model from multi-mission altimetry. In: Poster Presented at the Ocean Surface Topography Science Team Meeting, San Diego, October 19–21.

Schmerge, D., Francis, O., Henton, J., Ingles, D., Jones, D., Kennedy, J., Krauterbluth, K., Liard, J., Newell, D., Sands, R., Schiel, A., Silliker, J., Westrum, D., 2012. Results of the first North American comparison of absolute gravimeters, NACAG-2010. J. Geod. 86 (8), 591–596.

Schwiderski, E.W., 1980. On charting global ocean tides. Rev. Geophys. 18 (1), 243–268.

Simpson, M.J.R., Breili, K., Kierulf, H.P., 2013. Estimates of twenty-first century sea-level changes for Norway. Clim. Dyn. 42 (5), 1405–1424.

Šprlák, M., Gerlach, C., Pettersen, B.R., 2015. Validation of global gravitational field models in Norway. Newton's Bull. 5, 3–12.

Steffen, H., Wu, P., 2011. Glacial isostatic adjustment in Fennoscandia – a review of data and modeling. J. Geodyn. 52 (3-4), 169–204.

Steffen, H., Gitlein, O., Denker, H., Müller, J., Timmen, L., 2009. Present rate of uplift in Fennoscandia from GRACE and absolute gravimetry. Tectonophysics 474 (1-2), 69–77.

Timmen, L., Gitlein, O., Klemann, V., Wolf, D., 2011. Observing gravity change in the Fennoscandian uplift area with the hanover absolute gravimeter. Pure Appl. Geophys. 169 (8), 1331–1342.

Timmen, L., Engfeldt, A., Scherneck, H.-G., 2015. Observed secular gravity trend at Onsala station with the FG5 gravimeter from Hannover. J. Geod. Sci. 5, 1–8.

Timmen, L., 2010. Absolute and Relative Gravimetry. In: Sciences of Geodesy – I: Advances and Future Directions. Springer, Berlin, Heidelberg, pp. 1–48.

Torge, W., Müller, J., 2012. Geodesy. Walter de Gruyter, Berlin.

Van Camp, M., Williams, S.D.P., Francis, O., 2005. Uncertainty of absolute gravity measurements. J. Geophys. Res. 110 (B5.).

Van Camp, M., de Viron, O., Scherneck, H.-G., Hinzen, K.-G., Williams, S.D.P., Lecocq, T., Quinif, Y., Camelbeeck, T., 2011. Repeated absolute gravity measurements for monitoring slow intraplate vertical deformation in western Europe. J. Geophys. Res. 116 (B8.).

Van Camp, M., de Viron, O., Avouac, J.P., 2016. Separating climate-induced mass transfers and instrumental effects from tectonic signal in repeated absolute gravity measurements. Geophys. Res. Lett. 43, 4313–4320.

Vestøl, O., 2006. Determination of postglacial land uplift in fennoscandia from leveling, tide-gauges and continuous gps stations using least squares collocation. J. Geod. 80 (5), 248–258.

Virtanen, H., Tevo, M., Bilker-Koivula, M., 2006. Comparison of superconducting gravimeter observations with hydrological models of various spatial extents. In: Bull. d'Inf. Marées Terr, pp. 11361–11368.

Wahr, J., DaZhong, H., Trupin, A., 1995. Predictions of vertical uplift caused by changing polar ice volumes on a viscoelastic Earth. Geophys. Res. Lett. 22 (8), 977–980.

Wunsch, C., Stammer, D., 1997. Atmospheric loading and the oceanic inverted barometer effect. Rev. Geophys. 35 (1), 79–107.

Supplementary data for

Absolute gravity observations in Norway (1993-2014) for glacial isostatic adjustment studies: the influence of gravitational loading effects on secular gravity trends

Vegard Ophaug
Department of Mathematical Sciences and Technology, Norwegian University of Life Sciences (NMBU), Ås, Norway

Kristian Breili
Geodetic Institute, Norwegian Mapping Authority, Hønefoss, Norway

Christian Gerlach
Commission of Geodesy and Glaciology, Bavarian Academy of Sciences and Humanities, Munich, Germany

Jon Glenn Omholt Gjevestad
Department of Mathematical Sciences and Technology, Norwegian University of Life Sciences (NMBU), Ås, Norway

Dagny Iren Lysaker
Geodetic Institute, Norwegian Mapping Authority, Hønefoss, Norway

Ove Christian Dahl Omang
Geodetic Institute, Norwegian Mapping Authority, Hønefoss, Norway

Bjørn Ragnvald Pettersen
Department of Mathematical Sciences and Technology, Norwegian University of Life Sciences (NMBU), Ås, Norway

Contents of this file

Table S1

FG5 AG observations and refined corrections in Norway 1993-2014. Gravity in μGal. OTL and NTL computed for coastal gravity sites only (see text for more details).

Code	Epoch	FG5#	g_0	σ^0_{SET}	δg_{OTL}	Δg_{NTL}	σ_{SET}	OLM[1]	δg_{ATM}	Δg_{GH}	g
ANDO	2004.475	220	982 532 304.60 ± 2.29	3.80		−0.36	3.80	N+TG[2]	−0.2	0.1	982 532 304.14 ± 2.29
	2005.556	226	982 532 299.98 ± 2.07	2.73	0.05	0.20	1.24		−0.5	0.6	982 532 300.33 ± 2.03
	2007.479	226	982 532 298.26 ± 1.97	2.02	−0.02	−0.36	1.61		−0.8	0.3	982 532 297.38 ± 1.97
	2009.534	226	982 532 295.80 ± 2.00	2.24	0.32	−0.06	2.04		0.1	0.2	982 532 296.36 ± 1.99
	2010.447	226	982 532 297.71 ± 2.04	2.30	−0.01	0.16	1.86		1.1	0.0	982 532 298.96 ± 2.03
BODB	2006.510	226	982 359 943.63 ± 1.99	2.61	−0.31	−0.07	2.61	N+TG	−0.3	0.8	982 359 943.75 ± 1.99
	2007.529	226	982 359 940.75 ± 2.00	2.65	−0.45	−0.05	2.19		−0.2	0.6	982 359 940.65 ± 1.99
	2009.553	226	982 359 937.50 ± 2.01	2.06	0.10	0.06	1.96		−0.8	0.4	982 359 937.26 ± 2.01
	2010.482	226	982 359 940.02 ± 2.00	1.77	−0.46	−0.04	1.25		−0.1	0.2	982 359 939.62 ± 1.98
BODA	2004.489	220	982 372 238.80 ± 2.27	2.50		0.00	2.50	N+TG	−0.5	0.2	982 372 238.50 ± 2.27
	2005.545	226	982 372 233.54 ± 2.01	2.47	−0.32	−0.03	2.44		−0.7	0.7	982 372 233.19 ± 2.01
	2006.507	226	982 372 232.98 ± 2.01	2.79	−0.03	−0.00	2.66		0.2	0.7	982 372 233.85 ± 2.01
	2009.548	226	982 372 226.35 ± 2.02	2.24	−0.17	0.03	2.10		−0.7	0.4	982 372 225.91 ± 2.02
HAMM	2006.488	226	982 615 904.40 ± 2.03	3.39	0.35	−0.45	2.06	F+TG[3]	0.1	0.5	982 615 904.90 ± 1.99
	2010.471	226	982 615 898.68 ± 2.05	2.96	1.04	−0.27	1.98		−1.1	0.1	982 615 898.45 ± 2.00
HONN	2005.570	226	982 660 449.63 ± 2.04	4.39	0.49	−0.29	3.03	N+TG	−0.2	0.6	982 660 450.23 ± 2.00
	2006.428	226	982 660 454.22 ± 2.06	5.20	−0.08	−1.65	3.02		−0.1	0.4	982 660 452.79 ± 2.00
	2006.652	220	982 660 451.60 ± 2.28	3.80		0.23	3.80		0.2	1.0	982 660 453.03 ± 2.28
	2007.507	226	982 660 444.74 ± 2.01	4.85	1.32	0.83	1.90		1.1	0.3	982 660 448.29 ± 1.98
	2010.466	226	982 660 449.93 ± 2.10	4.42	0.76	−0.65	1.79		−1.0	0.0	982 660 449.04 ± 1.99

[1]Ocean Loading Model
[2]NAO99b(N50 coastline) combined with local tide-gauge observations.
[3]FES2012(N50 coastline) combined with local tide-gauge observations.

HONA	1993.668	102	981 905 974.72 ± 2.26						−0.4	0.5	981 905 974.72 ± 2.26
	2010.395	226	981 905 961.06 ± 1.99						−0.6	−0.4	981 905 960.06 ± 1.99
HONB	1993.666	102	981 809 514.35 ± 2.24						−0.3	0.5	981 809 514.05 ± 2.24
	1995.649	111	981 809 514.35 ± 2.22						−0.3	1.4	981 809 515.55 ± 2.22
	2003.466	301	981 809 504.99 ± 2.77						−0.1	0.5	981 809 505.29 ± 2.77
	2010.384	226	981 809 499.88 ± 1.97						−1.0	−0.5	981 809 498.58 ± 1.97
HONC	1995.748	111	981 900 653.24 ± 2.33						0.0	0.7	981 900 653.94 ± 2.33
	2003.471	301	981 900 648.27 ± 2.79						0.4	0.5	981 900 649.17 ± 2.79
	2003.734	220	981 900 643.20 ± 2.44						−0.9	1.0	981 900 643.30 ± 2.44
	2004.402	226	981 900 646.59 ± 1.94						−0.7	0.0	981 900 645.89 ± 1.94
	2005.532	226	981 900 646.86 ± 2.06						−0.7	1.0	981 900 647.26 ± 2.06
	2006.444	226	981 900 640.90 ± 2.03						−0.1	0.4	981 900 641.10 ± 2.03
	2007.362	220	981 900 644.90 ± 2.47						−0.7	−0.3	981 900 643.80 ± 2.47
	2007.452	226	981 900 643.31 ± 1.99						−0.1	0.7	981 900 643.91 ± 1.99
	2008.552	226	981 900 645.62 ± 2.00						−0.2	1.0	981 900 646.12 ± 2.00
	2009.510	226	981 900 647.16 ± 2.03						−0.7	0.4	981 900 646.76 ± 2.03
	2010.375	226	981 900 650.21 ± 1.99						−1.2	−0.6	981 900 648.51 ± 1.99
	2011.622	226	981 900 652.12 ± 2.02						−1.0	0.9	981 900 652.12 ± 2.02
JON2	2005.482	226	981 858 926.29 ± 2.05	1.20	−0.25	0.06	1.44	N+TG	−0.2	0.4	981 858 926.30 ± 2.05
	2014.479	226	981 858 919.08 ± 2.16	2.50	0.41	0.10	1.57		0.0	0.9	981 858 920.49 ± 2.12
KAUT	2005.581	226	982 454 534.36 ± 1.99						−0.6	0.9	982 454 534.86 ± 1.99
	2006.493	226	982 454 531.32 ± 1.98						−0.9	0.7	982 454 531.12 ± 1.98
	2006.666	220	982 454 530.60 ± 2.26						−0.5	1.5	982 454 531.60 ± 2.26
	2008.522	226	982 454 529.58 ± 2.02						−0.5	0.3	982 454 529.48 ± 2.02
	2010.460	226	982 454 522.46 ± 1.99						−1.2	0.1	982 454 521.66 ± 1.99

KOL1	1997.780	111	981 968 087.60 ± 4.21	4.90		0.02		N+TG	−1.0	0.5	981 968 087.12 ± 4.21
	2005.485	226	981 968 084.68 ± 1.98	2.11	0.20	−0.03	2.02		1.0	0.4	981 968 086.25 ± 1.98
KOL2	1997.780	111	981 972 825.40 ± 4.42	9.00		0.02		N+TG	−0.4	0.5	981 972 825.52 ± 4.42
	2005.488	226	981 972 818.24 ± 1.98	1.40	0.37	−0.01	1.19		0.5	0.4	981 972 819.50 ± 1.98
STVA	1993.679	102	981 832 863.13 ± 2.40	2.70	−0.03	0.08	2.45	CSR4.0	0.3	0.5	981 832 863.98 ± 2.40
	1995.658	111	981 832 868.48 ± 2.35	1.70	0.09	0.38	1.50		0.4	0.9	981 832 870.25 ± 2.35
	2003.460	301	981 832 861.03 ± 2.88	2.24		−0.09	2.24		0.0	0.4	981 832 861.34 ± 2.88
	2004.842	226	981 832 867.66 ± 2.31	5.19	−0.53	−0.22	5.03		−0.3	0.2	981 832 866.81 ± 2.29
	2006.855	226	981 832 860.56 ± 2.22	3.81	−0.55	−0.11	3.82		0.1	0.2	981 832 860.20 ± 2.22
	2007.633	226	981 832 859.48 ± 2.10	2.17	−0.42	−0.07	2.07		0.6	0.7	981 832 860.29 ± 2.10
	2008.863	226	981 832 857.87 ± 2.11	2.66	−0.12	−0.07	2.34		−0.7	0.1	981 832 857.08 ± 2.10
TROM	1993.641	102	982 539 927.27 ± 2.23	2.70	0.30	0.12	2.35	F+TG	0.2	0.5	982 539 928.39 ± 2.22
	1995.677	111	982 539 934.27 ± 2.20	1.00	0.15	0.25	1.04		−0.2	0.6	982 539 935.07 ± 2.20
	1998.490	101	982 539 929.64 ± 2.73	1.00		0.01	1.00		−0.1	0.1	982 539 929.65 ± 2.73
	2003.501	301	982 539 926.88 ± 2.73	1.00		−0.09	1.00		0.2	0.1	982 539 927.09 ± 2.73
	2004.464	220	982 539 933.20 ± 2.26	2.00		−0.22	2.00		−0.3	0.0	982 539 932.68 ± 2.26
	2005.589	226	982 539 927.73 ± 1.99	2.58	−0.14	−0.02	2.38		−0.8	0.7	982 539 927.47 ± 1.99
	2008.514	226	982 539 929.15 ± 4.10	2.52	0.48	0.11	2.29		0.4	0.3	982 539 930.44 ± 4.10
	2009.529	226	982 539 929.15 ± 4.12	3.12	0.40	0.00	2.64		−0.6	0.2	982 539 929.15 ± 4.11
TRDA	1995.666	111	982 146 021.09 ± 2.20	0.95	0.06	0.57	0.88	N+TG	0.0	0.8	982 146 022.52 ± 2.20
	1998.474	101	982 146 014.74 ± 2.78	2.79		−0.02	2.79		−0.2	0.2	982 146 014.72 ± 2.78
	2003.490	301	982 146 001.94 ± 2.78	2.79		0.06	2.79		0.3	0.3	982 146 002.60 ± 2.78
	2003.701	220	982 145 998.00 ± 2.28	3.80		0.33	3.80		0.1	0.8	982 145 999.23 ± 2.28
	2004.475	226	982 146 005.68 ± 2.12	6.39	0.01	0.08	6.31		−0.9	0.4	982 146 005.27 ± 2.12
	2005.537	226	982 145 998.34 ± 1.98	1.74	0.35	−0.11	1.14		0.2	0.9	982 145 999.68 ± 1.97
	2006.466	226	982 146 000.18 ± 1.98	3.54	0.52	−0.18	2.76		−0.2	0.5	982 146 000.82 ± 1.95

	2007.463	226	982 145 994.94 ± 2.01	3.11	0.12	0.25	1.98	1.0	0.6	982 145 996.91 ± 1.98
	2008.495	226	982 145 995.98 ± 2.02	3.73	0.13	0.06	2.38	0.3	0.6	982 145 997.07 ± 1.99
	2010.419	226	982 145 995.39 ± 2.00	2.60	0.16	0.25	1.93	0.7	−0.3	982 145 996.20 ± 1.98
TRYB	1993.614	101	981 827 021.38 ± 6.29					−0.8	0.7	981 827 021.28 ± 6.29
	1993.652	102	981 827 019.12 ± 2.22					0.0	0.6	981 827 019.72 ± 2.22
	1995.734	111	981 827 016.07 ± 2.22					−0.8	0.9	981 827 016.17 ± 2.22
	2007.578	233	981 827 000.19 ± 1.92					−0.9	1.1	981 827 000.39 ± 1.92
	2007.581	226	981 826 996.20 ± 1.98					−1.0	1.1	981 826 996.30 ± 1.98
	2008.254	226	981 827 010.03 ± 1.96					−0.4	−1.5	981 827 008.13 ± 1.96
	2010.400	226	981 826 994.91 ± 1.96					−0.5	−0.5	981 826 993.91 ± 1.96
TRYC	1993.616	101	981 827 014.50 ± 6.58					−0.3	0.7	981 827 014.90 ± 6.58
	1993.660	102	981 827 015.20 ± 2.22					−0.6	0.5	981 827 015.10 ± 2.22
	1995.732	111	981 827 014.05 ± 2.20					−0.5	0.9	981 827 014.45 ± 2.20
	1995.753	101	981 827 010.51 ± 2.73					0.7	0.8	981 827 012.01 ± 2.73
	1998.466	101	981 827 010.38 ± 2.73					−0.8	0.0	981 827 009.58 ± 2.73
	2003.477	301	981 827 003.78 ± 2.73					−0.4	0.3	981 827 003.68 ± 2.73
	2003.723	220	981 827 004.50 ± 2.27					−1.9	1.1	981 827 003.70 ± 2.27
	2004.418	226	981 827 005.14 ± 2.01					−1.8	0.1	981 827 003.44 ± 2.01
	2005.619	226	981 827 003.08 ± 1.98					−0.2	1.1	981 827 003.98 ± 1.98
	2006.614	226	981 826 999.98 ± 2.07					−0.9	1.7	981 827 000.78 ± 2.07
	2007.375	220	981 827 005.40 ± 2.26					−0.2	−0.4	981 827 004.80 ± 2.26
	2007.578	226	981 827 000.54 ± 1.98					−0.4	1.0	981 827 001.14 ± 1.98
	2007.581	233	981 827 002.85 ± 1.92					−1.0	1.1	981 827 002.95 ± 1.92
	2008.656	226	981 826 995.58 ± 2.02					−0.4	1.1	981 826 996.28 ± 2.02
	2009.567	226	981 826 996.56 ± 1.97					−0.9	0.4	981 826 996.06 ± 1.97
	2010.405	226	981 826 997.38 ± 1.98					−0.3	−0.5	981 826 996.58 ± 1.98
	2011.608	226	981 826 995.20 ± 1.96					0.0	1.1	981 826 996.30 ± 1.96

VAGA	2003.482	301	982 074 811.26 ± 2.78	2.79		−0.19	2.79	N+TG	0.9	0.3	982 074 812.27 ± 2.78
	2006.381	226	982 074 808.92 ± 1.98	1.75	1.47	−0.75	2.16		−1.0	−0.1	982 074 808.54 ± 1.99
	2007.581	233	982 074 808.67 ± 1.97	3.35	0.84	−0.35	1.21		0.0	0.7	982 074 809.86 ± 1.92
	2010.660	226	982 074 804.99 ± 2.01	2.64	−0.14	0.03	1.84		0.4	0.8	982 074 806.08 ± 1.99
VEGA	2010.433	226	982 340 766.64 ± 1.99	2.32	−0.34	0.02	2.27	CSR4.0	0.8	−0.1	982 340 767.02 ± 1.99
ALES	2003.715	220	982 063 297.00 ± 2.29	3.50		−1.86	3.50	F+TG	0.4	0.7	982 063 296.24 ± 2.29
	2004.549	226	982 063 296.81 ± 2.07	4.84	1.26	0.38	3.63		0.4	0.6	982 063 299.45 ± 2.01
	2006.384	226	982 063 296.79 ± 2.08	6.01	1.81	−1.76	3.16		−0.8	−0.1	982 063 295.94 ± 2.00
	2008.724	226	982 063 296.80 ± 2.00	3.89	−0.31	1.04	2.61		0.4	0.8	982 063 298.73 ± 1.98
	2010.666	226	982 063 294.42 ± 2.08	3.41	−0.34	0.82	2.47		1.1	0.8	982 063 296.80 ± 2.03
NMBU	2004.609	226	981 884 413.52 ± 2.04						−0.1	1.1	981 884 414.52 ± 2.04
	2005.605	226	981 884 413.18 ± 2.00						−1.2	1.0	981 884 413.32 ± 2.00
	2006.685	226	981 884 414.28 ± 2.00						0.2	1.1	981 884 415.58 ± 2.00
	2007.605	226	981 884 415.19 ± 1.97						−0.1	0.9	981 884 415.99 ± 1.97
	2008.642	226	981 884 414.21 ± 2.00						0.3	1.1	981 884 415.61 ± 2.00
	2009.592	226	981 884 410.37 ± 2.01						0.3	0.5	981 884 411.17 ± 2.01
	2010.595	226	981 884 409.85 ± 1.98						0.3	1.1	981 884 411.25 ± 1.98
	2011.600	226	981 884 409.76 ± 2.00						−0.7	0.9	981 884 409.96 ± 2.00
	2012.683	226	981 884 406.25 ± 1.98						−1.7	1.0	981 884 405.55 ± 1.98
	2014.458	226	981 884 412.50 ± 2.03						−0.1	1.1	981 884 413.50 ± 2.03

Paper C

Journal of Geodesy manuscript No.
(will be inserted by the editor)

On the equivalence of spherical splines with least-squares collocation and Stokes's formula for regional geoid computation

Vegard Ophaug · **Christian Gerlach**

Received: date / Accepted: date

Abstract This work is an investigation of three methods for regional geoid computation: Stokes's formula, least-squares collocation (LSC), and spherical radial base functions (RBFs) using the spline kernel (SK). It is a first attempt to compare the three methods theoretically and numerically in a unified framework. While Stokes integration and LSC may be regarded as classic methods for regional geoid computation, RBFs may still be regarded as a modern approach. All methods are theoretically equal when applied globally, and we therefore expect them to give comparable results in regional applications. However, it has been shown by de Min (1995) that the equivalence of Stokes's formula and LSC does not hold in regional applications without modifying the cross-covariance function. In order to make all methods comparable in regional applications, the corresponding modification has been introduced also in the SK. Ultimately, we present numerical examples comparing Stokes's formula, LSC and SKs in a closed-loop environment using synthetic noise-free data, to verify their equivalence. All agree on the mm level.

Keywords Regional geoid computation · Stokes's formula · Least-squares collocation · Spherical radial base functions · Spline kernel

V. Ophaug
Dept. of Mathematical Sciences and Technology
Norwegian University of Life Sciences (NMBU)
Drøbakveien 31, N-1430 Ås
E-mail: vegard.ophaug@nmbu.no

C. Gerlach
Commission of Geodesy and Glaciology
Bavarian Academy of Sciences and Humanities
Alfons-Goppel Str. 11, D-80539 München
E-mail: gerlach@keg.badw.de

1 Introduction

The global gravity field is typically represented using spherical harmonics (SH). Consequently, in regional gravity modeling, one usually splits the gravity signal into a global long-wavelength part which is modeled using SH, and a regional short-wavelength part, which is modeled using a suitable regional method (Sansò and Sideris, 2013).

There exist several methods for approximating Earth's regional gravity field, of which integral formula solutions to geodetic boundary value problems and least-squares techniques have emerged as common approaches (Nerem et al., 1995). A review and comparison of different regional gravity modeling concepts is given by Tscherning (1981). More recently, Schmidt et al. (2015) investigated different regional gravity modeling methods through an International Association of Geodesy Inter-Commission Committee on Theory Joint Study Group. Considering geoid computation in particular, Stokes's formula (Stokes, 1849) and least-squares collocation (LSC) (Krarup, 1969; Moritz and Sünkel, 1978; Moritz, 1980) are treated in most geodetic text books (Heiskanen and Moritz, 1967; Vaníček and Krakiwsky, 1986; Hofmann-Wellenhof and Moritz, 2006; Torge and Müller, 2012).

Radial base functions (RBFs) are limited to a certain spatial region, making them suitable for regional gravity field modeling due to their space-localizing properties. There is a vast amount of RBFs to choose from, as long as they represent harmonic kernel functions. They are versatile in that their approximation characteristics and spatial distribution can be adjusted, making it possible to use them for all kinds of data sets and for combining different types of observations (e.g., Lieb et al., 2016). Regional gravity field modeling with RBFs can be done using numerical integration (e.g., Freeden and Schneider, 1998; Schmidt et al., 2002; Liu and Sideris, 2003; Roland and Denker, 2005) or least-squares estimation approaches (e.g., Schmidt et al., 2007; Lieb et al.,

2016). In this work we use the latter, which is the common geodetic approach, facilitating error analysis and propagation. The mathematical foundation of RBFs, the special RBFs known as spherical wavelets, and their application in multiscale analysis are given by, e.g., Freeden et al. (1998), Schmidt (2001), Jekeli (2005) or Schmidt et al. (2007). In later years, we have observed an increased use of RBFs for regional gravity modeling (Roland, 2005; Klees et al., 2008; Eicker, 2008; Tenzer and Klees, 2008; Wittwer, 2009; Bentel, 2013; Naeimi, 2013; Bentel et al., 2013a,b; Eicker et al., 2014; Pock et al., 2014; Bucha et al., 2015; Naeimi et al., 2015; Farahani et al., 2016; Lieb et al., 2016).

In this work we aim to show that regional geoid computation with RBFs is equivalent to Stokes's formula and LSC, in theory and in practice. Theoretical and numerical comparisons of Stokes's formula and LSC was done by de Min (1995), while a theoretical comparison of LSC and SKs was discussed by Eicker (2008), both of which we review and present in a unified framework. We show the theoretical equivalence of Stokes's formula, LSC, and RBFs in the global case, as well as the breakdown of the equivalence of Stokes's formula and LSC in regional applications. We introduce the remedial modification of the cross-covariance function of LSC also in the SKs, such that all methods are equal also in regional applications. Ultimately we present numerical examples comparing the methods in a closed-loop environment, demonstrating their equivalence in practice.

Sect. 2 introduces the different modeling approaches, while their theoretical equivalence in the global case is shown in Sect. 3. The breakdown of their equivalence in regional applications is shown in Sect. 4, and the remedial modifications of LSC and SKs to restore their equivalence to Stokes's formula are applied. Numerical examples comparing the methods are given in Sect. 5, while Sect. 6 summarizes our results.

2 Modeling approaches

2.1 Stokes's formula

Geoid heights N may be obtained from block mean gravity anomalies $\Delta\bar{g}$ by the integral formula of Stokes (1849). It globally integrates the gravity anomalies over the whole sphere σ, using the Stokes function S as integration kernel (or weight),

$$N(P) = \frac{R}{4\pi\gamma} \iint_{\sigma} S(\psi_{Pq}) \Delta\bar{g}_q \, \mathrm{d}\sigma, \tag{1}$$

where R is the spherical Earth radius, γ is normal gravity evaluated on the surface of the reference ellipsoid, and ψ_{Pq} is the spherical distance between computation poit P and data point q. Eq. (1) is a spherical convolution of the $\Delta\bar{g}_q$ function with the kernel $S(\psi_{Pq})$, and can be solved exactly by either numerical integration or by a one-dimensional Fast Fourier Transform (1D-FFT) (Haagmans et al., 1993), where the FFT is performed along parallels only. We have used the FFT approach, implemented according to

$$N(\varphi_P) = \frac{R\Delta\varphi\Delta\lambda}{4\pi\gamma} \mathscr{F}_1^{-1} \left[\sum_{\varphi} \mathscr{F}_1 \left\{ S(\Delta\lambda) \right\} \cdot \mathscr{F}_1 \left\{ \Delta\bar{g}_q \cos\varphi \right\} \right], \tag{2}$$

where $\mathscr{F}_1$ denotes the 1D-FFT operator and $\mathscr{F}_1^{-1}$ its inverse, and $\Delta\varphi$ and $\Delta\lambda$ are the latitudinal and longitudinal spacing of the computation grid, respectively. Furthermore, the Stokes function is computed by its closed formula (Hofmann-Wellenhof and Moritz, 2006).

2.2 Least-squares collocation

LSC is an optimal estimation method in the statistical sense, allowing the estimation of arbitrary gravity field quantities from inhomogeneously distributed point observations. It takes advantage of the knowledge of the signal covariance and tries to minimize the prediction error.

Restricted to the case of geoid computation and in direct comparison with Eq. (1), LSC can be written as

$$N(P) = \mathbf{C}_{Pq}^{Ng} \left(\mathbf{C}_{qq}^{gg} \right)^{-1} \Delta g_q, \tag{3}$$

where $\mathbf{C}_{Pq}^{Ng}$ is a matrix containing the signal cross-covariances between the functionals N and Δg between computation point P and observations q, and $\mathbf{C}_{qq}^{gg}$ is the auto-covariance matrix between all combinations of observations.

All covariances are obtained from the same covariance function $C(\psi)$, assumed to depend only on the horizontal distance ψ between the considered points. In physical geodesy, we typically take the covariance function of the disturbing potential T to be the basic covariance function, from which all covariances are computed by covariance propagation. The covariance function can be written as

$$C(\psi_{Pq}) = \frac{1}{8\pi^2} \int_{\lambda=0}^{2\pi} \int_{\theta=0}^{\pi} \int_{\alpha=0}^{2\pi} T(\theta_P, \lambda_P) T(\theta_q, \lambda_q) \sin\theta \, \mathrm{d}\theta \mathrm{d}\lambda \mathrm{d}\alpha, \tag{4}$$

where (θ, λ) are spherical coordinates, and the points $P(\theta, \lambda)$, $q(\theta, \lambda)$ are on the surface of the unit sphere.

The global integral in Eq. (4) can also be expressed as a Legendre series,

$$C(\psi_{Pq}) = \sum_{n=2}^{\infty} (\lambda_n^T)^2 c_n P_n(\cos\psi_{Pq}), \tag{5}$$

where $P_n(\cos\psi_{Pq})$ are the Legendre polynomials, and c_n are the dimensionless signal degree variances, with $\lambda_n^T = GM/R$. The signal degree variances can be computed from a set of spherical harmonic coefficients $\{\Delta\bar{C}_{nm}, \Delta\bar{S}_{nm}\}$,

$$c_n = \sum_{m=0}^{n} \left(\Delta\bar{C}_{nm}^2 + \Delta\bar{S}_{nm}^2\right), \tag{6}$$

as obtained from a global gravity model (GGM), or by different empirical degree-variance models (Tscherning and Rapp, 1974; Jekeli, 1978; Flury, 2006; Rexer and Hirt, 2015).

2.3 Spherical splines

RBFs are isotropic functions which store most of their energy in a limited spherical cap around their origin, i.e., they have a distinct space-localizing ability and are therefore said to have quasi-local support.

Geoid computation with RBFs is performed according to

$$N(P) = \sum_{k=1}^{K} \hat{d}_k B(\psi_{Pk}), \tag{7}$$

where $B(\psi_{Pk})$ are the RBFs which are placed on spatially distributed grid points k, and $\hat{d}_k$ are point-specific gravity field parameters in the form of dimensionless coefficients.

As spherical isotropic functions, RBFs can be decomposed into a series of Legendre polynomials $P_n(\cos\psi_{Pk})$, where the spectral characteristics of a specific RBF depends on the choice of Legendre coefficients B_n (see Eq. (8)). One choice of B_n is to take the frequency response of the signal into account, characterized by the signal degree variances. These RBFs are known as spherical splines (Freeden et al., 1998; Jekeli, 2005; Eicker, 2008). In terms of a harmonic kernel, the spline kernel (SK) can be written as

$$\begin{aligned} B^{SK}(\psi_{Pk}) &= \sum_{n=2}^{\infty} \frac{\sqrt{2n+1}}{4\pi R^2} \lambda_n \sigma_n P_n(\cos\psi_{Pk}) \\ &= \sum_{n=2}^{\infty} \sum_{m=-n}^{n} \lambda_n B_n^{SK} Y_{nm}^R(\theta_P, \lambda_P) Y_{nm}^R(\theta_k, \lambda_k), \end{aligned} \tag{8}$$

where ψ_{Pk} is the spherical distance between computation point P and the origin of the SK at grid point k. The Legendre coefficients are given by

$$B_n^{SK} = \frac{\sigma_n}{\sqrt{2n+1}}, \tag{9}$$

where $\sigma_n = \sqrt{c_n}$ are the degree standard deviations, λ_n are the spectral eigenvalues including dimensioning, and

$$\begin{aligned} Y_{nm}^R(\theta,\lambda) = &\frac{1}{R\sqrt{4\pi}} \\ &\times \begin{cases} \bar{P}_{nm}(\cos\theta)\cos m\lambda, & m = 0,1,2,\ldots,n \\ \bar{P}_{n|m|}(\cos\theta)\sin|m|\lambda, & m = -n,\ldots,-2,-1 \end{cases} \end{aligned} \tag{10}$$

are the surface spherical harmonic base functions of degree n and order m, as defined by Schmidt (2001). $\bar{P}_{nm}(\cos\theta)$ are the fully normalized associated Legendre functions.

We note that the Legendre coefficients of the spherical splines differ slightly from the ones of the covariance function, and this is due to norm convergence issues (Eicker, 2008).

Eq. (7) represents the synthesis of geoid heights from known coefficients $\hat{d}_k$. The coefficients are obtained from gravity field observations by integration or parameter estimation techniques. We follow the latter approach, and write Eq. (7) in matrix notation as

$$N(P) = \mathbf{A}^N \mathbf{d}, \tag{11}$$

where $\mathbf{d}$ contains the spline coefficients $\hat{d}_k$ according to Eq. (7), and $\mathbf{A}^N$ represents the prediction matrix according to Eq. (8), with elements

$$A_{Pk}^N = \sum_{n=2}^{\infty} \sum_{m=-n}^{n} \lambda_n^N B_n^{SK} Y_{nm}^R(\theta_P, \lambda_P) Y_{nm}^R(\theta_k, \lambda_k), \tag{12}$$

and with $\lambda_n^N = GM/R\gamma$.

In agreement with geoid computation using Stokes's formula (Eq. (1)) or LSC (Eq. (3)) we derive the spline coefficients from observed gravity anomalies in an analysis step, by inversion of the linear model

$$\Delta\mathbf{g} + \mathbf{v} = \mathbf{A}^g \mathbf{d}. \tag{13}$$

Thereby, $\Delta\mathbf{g}$ is the observation vector and $\mathbf{v}$ is the error vector. $\mathbf{A}^g$ is the design matrix, with elements

$$A_{kk}^g = \sum_{n=2}^{\infty} \sum_{m=-n}^{n} \lambda_n^g B_n^{SK} Y_{nm}^R(\theta_k, \lambda_k) Y_{nm}^R(\theta_k, \lambda_k). \tag{14}$$

and with $\lambda_n^g = GM/R^2(n-1)$.

By inversion of the linear model (Eq. (13)), one coefficient for each SK needs to be determined. This is an ill-conditioned linear inverse problem, and the normal matrix must be regularized in order to solve the system. Numerous regularization techniques exist, and regularization remains

an important topic within gravity field modeling with RBFs (Bentel et al., 2013b; Naeimi et al., 2015). We have applied Tikhonov regularization (Tikhonov, 1963), where an extended norm which includes constraints on the unknowns is minimized. Thereby, we have a damped least-squares problem where not only the parameters which best fit the observations are determined, but also the solution is kept smooth enough to allow a stable inversion. The smoothness constraint is set a priori, and governed by the regularization matrix $\mathbf{R}$. The regularized solution can be written as

$$\hat{d}_k = \left[(\mathbf{A}^g)^T\mathbf{A}^g + \alpha\mathbf{R}\right]^{-1}(\mathbf{A}^g)^T\Delta\mathbf{g}, \tag{15}$$

where the regularization parameter α is a weight, balancing the contribution of observations and prior information to the solution. It is chosen as a compromise between a solution which is smoothed too much and significant parts of the signal is lost (α too large), and a solution which is corrupted by high-frequency errors, and no physically meaningful solution is obtained (α too small).

We determine the regularization parameter α by the L-curve method of Hansen and O'Leary (1993), as it has proven to be a suitable method for noise-free data (Bentel, 2013). Regardless of the regularization method, an initial guess of the regularization parameter, α_0, must be made. Here, we make an initial guess based on the condition number of the normal matrix and the maximum SH degree $N_{\max}$, i.e., $\alpha_0 = 8\|\mathbf{N}\|/N_{\max}^3$ (Naeimi, 2013).

In case of signal representation using SKs, $\mathbf{R}$ contains scalar products of the SKs located at different grid points (Eicker, 2008). If the SKs would be orthogonal, $\mathbf{R}$ would become a diagonal matrix which could be represented by a scaled identity matrix. If the scaling factor is combined with α, we can set $\mathbf{R} = \mathbf{I}$.

For bandlimited signals, as we employ them in discrete matrix computations, the SKs are not strictly orthogonal, and therefore $\mathbf{R}$ is not a diagonal matrix (Eicker, 2008). For non-bandlimited signals, orthogonality can theoretically be achieved, but at the cost of infinite energy along the main diagonal of $\mathbf{R}$. Eicker (2008) discussed different modifications which restrict the elements along the main diagonal to finite values. Among them is the modification of the a priori signal covariance function, which is used to define the smoothness of the solution. This modification could possibly lead to our SK solution becoming inconsistent with LSC, because implicitly, two different covariance functions are used. The solutions of both methods would not represent the same gravity field.

Eicker (2008) compared different modified and unmodified solutions using either a fully occupied $\mathbf{R}$, or the approximation $\mathbf{R} = \mathbf{I}$, and found that the considerations regarding infinite energy and non-orthogonality are of rather theoretical significance. The best solutions were in fact achieved using the approximation $\mathbf{R} = \mathbf{I}$. Even though the numerical experiments of Eicker (2008) are related to downward continuation of satellite gravity data of relatively low spectral resolution, our own numerical examples indicate that this approximation also holds for higher spectral resolutions.

Ultimately, the regularized solution for the dimensionless spline coefficients is given by

$$\hat{d}_k = \left[(\mathbf{A}^g)^T\mathbf{A}^g + \alpha\mathbf{I}\right]^{-1}(\mathbf{A}^g)^T\Delta\mathbf{g}, \tag{16}$$

representing the analysis step.

3 Global equivalence

In the global case, Eqs. (1), (3), and (7) are equivalent gravity field representations. Furthermore, all three are equal to SH, which is our point of departure.

The disturbing potential T on Earth's surface is a harmonic function satisfying Laplace's equation. Its solution may be formulated as a spherical harmonic expansion,

$$T(P) = \sum_{n=2}^{\infty} T_n(P) = \sum_{n=2}^{\infty} \lambda_n^T \times \sum_{m=0}^{n} \left[\Delta\bar{C}_{nm}\cos m\lambda + \Delta\bar{S}_{nm}\sin m\lambda\right]\bar{P}_{nm}(\cos\theta). \tag{17}$$

Stokes's formula (Eq. (1)) is the surface integral representation of the spherical harmonic expansion of T, subject to the boundary condition as given by the well-known spherical fundamental equation of physical geodesy,

$$\Delta g = -\frac{\partial T}{\partial r} - \frac{2}{R}T. \tag{18}$$

Taking the spherical harmonic expansion of Δg and Eq. (18) into account, we can establish the relationship between T and Δg as

$$T = \sum_{n=2}^{\infty} T_n = \sum_{n=2}^{\infty} \frac{R}{n-1}\Delta g_n. \tag{19}$$

Considering the orthogonality relations and addition theorem of SH, Δg_n is given by

$$\Delta g_n = \frac{2n+1}{4\pi}\iint_{\sigma} \Delta g P_n(\cos\psi)\,\mathrm{d}\sigma, \tag{20}$$

such that Eqs. (19) and (20) in combination with Bruns's formula, $N = T\gamma^{-1}$, gives Stokes's formula (cf. Eq. 1),

$$N(P) = \frac{R}{4\pi\gamma}\iint_{\sigma}\left[\sum_{n=2}^{\infty}\frac{2n+1}{n-1}P_n(\cos\psi_{Pq})\right]\Delta g_q\,\mathrm{d}\sigma, \tag{21}$$

where we identify the Stokes function expressed as a Legendre series,

$$S(\psi_{Pq}) = \sum_{n=2}^{\infty} \frac{2n+1}{n-1} P_n(\cos\psi_{Pq}). \tag{22}$$

Thus Stokes's integral formula and SH are equivalent in the global case, which is an omen for the practical application of Eq. (1): As the integration is performed globally, globally available Δg are needed.

Stokes's formula is equivalent to LSC, as the following review of the interpretation of de Min (1995) will show. Given an area of i gravity anomalies Δg_i, we can predict gravity anomalies Δg_q in any point q on Earth, by means of LSC. Then we can rewrite Eq. (1) as

$$\begin{aligned} N(P) &= \frac{R}{4\pi\gamma} \iint_{\sigma} S(\psi_{Pq}) \Delta g_q \,\mathrm{d}\sigma \\ &= \frac{R}{4\pi\gamma} \iint_{\sigma} S(\psi_{Pq}) \left[\mathbf{C}_{qi}^{gg} (\mathbf{C}_{ij}^{gg})^{-1} \Delta g_i \right] \mathrm{d}\sigma, \end{aligned} \tag{23}$$

and, because the gravity points i do not depend on the integration element,

$$N(P) = \frac{R}{4\pi\gamma} \left[\iint_{\sigma} S(\psi_{Pq}) \mathbf{C}_{qi}^{gg} \,\mathrm{d}\sigma \right] (\mathbf{C}_{ij}^{gg})^{-1} \Delta g_i. \tag{24}$$

As the integration is performed globally, both functions inside of the integral can be written in terms of SH. Thereby, we insert Eqs. (22) and $c_n^g = (\lambda_n^g)^2 c_n$ into Eq. (24), and apply the decomposition theorem and orthogonality relations of SH, to obtain

$$\begin{aligned} N(P) &= \frac{R}{4\pi\gamma} \left[\iint_{\sigma} \sum_{n=2}^{\infty} \frac{2n+1}{n-1} P_n(\cos\psi_{Pq}) \right. \\ &\quad \left. \times \sum_{n=2}^{\infty} c_n P_n(\cos\psi_{qi}) \,\mathrm{d}\sigma \right] (\mathbf{C}_{ij}^{gg})^{-1} \Delta g_i \\ &= \sum_{n=2}^{\infty} \left[\frac{R}{\gamma(n-1)} c_n^g P_n(\cos\psi_{Pi}) \right] (\mathbf{C}_{ij}^{gg})^{-1} \Delta g_i \\ &= \mathbf{C}_{Pi}^{Ng} (\mathbf{C}_{ij}^{gg})^{-1} \Delta g_i, \end{aligned} \tag{25}$$

which is the LSC formula (Eq. (3)). This derivation allows LSC to be interpreted as a two-step procedure. In the first step, least-squares prediction is performed continuously over the entire Earth, based on discrete point data. In the second step, global integration by Stokes's formula is performed on this continuous data set.

We now follow the interpretation of Eicker (2008) to show that the same prediction as in Eq. (3) can be done in RBF representation using SKs.

Omitting the regularization term $\alpha\mathbf{I}$ for simplicity, we insert the solution for the estimated spline parameters in Eq. (16) (analysis step) into Eq. (11) (synthesis step) and obtain

$$N(P) = \mathbf{A}^N \left[(\mathbf{A}^g)^T \mathbf{A}^g \right]^{-1} (\mathbf{A}^g)^T \Delta\mathbf{g}. \tag{26}$$

Using some matrix algebra, we can rearrange Eq. (26) as follows,

$$N(P) = \mathbf{A}^N (\mathbf{A}^g)^T \left[\mathbf{A}^g (\mathbf{A}^g)^T \right]^{-1} \Delta\mathbf{g}. \tag{27}$$

If we now compare Eqs. (3) and (27), we see that LSC and spline representation are identical if

$$\mathbf{A}^N (\mathbf{A}^g)^T = \mathbf{C}_{Pq}^{Ng} \tag{28}$$

and

$$\mathbf{A}^g (\mathbf{A}^g)^T = \mathbf{C}_{qq}^{gg}. \tag{29}$$

We now look at the matrix multiplications in Eqs. (28) and (29) in the limit case where the distribution of SKs becomes continuous. Suppose we have sets of K equidistant points k. In the limit, the sum will become the integral over the unit sphere, supposing an infinitely dense distribution of SKs. We get

$$\begin{aligned} \mathbf{A}^N (\mathbf{A}^g)_{(Pq)}^T &= \lim_{K\to\infty} \sum_{k=1}^{K} \\ &\quad \times \left[\sum_{n=2}^{\infty} \sum_{m=-n}^{n} \lambda_n^N B_n^{SK} Y_{nm}^R(\theta_P, \lambda_P) Y_{nm}^R(\theta_k, \lambda_k) \right] \\ &\quad \times \left[\sum_{\bar{n}=2}^{\infty} \sum_{\bar{m}=-\bar{n}}^{\bar{n}} \lambda_{\bar{n}}^g B_{\bar{n}}^{SK} Y_{\bar{n}\bar{m}}^R(\theta_q, \lambda_q) Y_{\bar{n}\bar{m}}^R(\theta_k, \lambda_k) \right] \\ &= \sum_{n=2}^{\infty} \sum_{m=-n}^{n} \sum_{\bar{n}=2}^{\infty} \sum_{\bar{m}=-\bar{n}}^{\bar{n}} \lambda_n^N \lambda_n^g \left(B_n^{SK} \right)^2 \\ &\quad \times Y_{nm}^R(\theta_P, \lambda_P) Y_{\bar{n}\bar{m}}^R(\theta_q, \lambda_q) \\ &\quad \times \overbrace{\iint_{\sigma} Y_{nm}^R(\theta_k, \lambda_k) Y_{\bar{n}\bar{m}}^R(\theta_k, \lambda_k) \,\mathrm{d}\sigma}^{=\delta_{n\bar{n}}\delta_{m\bar{m}}} \\ &= \sum_{n=2}^{\infty} \lambda_n^N \lambda_n^g \frac{c_n}{2n+1} \sum_{m=-n}^{n} Y_{nm}^R(\theta_P, \lambda_P) Y_{nm}^R(\theta_q, \lambda_q) \\ &= \sum_{n=2}^{\infty} \lambda_n^N \lambda_n^g c_n P_n(\cos\psi_{Pq}) = \mathbf{C}_{Pq}^{Ng}, \end{aligned} \tag{30}$$

and

$$
\begin{aligned}
\mathbf{A}^g(\mathbf{A}^g)^T_{(qq)} &= \lim_{K\to\infty}\sum_{k=1}^{K} \\
&\times\left[\sum_{n=2}^{\infty}\sum_{m=-n}^{n}\lambda_n^g B_n^{SK} Y_{nm}^R(\theta_q,\lambda_q)Y_{nm}^R(\theta_k,\lambda_k)\right] \\
&\times\left[\sum_{\bar{n}=2}^{\infty}\sum_{\bar{m}=-\bar{n}}^{\bar{n}}\lambda_{\bar{n}}^g B_{\bar{n}}^{SK} Y_{\bar{n}\bar{m}}^R(\theta_q,\lambda_q)Y_{\bar{n}\bar{m}}^R(\theta_k,\lambda_k)\right] \\
&= \sum_{n=2}^{\infty}\sum_{m=-n}^{n}\sum_{\bar{n}=2}^{\infty}\sum_{\bar{m}=-\bar{n}}^{\bar{n}}(\lambda_n^g)^2\left(B_n^{SK}\right)^2 \\
&\times Y_{nm}^R(\theta_q,\lambda_q)Y_{\bar{n}\bar{m}}^R(\theta_q,\lambda_q) \\
&\times\overbrace{\iint_\sigma Y_{nm}^R(\theta_k,\lambda_k)Y_{\bar{n}\bar{m}}^R(\theta_k,\lambda_k)\,\mathrm{d}\sigma}^{=\delta_{n\bar{n}}\delta_{m\bar{m}}} \\
&= \sum_{n=2}^{\infty}(\lambda_n^g)^2\frac{c_n}{2n+1}\sum_{m=-n}^{n}Y_{nm}^R(\theta_q,\lambda_q)Y_{nm}^R(\theta_q,\lambda_q) \\
&= \sum_{n=2}^{\infty}(\lambda_n^g)^2 c_n P_n(\cos\psi_{qq}) = \mathbf{C}_{qq}^{gg}. \qquad (31)
\end{aligned}
$$

Thus we are able to approximate the original covariance function by a finite sum of the similar harmonic SKs. With mathematical rigor, increasingly dense point distributions will never reach the continuous limit. Instead of the number of points, one may consider introducing area weights for points, and investigate the limit case where these area weights approach zero. This issue was discussed by, e.g., Rummel (1982), and later by Tscherning (1999). As we will see in Sect. 5 we do not need to reach the limit case in practice, as SKs and LSC tend to be identical already for moderate point densities. Therefore, we stick with the derivations in Eqs. (30) and (31), noting that in practical applications, the rigorous treatment of the surface integral does not deviate significantly from the point grid representation.

Finally, it may be shown that Tikhonov regularization and LSC are formally equivalent if we consider observation noise ε, giving $\bar{\mathbf{C}}_{qq}^{gg} = \mathbf{C}_{qq}^{gg} + \mathbf{C}_{\varepsilon\varepsilon}^{gg}$. Thereby, $\mathbf{C}_{\varepsilon\varepsilon}^{gg} = \sigma^2\mathbf{I} = \mathbf{R}$ is interpreted as the regularization matrix. Thus, LSC is equal to Tikhonov regularization with $\alpha = 1$, and LSC may be considered a particular form of regularization with a statistical rationale for determining the regularization matrix. The interested reader is referred to Rummel et al. (1979) or Bouman (1998) for more on this topic.

4 Regional applications

As seen in Sect. 3, all methods are equivalent in the global case, and they can, in principle, be applied globally. This, however, is not practical due to the requirement of globally distributed high-resolution gravity data. In addition, global integration using Stokes's integral, the LSC formula applied to large data sets, as well as the global analysis of spline coefficients all require huge computational efforts.

Terrestrial gravity data of high resolution are not available globally, while GGMs have global coverage, but lack high resolution. Consequently, in practical regional geoid computation, both data sources are combined. Thereby, the long-wavelength part of the gravity signal is determined from a GGM and removed from the terrestrial data. In turn, regional geoid computation is applied to the residual gravity data in a limited area only. The modeling results are residual geoid heights, and the long-wavelength part of the GGM is restored to obtain the final geoid. This procedure is commonly referred to as the *remove-restore* technique (Denker, 2013).

In the case of Stokes's formula we consider available terrestrial gravity data in a spherical cap with radius ψ_0 around the computation point only. Typically ψ_0 is chosen such that the resulting omission error is negligible, which depends on $N_{\max}$ of the GGM. The cap is usually called the inner zone and denoted by σ_0. Thus, Eq. (1) is only applied to the inner zone, and we get

$$
N(P) = \frac{R}{4\pi\gamma}\iint_\sigma \bar{S}(\psi_{Pq})\Delta\bar{g}_q\,\mathrm{d}\sigma, \qquad (32)
$$

with

$$
\bar{S}(\psi_{Pq}) = \begin{cases} S(\psi_{Pq}), & 0^\circ \le \psi < \psi_0 \\ 0, & \psi_0 \le \psi \le \pi \end{cases}. \qquad (33)
$$

In its spectral form, $\bar{S}(\psi_{Pq})$ is written as (de Min, 1995)

$$
\bar{S}(\psi_{Pq}) = \sum_{n=2}^{\infty}\left[\frac{2}{n-1} - Q_n(\psi_0)\right]\frac{2n+1}{2}P_n(\cos\psi_{Pq}), \qquad (34)
$$

where $Q_n(\psi_0)$ are the Molodensky or truncation coefficients, which can be computed by the recurrence relation of Paul (1973).

Considering the two-step interpretation of LSC in Sect. 3, we see that if Eq. (3) is applied to residual data in the inner zone only, we also include the implicitly extrapolated gravity signal outside the inner zone. Thus, as demonstrated theoretically and numerically by de Min (1995), LSC and Stokes's formula are not equivalent in regional applications.

Following de Min (1995), we insert Eq. (34) in Eqs. (24) and (25), and obtain

$$
N(P) = \bar{\mathbf{C}}_{Pi}^{Ng}(\mathbf{C}_{ij}^{gg})^{-1}\Delta g_i, \qquad (35)
$$

with

$$\bar{\mathbf{C}}_{Pi}^{Ng} = \sum_{n=2}^{\infty} \frac{R}{2\gamma} \left[\frac{2}{n-1} - Q_n(\psi_0) \right] c_n^g P_n(\cos\psi_{Pi}). \tag{36}$$

Thereby, in terms of the two-step interpretation, least-squares prediction is still performed continuously over the entire Earth, but Stokes's formula is applied in the inner zone only. Thus, LSC is again identical with Stokes's formula.

Eq. (34) may be rewritten as follows,

$$\bar{S}(\psi_{Pq}) = \sum_{n=2}^{\infty} \left[1 - \frac{n-1}{2} Q_n(\psi_0) \right] \frac{2n+1}{n-1} P_n(\cos\psi_{Pq}), \tag{37}$$

where we, in comparison with Eq. (22), isolate the modification of the Stokes function in brackets. Consequently, considering the global equivalence of LSC and SKs (Sect. 3), the modification must be introduced in the SKs in the synthesis step (Eq. (11)). By introducing the Molodensky coefficients in Eq. (11), the SKs get strict local support (Kusche, 2002). Then, the elements of $\mathbf{A}^N$ are given as follows,

$$A_{Pk}^N = \sum_{n=2}^{\infty} \sum_{m=-n}^{n} \lambda_n^N \left[1 - \frac{n-1}{2} Q_n(\psi_0) \right] B_n^{SK} Y_{nm}^R(\theta_P, \lambda_P) Y_{nm}^R(\theta_k, \lambda_k). \tag{38}$$

5 Numerical examples

Here we aim to demonstrate to what extent the different approaches are equivalent in practical geoid computation. To do this, we perform a comparative assessment of SKs, LSC, and Stokes's formula in a closed-loop environment using synthetic data, see Fig. 1. Both noise-free synthetic observations (in the form of gravity anomalies Δg) and the true validation geoid are computed by spherical harmonic synthesis (SHS) using the EGM2008 GGM (Pavlis et al., 2012), with $251 \le n \le 2190$, to simulate the remove-restore technique (where we assume that the long-wavelength part of the gravity signal has been removed using a typical GOCE-based GGM of $N_{\max} = 250$). Thereby, the residual gravity anomalies are computed as follows,

$$\Delta g(P) = \sum_{n=251}^{2190} \lambda_n^g \times \sum_{m=0}^{n} \left[\Delta\bar{C}_{nm} \cos m\lambda + \Delta\bar{S}_{nm} \sin m\lambda \right] \bar{P}_{nm}(\cos\theta). \tag{39}$$

Geoid heights by Stokes's formula, LSC, and SKs are compared in terms of RMS differences to the validation geoid computed by SHS (to which they should all be equivalent).

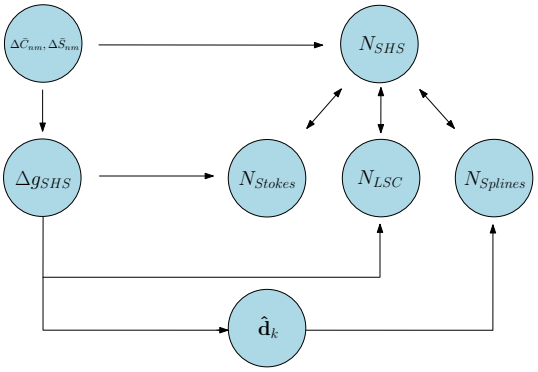

Fig. 1 Schematic of the closed-loop simulation

Table 1 Test regions

	East Frisia	Alpine region
Data area	$52^\circ \le \varphi \le 55^\circ$	$46^\circ \le \varphi \le 49^\circ$
	$5^\circ \le \lambda \le 10^\circ$	$7.5^\circ \le \lambda \le 13.5^\circ$
Target area	$53^\circ \le \varphi \le 54^\circ$	$47^\circ \le \varphi \le 48^\circ$
	$6.5^\circ \le \lambda \le 8.5^\circ$	$9^\circ \le \lambda \le 12^\circ$

By this approach, we not only validate the internal consistency of the methods, but also check whether the methods are correct by comparison with an external reference. However, in order to make the SH validation geoid equivalent to geoids computed by the regional methods, where a spherical cap with radius ψ_0 is considered, the truncation coefficients (Sect. 4) are also introduced in the SHS as follows,

$$N(P) = \sum_{n=251}^{2190} \lambda_n^N \left[1 - \frac{n-1}{2} Q_n(\psi_0) \right] \times \sum_{m=0}^{n} \left[\Delta\bar{C}_{nm} \cos m\lambda + \Delta\bar{S}_{nm} \sin m\lambda \right] \bar{P}_{nm}(\cos\theta). \tag{40}$$

For practical computational reasons, the input and output grid resolutions (directly related to the number of observations) were set to 5 arcmin (corresponding to the maximum resolution of EGM2008), and the radius of the spherical integration cap was set to $\psi_0 = 1^\circ$. This cap gives theoretical omission errors of approximately 2 cm and 6 cm for East Frisia and the Alpine region, respectively; however, the omission error is not relevant in our comparison as it is equal for all methods. We have considered two regions, namely the North Sea coastal region of East Frisia and the mountainous Alpine region, with respectively smooth and rough topography. Around the target areas, we consider enlarged data areas, to reduce edge effects, see Table 1.

Geoid heights by Stokes's formula were computed using Eq. (32), implemented according to Eq. (2) using the closed formula for computing Stokes kernel, while geoid heights by

LSC were computed using Eqs. (35) and (36). Considering the SKs, dimensionless spline coefficients were estimated using Eq. (16) with Eq. (14). Details regarding the stability of the linear system are shown in Table 2. Subsequently, the spline coefficients were used to compute geoid heights using Eq. (11) with Eq. (38). The SKs were developed to degree 2190, corresponding to the maximum resolution of the observations (5 arcmin).

There are several different point grids available for the RBF positions, known as the grid area. Bentel et al. (2013a) explore how different point grids affect RBF modeling results, and conclude that differences due to different point grids are very small ($\sim 1\times10^{-4}$ mm to $\sim$0.2 mm), provided the number of grid points is sufficiently large. We have placed the SKs on the equidistributed Reuter grid, where the spherical distance between grid points is almost constant. The number of SKs on the Reuter grid is defined through the control parameter γ, which is equal to the maximum SH degree $N_{\max}$, $\gamma = N_{\max}$ (Bentel et al., 2013b). The outer margin widths w of the RBF grid area were determined by the empirical formula of Bentel (2013), where $w \approx 4\cdot 180^\circ/(N_{\max}+1)$. As a result, the number of RBFs will typically be slightly larger than the number of observations, but practically equal. In the following statements regarding equality of the number of RBFs and the number of observations, it is this approximate equality that is meant.

First, we show that the unmodified LSC and SK formulas applied to the synthetic inner zone data set do not give the same results as Stokes's formula. Fig. 2 shows the error of LSC and SKs when leaving the covariance function unmodified. The validation geoid is the truncated SH geoid, so as to simulate Stokes's formula. We observe that there is a continuous residual pattern over both data and target areas. In East Frisia, using unmodified LSC (SKs), we get RMS differences of 1.75 cm and 1.83 cm (1.80 cm and 1.83 cm) in the data and target areas, respectively. In the Alpine region, using unmodified LSC (SKs), we get RMS differences of 5.73 cm and 5.18 cm (5.76 cm and 5.18) in the data and target areas, respectively. The RMS numbers for East Frisia and the Alpine region are in the same order of magnitude as the omission (or truncation) error in the respective regions. This shows that the unmodified LSC and SK formulas have taken signal content outside the data area into account when computing the geoid heighs, while Stokes's formula has not.

The results of the geoid computations using modified formulas are shown in Table 3 and Figs. 3 and 4. Table 3 shows that all methods agree on the mm level in the target area, with smaller errors in East Frisia than in the Alpine region. Stokes's formula gives larger errors outside the target area than LSC and the SKs. LSC and SKs show maximum RMS differences of 0.7 mm and 1.3 mm, respectively, while RMS differences of 1.7 mm (East Frisia) and 5.9 mm (Alpine region) are found using Stokes's formula. Of all three methods, LSC gives the smallest error.

Looking at Figs. 3 and 4 we see that the errors in the target areas are much lower than in their exterior, showing the effect of truncated computation. In particular, LSC and the SKs show smaller errors in the target area, which was not the case when using the unmodified formulas (Fig. 2). We also note the similarity in the error patterns of LSC and SKs.

The slightly larger RMS differences of Stokes's formula in comparison with LSC/SKs could be owing to the fact that the synthetic observations are point values, which SHS and LSC/SKs expect. However, Stokes integration, while applied point-wise, expects block mean values. SHS uses the exact observation grid values, while LSC/SKs interpolate and do not give exact values (at least not everywhere). To test to what extent the larger RMS differences for Stokes's formula are due to a discretization error, we set up the closed-loop simulation with 2.5 arcmin grid resolution, see Table 4. Increasing the grid resolution to 2.5 arcmin leaves the LSC and SK results largely unaffected (with maximum improvements of $\sim$0.5 mm, and even a slight degradation of the LSC solution in East Frisia), while results by Stokes's formula improves by 0.85 to 3.5 mm. Thus, we identify the larger discrepancies using Stokes's formula at the 5 arcmin grid resolution as a discretization error. Furthermore, as there is nothing to gain from increasing the grid resolution of the observations (at 5 arcmin they are already at their maximum signal resolution), we attribute the discretization error to the Stokes function and not the gravity data. The error is a result of the Stokes function being evaluated only at each grid point of the input data, instead of evaluating its surface integral over the corresponding blocks. Thus, with increased resolution and decreased block size, the function value at the grid nodes gives an increasingly better representation of the surface integral over the grid compartments, and Stokes's formula converges towards SHS.

Finally, we explored how the number of SKs affects the RMS differences (and thus the equivalence to the other methods). Fig. 5 shows the RMS difference between SHS and SKs for varying number of SKs in the Alpine target area, computed from observations provided on the original 5 arcmin grid. The vertical dotted lines denote the number of observations corresponding to the 5 arcmin and 2.5 arcmin grid resolutions, while the horizontal dotted line denotes the 1-mm RMS difference with respect to SHS. The regularization parameter was kept constant to make the computations as comparable as possible. Thus, the only variable in this test is the number of SKs. Indeed, in light of Eqs. (30) and (31), it seems that the SKs become similar to LSC only when the number of SKs is similar to or larger than the number of observations. At first glance, this does not seem promising when regarding any prospect of saving computational effort

Table 2 Spline representation

	East Frisia		Alpine region	
Resolution (arcmin)	5	2.5	5	2.5
No. of observations	2257	8833	2701	10585
No. of SKs	2374	1842	2868	2464
cond($\mathbf{N}$)	1.0×10^{20}	9.3×10^{18}	1.6×10^{20}	7.1×10^{19}
α_0	9192	2.8×10^4	8180	2.7×10^4
α	9146	284	8139	1.1×10^4
cond($\mathbf{N} + \alpha\mathbf{I}$)	6.0×10^5	6.0×10^7	6.0×10^5	1.5×10^6

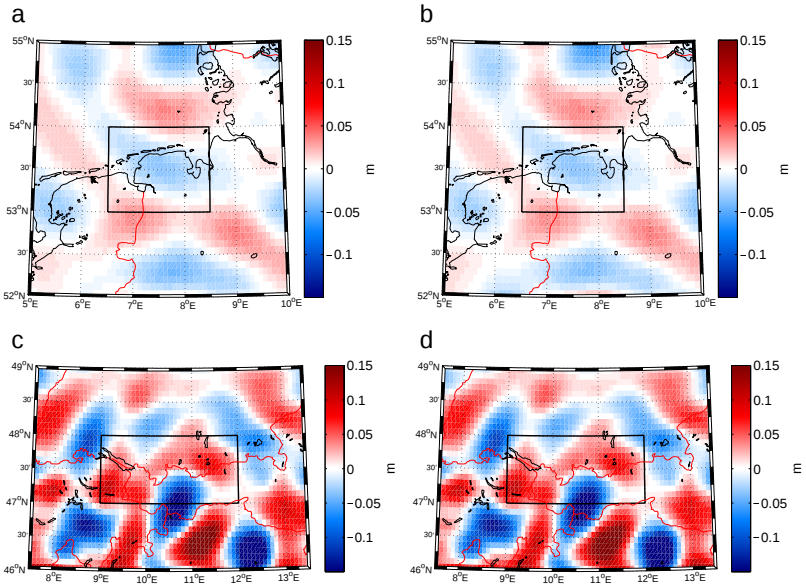

Fig. 2 Error of LSC and SKs when leaving the covariance function unmodified; error from (a) LSC and (b) SKs in East Frisia, error from (c) LSC and (d) SKs in the Alpine region.

Table 3 Results from the closed-loop simulation, 5 arcmin resolution. Gravity anomalies in mGal ($= 10^{-5}$ ms^{-2}) and geoid heights in cm.

		East Frisia				Alpine region			
		max	min	mean	RMS	max	min	mean	RMS
Data area									
	Δg_{SHS}	11.617	-6.881	0.316	3.242	46.704	-63.217	-0.677	12.762
	N_{SHS}	17.474	-10.942	0.513	5.200	66.092	-93.867	-1.013	18.765
	$N_{SHS} - N_{Stokes}$	14.165	-5.426	1.204	3.410	28.229	-35.504	-2.477	7.218
	$N_{SHS} - N_{LSC}$	1.880	-2.594	0.006	0.644	7.548	-7.952	-0.007	1.354
	$N_{SHS} - N_{Splines}$	2.229	-3.183	0.001	0.809	6.453	-6.498	-0.013	1.433
Target area									
	N_{SHS}	7.297	-9.076	1.870	4.241	40.613	-35.447	-1.669	13.678
	$N_{SHS} - N_{Stokes}$	0.419	-0.638	0.082	0.173	1.087	-1.598	-0.087	0.588
	$N_{SHS} - N_{LSC}$	0.003	-0.020	-0.001	0.002	0.212	-0.208	0.000	0.065
	$N_{SHS} - N_{Splines}$	-0.006	0.135	-0.022	0.028	0.180	0.021	0.120	0.127

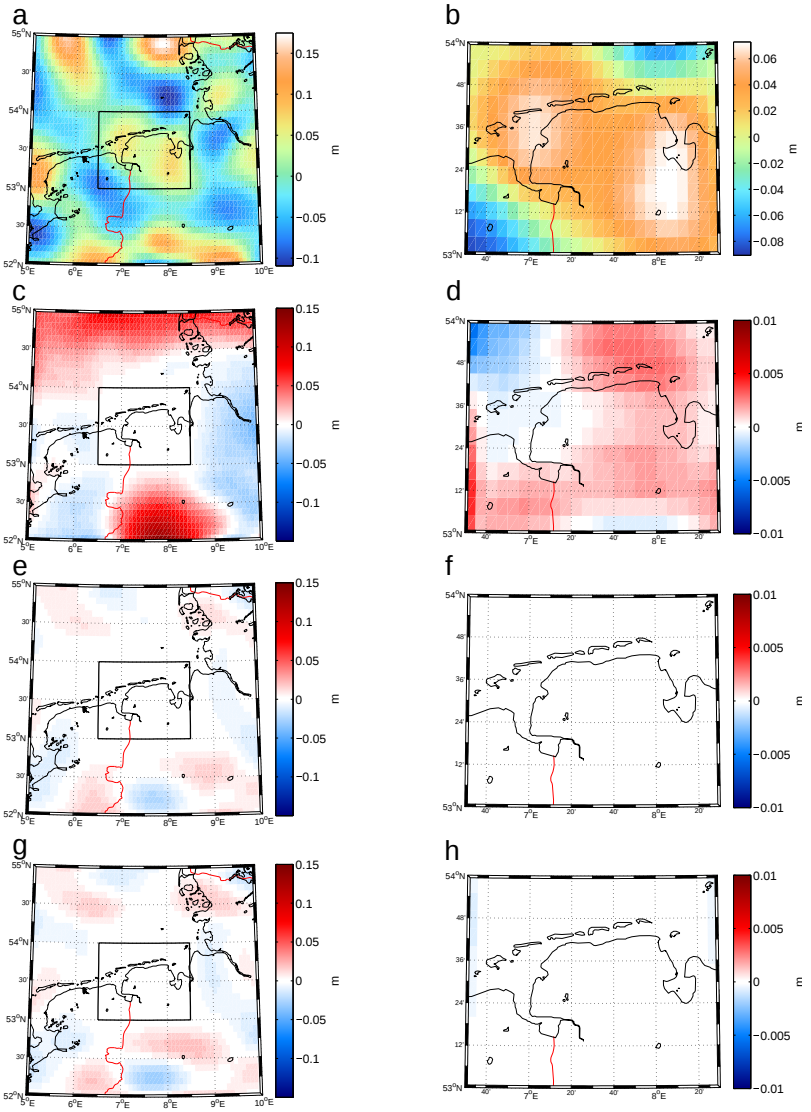

Fig. 3 Results in East Frisia; geoid from SHS in (a) data and (b) target areas, error from Stokes's formula in (c) data and (d) target areas, error from LSC in (e) data and (f) target areas, and error from SKs in (g) data and (h) target areas.

with RBFs as opposed to LSC. To test this, we computed spline solutions at the 2.5 arcmin grid resolution for two cases; (1) setting the number of splines equal to the number of observations (corresponding to 2.5 arcmin, not shown), and (2) setting the number of splines equal to the maximum resolution of the observations (corresponding to 5 arcmin, see Table 2). Both cases give practically equal results (maximum RMS differences of 23×10^{-3} mm and 6×10^{-3} mm in the data and target zones, respectively), suggesting that the SKs converge towards LSC depending on the resolution rather than the number of observations.

Thus, in our examples, when we place the observations on a 5 arcmin grid, the SKs will converge towards LSC when setting the number of SKs equal to the number of observations, because the number of observations is equal to their maximum signal resolution. Consequently, there is nothing

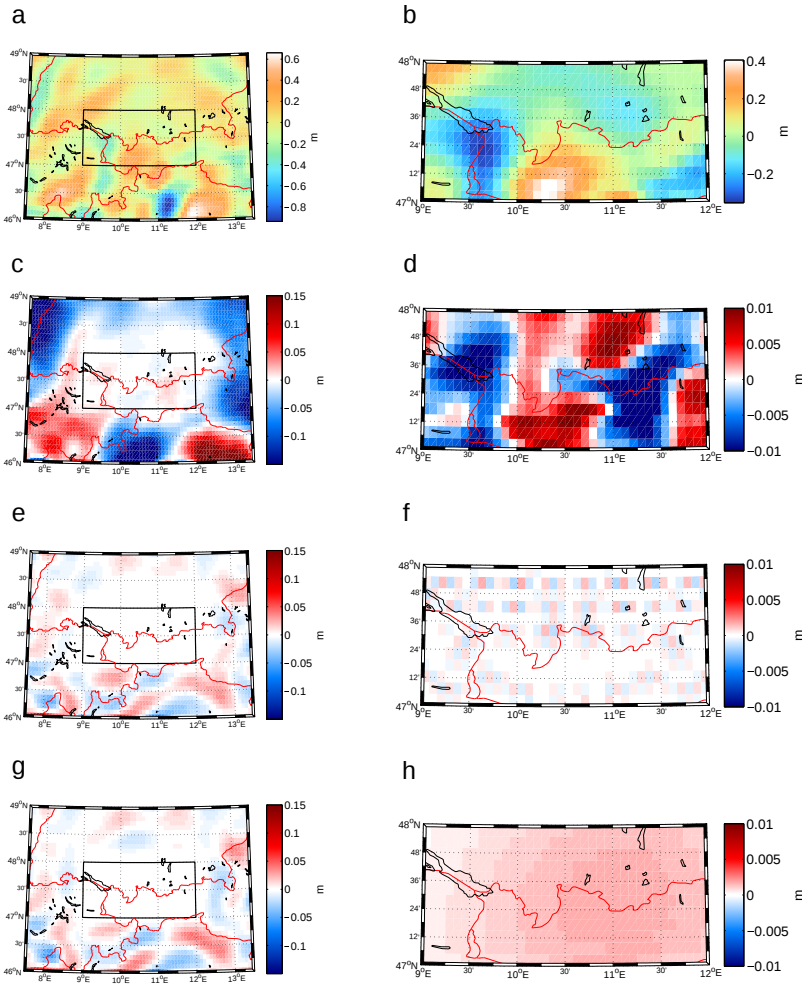

Fig. 4 Results in Alpine region; geoid from SHS in (a) data and (b) target areas, error from Stokes's formula in (c) data and (d) target areas, error from LSC in (e) data and (f) target areas, and error from SKs in (g) data and (h) target areas.

Table 4 Results from the closed-loop simulation, 2.5 arcmin resolution. Gravity anomalies in mGal ($= 10^{-5}$ ms^{-2}) and geoid heights in cm.

		East Frisia				Alpine region			
		max	min	mean	RMS	max	min	mean	RMS
Data area									
	Δg_{SHS}	11.794	-6.894	0.296	3.219	46.736	-63.347	0.634	12.723
	N_{SHS}	17.536	-10.942	0.481	5.158	66.515	-94.385	-0.955	18.729
	$N_{SHS} - N_{Stokes}$	14.422	-5.894	1.032	3.273	30.577	-37.650	-2.107	7.056
	$N_{SHS} - N_{LSC}$	3.717	-3.266	0.031	0.996	12.432	-10.639	-0.051	2.098
	$N_{SHS} - N_{Splines}$	2.317	-3.385	-0.022	0.786	4.377	-5.683	-0.019	1.257
Target area									
	N_{SHS}	7.333	-9.076	2.097	4.247	41.130	-35.447	-1.936	13.620
	$N_{SHS} - N_{Stokes}$	0.429	-0.512	0.037	0.088	0.529	-0.663	-0.041	0.242
	$N_{SHS} - N_{LSC}$	0.057	-0.103	-0.001	0.010	0.059	-0.054	0.000	0.015
	$N_{SHS} - N_{Splines}$	-0.002	-0.040	-0.004	0.006	0.110	0.024	0.079	0.082

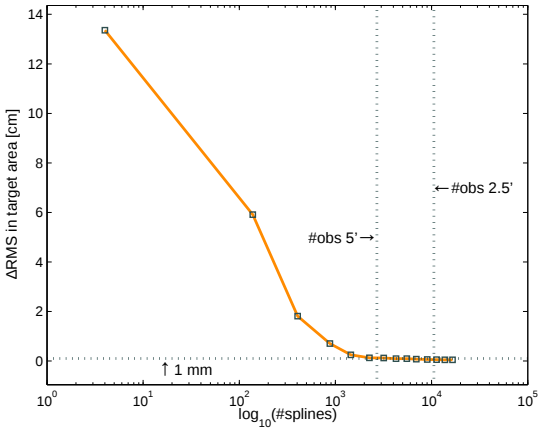

Fig. 5 Difference between SHS and SKs for varying number of SKs in the Alpine target area, with $\alpha = \alpha_0 = \text{const}$.

to gain from increasing the number of SKs beyond 5 arcmin, as Fig. 5 readily shows.

6 Summary

We have reviewed the theoretical equivalence of Stokes's formula, LSC, and SKs in the global case, as well as in regional applications, where Stokes integration is restricted to a spherical cap around the computation point, and no data outside this cap is considered. If LSC is not applied globally, its result will be different from Stokes's formula, because an unwanted extrapolation outside the cap takes place. If the cross-covariance function is modified appropriately, LSC and Stokes's formula are again equal. This has already been shown by de Min (1995). As SKs are equivalent to LSC, they have to be modified correspondingly to give equal results as Stokes's formula.

With a few numerical examples we have shown that the methods are equal also in practice. Two regions were considered, East Frisia and the Alpine region, with small and large gravity field variations, respectively. At the 5 arcmin resolution, all methods agree within 2×10^{-2} mm to 5.9 mm in the target areas, where the largest RMS differences are due to the discretization of Stokes's formula. At the 2.5 arcmin resolution, all methods agree within 6×10^{-2} mm to 2.4 mm. In general, the remaining discrepancies can be expected due to the varying numerical implementations. For example, Novák et al. (2001) found remaining differences on the mm level between the theoretically equivalent numerical integration and 1D-FFT evaluations of Stokes's formula at the 5 arcmin resolution, which they attribute to the numerical accuracy of the computational algorithms.

From a theoretical point of view, LSC should give the best results because the covariance function is the only kernel which has the minimum variance property (Moritz, 1980). Indeed, this is confirmed in our numerical examples, where LSC generally gives the smallest error. SKs perform very similar to LSC, but the solution strongly depends on the number of SKs used. Our numerical examples show that little is gained by using more SKs than the corresponding resolution of the observations, i.e., by reducing the grid spacing. This is because there is hardly any signal variability between the original grid nodes. Therefore, it is reasonable to stick with the original grid spacing, where the number of grid points corresponds to the number of SKs. In order to represent the actual signal, we need roughly the same number of observations. However, the number of observations may be much larger. In such a case, the auto-covariance matrix to be inverted in LSC becomes large, while we can keep the same number of SKs. Our numerical examples therefore suggest that the RBF method is similar to SHS or LSC in case the number of SKs corresponds to the signal resolution of the data, independent of the number of observations. By contrast, the size of the auto-covariance matrix to be inverted in LSC corresponds to the number of observations, independent of the signal resolution. However, as the number of SKs needed depends on the resolution, potentially huge matrices may result from this approach as well, rendering the computational effort comparable with LSC.

Finally, our aim has not been to decide which regional geoid computation method is the best, as there are advantages and drawbacks to all depending on the data situation. Our numerical examples do not represent the most efficient implementations of each method, as they rather aim to compare the outcome of the different methods. Thus, we have not compared the numerical implementations in terms of computation times and limitations. In addition, this work does not present new theory, but is a first attempt to compare the three methods both theoretically and numerically in a unified framework. We have demonstrated that the three methods give equal results in applications, for which a modification of LSC and SKs was necessary. We stress that this modification is not a general necessity when applying the LSC and RBF approaches. However, de Min (1995) points out a few advantages of modifying the covariance function. For example, the modification makes the LSC results less dependent on the validity of the covariance function, as its validity is of most importance for the extrapolated data, which is not considered anymore. Although the modification is not necessary when applying the LSC and RBF approaches, however, it is critical in direct comparison with Stokes's formula.

Acknowledgements The authors would like to thank R. Rummel and M. Šprlák for helpful comments on an early version of the manuscript. It was further improved by constructive comments from the Editor-in-

Chief and three anonymous reviewers, which are gratefully acknowledged. Figures were drafted using the M_Map package, with coastlines and political boundaries from the National Oceanic and Atmospheric Administration and Natural Earth, respectively.

References

Bentel K (2013) Regional gravity modeling in spherical radial basis functions – on the role of the basis function and the combination of different observation types. PhD thesis, Norwegian University of Life Sciences

Bentel K, Schmidt M, Denby CR (2013a) Artifacts in regional gravity representations with spherical radial basis functions. J Geod Sci 3:173–187, DOI 10.2478/jogs-2013-0029

Bentel K, Schmidt M, Gerlach C (2013b) Different radial basis functions and their applicability for regional gravity field representation on the sphere. Int J Geomath 4:67–96, DOI 10.1007/s13137-012-0046-1

Bouman J (1998) Quality of regularization methods. Tech. Rep. 98.2, DEOS Report, Delft University Press, Delft, The Netherlands

Bucha B, Bezděk A, Sebera J, Janák J (2015) Global and Regional Gravity Field Determination from GOCE Kinematic Orbit by Means of Spherical Radial Basis Functions. Surv Geophys 36(6):773–801, DOI 10.1007/s10712-015-9344-0

Denker H (2013) Regional gravity field modeling: Theory and practical results. In: Xu G (ed) Sciences of Geodesy – II, Springer, Berlin, pp 185–191, DOI 10.1007/978-3-642-28000-9_5

Eicker A (2008) Gravity field refinement by radial basis functions from in-situ satellite data. PhD thesis, University of Bonn

Eicker A, Schall J, Kusche J (2014) Regional gravity modelling from spaceborne data: case studies with GOCE. Geophys J Int 196:1431–1440, DOI 10.1093/gji/ggt485

Farahani HH, Slobbe DC, Klees R, Seitz K (2016) Impact of accounting for coloured noise in radar altimetry data on a regional quasi-geoid model. J Geod DOI 10.1007/s00190-016-0941-6

Flury J (2006) Short-wavelength Spectral Properties of the Gravity Field from a Range of Regional Data Sets. J Geod 79(10):624–640, DOI 10.1007/s00190-005-0011-y

Freeden W, Schneider F (1998) An integrated wavelet concept of physical geodesy. J Geod 72(5):259–281, DOI 10.1007/s001900050166

Freeden W, Gervens T, Schreiner M (1998) Constructive Approximation on the Sphere, with Applications in Geomathematics. Clarendon Press, Oxford

Haagmans R, de Min E, von Gelderen M (1993) Fast evaluation of convolution integrals on the sphere using 1D FFT, and a comparison with existing methods for Stokes's integral. Man Geod 18:227–241

Hansen PC, O'Leary DP (1993) The Use of the L-curve in the Regularization of Discrete Ill-posed Problems. SIAM J Sci Comput 14:1487–1503, DOI 10.1137/0914086

Heiskanen WA, Moritz H (1967) Physical geodesy. W. H. Freeman, San Francisco

Hofmann-Wellenhof B, Moritz H (2006) Physical geodesy, second ed. Springer, Wien

Jekeli C (1978) An investigation of two models for the degree variances of global covariance functions. Tech. Rep. 275, Dept. of Civil and Environmental Engineering and Geodetic Science, Ohio State University, Columbus

Jekeli C (2005) Spline representations of functions on a sphere for geopotential modeling. Tech. Rep. 475, Dept. of Civil and Environmental Engineering and Geodetic Science, Ohio State University, Columbus

Klees R, Tenzer R, Prutkin I, Wittwer T (2008) A data-driven approach to local gravity field modelling using spherical radial basis functions. J Geod 82:457–471, DOI 10.1007/s00190-007-0196-3

Krarup T (1969) A contribution to the mathematical foundation of physical geodesy. Tech. Rep. 44, Danish Geodetic Institute, Copenhagen

Kusche J (2002) Inverse Probleme bei der Gravitationsfeldbestimmung mittels SST- und SGG-Satellitenmissionen. Habilitation thesis, Deutsche Geodätische Kommission Reihe C, Nr. 548

Lieb V, Schmidt M, Dettmering D, Börger K (2016) Combination of various observation techniques for regional modeling of the gravity field. J Geophys Res Solid Earth 121:3825–3845, DOI 10.1002/2015JB012586

Liu Q, Sideris MG (2003) Wavelet evaluation of the Stokes and Vening Meinesz integrals. J Geod 77(5):345–356, DOI 10.1007/s00190-003-0333-6

de Min E (1995) A comparison of Stokes' numerical integration and collocation, and a new combination technique. Bull Géod 69:223–232, DOI 10.1007/BF00806734

Moritz H (1980) Advanced physical geodesy. Wichmann, Karlsruhe

Moritz H, Sünkel H (eds) (1978) Approximation methods in geodesy. Wichmann, Karlsruhe

Naeimi M (2013) Inversion of satellite gravity data using spherical radial base functions. PhD thesis, Deutsche Geodätische Kommission Reihe C, Nr. 711

Naeimi M, Flury J, Brieden P (2015) On the regularization of regional gravity field solutions in spherical radial base functions. Geophys J Int 202:1041–1053, DOI 10.1093/gji/ggv210

Nerem RS, Jekeli C, Kaula WM (1995) Gravity field determination and characteristics: Retrospective and prospective. J Geophys Res Solid Earth 100:15,053–15,074, DOI 10.1029/94JB03257

Novák P, Vaníček P, Véronneau M, Holmes S, Featherstone W (2001) On the accuracy of modified Stokes's integration in high-frequency gravimetric geoid determination. J Geod 74(9):644–654, DOI 10.1007/s001900000126

Paul M (1973) A method of evaluating the truncation error coefficients for geoidal height. Bull Géod 47:413–425

Pavlis NK, Holmes SA, Kenyon SC, Factor JK (2012) The development and evaluation of the Earth Gravitational Model 2008 (EGM2008). J Geophys Res Solid Earth 117:B04,406, DOI 10.1029/2011JB008916

Pock C, Mayer-Gürr T, Kühtreiber N (2014) Consistent combination of satellite and terrestrial gravity field observations in regional geoid modeling: A case study for Austria. In: Marti U (ed) Gravity, Geoid and Height Systems: Proceedings of the IAG Symposium GGHS2012, October 9-12, 2012, Springer, Berlin, pp 151–156, DOI 10.1007/978-3-319-10837-7_19

Rexer M, Hirt C (2015) Spectral analysis of the Earth's topographic potential via 2D-DFT: a new data-based degree variance model to degree 90,000. J Geod 89:887–909, DOI 10.1007/s00190-015-0822-4

Roland M (2005) Untersuchungen zur Kombination terrestrischer Schweredaten und aktueller globaler Schwerefeldmodelle. PhD thesis, Wissenschaftliche Arbeiten der Fachrichtung Vermessungswesen der Universität Hannover, Nr. 254

Roland M, Denker H (2005) Stokes Integration versus Wavelet Techniques for Regional Geoid Modelling. In: Sansò F (ed) A Window on the Future of Geodesy: Proceedings of the International Association of Geodesy IAG General Assembly Sapporo, Japan June 30 – July 11, 2003, Springer Berlin Heidelberg, pp 368–373

Rummel R (1982) Gravity parameter estimation from large and densely spaced homogeneous data sets. Boll Geod Sci Aff 41(2):149–160

Rummel R, Schwarz KP, Gerstl M (1979) Least squares collocation and regularization. Bull Géod 53:343–361, DOI 10.1007/BF02522276

Sansò F, Sideris MG (eds) (2013) Geoid Determination: Theory and Methods. Lecture Notes in Earth System Sciences, Springer, Berlin

Schmidt M (2001) Grundprinzipien der Wavelet-Analyse und Anwendungen in der Geodäsie. Shaker Verlag, Aachen

Schmidt M, Martínez W, Florez J (2002) General scheme for the computation of regional geoid undulations using spherical wavelets. In: Drewes H, Dodson AH, Fortes LPS, Sánchez L, Sandoval P (eds) Vertical Reference Systems: IAG Symposium Cartagena, Colombia, February 20–23, 2001, Springer Berlin Heidelberg, pp 209–214

Schmidt M, Fengler M, Mayer-Gürr T, Eicker A, Kusche J, Sánchez L, Han SC (2007) Regional gravity modeling in terms of spherical base functions. J Geod 81:17–38, DOI 10.1007/s00190-006-0101-5

Schmidt M, Gerlach C, Bouman J, Bentel K, Dettmering D, Eicker A, Herceg M, Kusche J, Lieb V, Schall J, Tscherning CC (2015) Results from IAG's Joint Study Group JSG0.3 on the Comparison of Current Methodologies in Regional Gravity Field Modelling. Poster presented at the 26th International Union of Geodesy and Geophysics General Assembly, Prague, Czech Republic, June 22–July 2.

Stokes GG (1849) On the variation of gravity on the surface of the Earth. Trans Cambridge Phil Soc 8:672–695

Tenzer R, Klees R (2008) The choice of the spherical radial basis functions in local gravity field modeling. Stud Geophys Geod 52(3):287–304, DOI 10.1007/s11200-008-0022-2

Tikhonov AN (1963) Regularization of incorrectly posed problems. Soviet Math Dokl 4:1624–1627

Torge W, Müller J (2012) Geodesy, fourth ed. De Gruyter, Berlin

Tscherning CC (1981) Comparison of some methods for the detailed representation of the Earth's gravity field. Rev Geophys 19:213–221, DOI 10.1029/RG019i001p00213

Tscherning CC (1999) Construction of anisotropic covariance functions using Riesz-representers. J Geod 73(6):332–336, DOI 10.1007/s001900050250

Tscherning CC, Rapp RH (1974) Closed covariance expressions for gravity anomalies, geoid undulations and deflections of the vertical implied by anomaly degree variance models. Tech. Rep. 208, Dept. of Geodetic Science and Surveying, Ohio State University, Columbus

Vaníček P, Krakiwsky EJ (1986) Geodesy: The Concepts, second ed. North Holland, Amsterdam

Wittwer T (2009) Regional gravity field modelling with radial basis functions. PhD thesis, Technical University of Delft

Paper D

Coastal Sea Level from CryoSat-2 SAR Altimetry in Norway

Martina Idžanović[1], Vegard Ophaug[1], Ole Baltazar Andersen[2,*]

Abstract

Conventional altimeters determine the sea surface height (SSH) with an accuracy of a few centimeters over the open ocean. However, in coastal areas the noise is seriously increased from numerous effects which degrade the quality. The Norwegian coast adds further complications to the use of satellite altimetry, due to its complicated coastline with many islands, mountains, and deep, narrow fjords. The European Space Agency (ESA) CryoSat-2 (CS2) satellite carries a synthetic aperture interferometric radar altimeter (SIRAL), which is able to observe sea level closer to the coast than conventional altimeters, without degradation. In this work, we investigate the potential of CS2 data to provide improved observations in the Norwegian coastal zone.

Initially we evaluate the performance of SAR altimetry by comparing CS2 SAR altimetry with 22 tide gauges, and investigate the performance of the two major geophysical corrections applied to CS2 data for the determination of the SSH. We demonstrate that we can significantly improve the comparison with tide-gauge observations if we substitute the standard ocean tide and dynamic atmosphere corrections with local corrections. Secondly, we compare CS2 with conventional altimetry at the Stavanger tide gauge, revealing an improvement of ∼2-3 cm.

Keywords: CryoSat-2; SAR altimetry; tide gauges

1. Introduction

Satellite altimetry is a well-proven and mature technique for observing sea level, with good spatial and temporal coverage over the open ocean. The effective footprint of an altimeter is controlled by the pulse duration and width of the analysis window and is typically between 2 and 7 km, depending on the sea state (Gommenginger et al., 2011). For conventional altimeters and typical wave heights of 2 m, this gives a circular footprint of ∼100 km^2. The coastal zone is particularly relevant to society considering, e.g., sea-level rise, shipping, fishery, and other offshore activities. Close to the coast, the application of satellite altimetry is difficult due to land-contamined radar echoes resulting in observation gaps in these zones (Cipollini et al., 2010). Furthermore, large variations in atmospheric pressure along the coast and complex tidal patterns degrade the geophysical corrections for dynamic atmosphere (DAC) and ocean tides (OT), which are applied to derive accurate SSHs (Andersen and Scharroo, 2011). Norway has the world's second longest coastline of 103,000 km, with many islands, steep mountains, and deep, narrow fjords. This makes the application of coastal altimetry particularly difficult in Norway.

In a recent comparison of conventional altimetry with tide gauges (TGs) along the Norwegian coast, the average distance between conventional altimetric observations (Jason-2 and Envisat) and local TGs was ∼54 km (Ophaug et al., 2015), suggesting room for improvement.

As the first of its kind, the European Space Agency (ESA) CryoSat-2 (CS2) satellite carries a synthetic aperture interferometric radar altimeter (SIRAL) which can operate in synthetic aperture radar (SAR), synthetic aperture interferometric (SARIn), as well as conventional low resolution (LR) modes. At high latitudes, the satellite operates in all three modes following geographically delimited masks as shown in Figure 1. Along the Norwegian coast, in a narrow strip with a typical width of less than ∼40 km, CS2 operates in SARIn mode, in which a Delay-Doppler modulation of the altimeter signal creates a synthetic footprint. The footprint is nominally 0.3 km by 8 km in respectively along- and across-track directions (Wingham et al., 2006). Hence, the risk that the footprint is contaminated by land is far less for CS2 in this mode compared with conventional altimeters.

This paper explores the potential for these data to provide improved sea-level observations in the Norwegian coastal zone. We do this by investigating whether CS2 observes the same ocean signal as the TGs, and compare CS2 with conventional altimeters.

*Corresponding author
Email address: oa@space.dtu.dk (Ole Baltazar Andersen)
[1]Dept. of Mathematical Sciences and Technology, Norwegian University of Life Sciences (NMBU), Drøbakveien 31, N-1430 Ås
[2]DTU Space, Technical University of Denmark, Elektrovej, DK-2800 Kgs. Lyngby

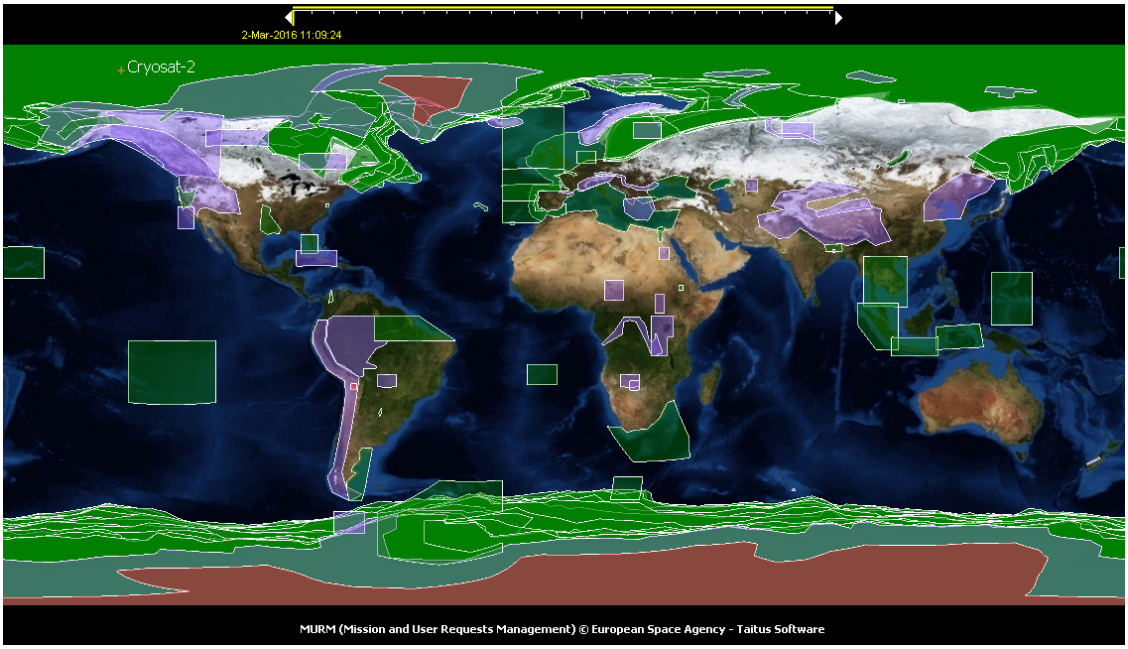

Figure 1: Geographical mode mask version 3.8 for CS2 (ESA, 2016). SARIn mode: purple, SAR mode: green, LR mode: red and areas not covered by other masks.

2. Data and methods

2.1. CryoSat-2 20 Hz SARIn data processing

Satellite altimetry is normally distributed through agencies like AVISO, EUMETSAT, MyOcean, NOAA, PO-DAAC, and RADS, focusing on the regular distribution of homogenized and quality-controlled 1 Hz data. However, these archives do not process and/or distribute the CS2 SARIn data. ESA provides CS2 data in two modes, Level 1 (L1) and Level 2 (L2). L1 data contain orbit information and waveforms, while L2 data contain range and geophysical corrections, as well as height estimates. The 20 Hz Level 1b (L1b) SARIn dataset was obtained by the Technical University of Denmark (DTU) Space retracker system (Stenseng and Andersen, 2012) for the period from 2010 to 2014. We used the simple threshold retracker (Nielsen et al., 2015), whereby the bin that contains 80% of the maximum power is taken as the retracking point.

Compared with other conventional satellites like Jason-2 and Envisat, CS2 does not carry a radiometer. Therefore, the wet and dry troposphere corrections must be derived using models (standard is ECMWF). CS2 is furthermore a single-frequency altimeter, hence the ionospheric corrections must also be provided by a model (standard is GIM). In general, these corrections are believed to be only slightly less accurate than the instrument-derived corrections applied on conventional altimeters (Andersen and Scharroo, 2011). The CS2 DAC consists of a high-frequency part (MOG2D) and a low-frequency part (inverse barometer, IB), and the OT correction is provided by the FES2004 global OT model, which is similar to data from conventional satellites.

A known bias of 69 cm was removed from the 20 Hz CS2 SSHs (Scagliola and Fornari, 2013). At the time of data processing, the SARIn/cross-track correction (Armitage and Davidson, 2014; Abulaitijiang et al., 2015) was not implemented in the retracker system. Consequently, the SARIn observations have been processed as SAR. Because the burst mode pulse repetition frequency in SAR mode is four times that of SARIn mode, the SARIn data are expected only to have half the precision of normal SAR altimetry (Wingham et al., 2006).

A suite of editing and outlier detection criteria are normally used to edit the altimeter data for the computation of 1 Hz data, e.g., (Scharroo et al., 2013). As most of these are not available for the CS2 L1 data, an two-step outlier detection was developed. After having removed all CS2 observations over land using a high-resolution coastline (1:50,000 map scale, provided by the Norwegian Mapping Authority (NMA)) as a mask, the first step in the outlier detection was to remove all observations deviating more than ± 1 m from DTU15MSS (Andersen et al., 2015). This first step led to a 28% data rejection. The second step of our outlier detection was based on a within-track gross error search using a multiple t test (Koch, 1999; Revhaug,

2007), applied to the centered SSH data.

For each track, assuming error-free observations, we get the following linear model,

$$E\{\mathbf{l}\} = \mathbf{A} \cdot \mathbf{x},\ D\{\mathbf{l}\} = \mathbf{C}, \tag{1}$$

where E stands for expectation and D for dispersion (or spread). In Eq. 1, $\mathbf{l}$ ($n\times1$) is the observation vector, $\mathbf{A}$ is the ($n \times e$) design matrix multiplied by the vector of unknown parameters $\mathbf{x}$ ($e\times1$). The dispersion of $\mathbf{l}$ equals the covariance matrix $\mathbf{C}$. Considering the observation noise, the functional part of the mathematical model is given by:

$$\mathbf{v} = \mathbf{A} \cdot \mathbf{x} - \mathbf{l}, \tag{2}$$

where $\mathbf{v}$ are the residuals. Using eqs. 1 and 2 the expectation of $\mathbf{v}$ equals a zero vector:

$$E\{\mathbf{v}\} = \mathbf{0}. \tag{3}$$

We now allow our observations $\mathbf{l}$ to contain gross errors ∇ ($q\times1$), and see that the observation vector can be corrected for these gross errors by the subtraction ($\mathbf{l} - \mathbf{E} \cdot \nabla$). Thereby, we extend Eq. 2 by a gross-error term:

$$\mathbf{l} - \mathbf{E} \cdot \nabla + \tilde{\mathbf{v}} = \mathbf{A} \cdot \tilde{\mathbf{x}}, \tag{4}$$

where $\mathbf{E}$ is a ($n \times q$) matrix containing ones where a gross error is present (at (n, q)) and zeros elsewhere. Correcting for the gross errors, we get new estimates for $\mathbf{v}$ and $\mathbf{x}$, annotated as $\tilde{\mathbf{v}}$ and $\tilde{\mathbf{x}}$. We use Eq. 4 to consecutively estimate possible gross errors in each observation.

A statistical outlier test using Eq. 4 is obtained if the null hypothesis $H_0 : \nabla = 0$ (all outliers equal zero) is tested against the alternative hypothesis $H_1 : \nabla = \nabla_1 \neq 0$. The least-squares solution for Eq. 4 gives:

$$\mathbf{Q}_\nabla = (\mathbf{E}^T \cdot \mathbf{P} \cdot \mathbf{Q}_v \cdot \mathbf{P} \cdot \mathbf{E})^{-1}, \tag{5}$$

$$\nabla = -\mathbf{Q}_\nabla \cdot \mathbf{E}^T \cdot \mathbf{P} \cdot \mathbf{v}, \tag{6}$$

where $\mathbf{Q}_v$ and $\mathbf{Q}_\nabla$ are cofactor matrices of $\mathbf{v}$ and ∇, respectively, and $\mathbf{P}$ is the weight matrix. Applying the multiple t test, one observation at a time can be tested, with an estimated standard deviation of ∇:

$$\tilde{s}^2_\nabla = \frac{1}{f-1} \cdot (\mathbf{v}^T \cdot \mathbf{P} \cdot \mathbf{v} - \frac{\nabla^2}{\mathbf{Q}_\nabla}), \tag{7}$$

where f represents the degrees of freedom.

First, we assume a solution without gross errors, based on Eq. 3, after which we perform the outlier test. The Student's t-distribution is a statistical distribution for estimating the mean of normally distributed observations, without knowing the standard deviation. The well-known t-statistic is given by:

$$t = \frac{\bar{x}_n - \mu}{s_n}, \tag{8}$$

where $\bar{x}_n$ is the mean of n independent and identically normally distributed observations, μ is defined as a mean, when the number of observations tends to infinity, and s_n is an estimated standard deviation of $\bar{x}_n$ (standard deviation of an observation divided by the square root of the number of observations).

If an observation is free of a gross error, ∇ is small. If no gross errors are present, the observations are normally distributed, i.e., $\mu = \mathrm{E}\{\nabla\} = 0$. Then Eq. 8 can be written as:

$$t = \frac{\nabla}{s_\nabla}, \tag{9}$$

where ∇ is the value of the gross error, and s_∇ is its estimated standard deviation. If there is no gross error present, t in Eq. 9 will follow the distribution of t in Eq. 8. Thus, if the absolute value of t is smaller than the threshold value (two-tailed, with $\alpha = 0.05$ and $f = n - 1$), we accept the observation, otherwise we classify it as an outlier. For further details, see Koch (1999). On average, ∼21% of the data points were classified as outliers (see Table 1).

2.2. Tide-gauge data

We have considered 22 TGs on the Norwegian mainland as shown in Figure 2. The figure shows one additional TG at Narvik (NARV), which was not considered for the comparison as it contained too few altimeter data. Tide-gauge data covering the 2010-2016 period were provided by the NMA (K. Breili, personal communication). The TG data have a 10-minute sampling rate, and include predicted ocean tides as well as local air pressure observations.

In order to make the TGs compatible with the altimeter, both IB and OT corrections must be applied to the TG observations. Before this was done, the annual astronomical tidal contribution, $\mathbf{S_a}$, was estimated from the OT predictions and removed, as it includes seasonal effects that to a large extent are already accounted for in the IB correction (Pugh and Woodworth, 2014). All TG observations were corrected for the IB effect using Wunsch and Stammer (1997, Eq. (1)), with respect to a reference value of 1011.4 mbar (Woodworth et al., 2012). At Hammerfest TG, no local pressure observations were available, and pressure data from a nearby meteorological station were used instead. These pressure observations were obtained from the eKlima database of the Norwegian Meteorological Institute, at `https://eklima.met.no/`.

2.3. CryoSat-2 tide gauges

Treating CS2 like an exact 369-day repeat altimeter would only give four observations for the 2010-2014 period. Consequently, we consider a different approach for CS2. We established 45×45 km boxes around each TG containing CS2 observations, forming "CS2 tide gauges" (CS2TGs). The CS2TGs, as seen in figures 3, 4, and 5, were positioned around each TG depending on topography, such that they cover as much marine area as possible, but still keep a minimum distance of 0.2° between the TG and the edge of the CS2TG.

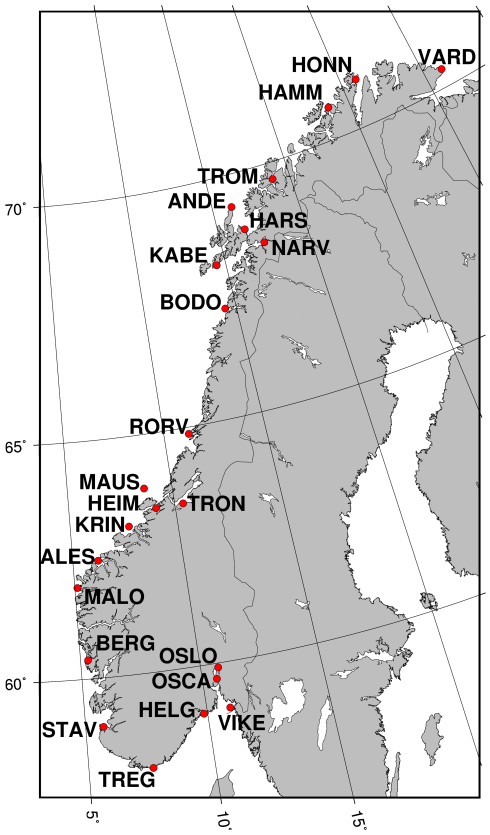

Figure 2: Norwegian tide gauges. Narvik (NARV) is left out of this study due to few altimeter observations.

As mentioned in Sect. 2.1, we did not downsample the 20 Hz observations to 1 Hz. This is normally done by the space agencies using iterative editing and averaging, and it will increase data accuracy. Instead, as the CS2 observations within a track are sampled very close in time (and all CS2 observations within a track would be assigned the same TG observation), we averaged all 20 Hz observations within a track, and linearly interpolated the TG observations to the time of the averaged CS2 observations using nearest-neighbor. On average, ∼76 CS2 tracks were available in each CS2TG. To quantify whether CS2 observes the same ocean signal as the TGs, the Spearman's (distribution-free) rank correlation coefficient, ρ, between the CS2TG and TG time series was computed. Spearman's ρ is a non-parametric method for detecting associations between two variables. Non-parametric methods are relatively insensitive to outliers, and do not assume that the observations are normally distributed (Hollander et al., 2013). In addition to the correlation coefficient, the standard deviations of differences between the CS2TGs and TGs were computed.

2.4. Conventional altimeter data

Jason-2, Envisat phase C, and SARAL/AltiKa 1 Hz altimetry data were extracted from the radar altimeter database system (RADS) (Scharroo et al., 2013), with standard corrections applied. For each altimeter, the two nearest tracks to the Stavanger TG were considered, and on each of these the closest point with the highest temporal correlation with the Stavanger TG was chosen for comparison, see Figure 3 and Table 2. For Jason-2, its entire 2010-2016 period could be used, while for Envisat only the period between 2010 and 2012 was used, where the satellite was in a 30-day repeat orbit. For SARAL/AltiKa only the period after 2013 could be used. Looking at Table 2 we note that the number of observations from the conventional altimeters do not always correspond with the expected number of observations considering the number of repeats for each altimeter time period. This is because the RADS data are not resampled to reference tracks, in combination with the fact that not necessarily all repeats have survived the RADS processing. Thus, when choosing the closest conventional altimeter point, we also set a lower threshold of 10 repeats. For consistency, the SSHs were extracted from RADS using the same geophysical corrections as for CS2 (FES2004 OT model, MOG2D+IB DAC).

Experimental coastal altimetry products are currently under development at, e.g., AVISO (`http://www.aviso.altimetry.fr`) or COASTALT (`http://www.coastalt.edu`). In their study along the Norwegian coast, Ophaug et al. (2015) found that tailored coastal altimetry products based on Jason-2 and Envisat offered only marginal improvements over the conventional observations, thus we did not consider coastal altimetry products in this study.

Table 1: CS2 at 23 Norwegian TGs.

Tide-gauge	Tide-gauge code	no. obs.	no. obs. ∈ [-1,1] m DTU15	used no. obs.	$t >$ $t_{(\alpha/2,f)}$ [%]	no. tracks	Standard (tide + IB) corrections $\sigma(\Delta)$ [cm]	Standard (tide + IB) corrections ρ [%]	Refined (tide + IB) corrections $\sigma(\Delta)$ [cm]	Refined (tide + IB) corrections ρ [%]	improv. of $\sigma(\Delta)$ using refined corr. [%]
Vardø	VARD	6111	5710	4637	19	93	9.6	69.7	8.9	70.7	6
Honningsvåg	HONN	6546	4457	3484	22	79	13.8	51.4	12.8	54.0	7
Hammerfest	HAMM	5611	3669	2954	19	90	17.5	63.3	9.2	69.4	47
Tromsø	TROM	2438	587	497	15	36	40.2	-17.9	29.9	21.3	25
Andenes	ANDE	8023	7662	6357	17	95	8.4	71.3	6.7	79.6	20
Harstad	HARS	6010	4031	3011	25	83	16.1	52.5	11.7	62.4	25
Narvik	NARV	2900	35	20	43	2	14.0	100.0	0.8	100.0	94
Kabelvåg	KABE	7319	6639	5277	21	92	10.3	72.7	5.4	89.5	47
Bodø	BODO	7463	5909	4480	24	85	13.4	69.6	6.3	89.4	53
Rørvik	RORV	7940	7060	5658	20	102	11.3	67.2	6.8	82.9	40
Mausund	MAUS	7489	6678	5097	24	94	6.9	79.2	6.6	81.8	5
Trondheim	TRON	4826	1940	1451	25	56	54.8	28.9	25.1	49.5	54
Heimsjø	HEIM	5018	3030	2360	22	89	21.0	38.1	11.2	59.8	47
Kristiansund	KRIN	9949	9125	7466	18	97	9.4	68.8	8.2	73.3	13
Ålesund	ALES	9653	7352	5814	21	89	10.0	77.2	10.2	74.4	-2
Måløy	MALO	9246	6411	5339	17	70	10.8	70.7	11.0	71.0	-2
Bergen	BERG	5820	3962	3085	22	74	18.0	65.6	10.9	78.5	40
Stavanger	STAV	9365	8433	6767	20	94	8.1	71.2	7.0	78.7	13
Tregde	TREG	7695	7453	6271	16	92	13.4	53.1	12.6	57.1	6
Helgeroa	HELG	7496	7121	5877	17	92	10.9	71.6	9.9	77.3	9
Oscarsborg	OSCA	2346	1747	1329	24	49	9.8	81.5	9.9	76.3	-1
Oslo	OSLO	493	255	228	11	21	18.1	61.8	15.8	63.0	13
Viker	VIKE	7407	6219	4493	28	67	7.8	85.7	7.0	88.1	10

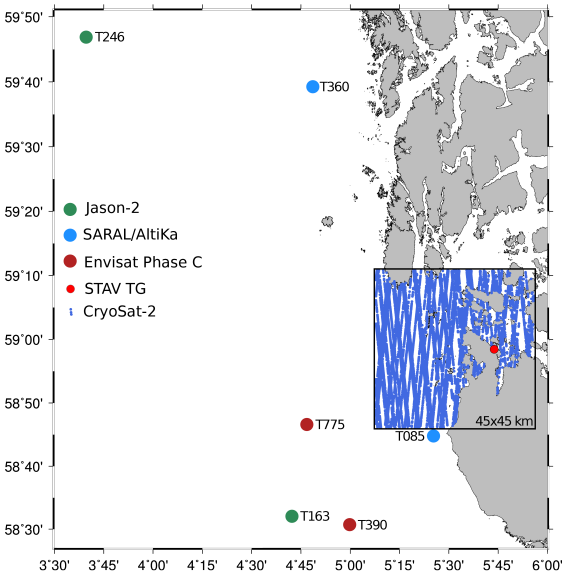

Figure 3: Location and track numbers of the closest altimeter data to the Stavanger (STAV) TG.

3. Results

3.1. Comparison of CryoSat-2 with tide gauges along the Norwegian coast

In order to investigate the accuracy of the DAC and OT geophysical corrections, we substituted the standard CS2 DAC/OT corrections with DAC and OT corrections derived from the local TG data. We name the latter refined corrections. Table 1 shows standard deviations of differences between the 22 TGs and CS2, as well as their correlations. The TGs are ordered such that the northernmost TG appears first in the table, moving southward along the Norwegian coastline. The smallest amount of observations was, as expected, found at TGs located well inside fjords, such as Oslo, Trondheim, and Tromsø. These TGs show large standard deviations of differences (∼20 cm or more). Figures 4a, 4d, and 4g show the data situation at these TGs, and highlight how complicated these fjords are. Although an improvement is observed when introducing refined corrections (Figures 4b, 4e, and 4h versus Figures 4c, 4f, and 4i, and also Table 1), they are highly unreliable. Tromsø drops from above 40 cm to below 30 cm in standard deviation, with clearly increased temporal correlation. By contrast, the smallest standard deviations and highest temporal correlations are typically found at TGs which are close to the open ocean. Mausund and Viker are clear examples of open-ocean TGs, while Stavanger is slightly more land-confined, see Figure 3. All three show smaller standard deviations of differences (∼7-8 cm).

When replacing the standard geophysical corrections with the refined corrections, we observe an improvement in the standard deviations of differences at 19 out of 22 TGs (exceptions are Ålesund, Måløy, and Oscarsborg). Figure 5 shows results for Bodø, Kabelvåg, and Viker, all of which benefited substantially from introducing refined corrections. At Bodø TG (Figure 5a), the time series using standard corrections (Figure 5b and Table 1) shows a standard deviation of 13.4 cm and temporal correlation of 69%. When introducing the refined corrections, the standard deviation drops to 6.3 cm, and the temporal correlation increases to 89% (Figure 5c and Table 1). The considerable improvement with refined corrections is also seen at Kabelvåg (Figures 5e, 5f, and Table 1), where the standard deviation of differences is 5.4 cm (dropped to nearly half), and the temporal correlation increases to 89.5% (from 72%). A slightly less improvement is seen at Viker (Figures 5h, 5i, and Table 1).

One explanation for the substantial improvement at the northern TGs could be that Bodø and Kabelvåg are located north of 66°N, which is outside the coverage of the Jason-type altimeter observations, partly on which the FES2004 OT model is based.

On average, using refined corrections gives better results than using standard corrections, with an improvement of ∼25% in standard deviations of differences, and ∼18% for correlations (Table 1).

3.2. Comparison of CryoSat-2 with conventional altimetry at Stavanger tide gauge

Figures 2 and 3 show the location of Stavanger TG, as well as the location of the 20 Hz CS2 SARIn data in a 45 km region close to it, the CS2TG. In addition, the closest conventional 1 Hz altimeter data around Stavanger TG is shown. The smaller ∼5 km^2 footprint and 20 Hz processing gives SSH observations from CS2 closer to the coast than other altimeters. By contrast, SARAL/AltiKa, Envisat, and Jason-2 have footprints of ∼25 km^2, ∼100 km^2, and ∼150 km^2, respectively (Verron et al., 2015). At distances from Stavanger TG of 31 km or more, the closest conventional altimeters are further away from the Stavanger TG than CS2, which has valid observations directly at the TG.

Table 2 shows standard deviations of differences between the TG and altimetry sites available in the Stavanger area. Although SARAL/AltiKa and Envisat show correlations of ∼80%, similar to CS2, their standard deviations of differences are 9 cm or more. The closest point for SARAL/AltiKa lies 31 km from the TG. It shows a correlation of 79% and standard deviation of 10.1 cm. In general, Jason-2 performs worse than the other two, but also shows the largest distances to the TG. It shows a temporal correlation of ∼30%, and standard deviations of ∼14 cm. CS2 shows a standard deviation of 7 cm and a temporal correlation of ∼80%, which can be considered accurate for a number of reasons. First, the CS2 wet troposphere correction was derived from the ECMWF model,

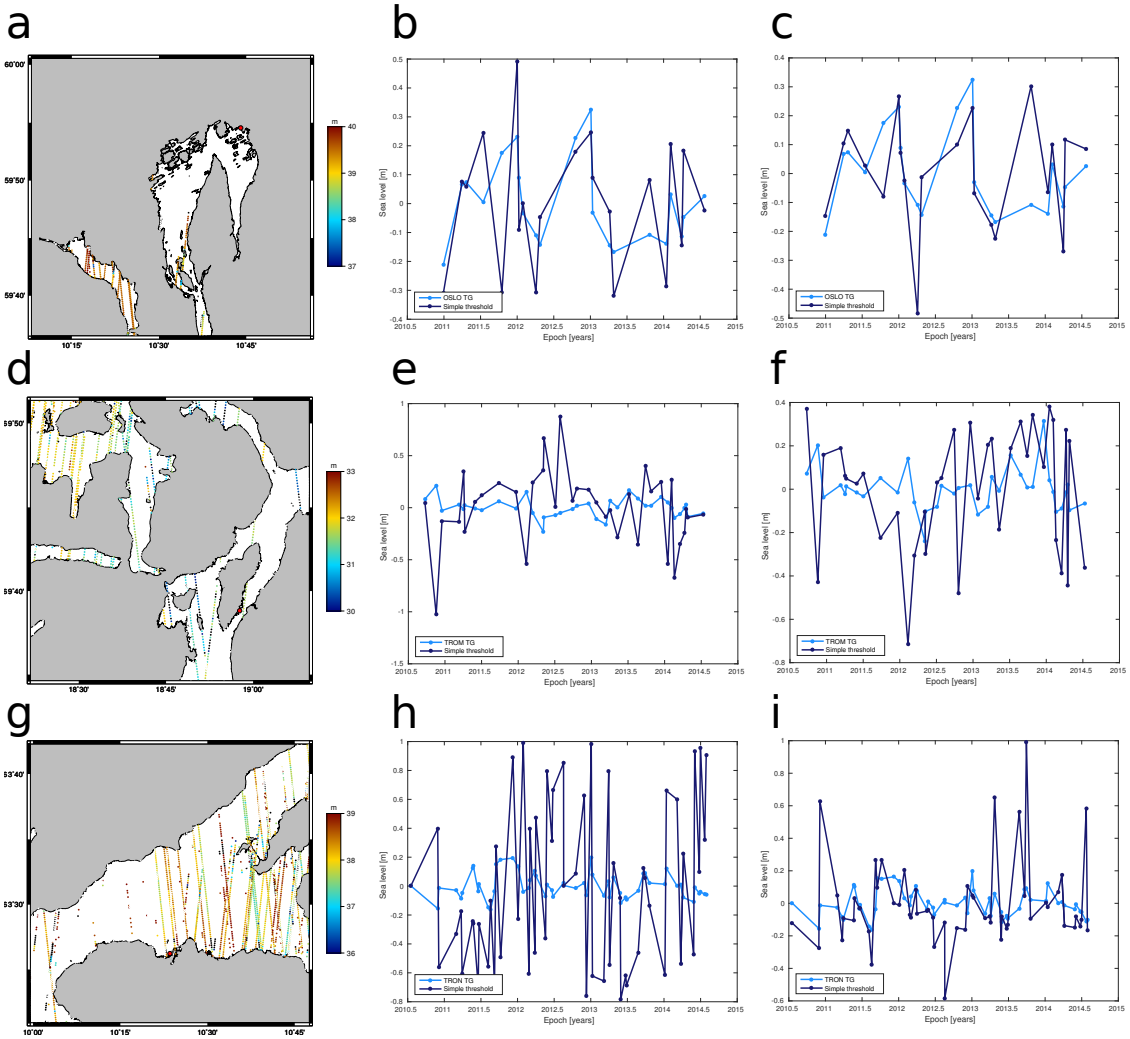

Figure 4: Comparison of CS2TGs and TGs at Oslo (a-c), Tromsø (d-f), and Trondheim (g-i). The TG (red dot) and CS2 SSHs are shown in a, d, and g. CS2TG and TG time series using standard corrections are shown in b, e, and h, while time series using refined corrections are shown in c, f, and i.

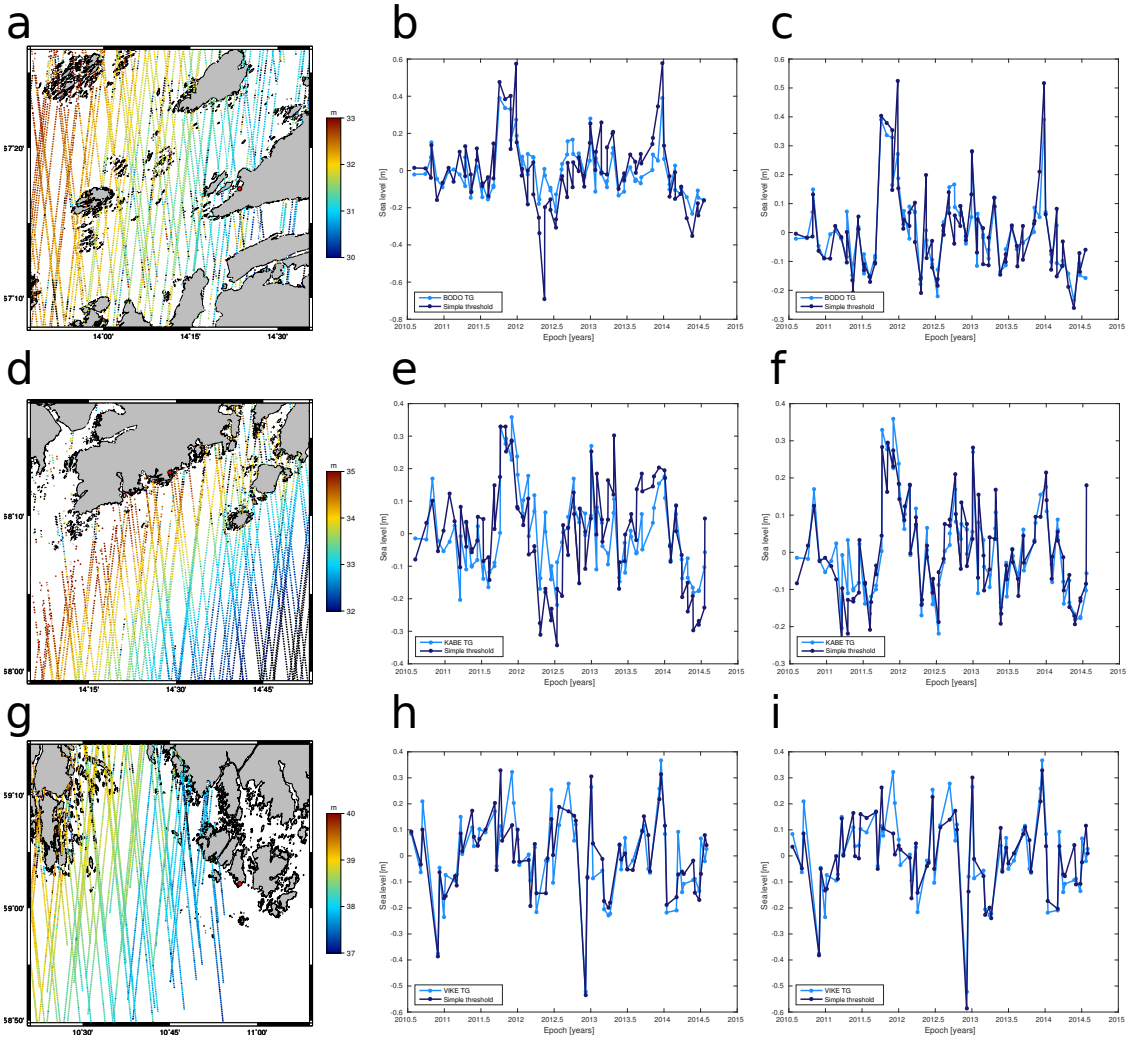

Figure 5: Comparison of CS2TGs and TGs at Bodø (a-c), Kabelvåg (d-f), and Viker (g-i). The TG (red dot) and CS2 SSHs are shown in a, d, and g. CS2TG and TG time series using standard corrections are shown in b, e, and h, while time series using refined corrections are shown in c, f, and i.

Table 2: Conventional altimetry sites and CS2TG at Stavanger TG.

Altimeter	Time period	track no.	no. obs.	dist. to tide-gauge [km]	$\sigma(\Delta)$ [cm]	ρ [%]
CryoSat-2	2010-2014	N/A	6767	<45	7.0	79
SARAL/AltiKa	2013-2016	T085	16	31	10.1	79
		T360	23	92	9.7	61
Envisat/C	2010-2012	T775	15	59	14.7	33
		T390	14	67	9.3	81
Jason-2	2010-2016	T163	139	77	14.3	24
		T246	197	148	14.4	29

which accuracy, when compared with a radiometer-based correction, is largely unknown this close to the coast (Andersen and Scharroo, 2011). Second, the CS2 SSHs are taken from multiple tracks within the CS2TG, which may be offset from each other. Such offsets would hamper the averaged CS2TG value. Finally, the raw 20 Hz data were used for the comparison, as discussed in the above.

4. Conclusions

CS2 delivers new coastal altimetry data along the Norwegian coast, over areas previously uncovered by conventional altimeters. Its geodetic orbit gives a denser spatial coverage than the conventional repeat orbits, with an average of 6398 20 Hz SSH observations within a 45×45 km area around TGs that are both close to the open ocean and more land-confined/inside fjords.

In terms of standard deviations of differences, CS2 shows an improvement of ∼3 cm over conventional altimeters for the comparison at Stavanger TG. We believe that this is due to the ability of CS2 to measure closer to the TGs than conventional altimeters.

Our study of the DAC and OT geophysical corrections applied to the altimeter data revealed that on average, we get an improvement between 2-5 cm at 19 out of 22 TGs when replacing the standard corrections with refined corrections based on local TG data. On average, we observe a slightly larger improvement for the TGs north of 66°N, where no altimetry was available for the standard FES2004 OT model.

These results highlight the great improvement in coastal sea-level recovery due to the SAR altimeter onboard CS2. We therefore have high hopes for Sentinel-3, which carries a SAR altimeter and has a 27-day repeat everywhere, and which will be equipped with a radiometer for improved range corrections.

Acknowledgments

We would like to thank K. Breili at the NMA, for providing TG data and helpful comments. This work is part of the Norwegian University of Life Science's GOCODYN project, supported by the Norwegian Research Council under project number 231017.

References

Abulaitijiang, A., Andersen, O.B., and Stenseng, L. (2015). Coastal sea level from inland CryoSat-2 interferometric SAR altimetry. *Geophys. Res. Lett.* **42**, 1841-1847. doi:10.1002/2015GL063131.

Andersen, O. B., Knudsen, P., and Stenseng, L. (2015), The DTU13 MSS (Mean Sea Surface) and MDT (Mean Dynamic Topography) from 20 Years of Satellite Altimetry, in IAG Symposia, Springer, Berlin Heidelberg, doi:10.1007/1345_2015_182.

Andersen, O. B., and Scharroo, R. (2011), Range and Geophysical Corrections in Coastal Regions: And Implications for Mean Sea Surface Determination, in Coastal Altimetry, edited by S. Vignudelli et al., pp. 103–145, Springer, Berlin Heidelberg, doi:10.1007/978-3-642-12796-0_5.

Armitage, T., and Davidson, M. (2014). Using the Interferometric Capabilities of the ESA CryoSat-2 Mission to Improve the Accuracy of Sea Ice Freeboard Retrievals. *IEEE Trans. Geosci. Remote Sens.* **52**(1), 529-536. doi:10.1109/TGRS.2013.2242082.

Cipollini, P., Beneviste, J., Bouffard, J., Emery, W., Fenoglio-Marc, L., Gommenginger, C., Griffin, D., Hoyer, J., Kurapov, A., Madsen, K., Mercier, F., Miller, L., Pascual, A., Ravichandran, M., Shillington, F., Snaith, H., Strub, P.T., Vandemark, D., Vignudelli, S., Wilkin, J., Woodworth, P.L., and Zavala-Garay, J. (2010). The Role of Altimetry in Coastal Observing Systems. In *Proceedings of OceanObs'09: Sustained Ocean Observations and Information for Society*, ESA WPP-306, ESA Publications Division, European Space Agency, Noordwijk, The Netherlands, pp181-191. doi:10.5270/OceanObs09.cwp.16.

European Space Agency (2016). Geographical Mode Mask. Online at https://earth.esa.int/web/guest/-/geographical-mode-mask-7107 (as of 27 April 2016).

Gommenginger, C., P. Thibaut, L. Fenoglio-Marc, G. Quartly, X. Deng, J. Gómez-Enri, P. Challenor, and Y. Gao (2011), Retracking altimeter waveforms near the coasts, in Coastal Altimetry, edited by S. Vignudelli et al., pp. 61–101, Springer, Berlin Heidelberg, doi:10.1007/978-3-642-12796-0_4.

Hollander, M., Wolfe, D.A., and Chicken, E. (2013). *Nonparametric Statistical Methods*. Third Edition, John Wiley & Sons, Inc., Hoboken, New Jersey.

Koch K.-R. (1999). *Parameter Estimation and Hypothesis Testing in Linear Models*. Second, updated and enlarged Edition, Springer-Verlag.

Nielsen, K., Stenseng, L., Andersen, O.B., Villadsen, H., and Knudsen, P. (2015). Validation of CryoSat-2 SAR mode lake levels. *Remote Sens. Environ.* **171**, 162-170. doi:10.1016/j.rse.2015.10.023.

Ophaug, V., Breili, K., and Gerlach, C. (2015). A comparative assessment of coastal mean dynamic topography in Norway by geodetic and ocean approaches. *J. Geophys. Res. Oceans* **120**, 7807?7826. doi:10.1002/2015JC011145.

Pugh, D., and P. L. Woodworth (2014). *Sea-Level Science: Understanding Tides, Surges, Tsunamis and Mean Sea-Level Changes*, Cambridge Univ. Press, Cambridge, U. K.

Revhaug I. (2007). Outlier detection in multiple testing using Students t-test and Fisher F-test. *Kart og Plan* **67**, 101-107.

Scagliola M., and Fornari M. (2013). Known biases in CryoSat-2 Level 1b products. DOC: C2-TN-ARS-GS-5135, 1.2.

Scharroo, R., Leuliette, E.W., Lillibridge, J.L., Byrne, D., Naeije, M.C., and Mitchum, G.T. (2013). RADS: Consistent multi-mission products. In *Proc. of the Symposium on 20 Years of Progress in Radar Altimetry*, ESA SP-710, ESA Publications Division, European Space Agency, Noordwijk, The Netherlands, p. 4 pp.

Stenseng, L., and Andersen, O. B. (2012). Preliminary gravity recovery from CryoSat-2 data in the Baffin Bay. *Adv. Space Res.* **50**(8), 1158-1163. doi:10.1016/j.asr.2012.02.029.

Verron, J., Sengenes, P., Lambin, J., Noubel, J., Steunou, N., Guillot, A., Picot, N., Coutin-Faye, S., Sharma, R., Gairola, R. M., Raghava Murthy, D. V. A., Richman, J. G., Griffin, D., Pascual, A., Rémy, F., and Gupta, P. K. (2015). The SARAL/AltiKa Altimetry Satellite Mission. *Mar. Geod.* **38**, 2-21. doi:10.1080/01490419.2014.1000471.

Wingham, D. J., Francis, C. R., Baker, S., Bouzinac, C., Brockley, D., Cullen, R., de Chateau-Thierry, P., Laxon, S. W., Mallow, U., Mavrocordatos, C., Phalippou, L, Ratier, G., Rey, L., Rostan, F., Viau, P., and Wallis, D. W. (2006). CryoSat: A mission to determine the fluctuations in Earth's land and marine ice fields. *Adv. Space Res.* **37**, 841-871. doi:10.1016/j.asr.2005.07.027.

Woodworth, P.L., Hughes, C.W., Bingham, R.J., and Gruber, T. (2012). Towards worldwide height system unification using ocean information. *J. Geod. Sci.* **2**(4), 302-312. doi:10.2478/v10156-012-0004-8.

Wunsch, C., and D. Stammer (1997), Atmospheric loading and the oceanic "inverted barometer" effect, *Rev. Geophys.*, *35*, 79–107, doi:10.1029/96RG030337.

Paper E

The Norwegian Coastal Current observed by CryoSat-2 and GOCE

Martina Idžanović[1]*, Vegard Ophaug[1], and Ole Baltazar Andersen[2]

[1]Faculty of Science and Technology, Norwegian University of Life Sciences (NMBU), Ås, Norway

[2]DTU Space, Technical University of Denmark, Kgs. Lyngby, Denmark

Key Points:

- CryoSat-2 (CS2) delivers new data along the Norwegian coast, in areas previously uncovered by altimetry
- CS2 MDTs agree on the ~3-5 cm level with both tide-gauge geodetic and ocean MDTs, and the NCC flow pattern is revealed
- The circulation patterns depend highly on the regional geoid, emphasizing the importance of terrestrial gravity information for the MDT

*Drøbakveien 31, 1433 Ås, Norway

Corresponding author: Martina Idžanović, martina.idzanovic@nmbu.no

Abstract

The Norwegian Coastal Current (NCC) has been studied by oceanographers using hydrographic in situ measurements, and is revealed by high-resolution coastal numerical ocean models (ocean approach). Until now, it has not been possible to complement the oceanographic results using space-geodetic observations, due to the proximity of the NCC to the coast, where conventional satellite altimetry observations are either nonexistent or unreliable. Using new regional geoid models as well as CryoSat-2 (CS2) data, we determine three geodetic coastal mean dynamic topography (MDT) models. The CS2 MDTs agree on the ~3-5 cm level with both tide-gauge geodetic and ocean MDTs along the Norwegian coast, and for the first time the NCC is revealed by space-geodetic techniques. However, even though the regional geoid models are all based on the latest satellite gravity data as provided by GOCE, the resulting circulation patterns differ substantially. This suggests that there is significant MDT signal at spatial scales beyond GOCE, and that the geodetic approach to MDT determination benefits from the additional terrestrial gravity information provided by a regional geoid model.

1 Introduction

The Norwegian Coastal Current (NCC) transports warm and relatively fresh water along the Norwegian coast and into the Barents Sea, with its origin in Baltic water entering Skagerrak [*Skagseth et al.*, 2011]. Along its way northward it is fed by additional freshwater discharge. The NCC is important for the regional marine ecosystem and contributes to the poleward transport of warm Atlantic Water, maintaining the relatively mild climate in northwest Europe [*Rhines et al.*, 2008]. The Norwegian Atlantic Current (NwAC) is a two-branch system where the eastern branch follows the bathymetry as a barotropic slope current (NwASC) [*Orvik et al.*, 2001]. The NCC also has a barotropic slope branch [*Skagseth et al.*, 2011], which is the focus of this work.

Although satellite altimetry is a mature technique, observing the sea surface height (SSH) globally with an accuracy of a few centimeters [e.g., *Chelton et al.*, 2001], numerous effects degrade the observations in the coastal zone [*Vignudelli et al.*, 2011]. For example, the radar footprint is contaminated by land and bright targets, and the range and geophysical corrections become difficult to model. The rugged Norwegian coast presents a further challenge, and the NCC typically falls into a zone where conventional altimeters do not deliver reliable observations [*Ophaug et al.*, 2015].

CryoSat-2 (CS2) [*Wingham et al.*, 2006] was launched by the European Space Agency (ESA) on April 8th 2010, orbiting the Earth at 717 km altitude and an inclination of 92°, in a repeat orbit of 369 days, with 30-day subcycles. Consequently, CS2 has a dense groundtrack spacing of around 5-7 km at high latitudes. It carries a synthetic aperture interferometric radar altimeter (SIRAL) which can operate in synthetic aperture radar (SAR), SAR interferometric (SARIn), as well as conventional low resolution (LR) modes. CS2 uses a geographical mode mask to decide which mode to operate in [*ESA and MSSL-UCL*, 2012]. CS2 is in LR mode (LRM) over flat surfaces and the open ocean, where it operates as a conventional altimeter with an almost circular footprint. The SAR mode improves the along-track resolution to ~300 m through a complex Doppler processing chain, and is used over sea ice. Over regions with significant topography, CS2 operates in SARIn mode, which also has an along-track resolution of ~300 m. In addition, the altimeter measures the phase difference of the backscattered signal at two antennas, from which the position of any backscattered point may be derived. Thus, the SARIn mode may help discriminating and mitigating land contamination signals from off-nadir land targets (e.g., steep cliffs) [*Armitage and Davidson*, 2014].

The geodetic dynamical ocean topography (DOT) is computed by [e.g., *Pugh and Woodworth*, 2014]

$$\mathrm{DOT} = h - N, \tag{1}$$

where h is the ellipsoidal height of sea level, and N is the geoid height, all referring to the same reference ellipsoid. If we average h over a specific time period, equation (1) will give the MDT for that period. Using equation (1), the mean dynamic topography (MDT) has a high dependence on the geoid model.

In this work we use three state-of-the-art regional geoid models as well as CS2 data in the Norwegian coastal zone, and determine coastal MDT models by equation (1). Our main goal is to validate the three CS2 MDTs against tide-gauge observations and the state-of-the-art operational coastal numerical ocean model NorKyst800. We further explore to which extent the CS2 MDTs observe realistic flow patterns.

As we compare coastal MDTs determined by the methodically different approaches of geodesy and oceanography, this work is a natural extension of such comparisons along different coasts [e.g., *Woodworth et al.*, 2012; *Higginson et al.*, 2015; *Hughes et al.*, 2015; *Lin et al.*, 2015; *Woodworth et al.*, 2015]. In particular, this work builds upon the bench-

mark comparison of geodetic and ocean MDTs along the Norwegian coast as presented by *Ophaug et al.* [2015].

Section 2 describes the data and methods we use to determine the CS2 MDTs and validate them. The CS2 data and MDT computation is described in Section 2.1. Section 2.2 concerns the data used to validate the CS2 MDTs, specifically the tide-gauge geodetic MDT (Section 2.2.1) and the NorKyst800 ocean MDT (Section 2.2.2). In Section 3 we assess the CS2 MDTs by comparing geodetic and ocean MDT profiles at the tide gauges, as well as comparing the flow patterns of the CS2 MDTs and NorKyst800. Finally, we discuss our results and give some concluding remarks in Section 4.

2 Data and methods

2.1 CryoSat-2 MDT

While equation (1) seems computationally simple, it is important that h and N cover the same wavelengths. Typically, when using satellite-only geoid models, h contains small-scale features that N lacks, requiring a suitable filtering of h to reduce the error of N.

In order to resolve the smallest spatial scales of the gravity field and thus reduce the filtering need, we have referenced ellipsoidal sea level to three regional geoid models, namely the operational regional geoid model for Norway, NMA2014, as described in *Ophaug et al.* [2015], the Nordic Geodetic Commission NKG2015 model [*Ågren et al.*, 2016], as well as the European Gravimetric Geoid EGG2015 [*Denker*, 2016], see supporting information Table S1. All are based on fifth-release data from the ESA satellite gravity mission Gravity and steady-state Ocean Circulation Explorer (GOCE) [*Drinkwater et al.*, 2003]. The geoid heights were transformed from the zero-tide system to the mean tide (MT) system using *Ekman* [1989, Eq. (17)]. They refer to the WGS84 ellipsoid.

CS2 operates in LRM over most of the Norwegian Sea, and in SAR mode in the North Sea and Skagerrak area. It switches to SARIn mode in the Norwegian coastal areas. SARIn data points are available in a zone stretching out ~40 km off the Norwegian coast. Thus we have considered SSH observations obtained in all three modes in this work.

The LR and SAR mode data was obtained through the Radar Altimeter Database System (RADS) [*Scharroo et al.*, 2013a]. It contains 1 Hz values referring to the TOPEX ellipsoid, and was referenced to WGS84 by considering an average difference of 0.686 m

between WGS84 and TOPEX [*Ophaug et al.*, 2015]. RADS provides SAR mode observations as so-called pseudo-LRM observations, i.e., they are reduced SAR observations using an incoherent processing of the pulse-limited echoes, similar to the the conventional LRM processing [*Scharroo et al.*, 2013b]. Therefore, we will refer to all RADS data as LRM data in the following.

SARIn mode observations were obtained from ESA, which provides CS2 data in two modes, Level 1 (L1) and Level 2 (L2). L1 contains orbit information and received radar echoes, while L2 contains range and geophysical corrections, and a height estimate. The CS2 SARIn mode dataset was obtained through the Technical University of Denmark (DTU) Space retracker system. This data processing is based on the L2 dataset, as well as the 20 Hz L1b dataset, which is retracked using an empirical retracker. The SARIn off-nadir range correction was applied in the processing [*Abulaitijiang et al.*, 2015]. The dataset covers the 2010-2015 time period, but was limited to the 2012-2015 period, to be in agreement with the ocean MDT (Section 2.2.2).

We have used the Narrow Primary Peak Threshold empirical retracker, which uses waveform statistics to determine the retracking point [*Jain et al.*, 2015]. Only the primary peak of the waveform is considered, which corresponds to the part of the waveform reflected from the sea surface in nadir. As coastal waveforms may be complex and contain multiple peaks due to reflections from other surfaces than the ocean [*Gommenginger et al.*, 2011], considering only the primary peak of the waveform will give the most precise information about the sea surface. Empirical retrackers generally only give the range, but provide a SSH estimate for all kinds of waveforms and are computationally efficient. A previous study by *Villadsen et al.* [2016] has shown that empirical retrackers perform as well as physical retrackers if only the SSH is wanted.

As opposed to the LRM data obtained from RADS, no editing or quality assessment has been performed on the SARIn data. Consequently, the SARIn data contains an unknown amount of erroneous data points (e.g., when CS2 has tracked land instead of ocean). First, we removed all observations over land, giving 462,862 data points over the ocean. Next, we removed observations deviating more than ± 1 m from the geoid, and performed a within-track outlier removal by multiple Student's t-test (two-tailed, with $\alpha = 0.05$) [e.g., *Koch*, 1999, chapter 4]. This two-step outlier removal led to a ~40% reduction in SARIn data points.

We have considered standard range and geophysical corrections for both LRM and SARIn datasets, and they were combined by considering a known bias for the SARIn dataset, see supporting information Table S2.

Geoid heights from each geoid model were interpolated to the CS2 SSH observations, from which they were subsequently subtracted. Next, the SARIn DOT observations were averaged in 7×7 km bins to correspond with the 1 Hz LRM DOT observations. Finally, all observations were averaged in 15×15 km bins, and interpolated onto a regular grid with 30 arcsec resolution, within an area delimited by $55.8092° \leq \varphi \leq 73°$ and $0° \leq \lambda \leq 34°$. The interpolation was done using least-squares collocation [*Moritz*, 1980], see supporting information Text S1. CS2 MDTs based on NKG2015, EGG2015, and NMA2014 will be referred to as $C2_{NKG}$, $C2_{EGG}$, and $C2_{NMA}$ in the following.

We have chosen to compare flow patterns in the form of geostrophic surface currents, see supporting information Text S1. Under the geostrophic assumption we look at the barotropic component of the flow. Considering the barotropic slope branch of the NCC, we expect the mean flow to follow the isobaths. Other contributors to the NCC exist, e.g., from the shallow shelf region and a baroclinic offshore region [*Skagseth et al.*, 2011]. However, as our main goal is to compare the CS2 MDTs with NorKyst800, we limit the flow pattern to a geostrophically balanced flow for simplicity.

2.2 Validation data

2.2.1 Tide-gauge MDT

We have considered a subset of 19 tide gauges (TGs) on the Norwegian mainland in this work, see Figure 1a and supporting information Table S3. Thereby, we have omitted four TGs due to their location well inside fjords not sufficiently covered by altimetry data [*Ophaug et al.*, 2015]. Monthly sea-level observations for 2012-2015 were obtained from the Permanent Service for Mean Sea Level (PSMSL) [*Holgate et al.*, 2013] at http://www.psmsl.org/data/obtaining/, while local pressure observations with 10-minute temporal resolution have been obtained from the database of the Norwegian Mapping Authority (NMA) (K. Breili, personal communication, 2016). As Mausund data is not yet available at PSMSL, these data were obtained from the NMA database.

The pressure observations were used to correct sea level for the ocean's inverted barometer (IB) effect, using *Wunsch and Stammer* [1997, Eq. (1)], with respect to a reference value of 1011.4 mbar [*Woodworth et al.*, 2012]. Local pressure observations are not available at Hammerfest, where we instead used local six-hourly sea-level pressure data obtained from the eKlima database of the Norwegian Meteorological Institute (MET Norway) at http://eklima.met.no. In addition, a correction for the nodal tide was applied, using *Woodworth* [2012, Eq. (1), scaled by 0.44 according to *Pugh and Woodworth*, 2014].

The sea-level observations are given as heights H in the national height system, NN2000. As none of the considered TGs have been observed directly by Global Navigation Satellite Systems (GNSS) with sufficient accuracy, we have derived ellipsoidal heights h of MSL using the Norwegian height reference surface HREF2016A [*Solheim*, 2000], and the simple relation $h = H + \mathrm{HREF}$. Ellipsoidal heights of MSL derived from HREF2016A refer to the GRS80 ellipsoid (which is practically equal to the WGS84 ellipsoid). They are given in the conventional tide free system, and were converted to the MT system using *Petit and Luzum* [2010, Eq. (7.14a)]. NKG2015, EGG2015, and NMA2014 were linearly interpolated to the tide-gauge sites, and by equation (1) $\mathrm{TG_{NKG}}$, $\mathrm{TG_{EGG}}$, and $\mathrm{TG_{NMA}}$ were determined, respectively.

2.2.2 NorKyst800

We have considered the operational coastal ocean model of MET Norway, NorKyst800, based on the Regional Ocean Modeling System (ROMS) [*Haidvogel et al.*, 2008]. It was obtained from http://met.no/Hav_og_is/English/Access_to_data/, where it is available in the form of daily mean values since July 2nd 2012.

NorKyst800 is a free-surface terrain-following hydrostatic numerical ocean model using finite difference horizontal and σ vertical coordinate systems. It is vertically discretized into 35 levels, where the σ coordinates follow a smoothed bathymetry. Moreover, it is forced by atmospheric datasets (mean sea-level pressure, wind, temperature, specific humidity, total cloud cover, and precipitation), where the equations of motion determine the model's response to these forces.

NorKyst800 uses a polar stereographic grid delimited by $55.8092° \leq \varphi \leq 75.2419°$ and $-1.5651° \leq \lambda \leq 38.0339°$, at an eddy-resolving resolution of 800 m. The NorKyst800 version of ROMS differs from the original version in that it replaces the atmospheric forc-

ing by that of *Røed and Debernard* [2004], and additionally considers a sea-ice component [*Budgell*, 2005]. It includes tidal forcing from the global TPXO model [*Egbert and Erofeeva*, 2002], and freshwater runoff from a hydrological model discharge at 256 main catchment areas.

To make our validation easier, NorKyst800 was resampled to a regular grid with 30 arcsec resolution using the NEARNEIGHBOR routine of the Generic Mapping Tools (GMT) [*Wessel et al.*, 2013]. The nearest-neighbor algorithm is favorable due to its simplicity, and because it does no extrapolation at the coast. Typically the coastal grid point of the native ocean model grid is used, relieving us from any special treatment of the coastal points.

As NorKyst800 is forced by atmospheric pressure it includes the IB effect. We corrected NorKyst800 for the IB effect by applying *Wunsch and Stammer* [1997, Eq. (1)] to a $0.25^\circ \times 0.25^\circ$ mean sea-level pressure field for the 2012-2015 period, obtained from the European Centre for Medium-Range Weather Forecasts (ECMWF) Interim Reanalysis (ERA Interim) [*Dee et al.*, 2011].

3 Results

CS2 MDTs (Figures 1b-d) are generally consistent with NorKyst800 (Figure 1a), with slightly larger values in the coastal zone (up to ~40 km off the coast) and smaller values to the open ocean. The general pattern of Norwegian Sea circulation is evident in all MDTs; we trace the NwASC northward and observe its branching at the Barents Sea Opening around 72°N, as well as the NCC originating in the Baltic Sea around 58°N flowing northwards along the coast all the way to its final destination in the Barents Sea. However, in comparison with NorKyst800, $C2_{EGG}$ shows a larger ~8 cm standard deviation of differences than the other two geodetic MDTs (~6 cm), see supporting information Table S4. All the geodetic MDTs have areas along the coast where the MDT shows smaller values than expected. For example, a fall towards the coast between 65-70°N, as well as along the north-eastern coast, is evident in all geodetic MDTs, although with slight variations. The most striking coastal feature of $C2_{EGG}$ and $C2_{NMA}$ is an MDT low seen in the area between the Lofoten-Vesterålen area and Senja island, roughly at 69°N, between 15-20°E. This feature is much less visible in $C2_{NKG}$.

The ocean and geodetic MDT profiles at TGs are shown in Figure 2. The coastal MDT profile obtained from NorKyst800 is smoother compared to the MDT profiles ob-

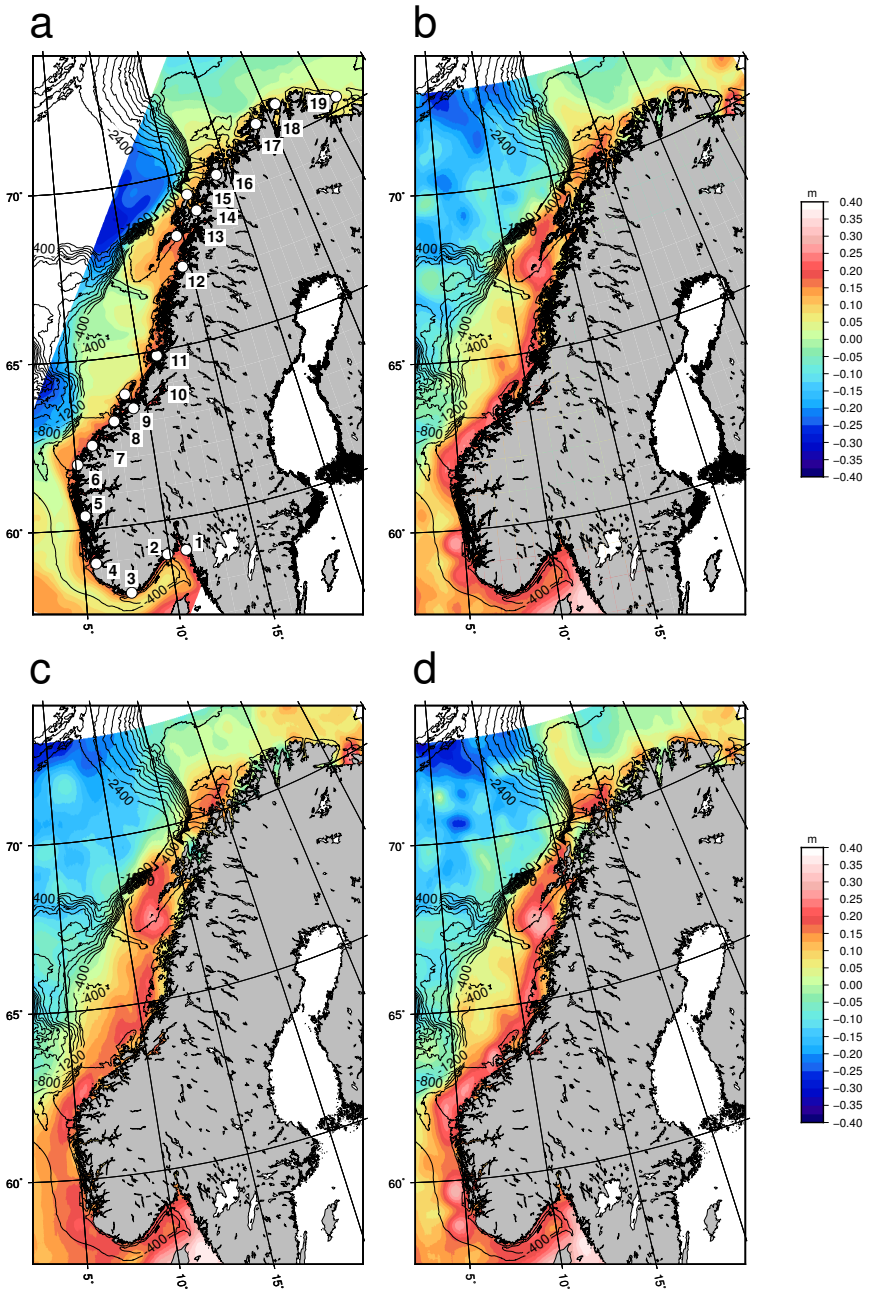

Figure 1. Coastal MDTs in Norway; (a) ocean, based on NorKyst800 and geodetic, based on (b) $C2_{NKG}$, (c) $C2_{EGG}$, and (d) $C2_{NMA}$. The mean value has been removed in all cases. The tide gauges considered in this work are shown in (a), for which a code is given in Figure 2. In all (a-d), 400 m isobaths from the 2014 General Bathymetric Charts of the Oceans (GEBCO) [*Weatherall et al.*, 2015] grid are shown.

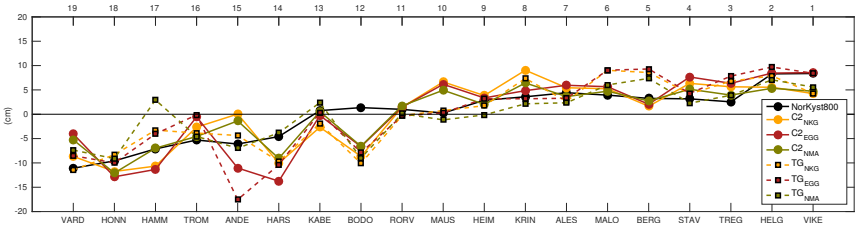

Figure 2. Tide-gauge MDT profiles using geodetic and ocean estimates, arranged from north to south. For all profiles the mean value has been removed. TG codes and IDs are given on the bottom and top x-axis, respectively.

tained from TGs and CS2. In accordance with the findings of *Ophaug et al.* [2015], we observe a 10 cm rise toward Kabelvåg, a flattening toward Stavanger, and another 10 cm rise toward Viker. We observe the largest differences in the Lofoten-Vesterålen area (~10 cm). The geodetic MDTs show a large spread at HAMM, ANDE, and HARS, but agree well at KABE, RORV, HEIM, and ALES. We further observe a polarization of TG and CS2 MDTs at some TGs. At HONN, MAUS, and STAV, the TG MDTs agree more with NorKyst800 than the CS2 MDTs, while the converse holds true at BERG. Notably, at BODO, all the geodetic MDTs show a ~10 cm disagreement with NorKyst800. In comparison with their respective TG MDT, $C2_{NKG}$, $C2_{EGG}$, and $C2_{NMA}$ show profile standard deviations of differences of 3.5 cm, 3.8 cm, and 3.9 cm, respectively. In comparison with NorKyst800, $C2_{NKG}$, $C2_{EGG}$, and $C2_{NMA}$ show values of 4.3 cm, 4.4 cm, and 3.4 cm, respectively. TG_{NKG}, TG_{EGG}, and TG_{NMA} show profile standard deviations of differences of 4.1 cm, 4.7 cm, and 3.9 cm to NorKyst800, respectively. We regard these numbers as promising considering previous studies of coastal MDT, which have shown an agreement between tide-gauge geodetic and ocean MDTs on the ~2-14 cm level [e.g., *Woodworth et al.*, 2012; *Higginson et al.*, 2015; *Lin et al.*, 2015; *Ophaug et al.*, 2015; *Woodworth et al.*, 2015], and between altimetric geodetic and ocean MDT on the ~5-11 cm level [e.g., *Ophaug et al.*, 2015; *Woodworth et al.*, 2015].

For the assessment of the NCC, geostrophic velocity fields were derived, see supporting information Text S1 and Figure 3. Prior to the differentiation, all MDTs were slightly filtered using a Gaussian kernel with a filter width of 12 km. The general pattern of the Norwegian Sea circulation is evident in NorKyst800, $C2_{NKG}$, and $C2_{NMA}$. We trace the NwASC northward and observe its branching at the Barents Sea Opening around

72°N, as well as the hot spots at Svinøy around 62.5°N and the Lofoten-Vesterålen area. We also see the NCC originating in the Baltic Sea around 58°N, flowing northwards, splitting from the NwASC at Svinøy and connecting with it again in the Lofoten-Vesterålen area, and continuing towards the Barents Sea. The strongest currents are visible in NorKyst800, which is highly correlated with the bathymetry (compare with Figure 1a). $C2_{NMA}$ shows the strongest currents and most distinct pattern of the geodetic MDTs, followed closely by $C2_{NKG}$. However, the narrow jet along the south-eastern coast, observed in NorKyst800, is less visible. Apart from the hot spot in the Lofoten-Vesterålen area, the circulation pattern is more or less absent in $C2_{EGG}$.

4 Summary and discussion

In this work, we have shown the promising abilities of CS2 SAR(In) altimetry to recover MDT directly at the Norwegian coast, even in skerry landscapes and fjords. At the tide gauges, the CS2 MDTs agree on the ~3-5 cm level with both tide-gauge and ocean MDTs, which are determined using fundamentally different methods. The NCC is revealed in the geostrophic current patterns of $C2_{NKG}$ and $C2_{NMA}$. However, in spite of these encouraging results, our CS2 MDTs show different artifacts requiring further investigations, which we would like to expand upon in the following.

The geodetic MDT is notorious for its reliance on the resolution and accuracy of the marine geoid. This is demonstrated in this work, where we observe different circulation patterns depending on the geoid. These variations are observed even though we have restricted ourselves to using new high-resolution gravimetric geoid models which are all based on the same satellite gravity information. This suggests there is significant MDT signal at smaller spatial scales than those resolved by GOCE, and that the geodetic MDT can be improved by considering regional geoid models which include terrestrial gravity data.

The three regional geoid models in this work are mostly based on the same terrestrial gravity data. However, while NKG2015 and NMA2014 are both almost completely free of altimetry-derived gravity information (and thus independent of the altimetry observations they are subtracted from), EGG2015 is heavily based on altimetry-derived gravity. Looking at Figure 3c, we note in particular that the branching of the NwASC is less emphasized in $C2_{EGG}$, and north-south flows generally seem less distinct. This could,

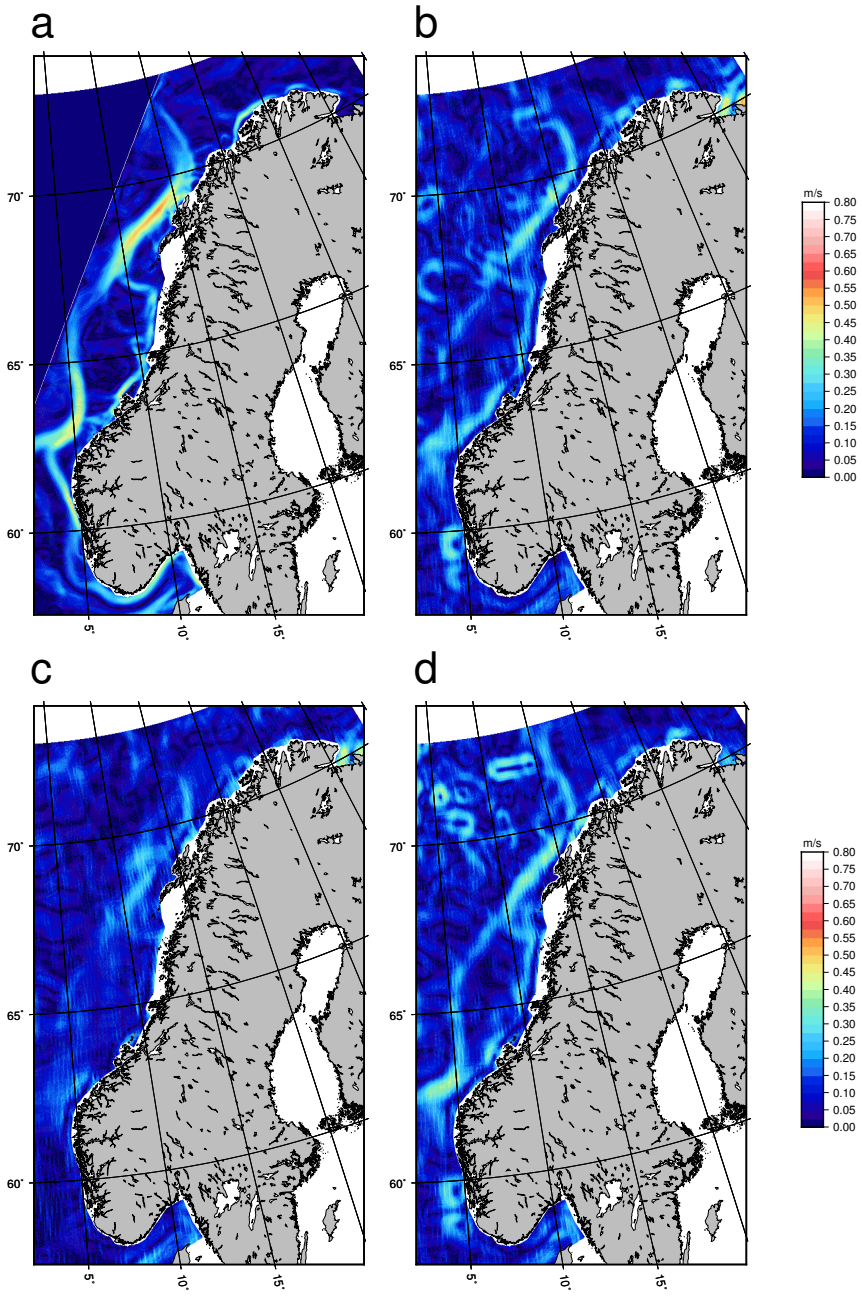

269 **Figure 3.** Geostrophic ocean surface currents derived from (a) NorKyst800, (b) $C2_{NKG}$, (c) $C2_{EGG}$, and (d)

270 $C2_{NMA}$. Areas not relevant to the geostrophic assumption, at the coast or inside fjords, have been masked out.

in part, be owing to the way gravity is derived from altimetry. However, other regional geoid computation issues, such as data weighting and interpolation may also play a role. For example, the MDT low in $C2_{NMA}$ mentioned in Section 3 is probably due to a gravity data interpolation issue in the computation of NMA2014, as gravity data is sparse in this particular area (O. C. D. Omang, NMA, personal communication, 2016). This seems to have been resolved in the more recent NKG2015 geoid model, which is based on the same gravity dataset. The MDT low in $C2_{EGG}$ is located slightly more to the southwest of the low in $C2_{NMA}$, which suggests it might be related to a different issue. However, as the problem is more or less solved in $C2_{NKG}$, it is still likely to be a geoid-related artifact rather than related to CS2.

As mentioned in Section 3, Figure 2 reveals a polarization of TG and CS2 MDTs at some sites. In some cases, the TG MDTs agree more with NorKyst800 than the CS2 MDTs. As all geodetic MDTs are based on the same geoid models, this suggests that the CS2 MDTs are off due to noisy CS2 observations rather than geoid errors. Using the same argument, in case the CS2 MDTs agree more with NorKyst800 than the TG MDTs, this suggests there could be an error in the ellipsoidal height of MSL. Our method for determining the ellipsoidal height of MSL at tide gauges make these values dependent on HREF accuracy, which in turn is dependent on GNSS/leveling and errors in the geoid it is based on. We continue to stress that ellipsoidal heights at tide gauges are best determined directly by GNSS techniques, simplifying the geodetic MDT error budget. In BODO, however, all geodetic MDTs agree well internally, but disagree with NorKyst800 by ~10 cm. In this case, the TG and CS2 agree on the ellipsoidal height of sea level, which suggests there could be an error in the geoids. BODO lies in the coastal area between 65-70°N, which shows an MDT low in all geoids.

At this point, we would like to stress that NorKyst800 errors also form a component of our MDT error estimates. Using the simple error budgeting approach of *Ophaug et al.* [2015], which relates the empirical standard deviation of differences to the formal error propagation, we get a 2-3 cm error contribution from NorKyst800. Thereby, we have used our MDT profile standard deviations and assume equal error contributions from ellipsoidal sea-level, geoid model, and NorKyst800.

In general, gravity data is sparse in a small coastal gap between terrestrial and marine gravity observations, which might explain the MDT lows that are observed in these

areas. Such gravity observation gaps could be filled efficiently with airborne gravimetry in a future regional geoid realization with particular focus on the coastal zone. Further, the regional geoid models are tuned to fit validation data on land, where also the bulk of gravimetric observations are found. Thus, they are not necessarily the best option for describing the short-scale marine gravity field off the Norwegian coast, which was pointed out by *Ophaug et al.* [2015].

Another challenge is posed by the geographical mode mask of CS2. The SARIn mode only stretches out to roughly ~40 km off the coast, where it blends into the LR or SAR mode. Often this border area coincides with the NCC, requiring special attention when combining the CS2 data. Furthermore, being more sparse at the border, the SARIn and LRM/SAR observations are more uncertain in this area. In particular, the border between the SARIn and SAR modes along the south-eastern coast of Norway coincides with the narrow jet of the NCC, making the jet highly dependent on the CS2 data weighting and interpolation methods. The jet is not a distinct feature in the current CS2 MDTs, which should be investigated in the future.

Finally, our CS2 MDTs are based on novel SARIn processing and data screening. The DTU Space retracking system is experimental and under continuous development. Our editing of the CS2 SARIn data is crude, and only ~60% of the raw CS2 data (omitting points on land) are used. This not only suggests that a considerable amount of valid data points did not pass the editing, but also reveals that the CS2 targets along the Norwegian coast are generally noisy and ridden with instrumental "contamination"; e.g., when CS2 passes a fjord with steep mountains on either side, and tracks its own noise instead of the fjord surface. Also, a large amount of CS2 observations inside fjords do not have a valid ocean tide (OT) correction, as they are outside the coverage of the standard global OT model. These observations have been disregarded in this work, but could be included in the future by considering local ocean tide corrections [*Idžanović et al.*, 2016]. Future improvements of the retracker system and the application of other retrackers may mitigate noise effects, and a more elaborate and robust statistical editing of the data may remediate a larger amount of valid observations.

At the current stage our results highlight the great improvement in coastal MDT determination due to the SAR(In) altimeter onboard CS2, giving a peek ahead of the results from new-generation SAR and SARIn altimeters such as the Sentinel-3 mission of the

Copernicus program, and the Surface Water and Ocean Topography (SWOT) mission of NASA/CNES, respectively.

Acknowledgments

We acknowledge the open data policy of ESA, MET Norway, PSMSL and RADS. We would like to thank Karina Nielsen at DTU Space for preparing the SARIn dataset, and Kristian Breili at NMA for providing data and helpful comments. Figures were drafted using GMT. Data used to produce Figures 1-3 and supporting information Table S4 are available upon request. This work is part of the Norwegian University of Life Science's GOCODYN project, supported by the Norwegian Research Council under project number 231017.

References

Abulaitijiang, A., O. B. Andersen, and L. Stenseng (2015), Coastal sea level from inland CryoSat-2 interferometric SAR altimetry, *Geophys. Res. Lett.*, *42*, doi:10.1002/2015GL063131.

Ågren, J., G. Strykowski, M. Bilker-Koivula, O. C. D. Omang, S. Märdla, T. Oja, A. Ellmann, I. Liepins, E. Parseliunas, R. Forsberg, J. Kaminskis, L. E. Sjöberg, and G. Valsson (2016), On the development of the new Nordic gravimetric geoid model NKG2015, paper presented at the IAG Symposium on Gravity, Geoid and Height Systems, Thessaloniki, Greece, September 19–23.

Armitage, T. W. K., and M. W. J. Davidson (2014), Using the Interferometric Capabilities of the ESA CryoSat-2 Mission to Improve the Accuracy of Sea Ice Freeboard Retrievals. *IEEE Trans. Geosci. Remote Sens.*, *52*(1), 529–536, doi:10.1109/TGRS.2013.2242082.

Budgell, W. P. (2005), Numerical simulation of ice-ocean variability in the Barents Sea region. Towards dynamical downscaling, *Ocean Dyn.*, *55*, 370–387, doi:10.1007/s10236-005-0008-3.

Chelton, D. B., J. C. Ries, B. J. Haines, L.-L. Fu, and P. S. Callahan (2001), Chapter 1 Satellite Altimetry, in Satellite Altimetry and Earth Sciences — A Handbook of Techniques and Applications, edited by L.-L. Fu and A. Cazenave, pp. 1–131, Academic Press, San Diego, California, doi:10.1016/S0074-6142(01)80146-7.

Dee, D. P., S. M. Uppsala, A. J. Simmons, P. Berrisford, P. Poli, S. Kobayashi, U. Andrae, M. A. Balmaseda, P. Bauer, P. Bechtold, A. C. M. Beljaars, L. van de Berg, J. Bidlot, N. Bormann, C. Delsol, R. Dragani, M. Fuentes, A. J. Geer, L. Haimberger, S. B. Healy, H. Hersbach, E. V. Hólm, L. Isaksen, P. Kållberg, M. Köhler, M. Matricardi, A. P. McNally, B. M. Monge-Sanz, J.-J. Morcrette, B.-K. Park, C. Peubey, P. de Rosnay, C. Tavolato, J.-N. Thépaut, and F. Vitart (2011), The ERA-Interim reanalysis: configuration and performance of the data assimilation system, *Quart. J. R. Met. Soc.*, *137*, 553–597, doi:10.1002/qj.828.

Denker, H. (2016), A new European gravimetric (quasi)geoid EGG2015, paper presented at the IAG Symposium on Gravity, Geoid and Height Systems, Thessaloniki, Greece, September 19–23.

Drinkwater, M. R., R. Floberghagen, R. Haagmans, D. Muzi, and A. Popescu (2003), GOCE: ESA's first Earth Explorer Core mission, in Earth Gravity Field from Space — From Sensors to Earth Sciences, Space Sciences Series of ISSI, edited by G. Beutler et al., pp. 419–432, Springer, Netherlands, doi:10.1007/978-94-017-1333-7_36.

Egbert, G. D., and S. Y. Erofeeva (2002), Efficient inverse modeling of barotropic ocean tides, *J. Atmos. Oceanic Technol.*, *19*, 183–204, doi:10.1175/1520-0426(2002)019<0183:EIMOBO>2.0.CO;2.

Ekman, M. (1989), Impacts of geodynamic phenomena on systems for height and gravity, *Bull. Geod.*, *63*, 281–296, doi:10.1007/BF02520477.

ESA and Mullard Space Science Laboratory - University College London (2012), CryoSat Product Handbook, 90pp.

Gommenginger, C., P. Thibaut, L. Fenoglio-Marc, G. Quartly, X. Deng, J. Gómez-Enri, P. Challenor, and Y. Gao (2011), Retracking altimeter waveforms near the coasts, in Coastal Altimetry, edited by S. Vignudelli et al., pp. 61–101, Springer, Berlin Heidelberg, doi:10.1007/978-3-642-12796-0_4.

Haidvogel, D. B., H. Arango, W. P. Budgell, B. D. Cornuelle, E. Curchitser, E. Di Lorenzo, K. Fennel, W. R. Geyer, A. J. Hermann, L. Lanerolle, J. Levin, J. C. McWilliams, A. J. Miller, A. M. Moore, T. M. Powell, A. F. Shchepetkin, C. R. Sherwood, R. P. Signell, J. C. Warner, and J. Wilkin (2008), Ocean forecasting in terrain-following coordinates: Formulation and skill assessment of the Regional Ocean Modeling System, *J. Comp. Phys.*, *227*, 3595–3624, doi:10.1016/j.jcp.2007.06.016.

Higginson, S., K. R. Thompson, P. L. Woodworth, and C. W. Hughes (2015), The tilt of mean sea level along the east coast of North America, *Geophys. Res. Lett.*, doi:10.1002/2015GL063186.

Holgate, S. J., A. Matthews, P. L. Woodworth, L. J. Rickards, M. E. Tamisiea, E. Bradshaw, P. R. Foden, K. M. Gordon, S. Jevrejeva, and J. Pugh (2013), New data systems and products at the Permanent Service for Mean Sea Level *J. Coastal Res.*, *29*, doi:10.2112/jcoastres-d-12-00175.1.

Hughes, C. W., R. J. Bingham, V. Roussenov, J. Williams, and P. L. Woodworth (2015), The effect of Mediterranean exchange flow on European time mean sea level, *Geophys. Res. Lett.*, *42*, 466–474, doi:10.1002/2014GL062654.

Idžanović, M., V. Ophaug, and O. B. Andersen (2016), Coastal sea level in Norway from CryoSat-2 SAR altimetry, in Proceedings of the 2016 European Space Agency Living Planet Symposium, ESA Special Publication SP-740 on CD-ROM, Prague, Czech Republic, May 9-13.

Jain, M., O. B. Andersen, J. Dall, and L. Stenseng (2015), Sea surface height determination in the Arctic using Cryosat-2 SAR data from primary peak empirical retrackers, *Adv. Space Res.*, *55*, 40–50, doi:10.1016/j.asr.2014.09.006.

Koch, K.-R. (1999), Parameter Estimation and Hypothesis Testing in Linear Models, Springer, Berlin.

Lin, H., K. R. Thompson, J. Huang, and M. Véronneau (2015), Tilt of mean sea level along the Pacific coasts of North America and Japan, *J. Geophys. Res. Oceans*, *120*, 6815–6828, doi:10.1002/2015JC010920.

Moritz, H. (1980), Advanced Physical Geodesy, Herbert Wichmann Verlag, Karlsruhe.

Ophaug, V., K. Breili, and C. Gerlach (2015), A comparative assessment of coastal mean dynamic topography in Norway by geodetic and ocean approaches, *J. Geophys. Res. Oceans*, *120*, 7807–7826, doi:10.1002/2015JC011145.

Orvik, K. A., Ø. Skagseth, and M. Mork (2001), Atlantic inflow to the Nordic Seas: Current structure and volume fluxes from moored current meters, VM-ADCP and SeaSoar-CTD observations, 1995-1999, *Deep Sea Res.*, *19*, 937–957, doi:10.1016/S0967-0637(00)00038-8.

Petit, G., and B. Luzum (eds.) (2010), IERS Conventions (2010), IERS Technical Note 36, 179pp, Verlag des Bundesamts für Kartographie und Geodäsie, Frankfurt am Main.

Pugh, D., and P. L. Woodworth (2014), Sea-Level Science: Understanding Tides, Surges, Tsunamis and Mean Sea-Level Changes, Cambridge University Press, Cambridge.

Rhines, P., S. Häkkinen, and S. A. Josey (2008), Is Oceanic Heat Transport Significant in the Climate System?, in Arctic-Subarctic Ocean Fluxes, edited by R. R. Dickson et al., pp. 87–109, Springer Netherlands, doi:10.1007/978-1-4020-6774-7_5.

Røed L. P., and J. Debernard (2004), Description of an integrated flux and sea-ice model suitable for coupling to an ocean and atmosphere model, *met.no Report 4/2004*, 56pp, Norwegian Meteorological Institute, Oslo, Norway.

Scharroo, R., E. W. Leuliette, J. L. Lillibridge, D. Byrne, M. C. Naeije, and G. T. Mitchum (2013a), RADS: Consistent multimission products, in Proc. of the Symposium on 20 Years of Progress in Radar Altimetry, ESA SP-710, ESA Spec. Publ.

Scharroo, R., W. H. F. Smith, E. W. Leuliette, and J. L. Lillibridge (2013b), RADS: The performance of CryoSat as an ocean altimeter, in Proc. of the Third CryoSat-2 User Workshop, ESA SP-717, ESA Spec. Publ.

Skagseth, Ø., K. F. Drinkwater, and E. Terrile (2011), Wind- and buoyancy-induced transport of the Norwegian Coastal Current in the Barents Sea, *J. Geophys. Res.*, *116*, C08007, doi:10.1029/2011JC006996.

Solheim, D. (2000), New height reference surfaces for Norway, in Report on the Symposium of the IAG Subcommission for Europe (EUREF) in Tromsø, June 22–24, edited by J. A. Torres and H. Hornik, pp. 154–158, Verlag der Bayerischen Akademie der Wissenschaften, Munich.

Vignudelli, S., A. G. Kostianoy, P. Cippolini, and J. Benveniste (eds.) (2011), Coastal Altimetry, Springer, Berlin Heidelberg, doi:10.1007/978-3-642-12796-0.

Villadsen, H., X. Deng, O. B. Andersen, L. Stenseng, K. Nielsen, and P. Knudsen (2016), Improved inland water levels from SAR altimetry using novel empirical and physical retrackers, *J. Hydrol.*, *537*, 234–247, doi:10.1016/j.jhydrol.2016.03.051.

Weatherall, P., K. M. Marks, M. Jakobsson, T. Schmidt, S. Tani, J. E. Arndt, M. Rovere, D. Chayes, V. Ferrini, and R. Wigley (2015), A new digital bathymetric model of the world's oceans, *Earth Space Sci.*, *2*, 331–345, doi:10.1002/2015SEA000107.

Wessel, P., W. H. F. Smith, R. Scharroo, J. Luis, and F. Wobbe (2013), Generic Mapping Tools: Improved Version Released *EOS Trans. AGU*, *94*, 409–410, doi:10.1002/2013EO450001.

Wingham, D. J., C. R. Francis, S. Baker, C. Bouzinac, D. Brockley, R. Cullen, P. de Chateau-Thierry, S. W. Laxon, U. Mallow, C. Mavrocordatos, L. Phalippou, G. Ratier, L. Rey, F. Rostan, P. Viau, and D. W. Wallis (2005), CryoSat: A mission to determine the fluctuations in Earth's land and marine ice fields, *Adv. Space Res.*, *37*, 841–871, doi:10.1016/j.asr.2005.07.027.

Woodworth, P. L. (2012), A note on the nodal tide in sea level records, *J. Coastal Res.*, *28*(2), 316–323, doi:10.2112/jcoastres-d-11A-00023.1.

Woodworth, P. L., C. Hughes, R. J. Bingham, and T. Gruber (2012), Towards world-wide height system unification using ocean information, *J. Geod. Sci.*, *2*, 302–318, doi:10.2478/v10156-012-0004-8.

Woodworth, P. L., M. Gravelle, M. Marcos, G. Wöppelmann, and C. W. Hughes (2015), The status of measurement of the Mediterranean mean dynamic topography by geodetic techniques, *J. Geod.*, *89*, 1–17, doi:10.1007/s00190-015-0817-1.

Wunsch, C., and D. Stammer (1997), Atmospheric loading and the oceanic "inverted barometer" effect, *Rev. Geophys.*, *35*, 79–107, doi:10.1029/96RG030337.

Supporting Information for
"The Norwegian Coastal Current observed by CryoSat-2 and GOCE"

Martina Idžanović[1]*, Vegard Ophaug[1], and Ole Baltazar Andersen[2]

[1]Faculty of Science and Technology, Norwegian University of Life Sciences (NMBU), Ås, Norway

[2]DTU Space, Technical University of Denmark, Kgs. Lyngby, Denmark

Contents

1. Text S1
2. Tables S1 to S4

Introduction

This supporting information includes a text describing the geostrophic equations and the optimal interpolation technique used for determining the geodetic MDTs in this work (see text for more details). In addition, four tables are included, showing covering areas and grids for the regional geoid models, the range and geophysical corrections applied to the CryoSat-2 altimetry data, the locations of the tide gauges used in this work, and statistics of the computed MDTs, respectively.

Text S1.

The geostrophic surface currents [e.g., *Wunsch and Stammer*, 1998] are given by

$$u = -\frac{g}{fR}\frac{\partial \mathrm{MDT}}{\partial \varphi}, \tag{1}$$

and

$$v = \frac{g}{fR\cos\varphi}\frac{\partial \mathrm{MDT}}{\partial \lambda}, \tag{2}$$

*Drøbakveien 31, 1433 Ås, Norway

Corresponding author: Martina Idžanović, martina.idzanovic@nmbu.no

Table 1. Covering areas and grids for the used geoid models

Geoid model	φ (°)	λ (°)	$\Delta\varphi$ (°)×$\Delta\lambda$ (°)
NMA2014	$53° \leq \varphi \leq 77.99°$	$-15° \leq \lambda \leq 40°$	$0.01° \times 0.02°$
NKG2015	$53° \leq \varphi \leq 73°$	$0° \leq \lambda \leq 34°$	$0.01° \times 0.02°$
EGG2015	$25.0083° \leq \varphi \leq 84.9917°$	$-49.9917° \leq \lambda \leq 69.9917°$	$0.017° \times 0.017°$

where u and v are the zonal (east-west) and meridional (north-south) components, respectively. R is the mean Earth radius, g is gravity, and $f = 2\omega \sin\varphi$ is the Coriolis parameter, of which the angular velocity of the Earth ω forms a part.

The interpolation of SARIn DOT observations was done with the GEOGRID routine [*Forsberg and Tscherning*, 2008]. It uses least-squares collocation [*Moritz*, 1980]

$$\hat{\mathbf{s}} = \mathbf{C}_{sl} \left(\mathbf{C}_{ss} + \mathbf{C}_{nn}\right)^{-1} \mathbf{l}, \tag{3}$$

where $\hat{\mathbf{s}}$ is the predicted MDT value, $\mathbf{l}$ contains the DOT observations, $\mathbf{C}_{ss}$ and $\mathbf{C}_{nn}$ are the signal and noise parts of the covariance matrix of the observations $\mathbf{l}$, respectively, and $\mathbf{C}_{sl}$ is the covariance matrix between signal and observations.

GEOGRID uses the second-order Gauss-Markov covariance function [*Moritz*, 1980], given by

$$C(r) = C_0 \left(1 + \frac{r}{\alpha}\right) \exp\left(-r/\alpha\right), \tag{4}$$

where r is the distance between prediction and observation points, C_0 is the signal variance, and α is the correlation length. In this work, α has been empirically determined to 80 km and an uncertainty of 3 cm was assigned to the data.

References

Cartwright, D. E., and R. J. Tayler (1971), New computations of the tide-generating potential, *Geophys. J. R. Ast. Soc.*, *33* (3), 253–264, doi:10.1111/j.1365-246X.1971.tb01803.x.

Table 2. Applied range and geophysical corrections

Correction	RADS LRM	ESA SARIn
Dry	ECMWF	ECMWF
Wet	ERA	ECMWF
Iono	GIM [a]	GIM
LF [b]	IB w/ECMWF	IB w/ECMWF
HF [c]	MOG2D	No HF
SSB	Non-param	No SSB
OT	GOT4.10	FES2004
SET	CT [d]	CT
PT	*Wahr* [1985]	*Wahr* [1985]
Range bias	-	+0.690 m
Period	2012-2015	2012-2015

[a] GIM: global ionosphere map.

[b] Low frequency contribution with periods > 20 days.

[c] High frequency contribution with periods < 20 days.

[d] CT: Tidal potential from *Cartwright and Tayler* [1971] and *Cartwright and Edden* [1973].

Table 3. Tide gauges in our work

Tide gauge	Code	ID	φ (°)	λ (°)
Vardø	VARD	19	70.375	31.104
Honningsvåg	HONN	18	70.980	25.973
Hammerfest	HAMM	17	70.665	23.683
Tromsø	TROM	16	69.647	18.961
Andenes	ANDE	15	69.326	16.135
Harstad	HARS	14	68.801	16.548
Kabelvåg	KABE	13	68.213	14.482
Bodø	BODO	12	67.288	14.391
Rørvik	RORV	11	64.860	11.230
Mausund	MAUS	10	63.869	8.666
Heimsjø	HEIM	9	63.425	9.102
Kristiansund	KRIN	8	63.114	7.734
Ålesund	ALES	7	62.469	6.152
Måløy	MALO	6	61.934	5.113
Bergen	BERG	5	60.398	5.321
Stavanger	STAV	4	58.974	5.730
Tregde	TREG	3	58.006	7.555
Helgeroa	HELG	2	58.995	9.856
Viker	VIKE	1	59.036	10.950

Table 4. Statistics of the MDTs used in this work (m).

Model	min	max	mean	$\hat{\sigma}$
NorKyst800	-0.6756	-0.0761	-0.3665	0.1178
$C2_{NKG}$	-0.3750	0.4180	0.0747	0.1281
$C2_{EGG}$	-0.2710	0.4780	0.1064	0.1255
$C2_{NMA}$	-0.3030	0.4780	0.1099	0.1296
$C2_{NKG}$ - NorKyst800	-0.2590	0.2423	-0.0573	0.0616
$C2_{EGG}$ - NorKyst800	-0.3310	0.3085	-0.0670	0.0765
$C2_{NMA}$ - NorKyst800	-0.2800	0.2345	-0.0650	0.0628

Cartwright, D. E., and A. C. Edden (1973), Corrected tables of tidal harmonics, *Geophys. J. R. Ast. Soc.*, *23* (1), 45–73, doi:10.1111/j.1365-246X.1973.tb03420.x.

Forsberg, R. and C. C. Tscherning (2008), An overview manual for the GRAVSOFT geodetic gravity field modelling programs, 2nd edn. Contract Report to JUPEM, Aug 2008.

Moritz, H. (1980), Advanced Physical Geodesy, Herbert Wichmann Verlag, Karlsruhe.

Wahr, J. M. (1985), Deformation induced by polar motion, *J. Geophys. Res.*, *90*, B11, doi:10.1029/JB090iB11p09363.

Wunsch, C., and D. Stammer (1998), Satellite altimetry, the marine geoid, and the oceanic general circulation, *Annu. Rev. Earth Planet. Sci.*, *26*, 219–253, doi:10.1146/annurev.earth.26.1.219.

Paper F

Noname manuscript No.
(will be inserted by the editor)

Accuracy of Regional Geoid Modelling with GOCE

Christian Gerlach · Vegard Ophaug

Received: date / Accepted: date

Abstract Regional geoid models are based on the combination of satellite-only gravity field information and terrestrial data. Satellite information is conveniently provided in terms of spherical harmonic global potential models. Terrestrial information is mostly provided in terms of point or block mean values of gravity in the region of interest. Combination of the two sources of information in the overlapping spectral band is either based on deterministic or on stochastic considerations. We have tested different schemas for weighting satellite and terrestrial information and compared the results to GNSS-levelling data in Norway. The results provide implications for the quality of terrestrial data in the study area and for regional geoid modeling based on GOCE satellite models in general.

In order to minimize the computational burden, we avoid field transformation (from gravity anomalies to geoid heights) by employing an already existing regional geoid model to represent the terrestrial information. Combination is then performed by filtering geoid grids in the spatial domain.

Keywords Regional Geoid · Spectral Combination · GNSS-Levelling · GOCE

Ch. Gerlach
Bavarian Acadamy of Sciences and Humanities
Commission for Geodesy and Glaciology
Alfons-Goppel-Str. 11, 80687 Munich, Germany
E-mail: gerlach@keg.badw.de
and
Norwegian University of Environmental and Life Sciences
Institute for Mathematical Sciences and Humanities
Døbakveien 31, 1433 Ås, Norway

V. Ophaug
Norwegian University of Environmental and Life Sciences
Institute for Mathematical Sciences and Humanities
Døbakveien 31, 1433 Ås, Norway
E-mail: vegard.ophaug@nmbu.no

1 Introduction

High resolution gravity field and geoid models are of interest for geodetic and geophysical applications. A high resolution geoid model may, e.g., be used to define the vertical datum of a certain region with a focus on efficient determination of physical heights by means of GNSS-levelling [14]

A state-of-the-arte high resolution geoid is based on (i) data from satellite gravity missions for modelling its large scale features and (ii) terrestrial (including airborne and shipborne) data for those smaller scales which are not observable from space. Today, combined GRACE/GOCE models allow reconstructing the global gravity field down to resolutions of about 100 km with accuracies at the centimeter-level [1]. In our study, we use the global potential models (GPM) DIR5 [1] and GOCO05s [10], both of which are based on GRACE and release 5 GOCE data.

In order to fully exploit the high quality of these GPMs, optimal combination with the terrestrial data available in the specific area of investigation is required. The selection of spectral weights for satellite and terrestrial data in the overlapping spectral band depends on the geographic location (due to slight inhomogenities in the quality of satellite-only GPMs, see Fig. 1) and on quality and distribution of terrestrial observations. For example, in a region with sparse and/or less accurate gravity data, satellites may still provide valuable information for scales well below 100 km resolution (maybe down to 70 km), i.e. satellite information dominates the overlapping spectral band. However, in regions with dense and high quality terrestrial data (like the USA or central Europe) terrestrial information may outperform satellite data even for scales well above 100 km (say, up to 150 km, or so). Then terrestrial data dominates the

common band. In the latter case the total error budget may end up at the level of some few centimeters in terms of geoid heights (see, e.g., [13], [4])

Optimal combination of satellite and terrestrial data requires selecting a weighting schema based on some optimization criterion. There exist deterministic and stochastic schemas, see, e.g., [15] or [5].

Here we specifically test the stochastically optimal spectral combination method proposed by Wenzel [16], [17]. Thereby, the error degree variances of the satellite-only global potential model, σ_l^{GPM}, and those of the terrestrial data, $\sigma_l^{\Delta g}$ are combined in a Wiener-type filtering schema according to

$$w_l = \frac{(\sigma_l^{\mathrm{GPM}})^2}{(\sigma_l^{\mathrm{GPM}})^2 + \left(\sigma_l^{\Delta g}\right)^2}. \quad (1)$$

For each spherical harmonic (SH) degree l, the w_l are spectral weights for the satellite information and $(1 - w_l)$ represent the complementary weights for the terrestrial data. The approach assumes, (i) that the errors are isotropic and homogenous (thus they can be represented by error degreee variances) and (ii) that they are uncorrelated. Both aspects need to be considered in the construction of the degree variances (see section 2) and when interpreting the results (see section 4).

The aim of our study is to investigate different combination schemas for a test region in the Nordic countries. The focus is on data weighting in the spectral transition zone from satellite-only to terrestrial-only information. Because the quality description of the terrestrial data is difficult to judge, we derive Wenzel-weights w_l under different assumptions for $\sigma^{\Delta g}$, namely {0.2, 1.0, 2.0} mGal, and we compare the results to independent GNSS-levelling data in Norway. In addition to the stochastic approach, we test deterministic approaches, like the classical Wong & Gore kernel modification [18] and simple data blending based on a Gaussian filter kernel as implemented, e.g., in [13]. The Wong & Gore filter is chosen, because it is traditionally applied in the computation of Norwegian geoid models. Here we use the 2014-version regional geoid model NMA2014, provided by the Norwegian Mapping Authority (Ove Omang, personal communication). The model is a combination of terrestrial data and the release-4 GOCE model DIR4 [2] employing a Wong & Gore type modification. The latter does not cut the kernel at one specific degree, but employs a linear transition of the weights (from 1 to 0) over the narrow spectral band between SH-degrees 130 and 140 (see the spectral weights in Fig. 2). The Gaussian filter is chosen, because it was used in [12] for the generation of a simplified update of NMA2014. Thereby NMA2014 was combined with DIR5 using a Gaussian filter (correlation length 80 km), thus effectively "replacing" DIR4 by DIR5. This update decreased the standard deviation of the residuals with respect to GNSS-levelling from 3.5 cm to 3.0 cm.

As the focus of this study is on data weighting, we do not go into specific methods for geoid computation, like Stokes integration, least-squares collocation or other alternatives. Actually we avoid field transformation from gravity anomalies to geoid heights, but represent the terrestrial data by a high-pass filtered version of the regional geoid model. Geoid heights generated on the same geographic grid from the the coefficients of a GPM are smoothed with the complementary low-pass filter and the two grids are added to form the combined geoid solution.

Section 2 presents the error degree variances used for construction of the spectral weights w_l. The latter are treated in section 3. Based on the error degree varainnces and the spectral weights, formal errors are derived for the combined geoid solutions. The actual geoid models are compared to GNSS-levelling data, thus providing empirical error estimates. Formal and empirical errors are discussed in section 4 and the results are summarized in section 5.

We may also have to mention, that, strictly speaking, the quantities we work with are height anomalies and normal heights. However, since our focus is on data weighting and the results should be independent from the technical differences between geoid and quasigeoid computation, we will consistently use the term geoid throughout the text, even though this may seem a bit loose in some places.

2 Error degree variances

2.1 Error degree variance of terrestrial gravity data

Regional geoid computation is based on point gravity data or corresponding area averages. Thereby the following error contributions are of relevance: (i) errors of original gravity observations, (ii) errors of the point coordinates when computing anomalies, (iii) any compuational errors that arise in the process of forming area averages, or in applying data reductions and (iv) last but not least, the representation error, i.e., the ability of a point value to represent the gravity field in its neighbourhood.

In many cases, information to fully account for all of the above errors is not readily available. In our case, we do not even go back to the original gravity data, but start with the regional geoid model derived from it. Trying to help out, we acknowledge, that NMA2014 is based on a set of terrestrial gravity values which was

in large parts provided for the computation of the European gravimetric geoid model EGG2008 [3]. Therefore, we approximate the short scale error behaviour of NMA2014 by the error description of EGG2008 as published in [3]. There it is provided in the form of the error covariance function of geoid heights; from this we have derived error degree variances $\sigma_l^{\mathrm{EGG2008}}$ by spectral analysis.

The error description of EGG2008 is based on a 1 mGal correlated noise model (for the terrestrial part) and on error degree variances of the GPM EIGEN-5S [8]; thus the satellite part is effectively represented by error degree variances from GRACE (see the error degree variances in Fig. 3). The spectral transition from pure GRACE to pure terrestrial information happens in the band between SH-degree 60 and 120. Thus the error model is effectively free from satellite information above degree 120. This does not exactly correspond to NMA2014, where satellite data is used up to degree 140. As will be shown later, optimal combination employs GOCE data even above degree 140. Therefore, this spectral range is reduced from NMA2014 by high-pass filtering and NMA2014 provides only information for the shorter scales well above degree 140. Thus, we may with good reason, set

$$\sigma_l^{\Delta g} \;\approx\; \sigma_l^{\mathrm{NMA2014}} \;\approx\; \sigma_l^{\mathrm{EGG2008}} \qquad (2)$$

for the spectral band above $l = 140$ and neglect the fact that, in theory, we violate the basic requirement for the Wenzel-approach in Equ. (1), namely that satellite and terrestrial information should be uncorrelated.

2.2 Error degree variances from satellite-only gravity models

The error description of DIR5 and GOCO05s is provided in the form of the full error variance-covariance matrix (VCM). However, Equ. (1) requires rather condensed information in terms of error degree variances. The full VCM does not represent a globally homogenous and isotropic error behaviour as implied by using error degree variances. Here we use a two-step procedure to construct a degree variance model that allows approximating the full VCM in the study area.

In the first step, we approximate the full VCM by the diagonal blocks of constant SH-order m, hereafter termed as the m-block or mbm-approach. The m-blocks contain the most significant correlations of the full VCM and describe about 99% of the geoid error, see [9]. The corresponding geoid error is perfectly latitude-dependent, but not homogenous, as shown in Fig. 1. It differs significantly from the geoid error derived from error degree variances only. This latter approach neglects not only all error correlations of the original VCM (it takes only error variances into account), but additionally assumes homogenous and isotropic error behaviour. The geoid error computed from this degree variance or c_{n}-approach is constant all over the globe (if evaluated on a sphere of constant radius).

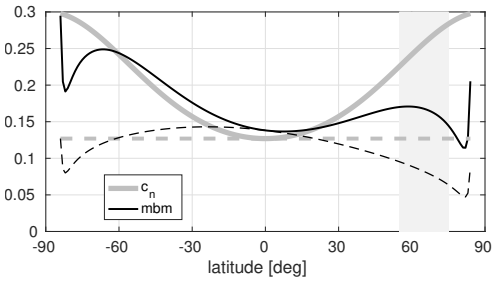

Fig. 1 Geoid height formal errors from GOCO05s (full resolution) as function of latitude in units of [m]. Error propagation is based on either the c_n-approach (gray curves) or the mbm-approach (black curves). Solid lines include downward continuation to the surface of the ellipsoid, while dashed lines refer to a sphere of radius $R = 6\,378$ km. The gray area marks the latitude range of our test region (Norway).

The second step provides a local approximation of the mbm-approach by rescaling the error degree variances. Practically, the error covariance function is derived from the c_{n}-approach, but its amplitude is scaled to fit its error variance (gray curve in Fig. 1) to the error variance from the mbm-approach (black curve in Fig. 1). The scaling factor is a function of latitude. Because the factor changes only smoothly with latitude, we may use an average scaling factor to generate a sufficient approximation of the mbm-based geoid error for local to regional applications. For our test area in Norway we have used the scaling factor for the average latitude of 65° and applied it to the whole study area (which stretches from about 55° to 75° latitude). The corresponding latitude band is marked with gray in Fig. 1.

Considering Fig. 1 it is also worth mentioning, that the dashed lines are valid on a sphere of constant radius $R = 6\,378\,137$ m, while the solid lines are valid on the surface of the ellipsoid, i.e., they involve downward continuation. Due to a slight orbit excentricity of the GOCE satellite, the error is not symmetric with respect to the equator. This asymmetry is amplified through downward continuation, because the orbit height is larger over the southern hemisphere and smaller over the northern hemisphere. Thus the error is significantly larger in southern latitudes than in the correspoding northern latitudes.

3 Spectral weights and filter functions

Figure 2 shows the spectral weights for some of the combination schemas. Comparing the three GOCO05s curves (each with different error assumption for the terrestrial data), it is obvious, that the worse the terrestrial data is assumed to be, the higher the weights for GOCE data are. Comparison of DIR5 and GOCO05s (employing the same assumption on $\sigma_l^{\Delta g}$) shows, that the DIR5-combination puts more weight on the satellite information. This is because the formal errors of DIR5 are smaller than the GOCO05s-errors.

As satellite-only GPMs should provide the best information for the long wavelength, the weights should be equal to one for the lower part of the spectrum. This is the case for Wenzel-type combinations which are based on the assumption, that $\sigma_l^{\Delta g} = 1.0$ mGal or worse. It is not the case, if the error degree variances for the terrestrial data are scaled to provide the smaler 0.2 mGal error amplitude. This is due to our specific definition of the error degree variances for the terrestrial data. As mentioned earlier, the errors for the lower SH-degrees are taken from the GRACE-based model EIGEN-5S and these error degree variances are also rescaled. This is of course rather crude and generates the artificial behaviour of the spectral weights (thin, black line in Fig. 2). However, we accepted this for our purpose as it hardly affects the overall cumulative error budget (effectively GOCO05s is partly replaced by the GRACE model EIGEN-5S, which also provides good information for the longer wavelengths).

Concerning the Gaussian weights, one may try to represent different quality of the terrestrial data by chosing a different filter length; if terrestrial data is assumed to be of good quality, the filter length will be larger. However, for various realistic error assumptions, the weights for the satellite data will always start decaying even for the longest wavelengths. Therefore, this approach can only provide good results, if both, terrestrial and satellite data are of good quality for long wavelengths. This is the case for our combination of NMA2014 and release 5 GOCE models. It may not be the case, when combining GOCE and an old regional geoid model, which is not already based on GRACE or GOCE data.

The isotropic spatial filter functions are constructed according to

$$W(\psi) \;=\; \sum_{l=2}^{\infty} w_l \, P_l \left(\cos\psi\right) \tag{3}$$

where $P_l(\cos\psi)$ are the conventional Legendre polynomials and ψ is the spherical distance between computation and integration point. In practise the summation is carried out to a high SH-degree (e.g. $l = 10\,000$) and the integration is limited to a certain spherical cap around the compution point. Here we have taken care, that the filter function smoothly tends to zero, by applying a Meissl-type modification. The effective integration cap for the different functions is around 2°. In addition, all functions are normalized (integral of the filter function over the spherical integration cap is equal to 1).

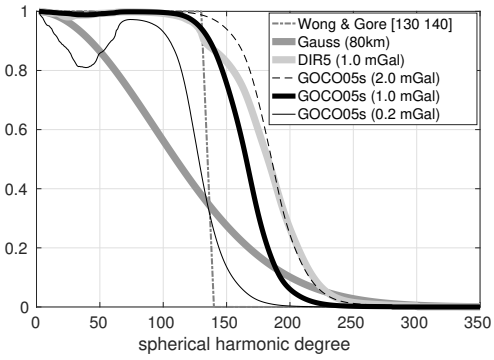

Fig. 2 Spectral filter weights w_l using different filtering schemas for combination. The Wong&Gore as well as the Gaussian weights are deterministic schemas. All other curves represent stochastic schemas according to Wenzel, employing scaled error degree variances for either DIR5 or GOCO05s along with different assumptions on the error amplitude of terresrial gravity data.

4 Results

Figures 3 and 4 show error degree variances resp. cumulative geoid errors of some selected geoid solutions. These numbers reflect the expected formal error of the geoid models. Table 1 shows the statistics of the comparison to GNSS-Levelling for several more scenarios. In contrast to the formal errors shown in the figures, these numbers represent empirical errors which also contain contributions from GNSS and levelling.

Tab. 1 also contains results for some older nordic geoid models, namely NKG96 [6] and NKG2004 [7]. The results nicely reflect the improvement brought by GRACE and GOCE during the last 10-15 years (part of the improvement is also due to improvements in the terrestrial databases). NKG96 (pre-GRACE era) gives an overall standard deviation of around 8 cm. This value is reduced to 6 cm for NKG2004 (which includes GRACE) and to around 3 cm for the latest, GOCE-based models.

The formal errors show the importance of optimal combination and of good knowledge of the quality of terrestrial data. The formal error of EGG2008 is estimated to be 2.5 cm. Including GOCE data, even based

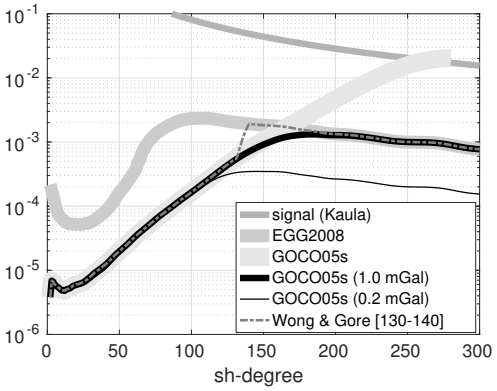

Fig. 3 Geoid height error degree variances for different geoid solutions in units of [m].

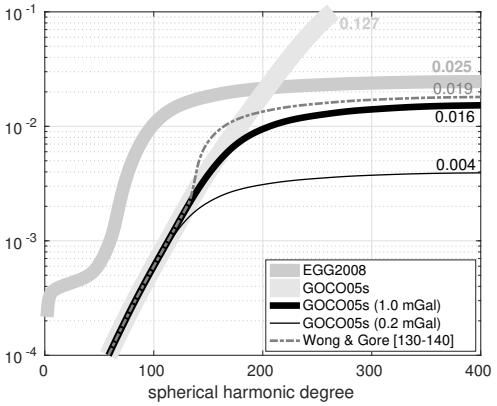

Fig. 4 Cumulative geoid height errors for different geoid solutions in units of [m].

on the quite crude Wong&Gore combination, allows to reduce the error to below 2 cm. Using different error assumptions for the terrestrial data allows to further reduce the error of the combined geoid model. Assuming an error level of 1 mGal, the geoid error goes further down to 1.6 cm; assuming 0.2 mGal yieds an even smaller error of 0.4 cm.

Such a strong variation (2.5 to 0.4 cm) is not reflected by the statistics in Tab. 1. Here all geoid models yield about a 3 cm fit to GNSS-levelling. This fits about to the error budget of the Norwegian height reference surface HREF as derived by [11].

There is only a slight tendency indicating that the Wong&Gore combination as well as the Wenzel-type combinations assuming high quality of terrestrial data (0.2 mGal) do obviously not take enough GOCE data into account. It also seems that the Gauss kernel proves

Table 1 Statistics of the residuals of different geoid solutions with respect to GNSS-levelling data in Norway (mean subtracted). All modified solutions are combinations of either GOCO05s or DIR5 with NMA2014. Units are [cm].

Geoid model	type of modification	min	max	std
NKG96	-	-35.99	19.47	8.48
NKG2004	-	-23.84	16.52	5.91
NMA2014	-	-14.94	12.23	3.41
EGG2015	-	-13.88	8.75	3.43
DIR5	Gauss (80 km)	-13.26	12.45	2.98
DIR5	mbm (2.0 mGal)	-13.25	12.31	2.93
DIR5	mbm (1.0 mGal)	-13.66	12.86	2.94
DIR5	mbm (0.2 mGal)	-13.88	13.10	3.10
DIR5	Wong & Gore	-13.79	13.13	3.11
GOCO05s	Gauss (80 km)	-12.66	12.19	3.00
GOCO05s	mbm (2.0 mGal)	-12.96	12.70	2.94
GOCO05s	mbm (1.0 mGal)	-13.30	12.97	3.01
GOCO05s	mbm (0.2 mGal)	-13.61	12.97	3.12

better than the Wong&Gore combination, however, it can further be improved by the Wenzel-modifications which take more GOCE data into account in the medium wavelength. Besides this, the statistics show that DIR5 gives slightly better results than GOCO05s (when comparing solutions with identical error assumptions for $\sigma^{\Delta g}$). Because the empirical errors do not vary as strong as the formal geoid errors, we assume, that the error budget is dominated by the error of GNSS and levelling.

5 Conclusions

We have generated several regional geoid models for our study area in Norway by applying different types of kernel modifications for optimal combination of GOCE and terrestrial data. The stochastically optimal Wenzel-modification was tested against deterministic modifications that have been used earlier for the study area, namely the Wong&Gore modifications and the Gaussian kernel. Empirical errors were derived from comparison to GNSS-levelling.

In general, the errors show, that GRACE and GOCE have strongly improved the regional geoid over the last decade. The fit to GNSS-levelling drops from 8.5 cm (before the GRACE era) down to about 3 cm (with GOCE data).

The empirical errors vary only slightly around 3 cm. However, in tendency they confirm that those combinations are best, which put more weight on GOCE. This is also reflected by the formal errors. Therefore the

Wong&Gore filter used for NMA2014, does not seem to be optimal.

The formal errors are lower and show larger discrepancies between the different combination schemas. This could be an indication, that the empirical error is dominated by the quality of GNSS-levelling data. Further inspection of these data sets will be valuable for future improvements of the regional geoid model and for deriving a realistic formal error budget.

Geoid modelling on the centimeter to sub-centimeter level is not an easy task. Our formal error budget shows significant differences depending on the quality of terrestrial data in the area of interest. The latest version of the European Gravimetric Geoid model, EGG2015, is optimized with respect to some other validation data sets and obviously not the optimal solution for Norway. It assumes $\sigma^{\Delta g} = 0.2$ mGal, which seems too optimistic for the Norwegian data set - an error of around 2.0 mGal seems more realistic. As the quality of terrestrial data is not necessarily constant for the area of interest, one may also pose the question, if further improvement of regional geoids can be achieved with the classical Stokes approach, where one chooses one single weighting schema for the whole area, i.e. one and the same modified Stokes function. This necessarily requires a compromise between subareas with highest and lowest quality (repectively density) of terrestrial data. Alternative approaches like least-squares collocation or spherical radial basis functions, which allow taking spatial variations in data quality into account, may prove to provide better results. This however, was out of the scope of this study and will be subject to future research.

References

1. Bruinsma, S.L., Förste, C., Abrikosov, O., Lemoine, J.M., Marty, J.C., Mulet, S., Rio, M.H., Bonvalot, S.: ESA's satellite-only gravity field model via the direct approach based on all GOCE data. Geophys. Res. Lett. **41**(21), 2014GL062,045 (2014). DOI 10.1002/2014GL062045
2. Bruinsma, S.L., Förste, C., Abrikosov, O., Marty, J.C., Rio, M.H., Mulet, S., Bonvalot, S.: The new ESA satellite-only gravity field model via the direct approach. Geophysical Research Letters pp. n/a–n/a (2013). DOI 10.1002/grl.50716
3. Denker, H.: Regional gravity field modeling: Theory and practical results. In: G. Xu (ed.) Sciences of Geodesy - II, pp. 185–291. Springer Berlin Heidelberg (2013)
4. Denker, H.: A new European Gravimetric (Quasi)Geoid EGG2015. Thessaloniki, Greece (2016)
5. Featherstone, W.E.: Deterministic, stochastic, hybrid and band-limited modifications of Hotine's integral. J Geod pp. 1–14 (2013). DOI 10.1007/s00190-013-0612-9
6. Forsberg, R., Kaminskis, J., Solheim, D.: The NKG-96 Geoid. In: Proceedings of the 13th General Meeting of the Nordic Geodetic Commision, pp. 255–262. Gävle, Sweden, May 25-29, 1998 (1999)
7. Forsberg, R., Strykowski, G., Solheim, D.: NKG-2004 geoid of the Nordic and Baltic area. Porto, Portugal, Aug. 30 – Sept. 3, 2004 (2004)
8. Förste, C., Flechtner, F., Schmidt, R., Stubenvoll, R., Rothacher, M., Kusche, J., Neumayer, K.H., Biancale, R., Lemoine, J.M., Barthelmes, F., Bruinsma, J., König, R., Meyer, U.: EIGEN-GL05C - A new global combined high-resolution GRACE-based gravity field model of the GFZ-GRGS cooperation. In: Geophysical Research Abstracts, Vol. 10, Abstract No. EGU2008-A-06944 (2008)
9. Gerlach, C., Fecher, T.: Approximations of the GOCE error variance-covariance matrix for least-squares estimation of height datum offsets. Journal of Geodetic Science **2**(4), 247–256 (2012). DOI 10.2478/v10156-011-0049-0
10. Mayer-Gürr, T., Kvas, A., Klinger, B., Rieser, D., Zehentner, N., Pail, R., Gruber, T., Fecher, T., Rexer, M., Schuh, W., Kusche, J., Brockmann, J., Loth, I., Müller, S., Eicker, A., Schall, J., Baur, O., Höck, E., Krauss, S., Jäggi, A., Meyer, U., Prange, L., Maier, A.: The new combined satellite only model GOCO05s. In: Geophysical Research Abstracts Vol. 17, EGU2015-12364 (2015). DOI 10.13140/RG.2.1.4688.6807
11. Mysen, E.: On the computation of reliable formal uncertainties in the densification of GPS-levelling networks by least-squares collocation. J Geod **88**(10), 917–926 (2014). DOI 10.1007/s00190-014-0732-x
12. Ophaug, V., Breili, K., Gerlach, C.: A comparative assessment of coastal mean dynamic topography in Norway by geodetic and ocean approaches. J. Geophys. Res. Oceans pp. n/a–n/a (2015). DOI 10.1002/2015JC011145
13. Rülke, A., Liebsch, G., Sacher, M.: Unification of European height system realizations. Journal of Geodetic Science **2**(4), 343–354 (2012)
14. Rummel, R.: Height unification using GOCE. Journal of Geodetic Science **2**(4), 355–362 (2012)
15. Sjöberg, L.: A general model for modifying Stokes' formula and its least-squares solution. Journal of Geodesy **77**(7), 459–464 (2003). DOI 10.1007/s00190-003-0346-1
16. Wenzel, H.G.: Zur Geoidbestimmung durch Kombination von Schweredaten und einem Kugelfunktionsmodell mit Hilfe von Integralformeln. Zeitschrift für Vermessungswesen **106**, 102–111 (1981)
17. Wenzel, H.G.: Geoid computation by least squares spectral combination using integral formulas. In: Proceedings IAG General Meeting, pp. 438–453. Tokyo, 7-15 May, 1982 (1982)
18. Wong, L., Gore, R.: Accuracy of geoid heights from modified Stokes kernels. Geophys. J. Roy. Astro. Soc. **18** (1969)